Development of a Clustering Algorithm for Universal Color Image Segmentation

By

SEENA JOSEPH

(21053794)

Submitted in fulfillment of the requirements of the

DOCTOR OF PHILOSOPHY IN INFORMATION TECHNOLOGY

In the

DEPARTMENT OF INFORMATION TECHNOLOGY

In the

FACULTY OF ACCOUNTING AND INFORMATICS

At

DURBAN UNIVERSITY OF TECHNOLOGY, SOUTH AFRICA

JULY 2022

DECLARATION

I, Seena Joseph hereby declare that this thesis is my work and has not been previously submitted in any form to any other university or institution of higher learning by other persons or myself. I further declare that all the sources of information used in this thesis have been acknowledged.

19/01/2023

Seena Joseph Date

Approved for final submission

Supervisor: ____ 29/01/2023

Professor O. O. Olugbara Date

PhD (Computer Science)

PUBLICATIONS FROM THIS RESEARCH

Published journal articles

i. Joseph, S. and Olugbara, O. O. 2021. Detecting salient image objects using color histogram clustering for region granularity. J. Imaging, 7 (9): 187.
ii. Joseph, S. and Olugbara, O. O. 2022. Preprocessing effects on performance of skin lesion saliency segmentation. Diagnostics, 12 (2): 344.

Published conference paper

i. Joseph, S. and Olugbara, O. O. 2022. Experimental comparison of ten state-of-the-art saliency detection algorithms for segmenting leukocyte nucleus. Proceedings of 2022 Conference on Information Communications Technology and Society (ICTAS). IEEE, 1-7.

Journal articles to be published

i. Joseph, S. and Olugbara, O. O. 2022. Multivariate meta-analysis of approaches for color image segmentation.
ii. Joseph, S. and Olugbara, O. O. 2023. Multiple correspondence analysis of color image segmentation studies.
iii. Joseph, S. and Olugbara, O. O. 2022. Community detection of color image segmentation studies.
iv. Joseph, S. and Olugbara, O. O. 2023. Spectral clustering of color image segmentation data.

ACKNOWLEDGMENTS

Undertaking this doctoral degree has been truly a life-changing experience for me and it would not have been possible without the support, encouragement, and guidance I received from many people.

I shall begin with God the Almighty for enlightening my life with his light and guidance. Without his will, I would have never found the right path to achieve my goal.

I am immensely grateful to my supervisor Professor Oludayo O. Olugbara who expertly guided me throughout this research. His deep scientific knowledge and unwavering enthusiasm for research was the major driving factor of this journey and kept me constantly engaged with my research. Without his guidance, support, and persistent help this study would not have been possible.

I am grateful to my colleagues for providing me the support and motivation throughout this journey. I owe special thanks to my friends and family for being so supportive by giving me strength, encouragement, and motivation to achieve my goals.

Words cannot express how grateful I am to my father, Mr. Joseph, and my late mother (Elsa Joseph), who made me what I am now.

Finally, to my beloved husband, Raji Joseph, who has been by my side to give all countless support to embark on this journey. Words are beyond to express my thanks to my two lovely sons Rehan and Rishan for being such understanding kids and always giving their love making it possible for me to complete what I started.

TABLE OF CONTENTS

LIST OF FIGURES

LIST OF TABLES

LIST OF ABBREVIATIONS

AHE	Adaptive Histogram Equalization
BGFG	BackGround and ForeGround
BPFS	Background Prior and Foreground Seeds
CA	Context-Aware
CHC	Color Histogram Clustering
CLAHE	Contrast Limited Adaptive Histogram Equalization
CLARA	Clustering LARge Applications
CNN	Convolutional Neural Networks
CNS	Color Name Space
COCO	Common Objects in Contexts
DBSCAN	Density Based Spatial Clustering of Applications with Noise
DCLC	Diffusion-based Compactness and Local Contrast
DPC	Density Peaks Clustering
DRFI	Discriminative Regional Feature Integration
DSR	Dense and Sparse Reconstruction
ECSSD	Extended Complex Scene Saliency Dataset
EM	Expectation-Maximization
FBSS	Foreground and Background Seed Selection
FCB	Foreground Center Background
FCM	Fuzzy C-Means
GMR	Graph-based Manifold Ranking
GR	Graph Regularized
HAM	Human Against Machine
HDCT	High-Dimensional Color Transform
HE	Histogram Equalization
HKU-IS	Hong Kong University Image Segmentation dataset
HSI	Hue, Saturation, Intensity
HSV	Hue, Saturation, Value
ISIC	International Skin Imaging Collaboration
LCNN	Low-level feature embedded CNN
LSC	Linear Spectral Clustering
MAE	Mean Absolute Error
MAP	Markov Absorption Probability
MC	Markov Chain
MCDL	Multi-Context Deep Learning
MRBF	Manifold Ranking Based on robust Foreground
MS	Mean Shift
MSNSD	Multi-Scale Network for Saliency Detection
MSRA	Microsoft Research Asia dataset
PH2	Pedro Hispano hospital image dataset
PICA	Pixel Intensity Clustering Algorithm
PRISMA	Preferred Reporting Items for Systematic reviews and Meta-Analyses
OR	Overlap Ratio
QRGB	Quantized Red Green Blue

RPC	Regional Principal Color
SED	Segmentation Evaluation Dataset
SOM	Self-Organizing Map
SLIC	Simple Linear Iterative Clustering
SOC	Saliency object in Clutter
SOD	Salient Object Detection
TNR	True Negative Rate
TPR	True Positive Rate
TSL	Temporal Sparse Labeling
WBC	White Blood Cell

ABSTRACT

Image segmentation is an important stage of many real-world image applications in the domain of computer vision as a core method for understanding and analyzing digital images. It is aimed to segregate the most salient objects in an image by clustering homogenous regions based on the characteristics of image pixels. Segmentation of salient objects is a complex process because of the existence of numerous inherent characteristics of images that can impede the performance of the process. Due to these diverse image characteristics, a model that is suitable for one category of images is essentially inappropriate for other image categories, which makes image segmentation an open problem. Myriads of classical segmentation algorithms have been developed over the years, yet generalization and universal optimum performance are far from ideal levels. Clustering algorithms have been developed in recent times for the effective segmentation of images. However, the performance of the majority of the existing clustering-based segmentation algorithms substantially relies on the selection of an optimal number of initial clusters. Incorrect cluster count selection may result in uneven highlighting of the target object and be susceptible to under- or over-segmentation of images. This opens an avenue to fully discover a universal clustering algorithm for image segmentation that would be appropriate for manifold classes of images.

In this study, the color histogram clustering algorithm has been proposed to automatically determine a suitable number of clusters that indicates homogenous regions in an image. The aim was to segment the most salient object from its surrounding regions using color histogram clustering that characterizes homogenous regions based on primitive features. The segmentation algorithm starts with histogram clustering-based on the quantized RGB color image to automatically identify the clusters that correspond to the homogenous regions in the image. The perceptual homogeneity of the input RGB color image is achieved by the transformation to L*a*b* color model based on four primitive features. The primitive features are color contrast, contrast ratio, spatial feature, and center prior that are extracted to compute the descriptor of each cluster. The cluster level saliency score is then computed as a function of the four primitive features extracted from the color image. The cluster level saliency is used to compute the final saliency score of each pixel to highlight the target object. The color histogram clustering method of this study combines the Otsu thresholding algorithm with the saliency map to represent the segmented image in a silhouette format. Morphological operations are finally performed to remove the

undesired artifacts that may be present at the segmentation stage. Hence, this present study has introduced a novel, simple, robust, and computationally efficient color histogram clustering algorithm that agglutinates color contrast, contrast ratio, spatial feature, and central prior for efficiently segmenting the target objects in diverse image categories.

The performance of the proposed algorithm was evaluated using the widely used metrics of precision, recall, F-measure, mean absolute error, and overlap ratio on six different categories of images selected from five benchmarked corpora of MSRA10K, ASD, SED2, ImgSal, and DUT OMRON. Moreover, 1000 images from ECSSD, 4447 images from HKU-IS, and 1500 images from COCO datasets were selected to validate the performance of the algorithm on more complex natural datasets. Experimental results have indicated that the proposed algorithm outperformed 30 bottom-up non-deep learning and seven top-down deep learning salient object detection algorithms. The performance of the proposed algorithm was further evaluated on four medical image datasets and the effects of image preprocessing were comprehensively investigated. The performance of the proposed image segmentation algorithm was analyzed in terms of accuracy, sensitivity, specificity, and dice similarity on 10015 images from HAM10000, 2594 images from ISIC2018 dataset, and 200 images from the PH2 dataset against six supervised and six unsupervised benchmark segmentation algorithms. The performance of the proposed algorithm was further validated on the segmentation of 1145 leukocyte nuclei images from the Raabin-WBC dataset in terms of accuracy, sensitivity, specificity, Dice similarity, and Jaccard index. In total, 22307 images with a variety of properties were used to test the performance of the proposed algorithm. In addition, the effects of image preprocessing on the performance of the proposed algorithm were further investigated in this study. The statistical results obtained have shown that the proposed algorithm is free from image preprocessing, and demonstrated its application on a wide class of images without any bounding to the heterogeneous characteristics of the input images. The novelty of the work reported in this thesis has demonstrated that the proposed algorithm is superior to the investigated supervised deep learning and prominent unsupervised segmentation algorithms in terms of quantitative results and visual effects.

CHAPTER ONE: INTRODUCTION

Digital images are one of the key media for information exchange in the field of computer vision. The proliferation of digital image data is fueled by technological advancements in computer vision technology and applications. The ultimate goal of computer vision is to emulate human vision by computers to draw meaningful inferences from visual data and take necessary actions based on it. Human vision can differentiate the multiple features of a scene and extract the region of interest. Though the human vision system can promptly distinguish the region of interest from the background scene, to copycat the human visual system, understanding the image and automatically extracting the region of interest is a challenging task in computer vision applications.

A crucial step for producing meaningful inference to support further image analysis is segmenting an image into homogenous clusters. Image segmentation is an integral stage in computer vision applications that aims to divide the image into meaningful clusters useful for analyzing and recognizing the region of interest. The success of the segmentation process has a direct impact on pattern recognition and classification. Hence precise and robust image segmentation is a crucial prerequisite for image analysis in a variety of fields and is practically applied in numerous application domains, including medical image analysis, object detection and recognition, content-based image retrieval, object tracking, satellite, and aerial image analysis, and video surveillance. The application of image segmentation has resulted in extensive research and numerously proposed segmentation methods. This chapter is organized as follows. An overview of image segmentation, different types of image segmentation algorithms, research problem, research aim and objectives, research contributions, and the thesis outline are provided in the subsequent sections.

1.1 Image segmentation

Image segmentation is the process of partitioning an image into homogenous and disjoint sets that share similar properties such as intensity, color, and contour (Alihodzic and Tuba 2014; Bora and Gupta 2014, 2015; Cuevas *et al.* 2021; Guan *et al.* 2021; Liu and Zhao 2021; Ramesh *et al.* 2021; Zhong and Shih 2021). It aims to recognize homogenous clusters within an image and segregate the region of interest or the most salient objects from the image background making object recognition and interpretation simpler (Feng *et al.* 2020; Oskouei *et al.* 2021). Image segmentation extracts the individual characteristics from a digital image in a form suitable for analyzing and recognizing the

extracted features to meet the demands of various computer vision applications. A digital image is regarded as a spatial dataset that includes enormous amounts of data that require analysis to make it understandable (Dhua *et al.* 2015). It is a two-dimensional function, $f(x, y)$, where $x\ and\ y$ are spatial coordinates. The intensity of the image at a given point (x, y) is defined as the amplitude of f at that point. According to Gonzalez and Woods (2008) a digital image $f(x, y)$ contains M rows and N columns and can be represented as:

$$f(x,y) = \begin{bmatrix} f(0,0) & f(0,1) & \cdots & f(0,N-1) \\ f(1,0) & f(1,1) & \cdots & f(1,N-1) \\ \vdots & \vdots & \cdots & \vdots \\ f(M-1,0) & f(M-1,1) & \cdots & f(M-1,N-1) \end{bmatrix}$$

A picture element, often known as a pixel, is the name of each component in this two-dimensional array. An image is not merely a collection of random pixels, but a meaningful organization of regions and clusters (Bora and Gupta 2014). Extracting the information from images and understanding the extracted images are the key features of computer vision applications. A crucial step in many computer vision applications, including object detection, object recognition, target tracking, and classification, is the segmentation of salient objects from images (Shan 2018; Feng *et al.* 2020).

Predominantly the segmentation process assembles the image pixels into homogeneous clusters based on the characteristics of pixels (Alihodzic and Tuba 2014; Bora and Gupta 2014, 2015; Ramella and Di Baja 2016; Zhang *et al.* 2020c; Mittal *et al.* 2021) to represent an image that is more meaningful and manageable for further analysis and interpretation (Dhanachandra and Chanu 2017; Ghosal *et al.* 2020; Jing, Jin and Xiang 2022). Effective and efficient image segmentation is vital because of its critical role in image processing and computer vision applications (Bora and Gupta 2015; Shan 2018; Khan *et al.* 2020; Cuevas *et al.* 2021; Zhang *et al.* 2021b).

The ultimate objective of image segmentation is domain independent partition of an image into a collection of visually distinct regions that have a meaning related to some characteristics such as color, intensity, or texture to facilitate simple image analysis (Abdel-Maksoud, Elmogy and Al-Awadi 2015; Lamine and Nadia 2016; Monteiro, Dhanush and Nausheeda 2016; Ramella and Di Baja 2016; Cuevas *et al.* 2021; Guan *et al.* 2021; Liu and Zhao 2021). It is the method of assessing the semantic depiction of an image at the pixel or superpixel level (Bargoti and Underwood 2017). In recent years image segmentation became a fast-growing research field as it has an integral component of computer vision applications.

The utility of image segmentation has resulted in extensive research and numerously proposed segmentation algorithms in numerous applications such as face recognition and analysis (Kamencay *et al.* 2013; El Sayed *et al.* 2017; Farhang 2017; Benini *et al.* 2019; Yu *et al.* 2021a), skin lesion detection and segmentation (Soni *et al.* 2015; Devi, Singh and Laskar 2020; Zafar *et al.* 2020; Khan *et al.* 2021; Okuboyejo and Olugbara 2021; Rajput, Tanwar and Raman 2021; Joseph and Olugbara 2022b), medical image analysis and diagnosis (Sridevi and Sundaresan 2013; Masood *et al.* 2015; Krestanova *et al.* 2020; Yang, Wang and Feng 2020; Zhao *et al.* 2021b), white blood cell segmentation (Zhang *et al.* 2014; Ananthi and Balasubramaniam 2016; Wang and Cao 2019b; Joseph and Olugbara 2022a), lung cancer classification(He *et al.* 2021a), plant phenotyping (Kaiyan *et al.* 2013; Scharr *et al.* 2014), road detection (Qi *et al.* 2019), fruit and vegetation image detection and classification (Rocha *et al.* 2010; Bai *et al.* 2014; Xiang, Jiang and Ying 2014; Bargoti and Underwood 2017; He *et al.* 2019; Sun *et al.* 2019; Xu, He and Lv 2019; Khan *et al.* 2020; Wang *et al.* 2021b), pests or disease detection in plants (Bodhe and Mukherji 2013; Niu *et al.* 2014; Singh and Misra 2017; Adeel *et al.* 2019; Deng *et al.* 2020; Zhang *et al.* 2020a), sport technology (Zhao, Qu and Zhang 2014), video surveillance (Singh and Patnaik 2015), anomaly detection (Mokayed *et al.* 2021), remote sensing (Yuan, Wang and Li 2014; Zhang and Yang 2014; Zhang *et al.* 2015; Li *et al.* 2017d; Zhang *et al.* 2020b; Lyu *et al.* 2021), marine surveliance (Jin and Bai 2020), underwater object tracking (Huo *et al.* 2018; Kannan 2020; Zhang, Li and Sun 2022), satellite and aerial imaging (Sammouda *et al.* 2014; Li *et al.* 2017a; Zhao *et al.* 2018; Nailussa'ada, Harsono and Basuki 2019; Jaimes, Ferreira and Castro 2022), and land cover image classification (Ma *et al.* 2017). Due to the diverse application of image segmentation, myriads of segmentation algorithms have been proposed by researchers and become a classic problem in the field of computer vision.

1.1.1 Image segmentation algorithms

Countless applications of image segmentation have led to the occurrence of myriads of image segmentation algorithms. These algorithms are broadly classified into supervised and unsupervised approaches. In the supervised segmentation approach training, learning, and extraction of hierarchical image features from large image datasets are performed based on Support Vector Machines, and Convolutional Neural Networks (CNN) based deep learning algorithms (Bi *et al.* 2017; Jahanifar *et al.* 2017; Alom *et al.* 2018; Ali *et al.* 2019; Jiao, Chen and Dong 2020; Tan, Zhang and Lim 2020; Li *et al.* 2021b; Zuo, Chen and Wang 2021). Supervised methods are exploited with a huge dataset of images with ground truth labels to train the deep neural network to generate highly accurate and robust

segmentation results (Zhang *et al.* 2018b; Gupta *et al.* 2020 ; Qi 2021). As a data-driven approach, the supervised learning methods demand a high volume of training datasets and a large number of parameter tuning for outstanding image segmentation performance. Obtaining quality per-pixel annotation training data is a difficult and time-consuming task (Shin *et al.* 2012; Ahn *et al.* 2017; Hu *et al.* 2020; Jing, Jin and Xiang 2022), and the demands for obtaining quality annotation data limits the application generality of supervised methods. Providing a large and adequate dataset with labeled ground truth images for the uncommon image class may add further challenges to supervised methods (Abdalla *et al.* 2019; Jing, Jin and Xiang 2022; Mohammdian-Khoshnoud *et al.* 2022).

Conversely, the unsupervised segmentation approach does not require any prior knowledge about the model to segment the region of interest, instead, it uses similarity measures to cluster similar features (Mukherjee and Lall 2017; Abdalla *et al.* 2019; Mohammdian-Khoshnoud *et al.* 2022). Segmentation methods based on an unsupervised approach are independent of the requirement of training datasets and more applicable to a variety of image classes. These methods are focused on clustering the homogenous pixels without labeling the data in advance. Considering the computational complexity and the difficulty in advanced pixel labeling of supervised methods, simple and computationally efficient unsupervised methods are in more demand for image segmentation applications (Jiao, Chen and Dong 2020; Kim, Kanezaki and Tanaka 2020; Mohammdian-Khoshnoud *et al.* 2022). The unsupervised methods mainly focus on thresholding (Garnavi *et al.* 2011; Khan *et al.* 2019), clustering (Agarwal *et al.* 2017; Filali, Abdelouahed and Aarab 2019; Devi, Singh and Laskar 2020; Okuboyejo and Olugbara 2021), statistical region merging (Emre Celebi *et al.* 2008; Salih and Viriri 2020), edge detection (Jin *et al.* 2021; Wang *et al.* 2022b) and most recently the saliency based (Bozorgtabar, Abedini and Garnavi 2016; Ahn *et al.* 2017; Fan *et al.* 2017; Jahanifar *et al.* 2017; Olugbara, Taiwo and Heukelman 2018; Khan *et al.* 2019; Hu *et al.* 2020). Among the diverse collection of unsupervised segmentation methods, clustering-based methods are ubiquitous because of their simplicity and reliability (Feng *et al.* 2020; Guan *et al.* 2021).

1.2 Clustering algorithms

Clustering is an unsupervised learning method with the aim of grouping datasets into clusters with homogenous properties (Yang, Wang and Feng 2020; Guan *et al.* 2021; Mittal *et al.* 2021). Clustering algorithms identify clusters in an unlabeled set of multidimensional data (Zhong and Shih 2021). It divides data into various clusters such that objects within the clusters show high similarity and

high dissimilarity with objects in other clusters (Dhua *et al.* 2015; Dhanachandra and Chanu 2017; Ramesh and Nandhini 2017; Cornuejols *et al.* 2018; Mittal *et al.* 2021). The clustering algorithms are based on distance (dissimilarity) and similarity features of data (Xu and Tian 2015) and a good clustering method produces distinct clusters that exhibit maximum intra-class similarity and minimum inter-class similarity. Conventionally the clustering structure can be denoted as a set of subsets. The structure of clustering can be presented as a set,

S of subsets $S_1, S_2, S_3, ...S_k$ such that $S_1 \cap S_2 \cap S_3 ... S_k = \phi$, *where* ϕ *is the empty set* .

Clustering analysis is the identification of natural groups in an unlabeled set of multidimensional data. Image segmentation can be viewed as a clustering problem where image pixels are considered unlabeled data and the image features describe the data dimensionality (Jain, Murty and Flynn 1999; Zhong and Shih 2021), and pixels with similar characteristics are clustered in one group and dissimilar pixels are in different groups (Kim, Kanezaki and Tanaka 2020; Mittal *et al.* 2021). Thus image clustering divides the image data into the desired number of subparts known as clusters (Lei *et al.* 2016; Qi 2021) by preserving high intra-class similarity and low interclass similarity (Chebbout and Merouani 2012; Saxena *et al.* 2017; Wazarkar and Keshavamurthy 2018; Feng *et al.* 2020). The clustering process on an image, I of dimension $m \times n$ defined over d-dimension, creates K clusters $C_1, C_2, C_3, ...C_k$ such that

$Ci \neq \phi$ *for* $i = 1,2,3,...,k$ *Condition* (1)

$C_1 \cap C_2 \cap C_3 ... C_k = \phi$ *where* ϕ *is the empty set* *Condition* (2)

$\bigcup_{i=1}^{k} C_i = I$ *Condition* (3)

Where these three conditions respectively imply that there will be at least one pixel in every cluster, all clusters must be mutually exclusive, meaning that a pixel cannot be allocated to more than one cluster, and all pixels allocated to all clusters must collectively represent the entire image (Xu and Wunsch 2005; Mittal *et al.* 2021).

1.2.1 Clustering algorithms for image segmentation

Among the myriads of segmentation algorithms, clustering-based methods are ubiquitous because of their simplicity, robustness, effectiveness, and rapidness (Dubey *et al.* 2013; Kirati and Tlili 2014; Feng *et al.* 2020; Guan *et al.* 2021). The segmentation process represents the image into a

significant number of regions and these regions allow the delineation of the objects by representing the homogenous pixels with object category labels (Mujica-Vargas, Kinani and Rubio 2020; Mittal *et al.* 2021). As a result, image segmentation can be formulated as a separation of foreground and background regions or the extraction of the most salient objects from the background region. The most ideal method to extract the object from the background is to assemble the object pixels into one group and the background pixels into another group as illustrated in Figure 1-1 where the first row and second rows respectively indicate the input image and the segmented image. The partition of pixels into two groups can be considered a two-class clustering problem (Pont-Tuset and Marques 2013).

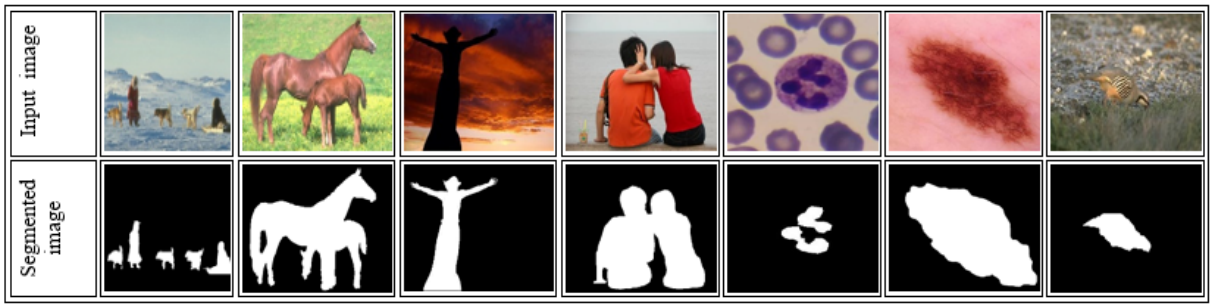

Figure 1-1 Example of clustering-based image segmentation

Myriads of clustering algorithms such as K-Means (Sulakshana A. Gaikwad and Priyanka R.Dudhane 2017; Babu, Subudhi and Sabut 2018; Yurtsever, Evirgen and Avunduk 2018; Gopi Krishna *et al.* 2020; Inbarani and Azar 2020; Rosyadi and Suciati 2020; Song *et al.* 2020b; Yu *et al.* 2020; Hafeez, Yan and Guoliang 2021), Fuzzy C-Means (FCM) (ShanmugaPriya and Valarmathi 2018; Zanaty 2018; Huang *et al.* 2019; Nida *et al.* 2019; Devi, Singh and Laskar 2020; Feng *et al.* 2020; Jin and Bai 2020; Lei *et al.* 2020; Xiong *et al.* 2020), and Pixel Intensity Clustering Algorithm (PICA)(Olugbara, Adetiba and Oyewole 2015), density based algorithms such as Density Based Spatial Clustering of Applications with Noise (DBSCAN) (Karthik, Kathirvelan and Srilatha 2017; Nailussa'ada, Harsono and Basuki 2019), and Mean shift (MS)(Michel, Youssefi and Grizonnet 2015; Su *et al.* 2015; Salve, Salve and Jondhale 2017; Guo *et al.* 2018; Zhao *et al.* 2021b), Self-organizing Map (SOM)(García-Lamont, Cervantes and López-Chau 2018; Ouyang, Xu and Yuan 2019; Zhang 2020), and Expectation-Maximization (EM) (Prabhu *et al.* 2018; Pravitasari *et al.* 2020; Qaddoura *et al.* 2020) have been extensively used in image segmentation applications.

However, the unpredictability in the shape and appearance of objects and complex background scenes make image segmentation a challenging task, and detection of the optimum number of cluster count is the major constraint of the majority of the traditional clustering-based image segmentation

(Feng *et al.* 2020; Joseph and Olugbara 2021; Mohammdian-Khoshnoud *et al.* 2022). Recently, researchers have proposed several modified versions of these classical clustering algorithms to significantly enhance the segmentation process. According to Kim, Kanezaki and Tanaka (2020), the results of good segmentation is corresponding with the solution provided by the human vision. Human vision generally tends to identify the complete or major part of more salient objects. Hence models that imitate the human visual system to group spatially continuous pixels with similar characteristics into the same cluster is a reasonable image segmentation strategy.

1.2.2 Saliency algorithms for image segmentation

Saliency algorithms are focused on the accurate detection and segmentation of the region of interest from the image by simulating the human visual system (Gupta *et al.* 2020). The ability of the human visual system to rapidly recognize distinct or salient regions in the visual fields has been shown through research by several cognitive neuroscientists (Ahn *et al.* 2017; Ndayikengurukiye and Mignotte 2022). Recently, these discoveries have been used in computer vision to locate and segment regions of interest that aid in understanding and representing an image. Saliency algorithms generally attempt to extract points and regions of a visual scene that are more salient to human visual attention. Useful information about the target objects provided by the saliency methods, for the detection of salient objects is an integral step in image segmentation (Nawaz and Yan 2021). Hence, saliency detection gained popularity in computer vision and artificial intelligence applications and has been comprehensively utilized and benefited in many areas including image segmentation (Khan *et al.* 2017; Yuheng and Hao 2017; Olugbara, Taiwo and Heukelman 2018; Joshi *et al.* 2020; Joseph and Olugbara 2021; Joseph and Olugbara 2022b; Joseph and Olugbara 2022a).

Saliency-based image segmentation methods are well known for the accurate clustering of foreground and background pixels by estimating the image pixel saliency. Saliency estimation is an operation to highlight the most attractive objects out of the background which is a significant task in image segmentation. In image segmentation, saliency defines, the perceptual quality of the region of interest that makes them prominent from the surrounding regions (Joshi *et al.* 2020). The saliency measure indicates the distinction of objects to their background by forming a saliency map that defines how a pixel or region stands out from its background (Wang *et al.* 2016; Ye *et al.* 2017; Wu *et al.* 2021). Computation of a saliency map that integrates various features such as color, intensity, contrast, texture, and spatial features can accelerate the detection of the most salient or the region of interest in an image.

Since saliency detection models can rapidly locate the salient object by analyzing the image surroundings, saliency detection is widely used to mitigate the complexity of image analysis and speed up image processing (Zhang *et al.* 2020d).

One of the initial saliency algorithms presented by Itti, Koch and Niebur (1998) is referred to as the cornerstone model and is categorized under the eye-fixation prediction model which is grounded on the biological model for human eye-fixation activity. This model is based on the earlier computational framework and psychological theories of bottom-up attention based on center-surround variances in color, intensity, and orientation. Additionally, by computing multi-scale feature maps using the Gaussian pyramid method, this method detects spatial discontinuities in the image and infers the places of visual gaze. Saliency is described as a binary segmentation problem in the works of (Achanta *et al.* 2008) and (Liu *et al.* 2011) and this has led to the emergence of the second category of saliency detection models. The third wave of interest was sparked by fully convolutional neural networks (CNN), which reduce the requirement for center bias knowledge. The most salient region in an image can be more accurately identified by neurons in CNN models with broad receptive fields and global information (Borji *et al.* 2015). A plethora of saliency region detection models have been developed since then and shows the evidence of devotion taken by multiple disciplines to develop novel methods for retrieving salient regions as the quality of saliency results has a crucial impact on image segmentation. Saliency map values can be used for labeling pixels in image segmentation thereby clustering the image into foreground and background regions. Reasonably salient regions are highly different from the background; hence the detection of salient regions can be considered a two-class clustering problem.

1.3 Motivation

The motivation of this study is based on the fact that myriads of image segmentation methods are developed over the years yet an efficient method that works on a large category of images is still imperative (Sonawane and Dhawale 2015; Abdalla *et al.* 2019; Jaglan, Dass and Duhan 2019; Nikbakhsh, Baleghi and Agahi 2021). The application of segmentation methods varies from image to image because of the variation in image context and the heterogeneous properties of the region of interest (Brunda, Divyashree and Rani 2018). Image segmentation is a prominent and classical research topic in the field of computer vision and is considered a significant fundamental operation for meaningful analysis and elucidation of the image acquired (Feng *et al.* 2020; Zhou and Xu 2020).

Object identification and segmentation is become a non-trivial and challenging task in image processing and analysis systems because of various factors such as multifaceted image content, cluttered and occluded objects, image noise, uneven image texture, and image acquisition and reconstruction artifacts (Abdel-Maksoud, Elmogy and Al-Awadi 2015; Guan *et al.* 2021). A robust and efficient segmentation process brings a successful solution to the object recognition process by partitioning the image into a set of non-overlapped regions. The accuracy of image segmentation determines the eventual failure or success of high-level processes. Generally, the accuracy of image segmentation is directly proportional to efficient and successful high-level processes such as image analysis, classification, scene understanding, and autonomous navigation. Weak or inefficient segmentation algorithms will always result in inaccurate object recognition. This highlights the importance of having efficient and robust image segmentation algorithms in computer vision applications.

The segmentation of the region of interest from a diverse class of images with heterogeneous properties such as multiple objects, cluttered and complex background, and low dissimilarity between objects and background as in Figure 1-2 makes the segmentation process even more complex and laborious. Due to the diverse characteristics of the images, accomplishing a near-perfect solution for segmenting the region of interest requires an immensely intellectual process. Considering the enormous training required by the supervised techniques, and the scenario where the training is prohibitive, an unsupervised technique is a desirable alternative. These scenarios highlight the need of an unsupervised segmentation algorithm that effectively and efficiently segments the region of interest from a diverse class of images.

Figure 1-2 Example of various image categories: (a) foreground objects with various sizes, positions, and count; (b) complex background region with low dissimilarity between foreground and background regions

Among the many unsupervised image segmentation algorithms, clustering-based algorithms are widely used because of their ability to group pixels with similar characteristics into meaningful clusters without any prior knowledge (Guan *et al.* 2021). Considering the simplicity, rapidity, and effectiveness the demand for clustering-based image segmentation is enormous. In clustering-based image

segmentation, the most effective segmentation of various images is achieved by different sets of features depending on the nature of the images (Coleman and Andrews 1979). However, the presence of heterogeneous object properties and background complexity as shown in Figure 1-2 makes the segmentation process even more challenging. These complexities can be mitigated by grouping the pixels according to some features of similarity or dissimilarity followed by an appropriate pixel labeling method.

The selection of an image segmentation algorithm over another and the degree of segmentation depend on the specifics of the image and aspects of the problem being solved (Saini and Arora 2014). Due to the heterogeneous characteristics of images, unsupervised segmentation algorithms may be effective in segmenting a particular class of images, but promising segmentation results in a much more challenging class of images are not adequately addressed. Clustering guided by saliency has the benefit of rapidly identifying the features of the foreground region in an unsupervised way and the ability to suppress the background region by uniformly highlighting the region of interest. The foreground and background clustering processes can be guided by saliency-based clustering algorithms (Tao *et al.* 2019). General clustering algorithms are useful to treat homogenous segments as a preprocessing unit to reduce the computational complexity, but saliency-based clustering is more applicable to segment the salient object as a whole (Zhou *et al.* 2019).

The salient object detection method proposed by Liu and Yang (2019) integrated foreground, center, and background priors to detect the salient objects that touch the image boundary. A deep learning-based supervised method developed by (Singh *et al.* 2019) is mainly focused on the segmentation of salient objects from noisy images and this method utilized the K-Means clustering approach for homogenous region detection and color and spatial features for regional saliency estimation. The segmentation method proposed by Song *et al.* (2020b) applies to images with severe heterogeneity and complex background. However, this automated image segmentation method based on Gaussian function and K-Means uses gray intensity information and is not suitable for color images. The supervised method with affinity-based background subtraction technique by Nawaz and Yan (2021) and another supervised method that uses complementary saliency prior by Tian *et al.* (2015) is developed for detecting objects from complex backgrounds. The recent method by Ndayikengurukiye and Mignotte (2022) integrated color and texture features that are mainly focused on the salient object detection and segmentation of natural images. These various contributions have emphasized the development of myriads of methods to address some of the challenging image categories, yet a single

segmentation method that can be used for a wide range of image categories is still far away. A method that is suitable for one category of the image is not essentially appropriate for other image categories, thus accurate image segmentation for a diverse class of images is an open issue.

1.4 Problem

Image segmentation is one of the hardest challenges in image processing and computer vision because it appears to be application-dependent usually with no prior knowledge of image structure (Lei *et al.* 2016). Segmentation of homogenous regions from an image may be a simple task for human vision, but it may be a convolution task from the viewpoint of computer vision. Myriads of classical image segmentation algorithms have been developed over the years yet generalization and universal optimum performance are far away from ideal levels (Xu and Wunsch 2005; Sharma, Mishra and Shrivastava 2012; Kirati and Tlili 2014; Jaglan, Dass and Duhan 2019; Pereira *et al.* 2020; Liu *et al.* 2021; Nikbakhsh, Baleghi and Agahi 2021).

The presence of cluttered and non-homogenous background regions, inter-object dissimilarity, high similarity appearance of foreground and background regions, and heterogeneous properties of the object can hamper the segmentation process (Song *et al.* 2020b; Mittal *et al.* 2021). Additionally, a significant problem in clustering-based image segmentation is a lack of prior knowledge of the ideal cluster count. Clustering algorithms are bounded by the requirements of an optimum number of clusters to avoid the over and under-segmentation problem (Abdalla *et al.* 2019; Oskouei *et al.* 2021; Zhang *et al.* 2021b). The selection of an optimum number of clusters is a major challenge experienced by many of the clustering-based image segmentation algorithms (Feng *et al.* 2020; Jing, Jin and Xiang 2022).

Another problem is the demand for multilevel image preprocessing to address the intensity variation and contrast imbalance brought on by noise incursion in the input image (Song *et al.* 2020b). In the fields of image processing and computer vision, a generalized single preprocessing approach to handle the numerous kinds of artifacts and heterogeneous properties contained in the input image remains an unsolved problem. As a result, myriads of studies have largely depended on the various stages of preprocessing to deal with the innumerable types of artifacts and uneven color contrast of input images (Garnavi *et al.* 2011; Jamil *et al.* 2016; Pennisi *et al.* 2016; Premaladha and Ravichandran 2016; Agarwal *et al.* 2017; Jahanifar *et al.* 2017; Jaisakthi, Chandrabose and Mirunalini 2017; Guarracino and Maddalena 2019; Javed *et al.* 2019; Nida *et al.* 2019; Lee, Wee and Jeong 2021; Okuboyejo and Olugbara 2021; Mohammdian-Khoshnoud *et al.* 2022).

While the existing image segmentation algorithms have achieved reasonable segmentation results, an optimum solution for a wide range of image classes is still an open problem because of the multifariousness of image types (Brunda, Divyashree and Rani 2018; Guan *et al.* 2021). The heterogeneous properties of the input image, dependence on the optimal cluster count, and parameter tuning required for multilevel image preprocessing are the key issues that hinder quality segmentation results on a wide range of images. A single method that can be used for a wide gamut of image categories is still far away from a breakthrough in image segmentation research. There is no solitary method that can be believed superior for all classes of images and not every method is evenly fine for a particular kind of image (Sonawane and Dhawale 2015; Abdalla *et al.* 2019; Liu *et al.* 2021; Nikbakhsh, Baleghi and Agahi 2021). Hence it is vital to explore new methodologies to extend the application of unsupervised segmentation algorithms of various classes of images.

1.5 Aim and objectives

The main aim of this study is to develop a clustering-based image segmentation algorithm that automatically identifies an optimum cluster count to represent the homogenous regions and uses a set of salient features that would work effectively on a large class of images with a more generalized approach and optimum performance.

The main aim of this study is accomplished by setting the following objectives:

i. To conduct a meta-analysis of existing studies on image segmentation methods.
ii. To develop an effective and efficient clustering-based image segmentation algorithm that automatically identifies an optimum number of clusters and integrates a set of salient features to increase the generalizability of the segmentation method.
iii. To investigate the effect of image preprocessing on the performance of the newly developed image segmentation algorithm.

1.6 Contributions

The main contributions of this thesis work are:

i. A meta-analysis of existing image segmentation methods is one of the contributions of this study. There have been numerous studies on image segmentation, but there is a lack of meta-analysis of image segmentation methods. A meta-analysis is used to systematically synthesize the primary

studies to discover the characteristics, trends, uniqueness, and relevance of the image segmentation methods.

ii. The development of a color histogram algorithm that can work on a large class of images is a significant contribution to this study. An unsupervised clustering-based image segmentation algorithm, Color Histogram Clustering (CHC) that agglutinates the strategy of color contrast, contrast ratio, center prior, and spatial features to effective separation of the region of interest from the background is developed. The identification of perceptually distinct image parts that are dissimilar to their background is accomplished by computing the saliency of the initially identified clusters. This cluster level saliency is computed for the robust and accurate segmentation of the region of interest from the background. Finally, the object borders are retrieved by using the thresholding approach to segment the region of interest from the background regions. The image segmentation algorithm that exploited the color histogram clustering and the strategy of color contrast, contrast ratio, center prior, and spatial features can be applied to a variety of image types.

iii. Another important contribution of this study is the automatic selection of an optimum cluster count for image segmentation to increase the generalizability of the application of the image segmentation method. Color histogram clustering was employed to expose the underlying color structure of the image and cluster the image pixels based on the color features. The method of color histogram-based clustering has been proposed for the estimation of true cluster count.

iv. The development of an image segmentation algorithm that is free from the requirement of preprocessing is another important contribution of this study. Generally better segmentation results are achieved by including preprocessing steps in image segmentation. The reliance on numerous preprocessing stages limits the generalizability of the current segmentation methods and raises their computational complexity. The effect of preprocessing techniques for image segmentation is investigated and the results were reported based on an extensive evaluation of numerous images. The results obtained highlighted the ability of the proposed algorithm to segment the region of interest without preprocessing and thereby increase the generalizability of the proposed segmentation algorithm.

v. Furthermore, the proposed segmentation algorithm has been objectively evaluated using different performance evaluation metrics and compared against numerous state-of-the-art methods on the widely known benchmarked corpora. A variety of images from different classes of images are

used for evaluation where existing studies are confined to a specific class of images or application domain.

1.7 Thesis structure

This thesis is succinctly structured as follows. Chapter 1 presents the introduction and the research background. Chapter 2 provides a meta-analysis of image segmentation methods with a special focus on clustering and saliency. Chapters 3 and 4 respectively present the theoretical foundation and the methods and materials used for the novel image segmentation algorithm. The detailed experimental comparison of the proposed algorithm to the state-of-the-art methods based on well-known benchmarked corpora and performance evaluation criteria is explained in Chapter 5. Chapter 6 provides a discussion of experimental results and the last chapter presents the summary of the thesis, concluding remarks, and future works. The chapters of this thesis are organized as follows:

Chapter one, Introduction: this chapter presents the background study of image segmentation by giving highlights to the clustering and saliency-based image segmentation methods. Also presents a succinct description of the research motivation, problem statement, aim, objectives, contribution, and thesis structure.

Chapter two, Meta-analysis of related literature: presents a meta-analysis on image segmentation methods with a focus on clustering and saliency map. This chapter provides an overview of segmentation approaches and methods, the trends in publication, image datasets used, and segmentation techniques. The preferred reporting items for systematic reviews and meta-analyses are employed in this chapter to combine the findings of various primary studies related to image segmentation. Further, this chapter investigates the publication bias and sources of heterogeneity among reviewed primary studies.

Chapter three, Theoretical foundation – This chapter presents the process of image segmentation that explain the different stages incorporated in a typical segmentation process. In this chapter, the common preprocessing techniques in image segmentation, color model transformation, classical clustering methods used in image segmentation, details of saliency methods, and post-processing based on mathematical morphology are presented.

Chapter four, methods and materials –This chapter highlights the methods and materials used to achieve the research objectives. A detailed explanation of the proposed algorithm in terms of flow chart, mathematical formulation, and algorithm is presented here. The statistical methods used for investigating the preprocessing effects on the proposed algorithm are also reported in this chapter. Further, the details of image datasets and the evaluation metrics used to validate the proposed algorithm are presented.

Chapter five, Experimental results – This chapter presents the extensive experiments performed to validate the proposed color image segmentation algorithm. Experimental comparisons of the proposed algorithm against the state-of-the-art methods on a diverse class of images are presented using qualitative and quantitative approaches. Further, this chapter investigates the effect of preprocessing on the proposed image segmentation algorithm. Results of run-time analysis conducted to evaluate the computational efficiency of the proposed algorithm and the optimum cluster count generated by the proposed algorithm are also detailed in this chapter.

Chapter six, Discussion – This chapter reports the findings and discussions on the extensive experimental analysis performed in chapter 5. Interpretation and critical analysis of the experimental results are also provided in this chapter.

Chapter seven, Summary, Conclusion, and future work – This is the final chapter and it provides the summary of this study with an explanation of the contribution drawn from this study. The concluding remarks, limitations of this study, and the future direction for the related research are presented in this chapter.

CHAPTER TWO: META-ANALYSIS OF RELATED LITERATURE

This chapter presents a meta-analysis of color image segmentation methods. Image segmentation is an indispensable part of many computer vision applications. Several segmentation methods have been proposed for color image segmentation during the past few decades. Among these methods, clustering and saliency-based methods have drawn attention to image segmentation in several applications. This chapter reviews color image segmentation advances with a special focus on clustering and saliency-based image segmentation methods and applies a meta-analysis of 151 primary studies. The meta-analysis focused predominantly on the analysis of the general characteristics of primary studies, including frequency of pertinent publications, spatial distribution, description of segmentation methods such as approaches, methods, unit of processing, image preprocessing status, number and type of image segmentation datasets, number of images, and segmentation performances in terms of precision, recall and F-Score. This chapter presents the overview of the systematic literature search query that was carried out using the Preferred Reporting Items for Systematic reviews and Meta-Analyses (PRISMA). In the sections that follow, meta-analysis data are presented together with graphical representation, with trends in image segmentation approaches, methods, preprocessing stage, and image data sources to name a few.

2.1 Introduction

The use of image segmentation is rapidly expanding due to the rising demand for image analysis in various computer vision applications. This includes content-based image retrieval, machine vision, object detection and classification, medical imaging, and video surveillance (Mittal *et al.* 2021). As a result, myriads of methods have emerged to address the various demands of image segmentation applications. Among these, supervised methods comparatively exhibit high segmentation results than unsupervised methods, but the computational complexity is the major challenge of supervised methods. Generation of the huge training dataset is an expensive and laborious task. Further, the new image classes are constantly evolving, and the generation of training datasets for supervised segmentation methods is an arduous and ongoing challenge (Aganj *et al.* 2018; Gupta *et al.* 2020; Salih and Viriri 2020; Zhang and Wang 2021; Mohammdian-Khoshnoud *et al.* 2022; Wang *et al.* 2022a). The demand for extensive training can be eliminated with unsupervised approaches and it is better suited to application domains with no prior data knowledge (Mukherjee and Lall 2017; Abdalla *et al.* 2019; Jaimes, Ferreira and Castro 2022). In the unsupervised segmentation approach, the pixel labeling for

the segmentation is controlled by the similarity measures (Abdalla *et al.* 2019; Mohammdian-Khoshnoud *et al.* 2022). Generally, the segmentation results of the unsupervised methods are influenced by parameter settings such as the initial cluster count, preprocessing requirements, and the selection of feature vectors. Researchers have created unsupervised methods that are specifically aimed at types of images to deal with these uncertainties.

For example, a graph-based saliency detection model based on global and local cues by integrating background and objectness saliency maps is introduced by Pang *et al.* (2020a) to overcome the inadequacy of existing graph-based models in successfully detecting salient objects from complex scenes. The two segmentation methods based on Fuzzy C-Means clustering developed by (Wu and Yang 2020) and Wu and Zhang (2020) address the problem of efficient segmentation of highly noisy images. Similarly, Liu and Zhao (2021) proposed a segmentation algorithm based on fuzzy clustering to segment objects from noisy color images. A saliency model that applied deformed smoothness-based manifold ranking is proposed by Wu *et al.* (2018) to overcome the problem of detecting misclassified salient objects that have low contrast with the background. Tian *et al.* (2015) proposed a method based on learning complementary saliency priors to address the segmentation of foreground objects from complex scenes. Jiang *et al.* (2013b) developed a supervised learning-based salient object detection model to detect salient objects that are far away from the image center and located at the image boundary.

Due to various image properties, no segmentation method can find the ideal segmentation solution for all datasets or image types (Sonawane and Dhawale 2015; Abdalla *et al.* 2019; Gupta *et al.* 2020; Nikbakhsh, Baleghi and Agahi 2021). As a result, several segmentation approaches that are based on various methods and techniques have emerged over the years. Therefore, this chapter is focused to determine the current trends in image segmentation to outline the approaches, methods, image data sources, and the factors affecting the segmentation results. This can be accomplished by synthesizing the collective knowledge in this area instead of leveraging individual studies and results. Meta-analysis offers a unique way of integrating the findings that allow for statistical examination of the patterns and correlations of effect resulting from various factors, as opposed to merely presenting the data from the current literature (Chirici *et al.* 2016). Meta-analysis is essential because it enables a comprehensive synthesis of the findings from the existing literature to reveal novel insights. Additionally, meta-analysis will typically improve accuracy and offer assurance regarding the results of previous research (Olugbara *et al.* 2021).

The main objective of this chapter is to:

i. Present the general trends of studies related to image segmentation methods with a special focus on clustering and saliency.
ii. Examine the sources of heterogeneity among reviewed studies on the F-Score level of segmentation output.
iii. Examine the publication bias in reviewed studies on the F-Score level of segmentation output.

The meta-analysis followed the PRISMA protocol (Moher *et al.* 2009). PRISMA protocol is selected as it is recognized for its comprehensiveness and potential in increasing consistency across reviews. The remainder of this chapter explains the methods followed for conducting the meta-analysis and the meta-analysis results.

2.2 Search strategy

The search strategy was performed by following the reporting checklist of PRISMA. A comprehensive search was conducted using the bibliographic databases of Web of Science and PubMed, to identify potentially relevant papers. More specifically, the comparison among segmentation methods presented in the study was extracted from peer-reviewed articles published in English between 2012 and 2022 February. Following the search, strings were formulated and executed on the selected publication platforms.

Search string (Web of Science):

(((color image segment) AND (cluster* OR salien*)) OR ((salien* detect*) or (salien* segment*))) and 2022 or 2021 or 2020 or 2019 or 2018 or 2017 or 2016 or 2015 or 2014 or 2013 or 2012 (Publication Years) and Articles (Document Types) and English (Languages).*

Search String (PubMed):

(("color image segmentation"[Title] AND ("cluster"[Title] OR "salien*"[Title])) OR ("salien*"[All Fields] AND "detect*"[Title]) OR ("salien*"[All Fields] AND "segment*"[Title])) AND ((y_10[Filter]) AND (ffrft[Filter]) AND (fft[Filter]) AND (english[Filter])).*

The defined search query consisted of three main parts and was separated by ‘AND’ and ‘OR’ operators to retrieve the relevant studies related to image segmentation using clustering and saliency. The first part focused to retrieve the publication that used color image segmentation and the second

part, and third part respectively aimed at the relevant publications that used clustering or saliency methods.

The initial literature searches in the two databases yielded 2025 studies. 70 studies were excluded because of duplication and 150 studies were excluded as the full text was not available. 1805 studies were assessed for eligibility and 1624 studies that are excluded based on the exclusion criteria listed in Table 2-1. Finally, 151 studies that met the inclusion criteria were considered for the meta-analysis. The flow diagram of the systematic literature search is depicted in Figure 2-1 (Olugbara *et al.* 2021).

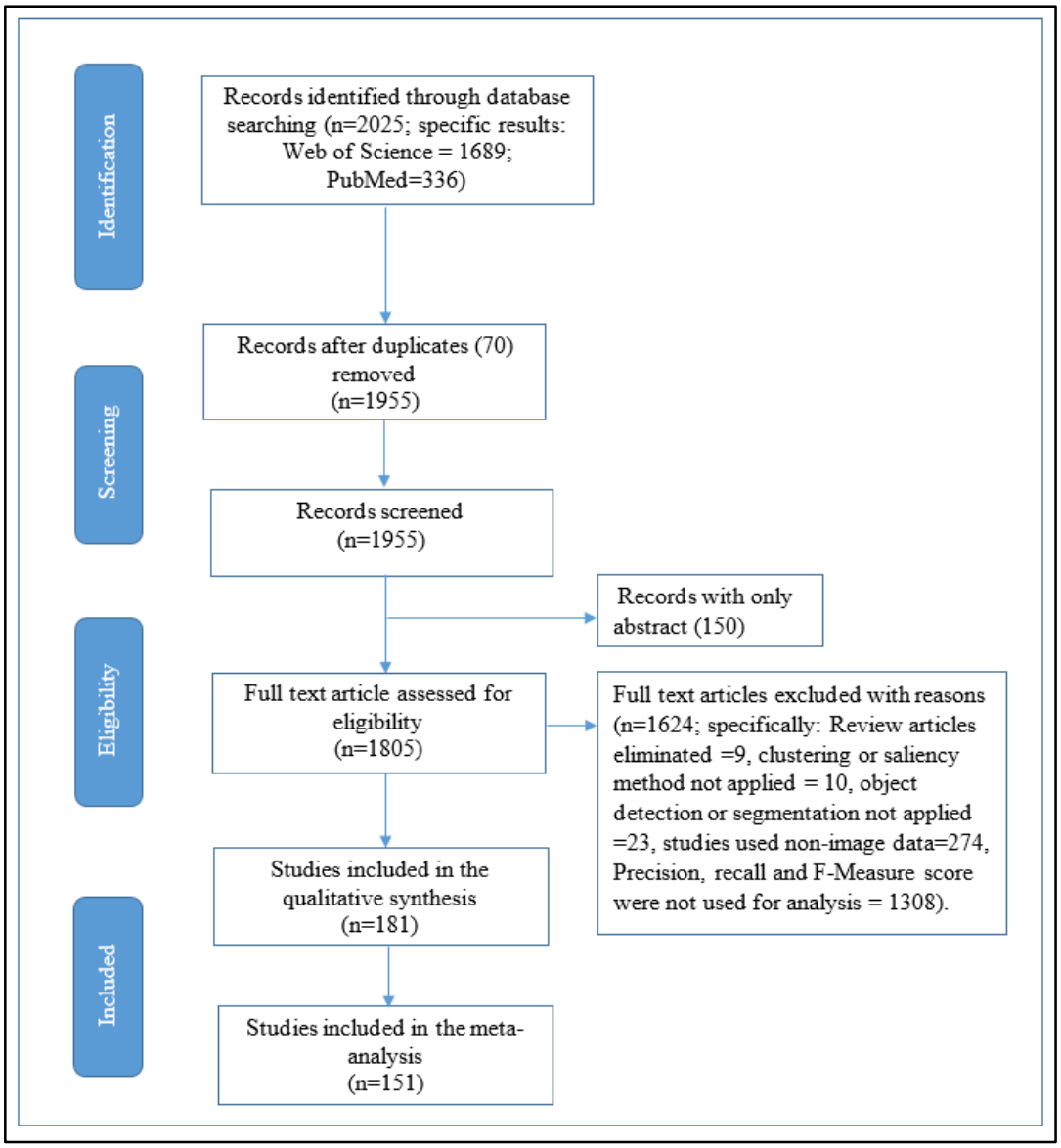

Figure 2-1 PRISMA protocol for image segmentation methods

2.3 Selection criteria

The selection criteria were based on a set of inclusion and exclusion criteria as listed in Table 2-1. The defined search query guided the automatic extraction of the publications from the selected bibliographic databases. The publication year, name of authors and affiliation, article title, abstract, and journal name of the extracted records were exported to an MS Excel spreadsheet. The extracted publications were manually screened by reading the abstract, and the introduction section, and also based on the selection criteria that were formulated to identify the trends in image segmentation based on clustering and saliency.

Table 2-1 Exclusion and inclusion criteria

ID	Criterion
Exclusion criteria	
EC1	Papers in which only the abstract is available
EC2	Review and conference papers
EC3	Duplicates records
EC4	Papers are not written in the English language
EC5	Papers are not aimed at the color image segmentation
EC6	Papers do not apply the clustering or saliency methods for image segmentation
EC7	Papers do not directly apply object detection or segmentation
EC8	Papers that used non-image data for segmentation
EC9	Papers do not report the segmentation evaluation metrics in terms of average precision, recall, and F-Score.
Inclusion criteria	
IC1	Articles published in English.
IC2	Papers that clearly stated the segmentation methods and the techniques used for image segmentation.
IC3	Papers that provided clear information about the image database and the number of images used for evaluation.
IC4	Papers that provided the segmentation results in terms of average precision, recall, and F-Score.

2.4 Data extraction

Data and information from the selected papers were extracted based on the extraction form as shown in Table 2-2. This includes the attributes for general information such as publication details and for the study description including, the segmentation approach, methods used for segmentation, segmentation technique, preprocessing stage, unit of processing, image datasets, number of images, segmentation results in terms of precision, recall and F-Score. The general information is extracted by the initial screening of the papers while information related to the study is extracted by careful reading

and reviewing of the papers. Thus, a database with 15 fields was constructed and populated with qualitative and quantitative data extracted from the literature review. Hence, the information source for the meta-analysis consists of a matrix with 15 fields and 151 rows with information for the image segmentation methods.

Table 2-2 Fields created to extract the relevant information for meta-analysis

#	**Extraction element**	**Contents**	**Type**
General Information			
1	Title	Title of the article	Text
2	Author	The authors of the article	Text
3	Country	The country of the research institute	Text
4	Year	The year of publication	Numeric
Description of the study			
5	Segmentation approach	☐ Supervised ☐ Unsupervised	Classes
6	Segmentation method	☐ Clustering ☐ Saliency ☐ Clustering and saliency	Classes
7	Segmentation technique	For instance, K-Means Algorithm, SLIC, Mean shift, Deep learning, bottom-up saliency, and top-down saliency.	Text
8	Preprocessing stage is implemented	☐ Yes ☐ No	Classes
9	Unit of processing	☐ Pixel ☐ Patch ☐ Region	Classes
10	Dataset	List of the dataset used for evaluation	Text
11	Number of datasets	Number of datasets used for the evaluation	Numeric
12	Number of images	Number of images used for the evaluation	Numeric
13	Precision	The average precision of the produced results	Numeric
14	Recall	The average recall of the produced results	Numeric
15	F-Score	The average F-Score of the produced results	Numeric

2.5 Data synthesis

Data synthesis is performed by the statistical analysis of the extracted data using meta set, meta summarize, meta-Galbraith, meta forest plot, meta funnel plot, and meta regress of Stata software

(StataCorp. 2021, College Station, StataCorp LLC) of version 17. Stata is a programmable general-purpose statistical software package. This statistical software provides comprehensive commands for meta-analysis. Hence it has been widely adopted by researchers to perform meta-analyses (Dai *et al.* 2020; Poorolajal and Noornejad 2021; Fisher *et al.* 2022). In this study, a meta-analysis of image segmentation methods was conducted to compute the effect of individual studies and the pooled effect size of all included studies.

2.5.1 Computing effect sizes

The effect sizes of each primary study included and the pooled effect size of all primary studies were computed using the extracted data. The meta-analysis was performed based on the random-effect model as in this model the inference is not limited to the samples represented in the studies rather it incorporates the inference to a universe of studies exhibiting various study characteristics (Hedges and Vevea 1998). Since the extracted data were from several published articles written by various authors who implemented different segmentation approaches, methods, and techniques on different categories of image sets, the selection of the random-effect model is plausible. A forest plot is used to achieve the visual representation of the effect size of all included studies and the pooled effect size, and it graphically summarizes how the effect size of the individual studies is distributed around zero and pooled effect size. A forest plot is an orthodox tool for visually summarizing the study heterogeneity and the biases in the outcome of the included studies (Olugbara *et al.* 2021). Traditionally, a diamond that represents the confidence interval has been used to show the summary effect in a forest plot. Further, this study used Galbraith plots (Galbraith 1990) to summarize the meta-analysis results graphically, report the study-specific effect size, detect the expected outliers, and also to assess the heterogeneity among the effect sizes. It shows the standardized effect size of each study on the vertical axis and the inverse of the standard error or precision on the horizontal axis.

2.5.2 Detecting statistical heterogeneity

The statistical heterogeneity test which is a measure of variation in the true effect sizes was conducted using the random-effect model to identify the pattern of effects (Borenstein *et al.* 2009). In the meta-analysis, identification of the patterns of effects is an important aspect to understand whether the effect size is consistent across studies or whether is there a variance in effect size. The measure of weighted squared deviation (Q statistics), between-study variance (τ^2), the proportion of the true

heterogeneity and the total observed variations (I^2) are the widely accepted measures for estimating statistical heterogeneity (Borenstein *et al.* 2009) and hence this study used these metrics to estimate the global measure of variations.

2.5.3 Conducting moderator analysis

The source of heterogeneity can be unveiled using the moderator analysis which is frequently applied to test the factors that contribute to the statistical heterogeneity of the research and to explain the conflicting results stated in the literature (Crocetti 2016). Statistical heterogeneity metrics are intended to provide the global measure of variation without demonstrating the sources of heterogeneity. The intrinsic void necessitates the use of moderator analysis to identify the origins of heterogeneity. In a systematic review with meta-analysis, the moderator analysis is performed using subgroup analysis and meta-regression (Borenstein *et al.* 2009). Data are divided into smaller groups for subgroup analyses, which examine how the subsets of data compare to one another. Subgroup analysis compares overall effect sizes and examines subgroup heterogeneity. In this study two subgroup analysis is conducted based on segmentation approaches (supervised and unsupervised), and segmentation methods (clustering, saliency, saliency and clustering) to investigate the heterogeneity among the studies. Meta-regression was used to investigate the possible sources of the between-study heterogeneity. The variables, publication year, pre-preprocessing, number of datasets, and number of images were all subjected to univariate regression analysis.

2.5.4 Examining publication bias

Publication bias is a recognized risk to the strength of meta-analysis and it occurs when studies with statistically significant results or higher quality studies are more likely to be reflected in the literature than the studies without these characteristics (Sutton *et al.* 2000; Borenstein *et al.* 2009). Investigation of publication bias in meta-analysis is a critical step to assess the reliability of primary findings and determine the generalizability and shortcoming of the cumulative findings (Ogunsakin *et al.* 2021; Olugbara *et al.* 2021). Hence in this study, the publication bias was visually assessed using a funnel plot (Light *et al.* 1984) which is a visual tool to evaluate the publication bias (Rothstein, Sutton and Borenstein 2006). Since the visual interpretation of the funnel plot is difficult and subjective, a statistical method such as Egger's linear regression has been developed to investigate the publication bias (Crocetti 2016). Hence in this study, Egger's test is utilized to examine the potential statistical indicative of publication bias to complement the visual assessment of publication by funnel plot.

2.6 Results

A meta-analysis based on the random-effect model was applied for synthesizing the quantitative results of the 151 reviewed studies to discover the effect size, statistical heterogeneity, and publication biases. The meta-analysis was carried out based on the precision and recall effects on the F-Score, and the standard error of the effect size to estimate the performance of segmentation methods.

2.6.1 Meta-analysis summary

Results demonstrated in Table 2-3 showed that the between-study variability is high as per the statistics $\tau^2 = 37.787$, the ratio of true heterogeneity to total observed variation, I^2 =56.99%, with heterogeneity chi-square(Q)=348.76, degree of freedom=150, and p<0.001. The high value of Q denotes the presence of variation and moderate heterogeneity. The I^2 value of 25%, 50%, and 75% are considered respectively small, medium, and high levels of heterogeneity (Higgins *et al.* 2003). The value, 56.99% of I^2 supplements the extent of moderate heterogeneity and it demonstrated that the variability across the studies is because of heterogeneity and not by chance. The model fit gives a combined effects size estimation of -7.848 within a 95% confidence interval, [-9.359, -6.337].

Table 2-3 Meta-analysis summary

Meta-analysis summary **Random Effect model: DerSimonian–Laird**					**Number of studies**			**151**
					Heterogeneity			
					τ^2			**37.787**
					I^2			**56.99%**
Study	**Effect Size**	**[95% CI]**		**Weight**	**Study**	**Effect Size**	**[95% CI]**		**Weight**
(Gion *et al.* 2015)	-1.525	-6.239	3.189	1.36	(Jahanifar *et al.* 2019)	-4.026	-19.039	10.987	0.62
(Ramella 2021)	-6.162	-23.026	10.702	0.53	(Jing *et al.* 2018)	0.99	-21.13	23.11	0.36
(Ren *et al.* 2017)	-0.733	-22.391	20.925	0.37	(Zhou *et al.* 2019)	-2.373	-7.632	2.886	1.32
(Li *et al.* 2021a)	-6.67	-20.67	7.33	0.67	(Manno-Kovacs 2018)	-7.439	-12.396	-2.482	1.34
(Tu *et al.* 2021)	-20.616	-31.588	-9.644	0.86	(Zhang *et al.* 2019)	-13.85	-49.6	21.9	0.16
(Ren *et al.* 2020)	-6.668	-24.586	11.25	0.49	(Liu and Yang 2019)	-12.679	-50.016	24.658	0.15
(Kompella and Kulkarni 2020)	-9.977	-16.631	-3.323	1.2	(Liu and Yuan 2019)	-15.128	-26.915	-3.341	0.8
(Galiano, Ramírez and Schiavi 2020)	-18.989	-34.7	-3.278	0.58	(Zhao *et al.* 2019)	-5.97	-19.347	7.407	0.7
(Joshi *et al.* 2020)	13.949	-18.449	46.347	0.19	(Abkenar, Sadreazami and Ahmad 2018)	-12.775	-26.746	1.196	0.67
(Kim 2019)	-0.248	-19.307	18.811	0.45	(Li, Du and Wang 2018)	-35.017	-53.545	-16.489	0.47
(Xu, He and Lv 2019)	3.779	-6.742	14.3	0.89	(Yang *et al.* 2018)	-12.076	-39.858	15.706	0.25
(Song *et al.* 2017)	-26.043	-37.078	-15.008	0.85	(Li, Zhou and Bai 2018)	-9.013	-14.336	-3.69	1.32
(Zou *et al.* 2015)	-21.158	-38.633	-3.683	0.51	(Jian *et al.* 2018)	-22.319	-55.807	11.169	0.18
(Zhou and Liu 2015)	-1.779	-6.422	2.864	1.37	(Li *et al.* 2018b)	-15.486	-29.486	-1.486	0.67

(Xu *et al.* 2013)	-6.575	-23.178	10.028	0.54	(Singh, Arya and Agrawal 2018)	-16.787	-26.332	-7.242	0.97
(Yanulevskaya, Uijlings and Geusebroek 2013)	-11.002	-18.777	-3.227	1.11	(Annum, Riaz and Ghafoor 2018)	-15.384	-27.116	-3.652	0.81
(Jung and Kim 2012)	-5.508	-22.189	11.173	0.54	(Zhao *et al.* 2018)	6.76	-18.271	31.791	0.3
(Ning *et al.* 2022)	-16.083	-29.334	-2.832	0.71	(Ayoub *et al.* 2018)	-10.893	-32.611	10.825	0.37
(Singh and Karthikeyan 2022)	-11.503	-18.982	-4.024	1.13	(Feng *et al.* 2018)	-40.679	-82.056	0.698	0.12
(Kumar and Meenpal 2022)	2.933	-21.118	26.984	0.32	(Olugbara, Taiwo and Heukelman 2018)	-3.046	-27.495	21.403	0.31
(Liu *et al.* 2022)	-9.086	-17.226	-0.946	1.08	(Zhou *et al.* 2017)	-13.948	-25.165	-2.731	0.84
(Song *et al.* 2022)	-14.148	-26.386	-1.91	0.77	(Yang *et al.* 2017)	-10.341	-39.791	19.109	0.23
(Moghaddam *et al.* 2021)	-10.75	-26.573	5.073	0.58	(Zhang, Xia and Gao 2017)	1.093	-4.14	6.326	1.32
(Li *et al.* 2022)	1.49	-14.627	17.607	0.56	(Ye *et al.* 2017)	-12.482	-19.087	-5.877	1.21
(Shahin and Almotairi 2021)	-23.476	-47.817	0.865	0.31	(Zhang *et al.* 2017a)	-18.4	-39.846	3.046	0.38
(Zhang and Ma 2021)	-0.249	-6.098	5.6	1.27	(Lou *et al.* 2017)	-30.222	-50.078	-10.366	0.42
(Zhang *et al.* 2021c)	-12.733	-30.049	4.583	0.51	(Fan *et al.* 2017)	3.877	-11.952	19.706	0.58
(Joseph and Olugbara 2021)	-0.2	-5.878	5.478	1.29	(Zhao *et al.* 2017)	-27.209	-48.245	-6.173	0.39
(Yu *et al.* 2021b)	-0.413	-18.372	17.546	0.49	(Huang, Feng and Sun 2017)	16.282	4.632	27.932	0.81
(Moradi, Bayat and Charmi 2021)	-15.674	-36.581	5.233	0.39	(Wang and Wang 2017)	-30.324	-57.777	-2.871	0.25
(Zhang and Wang 2021)	-6.301	-43.054	30.452	0.15	(Singh, Arya and Agrawal 2017)	-10.329	-21.025	0.367	0.88
(Wang *et al.* 2021b)	3.022	-14.51	20.554	0.5	(Wang *et al.* 2017a)	4.675	-22.216	31.566	0.26
(Song, Sui and Hua 2021)	-1.986	-24.526	20.554	0.35	(Hwang *et al.* 2017)	4.696	-9.867	19.259	0.64
(Jian *et al.* 2021)	10.981	-21.647	43.609	0.19	(Zhang *et al.* 2016)	0.466	-9.179	10.111	0.96
(Moradi and Bayat 2021)	-5.661	-36.184	24.862	0.21	(Singh, Arya and Agrawal 2016)	-11.212	-24.142	1.718	0.73
(Zhao *et al.* 2021a)	-3.035	-16.304	10.234	0.71	(Arya, Singh and Agrawal 2016)	-29.32	-45.815	-12.825	0.55
(Zhang *et al.* 2021a)	-78.486	-145.331	-11.641	0.05	(Wang and Wu 2016)	-8.53	-17.181	0.121	1.04
(Niu *et al.* 2021)	-11.693	-18.48	-4.906	1.19	(Zhao *et al.* 2016)	-19.189	-40.751	2.373	0.37
(Yuan, Han and Yan 2021)	-13.546	-46.144	19.052	0.19	(Shi *et al.* 2015)	-17.049	-39.22	5.122	0.36
(He *et al.* 2021b)	-3.191	-7.867	1.485	1.37	(Aytekin, Kiranyaz and Gabbouj 2016)	-12.108	-18.868	-5.348	1.2
(Ma *et al.* 2021a)	-1.132	-16.675	14.411	0.59	(Kim *et al.* 2016)	-8.524	-31.748	14.7	0.33
(Nawaz and Yan 2021)	-11.504	-20.839	-2.169	0.98	(Sun, Tang and Zhang 2016)	-9.051	-22.555	4.453	0.7
(Zhou *et al.* 2021)	-6.68	-16.004	2.644	0.98	(Nan *et al.* 2015)	-0.866	-6.399	4.667	1.3
(Tang *et al.* 2020)	-9.038	-25.925	7.849	0.53	(Ma *et al.* 2015)	-5.087	-9.589	-0.585	1.38
(Li *et al.* 2020a)	3.502	-3.521	10.525	1.17	(Wang, Ning and Xu 2015)	-28.009	-50.523	-5.495	0.35
(Jing *et al.* 2020)	4.462	-22.946	31.87	0.25	(Qi *et al.* 2015)	-6.765	-17.18	3.65	0.9
(Takács, Kovács and Manno-Kovacs 2021)	-0.351	-7.866	7.164	1.13	(Bao *et al.* 2015)	-26.663	-62.822	9.496	0.16
(Li *et al.* 2020b)	12.946	1.7	24.192	0.84	(Steen *et al.* 2015)	-14.229	-74.292	45.834	0.06
(Song *et al.* 2020a)	-20.625	-48.286	7.036	0.25	(Singh and Agrawal 2015)	-20.129	-30.915	-9.343	0.87
(Pang *et al.* 2020b)	-9.366	-30.202	11.47	0.39	(Manke and Jalal 2015)	-12.831	-52.224	26.562	0.13
(Ma *et al.* 2020)	-35.511	-56.002	-15.02	0.4	(Tian *et al.* 2015)	-10.174	-19.652	-0.696	0.97
(Liang *et al.* 2020)	-23.705	-34.43	-12.98	0.88	(Lou, Ren and Wang 2014)	-8.076	-19.436	3.284	0.83
(Singh and Kumar 2020)	-13.771	-33.596	6.054	0.42	(Chuang, Chen and Chen 2014)	-37.825	-56.421	-19.229	0.46

(Hu *et al.* 2020)	0.196	-13.102	13.494	0.71	(Imamoglu *et al.* 2014)	2.733	-22.701	28.167	0.29
(Zhang and He 2020)	14.091	5.896	22.286	1.07	(Kim and Kim 2014)	-25.486	-38.826	-12.146	0.71
(Du *et al.* 2020)	-2.717	-26.037	20.603	0.33	(Singh, Arya and Agrawal 2014)	-16.693	-33.241	-0.145	0.54
(He, Guo and Yuan 2020)	-2.376	-28.087	23.335	0.28	(Yeh, Liu and Chen 2014)	-6.944	-18.678	4.79	0.81
(Srivastava and Srivastava 2020)	-10.29	-21.005	0.425	0.88	(Kim, Sim and Kim 2014)	-34.11	-95.751	27.531	0.06
(Lopez-Alanis *et al.* 2020)	-7.51	-17.531	2.511	0.93	(Liang *et al.* 2014)	6.001	-34.372	46.374	0.13
(Singh, Mishra and Bhatia 2020)	-5.749	-22.205	10.707	0.55	(Chuang *et al.* 2014)	-37.825	-56.421	-19.229	0.46
(Deeba, Bui and Wahid 2020)	-36.584	-87.112	13.944	0.08	(Zheng *et al.* 2014)	-2.598	-28.858	23.662	0.27
(Huang *et al.* 2020)	-8.151	-21.516	5.214	0.7	(Li, Meng and Ngan 2013)	-32.246	-69.093	4.601	0.15
(Jiang *et al.* 2020)	-21.45	-35.27	-7.63	0.68	(Zhou and Jin 2013)	-2.101	-15.407	11.205	0.71
(Piao *et al.* 2020)	-3.471	-7.814	0.872	1.39	(Liu *et al.* 2012)	-0.032	-8.36	8.296	1.06
(Qiu *et al.* 2020)	-15.085	-26.886	-3.284	0.8	(Thi Le *et al.* 2022)	-4.578	-15.426	6.27	0.87
(Tu *et al.* 2020)	-11.908	-26.188	2.372	0.65	(Joseph and Olugbara 2022b)	-9.248	-15.616	-2.88	1.23
(Yao and Gong 2020)	-2.325	-31.922	27.272	0.22	(Hui *et al.* 2021)	-21.951	-58.828	14.926	0.15
(Zhang *et al.* 2020f)	-4.833	-27.514	17.848	0.35	(Karthik, Menaka and Hariharan 2021)	9.383	-18.741	37.507	0.24
(Qian *et al.* 2019)	-16.499	-30.832	-2.166	0.65	(Liu, Kuang and Ji 2020)	1.523	-6.293	9.339	1.11
(Li *et al.* 2019a)	-3.01	-8.206	2.186	1.33	(Shan *et al.* 2019)	-29.532	-46.066	-12.998	0.55
(Song *et al.* 2019)	-7.329	-12.74	-1.918	1.31	(Saleem *et al.* 2019)	9.397	2.22	16.574	1.16
(Jia *et al.* 2019b)	-12.203	-38.341	13.935	0.28	(Zhuang *et al.* 2018)	-10.605	-23.184	1.974	0.75
(Singh *et al.* 2019)	-11.526	-24.174	1.122	0.75	(Qin *et al.* 2018)	5.585	-5.326	16.496	0.86
(Wang *et al.* 2019)	-13.145	-22.89	-3.4	0.95	(Zhu *et al.* 2017)	-6.57	-11.921	-1.219	1.31
(Lopez-Alanis *et al.* 2019)	12.146	-16.881	41.173	0.23	(Paramanandam *et al.* 2016)	1.172	-3.844	6.188	1.34
(Huang, Xing and Wang 2019)	-7.526	-21.399	6.347	0.68	**Theta**	**-7.848**	**-9.359**	**-6.337**	
Test of theta=0;		**Z= -10.18**			**Prob > |z| =0.000**				
Test of homogeneity: Q= chi2(150) = 348.76					**Prob > Q =0.000**				

Figure 2-2 illustrates the forest plot derived from the meta-analysis describing the study, effect size, confidence interval, and weight.

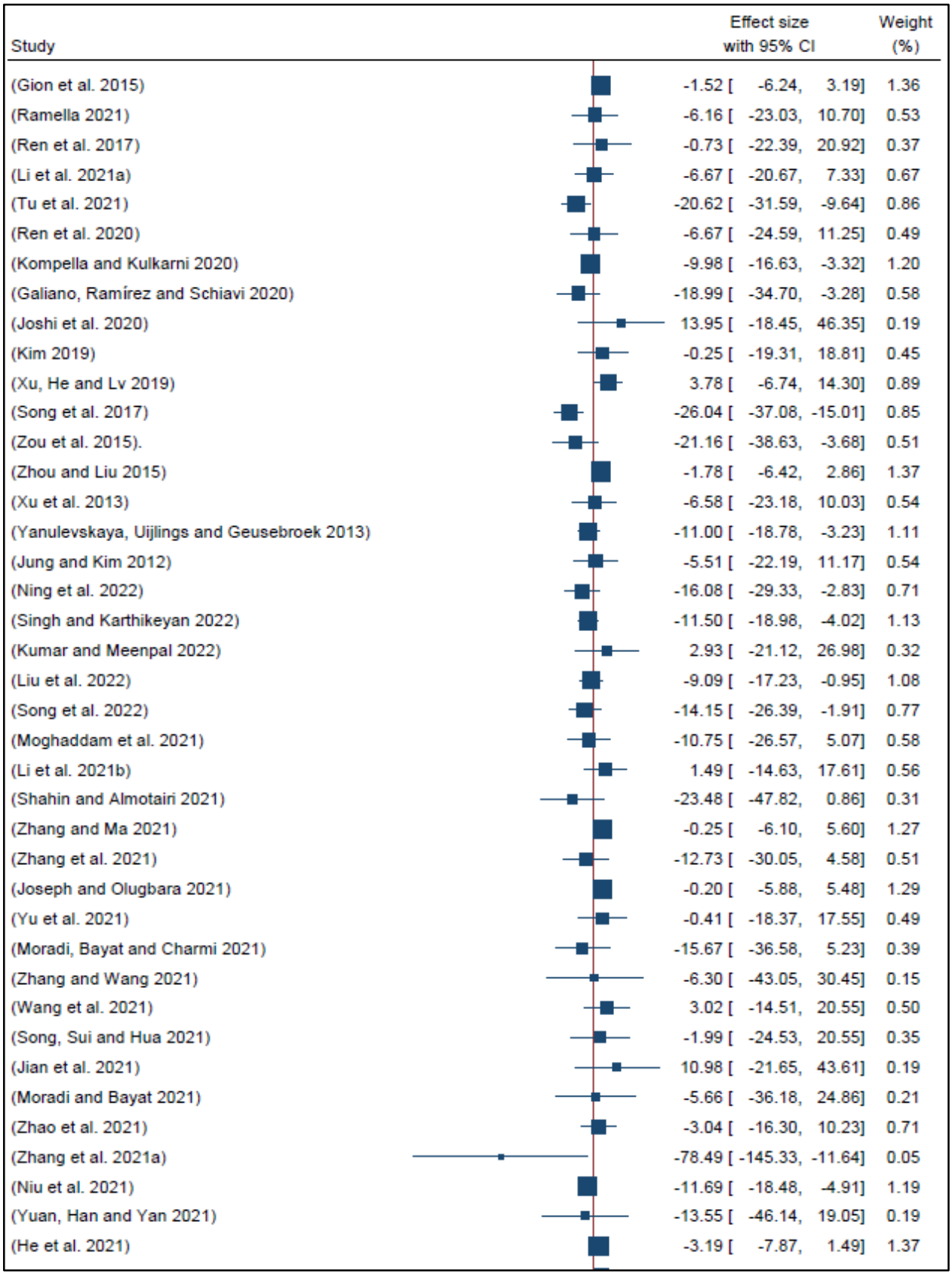
Study
Effect size with 95% CI
Weight (%)
(Gion et al. 2015) -1.52 [-6.24, 3.19] 1.36
(Ramella 2021) -6.16 [-23.03, 10.70] 0.53
(Ren et al. 2017) -0.73 [-22.39, 20.92] 0.37
(Li et al. 2021a) -6.67 [-20.67, 7.33] 0.67
(Tu et al. 2021) -20.62 [-31.59, -9.64] 0.86
(Ren et al. 2020) -6.67 [-24.59, 11.25] 0.49
(Kompella and Kulkarni 2020) -9.98 [-16.63, -3.32] 1.20
(Galiano, Ramírez and Schiavi 2020) -18.99 [-34.70, -3.28] 0.58
(Joshi et al. 2020) 13.95 [-18.45, 46.35] 0.19
(Kim 2019) -0.25 [-19.31, 18.81] 0.45
(Xu, He and Lv 2019) 3.78 [-6.74, 14.30] 0.89
(Song et al. 2017) -26.04 [-37.08, -15.01] 0.85
(Zou et al. 2015). -21.16 [-38.63, -3.68] 0.51
(Zhou and Liu 2015) -1.78 [-6.42, 2.86] 1.37
(Xu et al. 2013) -6.58 [-23.18, 10.03] 0.54
(Yanulevskaya, Uijlings and Geusebroek 2013) -11.00 [-18.78, -3.23] 1.11
(Jung and Kim 2012) -5.51 [-22.19, 11.17] 0.54
(Ning et al. 2022) -16.08 [-29.33, -2.83] 0.71
(Singh and Karthikeyan 2022) -11.50 [-18.98, -4.02] 1.13
(Kumar and Meenpal 2022) 2.93 [-21.12, 26.98] 0.32
(Liu et al. 2022) -9.09 [-17.23, -0.95] 1.08
(Song et al. 2022) -14.15 [-26.39, -1.91] 0.77
(Moghaddam et al. 2021) -10.75 [-26.57, 5.07] 0.58
(Li et al. 2021b) 1.49 [-14.63, 17.61] 0.56
(Shahin and Almotairi 2021) -23.48 [-47.82, 0.86] 0.31
(Zhang and Ma 2021) -0.25 [-6.10, 5.60] 1.27
(Zhang et al. 2021) -12.73 [-30.05, 4.58] 0.51
(Joseph and Olugbara 2021) -0.20 [-5.88, 5.48] 1.29
(Yu et al. 2021) -0.41 [-18.37, 17.55] 0.49
(Moradi, Bayat and Charmi 2021) -15.67 [-36.58, 5.23] 0.39
(Zhang and Wang 2021) -6.30 [-43.05, 30.45] 0.15
(Wang et al. 2021) 3.02 [-14.51, 20.55] 0.50
(Song, Sui and Hua 2021) -1.99 [-24.53, 20.55] 0.35
(Jian et al. 2021) 10.98 [-21.65, 43.61] 0.19
(Moradi and Bayat 2021) -5.66 [-36.18, 24.86] 0.21
(Zhao et al. 2021) -3.04 [-16.30, 10.23] 0.71
(Zhang et al. 2021a) -78.49 [-145.33, -11.64] 0.05
(Niu et al. 2021) -11.69 [-18.48, -4.91] 1.19
(Yuan, Han and Yan 2021) -13.55 [-46.14, 19.05] 0.19
(He et al. 2021) -3.19 [-7.87, 1.49] 1.37

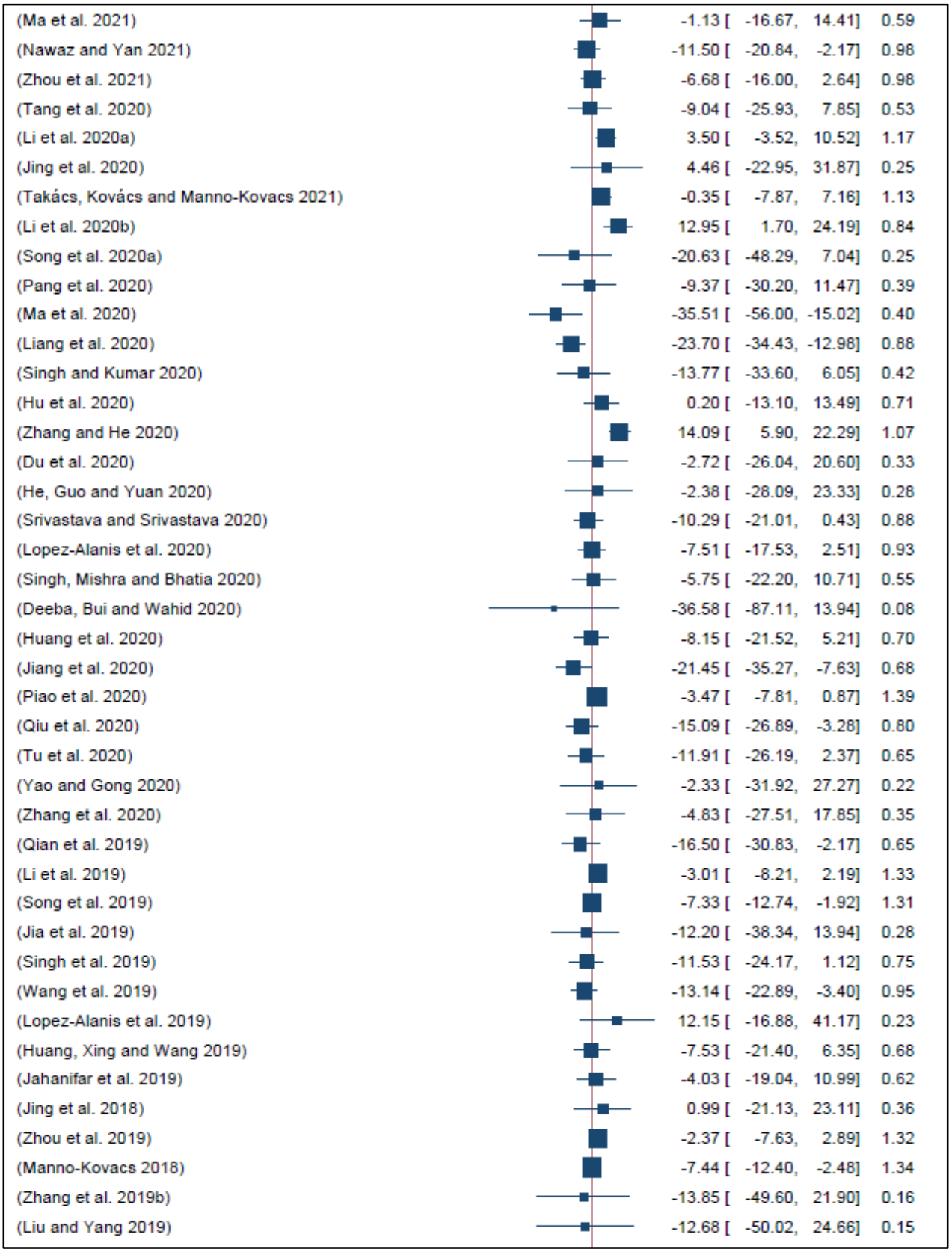
(Ma et al. 2021) -1.13 [-16.67, 14.41] 0.59
(Nawaz and Yan 2021) -11.50 [-20.84, -2.17] 0.98
(Zhou et al. 2021) -6.68 [-16.00, 2.64] 0.98
(Tang et al. 2020) -9.04 [-25.93, 7.85] 0.53
(Li et al. 2020a) 3.50 [-3.52, 10.52] 1.17
(Jing et al. 2020) 4.46 [-22.95, 31.87] 0.25
(Takács, Kovács and Manno-Kovacs 2021) -0.35 [-7.87, 7.16] 1.13
(Li et al. 2020b) 12.95 [1.70, 24.19] 0.84
(Song et al. 2020a) -20.63 [-48.29, 7.04] 0.25
(Pang et al. 2020) -9.37 [-30.20, 11.47] 0.39
(Ma et al. 2020) -35.51 [-56.00, -15.02] 0.40
(Liang et al. 2020) -23.70 [-34.43, -12.98] 0.88
(Singh and Kumar 2020) -13.77 [-33.60, 6.05] 0.42
(Hu et al. 2020) 0.20 [-13.10, 13.49] 0.71
(Zhang and He 2020) 14.09 [5.90, 22.29] 1.07
(Du et al. 2020) -2.72 [-26.04, 20.60] 0.33
(He, Guo and Yuan 2020) -2.38 [-28.09, 23.33] 0.28
(Srivastava and Srivastava 2020) -10.29 [-21.01, 0.43] 0.88
(Lopez-Alanis et al. 2020) -7.51 [-17.53, 2.51] 0.93
(Singh, Mishra and Bhatia 2020) -5.75 [-22.20, 10.71] 0.55
(Deeba, Bui and Wahid 2020) -36.58 [-87.11, 13.94] 0.08
(Huang et al. 2020) -8.15 [-21.52, 5.21] 0.70
(Jiang et al. 2020) -21.45 [-35.27, -7.63] 0.68
(Piao et al. 2020) -3.47 [-7.81, 0.87] 1.39
(Qiu et al. 2020) -15.09 [-26.89, -3.28] 0.80
(Tu et al. 2020) -11.91 [-26.19, 2.37] 0.65
(Yao and Gong 2020) -2.33 [-31.92, 27.27] 0.22
(Zhang et al. 2020) -4.83 [-27.51, 17.85] 0.35
(Qian et al. 2019) -16.50 [-30.83, -2.17] 0.65
(Li et al. 2019) -3.01 [-8.21, 2.19] 1.33
(Song et al. 2019) -7.33 [-12.74, -1.92] 1.31
(Jia et al. 2019) -12.20 [-38.34, 13.94] 0.28
(Singh et al. 2019) -11.53 [-24.17, 1.12] 0.75
(Wang et al. 2019) -13.14 [-22.89, -3.40] 0.95
(Lopez-Alanis et al. 2019) 12.15 [-16.88, 41.17] 0.23
(Huang, Xing and Wang 2019) -7.53 [-21.40, 6.35] 0.68
(Jahanifar et al. 2019) -4.03 [-19.04, 10.99] 0.62
(Jing et al. 2018) 0.99 [-21.13, 23.11] 0.36
(Zhou et al. 2019) -2.37 [-7.63, 2.89] 1.32
(Manno-Kovacs 2018) -7.44 [-12.40, -2.48] 1.34
(Zhang et al. 2019b) -13.85 [-49.60, 21.90] 0.16
(Liu and Yang 2019) -12.68 [-50.02, 24.66] 0.15

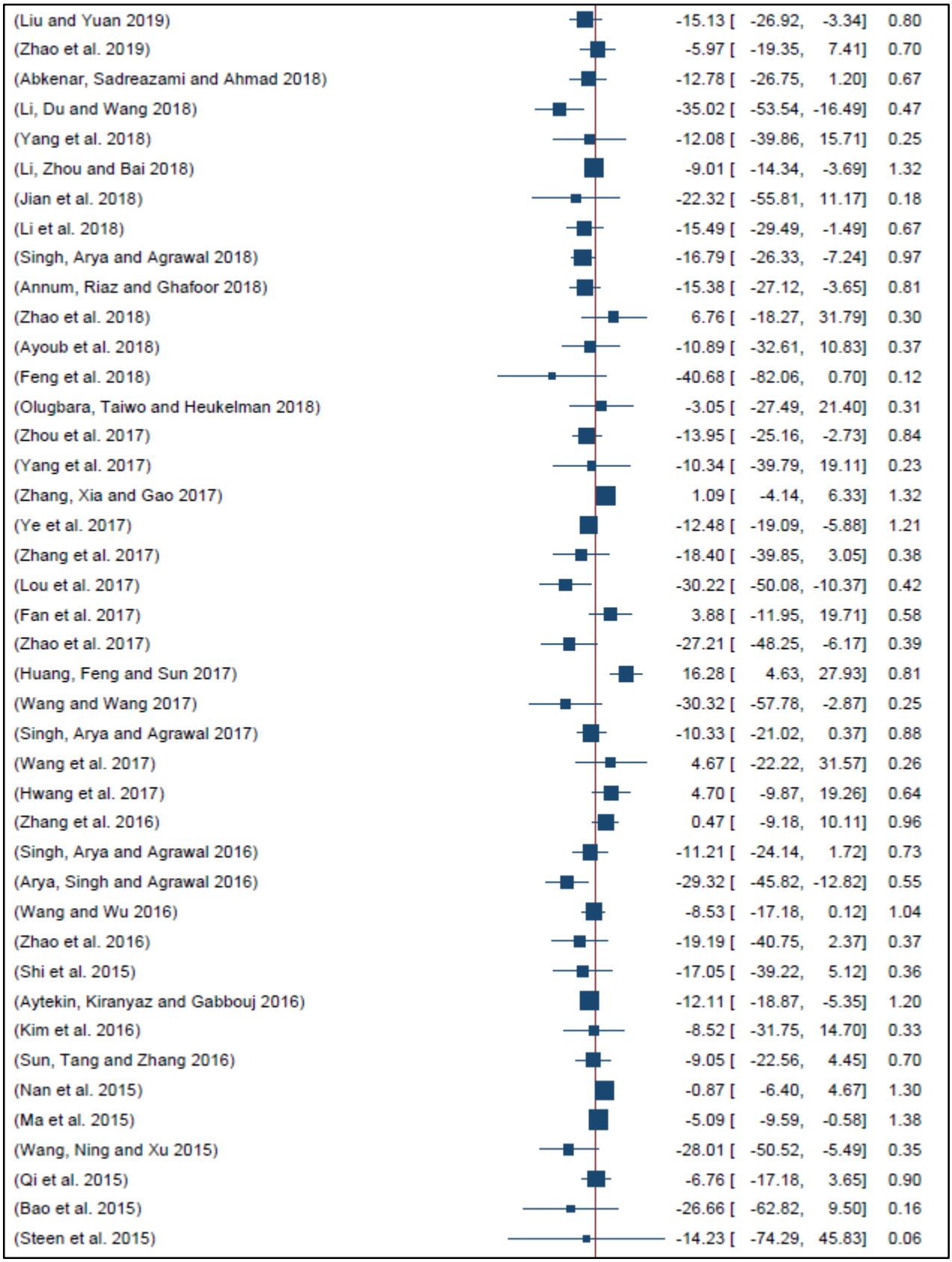
(Liu and Yuan 2019) -15.13 [-26.92, -3.34] 0.80
(Zhao et al. 2019) -5.97 [-19.35, 7.41] 0.70
(Abkenar, Sadreazami and Ahmad 2018) -12.78 [-26.75, 1.20] 0.67
(Li, Du and Wang 2018) -35.02 [-53.54, -16.49] 0.47
(Yang et al. 2018) -12.08 [-39.86, 15.71] 0.25
(Li, Zhou and Bai 2018) -9.01 [-14.34, -3.69] 1.32
(Jian et al. 2018) -22.32 [-55.81, 11.17] 0.18
(Li et al. 2018) -15.49 [-29.49, -1.49] 0.67
(Singh, Arya and Agrawal 2018) -16.79 [-26.33, -7.24] 0.97
(Annum, Riaz and Ghafoor 2018) -15.38 [-27.12, -3.65] 0.81
(Zhao et al. 2018) 6.76 [-18.27, 31.79] 0.30
(Ayoub et al. 2018) -10.89 [-32.61, 10.83] 0.37
(Feng et al. 2018) -40.68 [-82.06, 0.70] 0.12
(Olugbara, Taiwo and Heukelman 2018) -3.05 [-27.49, 21.40] 0.31
(Zhou et al. 2017) -13.95 [-25.16, -2.73] 0.84
(Yang et al. 2017) -10.34 [-39.79, 19.11] 0.23
(Zhang, Xia and Gao 2017) 1.09 [-4.14, 6.33] 1.32
(Ye et al. 2017) -12.48 [-19.09, -5.88] 1.21
(Zhang et al. 2017) -18.40 [-39.85, 3.05] 0.38
(Lou et al. 2017) -30.22 [-50.08, -10.37] 0.42
(Fan et al. 2017) 3.88 [-11.95, 19.71] 0.58
(Zhao et al. 2017) -27.21 [-48.25, -6.17] 0.39
(Huang, Feng and Sun 2017) 16.28 [4.63, 27.93] 0.81
(Wang and Wang 2017) -30.32 [-57.78, -2.87] 0.25
(Singh, Arya and Agrawal 2017) -10.33 [-21.02, 0.37] 0.88
(Wang et al. 2017) 4.67 [-22.22, 31.57] 0.26
(Hwang et al. 2017) 4.70 [-9.87, 19.26] 0.64
(Zhang et al. 2016) 0.47 [-9.18, 10.11] 0.96
(Singh, Arya and Agrawal 2016) -11.21 [-24.14, 1.72] 0.73
(Arya, Singh and Agrawal 2016) -29.32 [-45.82, -12.82] 0.55
(Wang and Wu 2016) -8.53 [-17.18, 0.12] 1.04
(Zhao et al. 2016) -19.19 [-40.75, 2.37] 0.37
(Shi et al. 2015) -17.05 [-39.22, 5.12] 0.36
(Aytekin, Kiranyaz and Gabbouj 2016) -12.11 [-18.87, -5.35] 1.20
(Kim et al. 2016) -8.52 [-31.75, 14.70] 0.33
(Sun, Tang and Zhang 2016) -9.05 [-22.56, 4.45] 0.70
(Nan et al. 2015) -0.87 [-6.40, 4.67] 1.30
(Ma et al. 2015) -5.09 [-9.59, -0.58] 1.38
(Wang, Ning and Xu 2015) -28.01 [-50.52, -5.49] 0.35
(Qi et al. 2015) -6.76 [-17.18, 3.65] 0.90
(Bao et al. 2015) -26.66 [-62.82, 9.50] 0.16
(Steen et al. 2015) -14.23 [-74.29, 45.83] 0.06

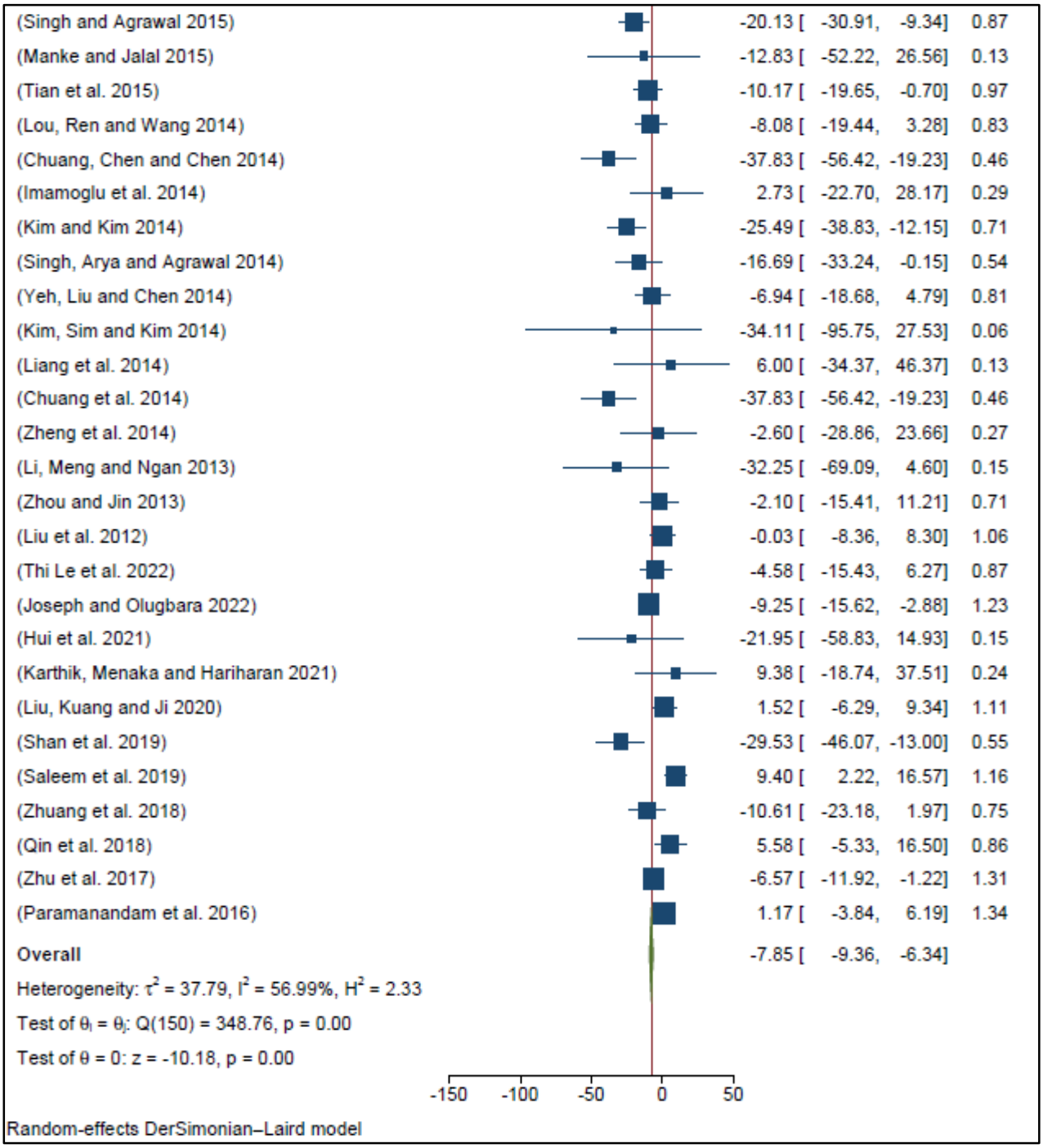

Figure 2-2 Forest plot for distribution of effect sizes of precision of image segmentation methods

Further, the Galbraith plot depicted in Figure 2-3 summarize the meta-analysis results. The inverse of the standard error (z-score) is displayed on the x-axis of the Galbraith plot, and the y-axis displays the effect size divided by the standard error. The regression line runs through the center of the graph, and each study is represented by a single dot. The slope of the regression line (red reference line) is equal to the overall effect size is -7.85. The presence of studies outside the 95% confidence

interval region (shaded area) highlights the occurrence of substantial heterogeneity. Only 10 studies (7%) in this random effect meta-analysis fall outside the gray area, while most studies (93%) are grouped within the shaded area. This demonstrates the weak evidence of heterogeneity. Studies with more precision are those that are further away from the y-axis, and in this study, all of the studies are away from the y-axis. Additionally, studies with higher precision are those that are more to the right on the x-axis. Ten studies are found beyond the graded region of the Galbraith plot, suggesting that these studies may be a source of heterogeneity.

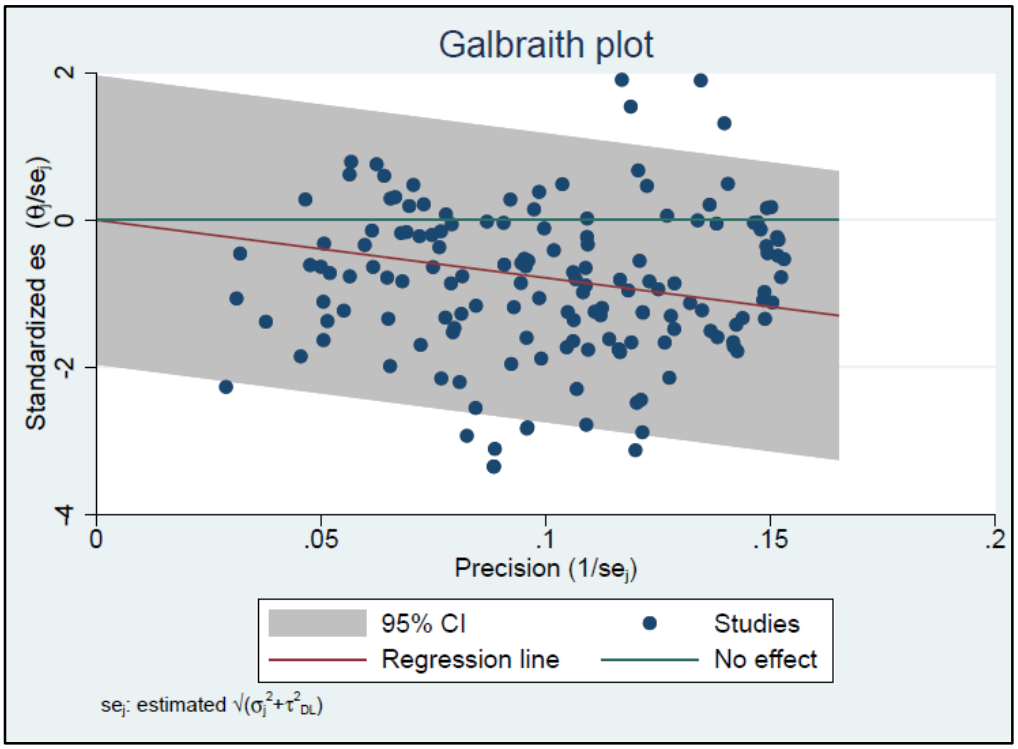

Figure 2-3 Galbraith plot of reviewed studies

2.6.2 Subgroup analysis

Since moderate heterogeneity is identified, the subgroup analysis was performed to unveil the causes of heterogeneity. Tables 2-4 and 2-5 respectively show the results of the subgroup analysis performed based on the image segmentation approaches and methods. Table 2-5 illustrates the subgroup analysis results with non-trivial intra-group heterogeneity found at p <0.001 with $I^2 = 57.57\%$ with an effect size of -8.131 at 95% CI [-10.029, -6.232] for the unsupervised segmentation approach. This result was followed by intra-group significant heterogeneity of supervised methods with p <0.001 with $I^2 = 56.47\%$ with an effect size of -7.380 within 95% CI [-9.896, -4-865] for supervised segmentation approach.

Table 2-4 Subgroup analysis for comparison of different segmentation approaches

Group	Number of studies	ES 95%CI	Q	I^2	Test for heterogeneity	
					df	P value
Supervised	46	-7.380 [-9.896, -4.865]	103.37	56.47	45	0.000 *
Unsupervised	105	-8.131 [-10.029, -6.232]	245.13	57.57	104	0.000*
Overall	151	-7.848 [-9.359, -6.337]	348.76	56.99	150	0.000*

Table 2-5 illustrates the subgroup analysis results with non-trivial intra-group heterogeneity detected at p <0.001 with $I^2 = 59.78\%$ with an effect size of -7.612 at 95% CI [-9.711,-5.513] for segmentation methods based on saliency and clustering. This result was followed by intra-group significant heterogeneity of saliency-based segmentation methods with p <0.001, $I^2 = 54.59\%$ and effect size of -8.441 at 95% CI [-10.686, -6.196]. However, the subgroup analysis based on the clustering-based method with $I^2 = 0.00\%$ and p = 0.848 did not reveal any statistical heterogeneity. The non-significant heterogeneity within this subgroup is mainly because of a small number of studies reported in this category of image segmentation.

Table 2-5 Subgroup analysis for comparison of different segmentation methods

Group	Number of studies	ES 95%CI	Q	I^2	Test for heterogeneity	
					df	P value
Clustering	2	1.263 [-6.089, 8.615]	0.04	0.00	1	0.848
Saliency	74	-8.441 [-10.686, -6.196]	160.76	54.59	73	0.000*
Saliency and clustering	75	-7.612 [-9.711, -5.513]	184.00	59.78	74	0.000*
Overall	151	-7.848 [-9.359, -6.337]	348.76	56.99	150	0.000*

Graphical illustration of the subgroup analysis based on image segmentation approach and method is respectively depicted in Figures 2-4 and 2-5.

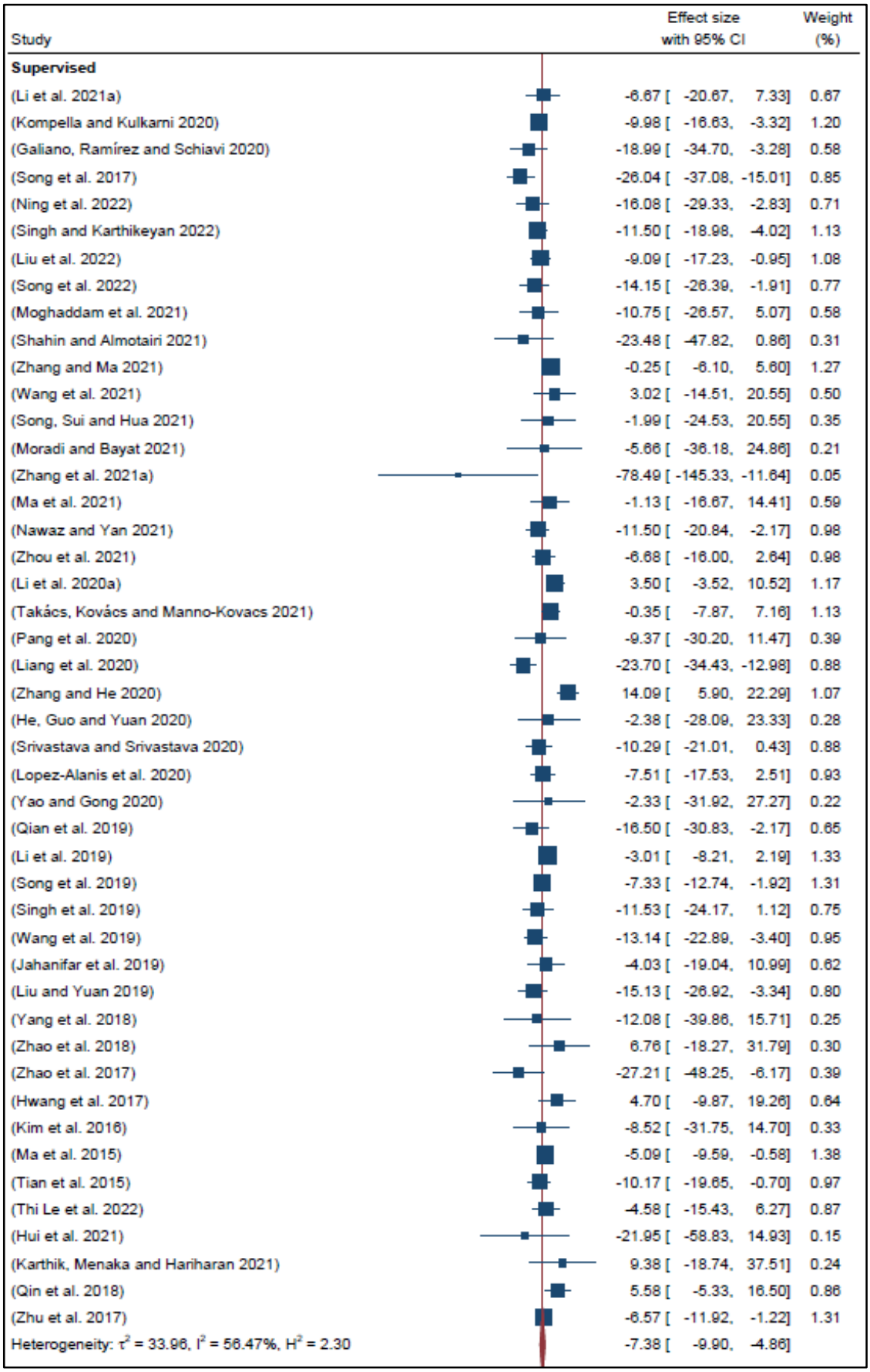
Study
Effect size with 95% CI
Weight (%)
Supervised
(Li et al. 2021a) -6.67 [-20.67, 7.33] 0.67
(Kompella and Kulkarni 2020) -9.98 [-16.63, -3.32] 1.20
(Galiano, Ramírez and Schiavi 2020) -18.99 [-34.70, -3.28] 0.58
(Song et al. 2017) -26.04 [-37.08, -15.01] 0.85
(Ning et al. 2022) -16.08 [-29.33, -2.83] 0.71
(Singh and Karthikeyan 2022) -11.50 [-18.98, -4.02] 1.13
(Liu et al. 2022) -9.09 [-17.23, -0.95] 1.08
(Song et al. 2022) -14.15 [-26.39, -1.91] 0.77
(Moghaddam et al. 2021) -10.75 [-26.57, 5.07] 0.58
(Shahin and Almotairi 2021) -23.48 [-47.82, 0.86] 0.31
(Zhang and Ma 2021) -0.25 [-6.10, 5.60] 1.27
(Wang et al. 2021) 3.02 [-14.51, 20.55] 0.50
(Song, Sui and Hua 2021) -1.99 [-24.53, 20.55] 0.35
(Moradi and Bayat 2021) -5.66 [-36.18, 24.86] 0.21
(Zhang et al. 2021a) -78.49 [-145.33, -11.64] 0.05
(Ma et al. 2021) -1.13 [-16.67, 14.41] 0.59
(Nawaz and Yan 2021) -11.50 [-20.84, -2.17] 0.98
(Zhou et al. 2021) -6.68 [-16.00, 2.64] 0.98
(Li et al. 2020a) 3.50 [-3.52, 10.52] 1.17
(Takács, Kovács and Manno-Kovacs 2021) -0.35 [-7.87, 7.16] 1.13
(Pang et al. 2020) -9.37 [-30.20, 11.47] 0.39
(Liang et al. 2020) -23.70 [-34.43, -12.98] 0.88
(Zhang and He 2020) 14.09 [5.90, 22.29] 1.07
(He, Guo and Yuan 2020) -2.38 [-28.09, 23.33] 0.28
(Srivastava and Srivastava 2020) -10.29 [-21.01, 0.43] 0.88
(Lopez-Alanis et al. 2020) -7.51 [-17.53, 2.51] 0.93
(Yao and Gong 2020) -2.33 [-31.92, 27.27] 0.22
(Qian et al. 2019) -16.50 [-30.83, -2.17] 0.65
(Li et al. 2019) -3.01 [-8.21, 2.19] 1.33
(Song et al. 2019) -7.33 [-12.74, -1.92] 1.31
(Singh et al. 2019) -11.53 [-24.17, 1.12] 0.75
(Wang et al. 2019) -13.14 [-22.89, -3.40] 0.95
(Jahanifar et al. 2019) -4.03 [-19.04, 10.99] 0.62
(Liu and Yuan 2019) -15.13 [-26.92, -3.34] 0.80
(Yang et al. 2018) -12.08 [-39.86, 15.71] 0.25
(Zhao et al. 2018) 6.76 [-18.27, 31.79] 0.30
(Zhao et al. 2017) -27.21 [-48.25, -6.17] 0.39
(Hwang et al. 2017) 4.70 [-9.87, 19.26] 0.64
(Kim et al. 2016) -8.52 [-31.75, 14.70] 0.33
(Ma et al. 2015) -5.09 [-9.59, -0.58] 1.38
(Tian et al. 2015) -10.17 [-19.65, -0.70] 0.97
(Thi Le et al. 2022) -4.58 [-15.43, 6.27] 0.87
(Hui et al. 2021) -21.95 [-58.83, 14.93] 0.15
(Karthik, Menaka and Hariharan 2021) 9.38 [-18.74, 37.51] 0.24
(Qin et al. 2018) 5.58 [-5.33, 16.50] 0.86
(Zhu et al. 2017) -6.57 [-11.92, -1.22] 1.31
Heterogeneity: τ^2 = 33.96, I^2 = 56.47%, H^2 = 2.30 -7.38 [-9.90, -4.86]

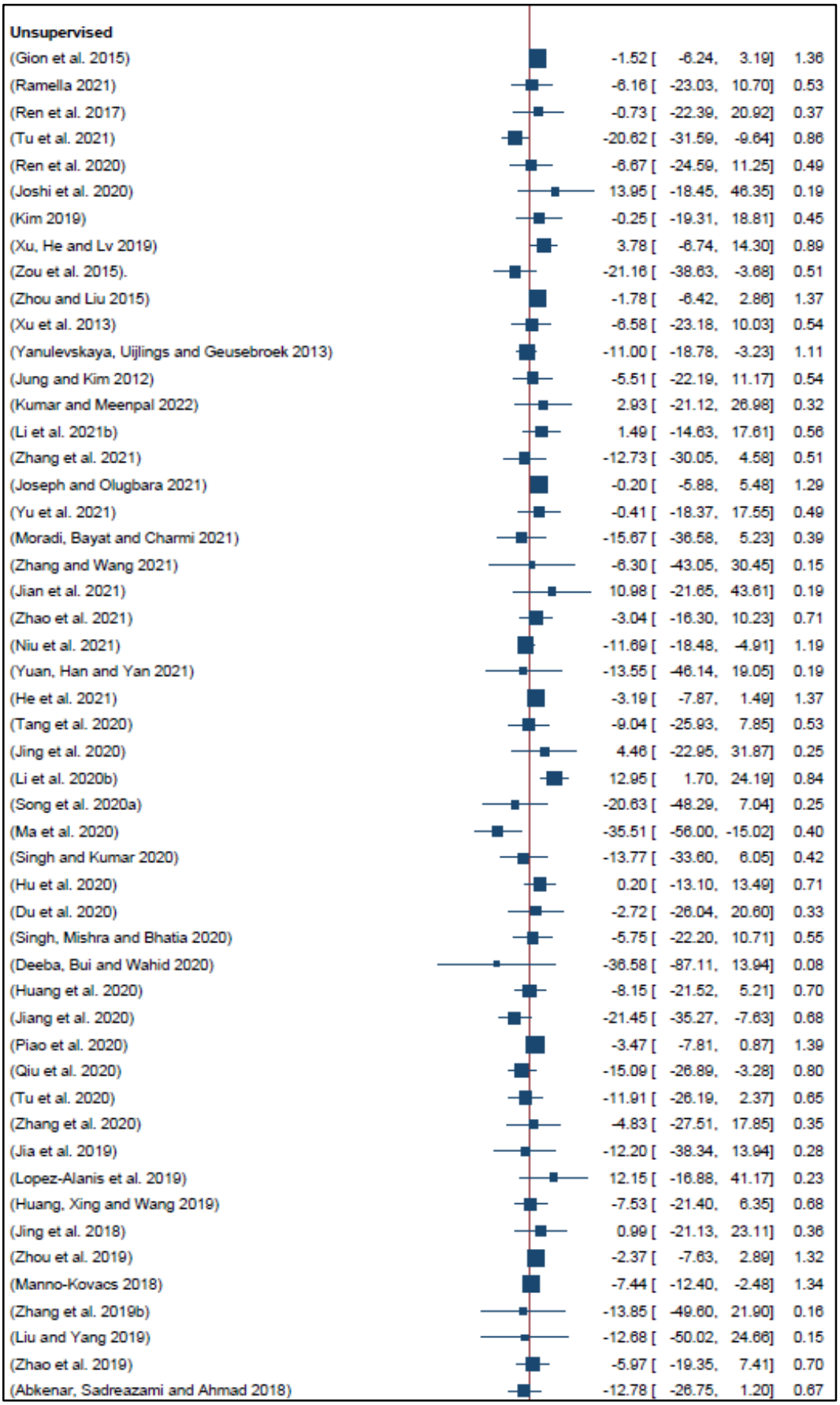
Unsupervised
(Gion et al. 2015) -1.52 [-6.24, 3.19] 1.36
(Ramella 2021) -6.16 [-23.03, 10.70] 0.53
(Ren et al. 2017) -0.73 [-22.39, 20.92] 0.37
(Tu et al. 2021) -20.62 [-31.59, -9.64] 0.86
(Ren et al. 2020) -6.67 [-24.59, 11.25] 0.49
(Joshi et al. 2020) 13.95 [-18.45, 46.35] 0.19
(Kim 2019) -0.25 [-19.31, 18.81] 0.45
(Xu, He and Lv 2019) 3.78 [-6.74, 14.30] 0.89
(Zou et al. 2015). -21.16 [-38.63, -3.68] 0.51
(Zhou and Liu 2015) -1.78 [-6.42, 2.86] 1.37
(Xu et al. 2013) -6.58 [-23.18, 10.03] 0.54
(Yanulevskaya, Uijlings and Geusebroek 2013) -11.00 [-18.78, -3.23] 1.11
(Jung and Kim 2012) -5.51 [-22.19, 11.17] 0.54
(Kumar and Meenpal 2022) 2.93 [-21.12, 26.98] 0.32
(Li et al. 2021b) 1.49 [-14.63, 17.61] 0.56
(Zhang et al. 2021) -12.73 [-30.05, 4.58] 0.51
(Joseph and Olugbara 2021) -0.20 [-5.88, 5.48] 1.29
(Yu et al. 2021) -0.41 [-18.37, 17.55] 0.49
(Moradi, Bayat and Charmi 2021) -15.67 [-36.58, 5.23] 0.39
(Zhang and Wang 2021) -6.30 [-43.05, 30.45] 0.15
(Jian et al. 2021) 10.98 [-21.65, 43.61] 0.19
(Zhao et al. 2021) -3.04 [-16.30, 10.23] 0.71
(Niu et al. 2021) -11.69 [-18.48, -4.91] 1.19
(Yuan, Han and Yan 2021) -13.55 [-46.14, 19.05] 0.19
(He et al. 2021) -3.19 [-7.87, 1.49] 1.37
(Tang et al. 2020) -9.04 [-25.93, 7.85] 0.53
(Jing et al. 2020) 4.46 [-22.95, 31.87] 0.25
(Li et al. 2020b) 12.95 [1.70, 24.19] 0.84
(Song et al. 2020a) -20.63 [-48.29, 7.04] 0.25
(Ma et al. 2020) -35.51 [-56.00, -15.02] 0.40
(Singh and Kumar 2020) -13.77 [-33.60, 6.05] 0.42
(Hu et al. 2020) 0.20 [-13.10, 13.49] 0.71
(Du et al. 2020) -2.72 [-26.04, 20.60] 0.33
(Singh, Mishra and Bhatia 2020) -5.75 [-22.20, 10.71] 0.55
(Deeba, Bui and Wahid 2020) -36.58 [-87.11, 13.94] 0.08
(Huang et al. 2020) -8.15 [-21.52, 5.21] 0.70
(Jiang et al. 2020) -21.45 [-35.27, -7.63] 0.68
(Piao et al. 2020) -3.47 [-7.81, 0.87] 1.39
(Qiu et al. 2020) -15.09 [-26.89, -3.28] 0.80
(Tu et al. 2020) -11.91 [-26.19, 2.37] 0.65
(Zhang et al. 2020) -4.83 [-27.51, 17.85] 0.35
(Jia et al. 2019) -12.20 [-38.34, 13.94] 0.28
(Lopez-Alanis et al. 2019) 12.15 [-16.88, 41.17] 0.23
(Huang, Xing and Wang 2019) -7.53 [-21.40, 6.35] 0.68
(Jing et al. 2018) 0.99 [-21.13, 23.11] 0.36
(Zhou et al. 2019) -2.37 [-7.63, 2.89] 1.32
(Manno-Kovacs 2018) -7.44 [-12.40, -2.48] 1.34
(Zhang et al. 2019b) -13.85 [-49.60, 21.90] 0.16
(Liu and Yang 2019) -12.68 [-50.02, 24.66] 0.15
(Zhao et al. 2019) -5.97 [-19.35, 7.41] 0.70
(Abkenar, Sadreazami and Ahmad 2018) -12.78 [-26.75, 1.20] 0.67

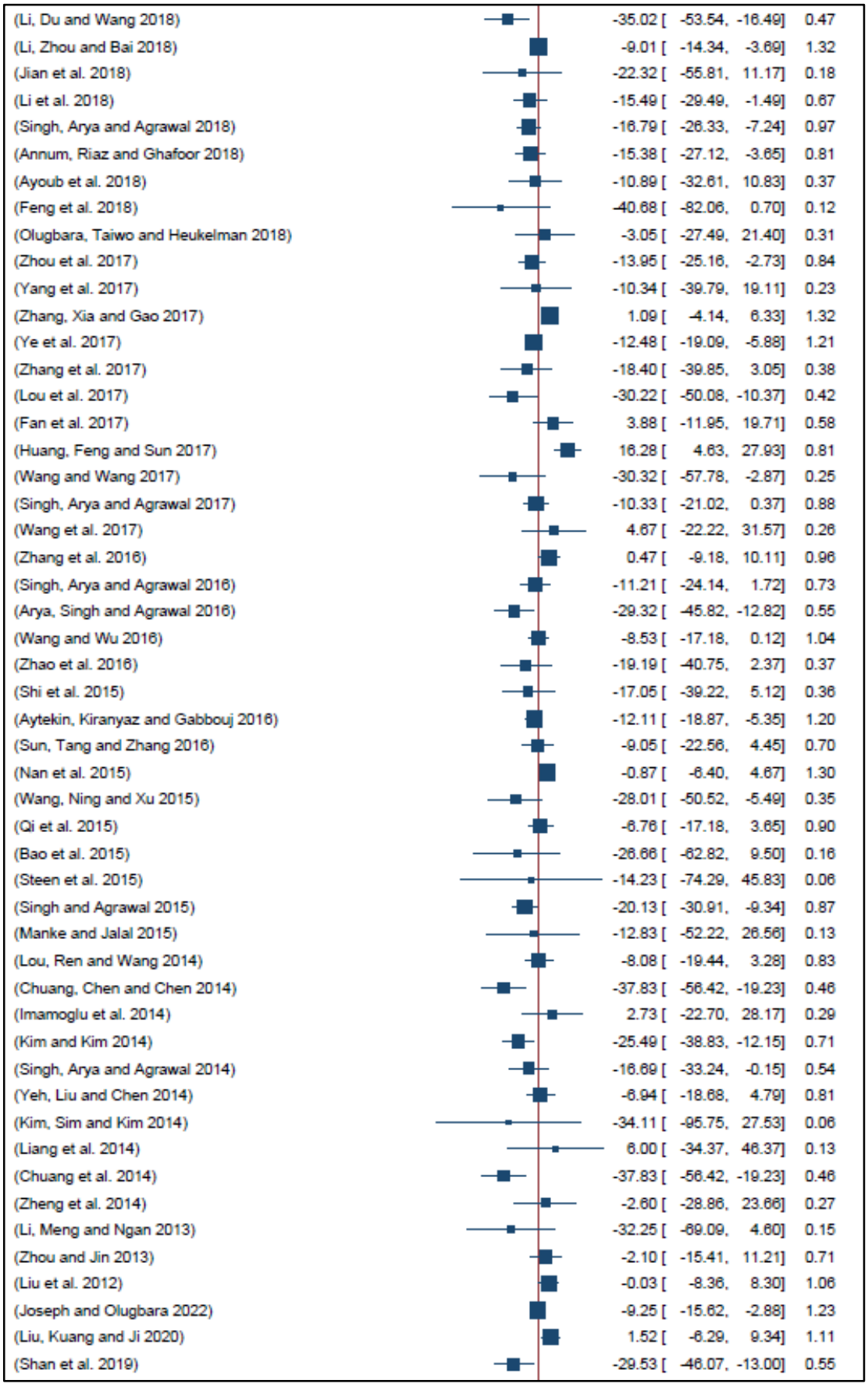
(Li, Du and Wang 2018) -35.02 [-53.54, -16.49] 0.47
(Li, Zhou and Bai 2018) -9.01 [-14.34, -3.69] 1.32
(Jian et al. 2018) -22.32 [-55.81, 11.17] 0.18
(Li et al. 2018) -15.49 [-29.49, -1.49] 0.67
(Singh, Arya and Agrawal 2018) -16.79 [-26.33, -7.24] 0.97
(Annum, Riaz and Ghafoor 2018) -15.38 [-27.12, -3.65] 0.81
(Ayoub et al. 2018) -10.89 [-32.61, 10.83] 0.37
(Feng et al. 2018) -40.68 [-82.06, 0.70] 0.12
(Olugbara, Taiwo and Heukelman 2018) -3.05 [-27.49, 21.40] 0.31
(Zhou et al. 2017) -13.95 [-25.16, -2.73] 0.84
(Yang et al. 2017) -10.34 [-39.79, 19.11] 0.23
(Zhang, Xia and Gao 2017) 1.09 [-4.14, 6.33] 1.32
(Ye et al. 2017) -12.48 [-19.09, -5.88] 1.21
(Zhang et al. 2017) -18.40 [-39.85, 3.05] 0.38
(Lou et al. 2017) -30.22 [-50.08, -10.37] 0.42
(Fan et al. 2017) 3.88 [-11.95, 19.71] 0.58
(Huang, Feng and Sun 2017) 16.28 [4.63, 27.93] 0.81
(Wang and Wang 2017) -30.32 [-57.78, -2.87] 0.25
(Singh, Arya and Agrawal 2017) -10.33 [-21.02, 0.37] 0.88
(Wang et al. 2017) 4.67 [-22.22, 31.57] 0.26
(Zhang et al. 2016) 0.47 [-9.18, 10.11] 0.96
(Singh, Arya and Agrawal 2016) -11.21 [-24.14, 1.72] 0.73
(Arya, Singh and Agrawal 2016) -29.32 [-45.82, -12.82] 0.55
(Wang and Wu 2016) -8.53 [-17.18, 0.12] 1.04
(Zhao et al. 2016) -19.19 [-40.75, 2.37] 0.37
(Shi et al. 2015) -17.05 [-39.22, 5.12] 0.36
(Aytekin, Kiranyaz and Gabbouj 2016) -12.11 [-18.87, -5.35] 1.20
(Sun, Tang and Zhang 2016) -9.05 [-22.56, 4.45] 0.70
(Nan et al. 2015) -0.87 [-6.40, 4.67] 1.30
(Wang, Ning and Xu 2015) -28.01 [-50.52, -5.49] 0.35
(Qi et al. 2015) -6.76 [-17.18, 3.65] 0.90
(Bao et al. 2015) -26.66 [-62.82, 9.50] 0.16
(Steen et al. 2015) -14.23 [-74.29, 45.83] 0.06
(Singh and Agrawal 2015) -20.13 [-30.91, -9.34] 0.87
(Manke and Jalal 2015) -12.83 [-52.22, 26.56] 0.13
(Lou, Ren and Wang 2014) -8.08 [-19.44, 3.28] 0.83
(Chuang, Chen and Chen 2014) -37.83 [-56.42, -19.23] 0.46
(Imamoglu et al. 2014) 2.73 [-22.70, 28.17] 0.29
(Kim and Kim 2014) -25.49 [-38.83, -12.15] 0.71
(Singh, Arya and Agrawal 2014) -16.69 [-33.24, -0.15] 0.54
(Yeh, Liu and Chen 2014) -6.94 [-18.68, 4.79] 0.81
(Kim, Sim and Kim 2014) -34.11 [-95.75, 27.53] 0.06
(Liang et al. 2014) 6.00 [-34.37, 46.37] 0.13
(Chuang et al. 2014) -37.83 [-56.42, -19.23] 0.46
(Zheng et al. 2014) -2.60 [-28.86, 23.66] 0.27
(Li, Meng and Ngan 2013) -32.25 [-69.09, 4.60] 0.15
(Zhou and Jin 2013) -2.10 [-15.41, 11.21] 0.71
(Liu et al. 2012) -0.03 [-8.36, 8.30] 1.06
(Joseph and Olugbara 2022) -9.25 [-15.62, -2.88] 1.23
(Liu, Kuang and Ji 2020) 1.52 [-6.29, 9.34] 1.11
(Shan et al. 2019) -29.53 [-46.07, -13.00] 0.55

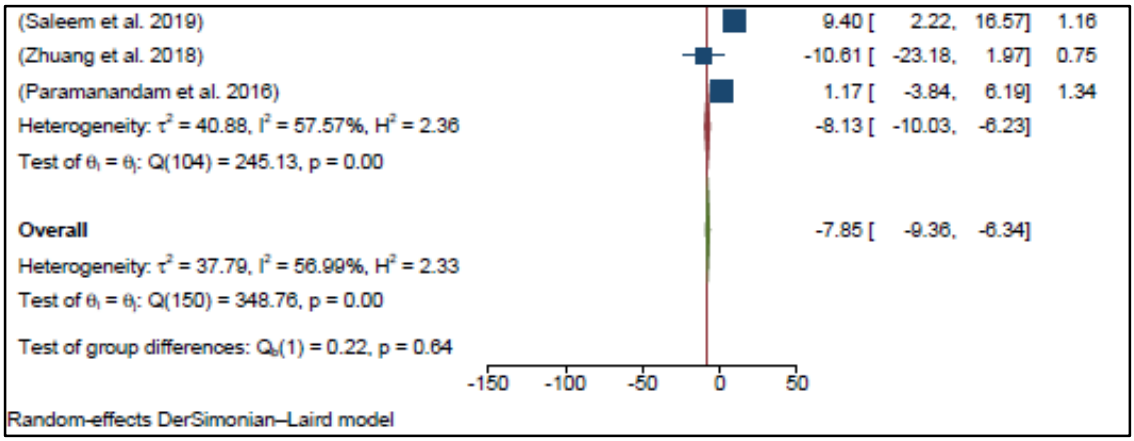

Figure 2-4 Forest plot derived from subgroup analysis-based segmentation approach

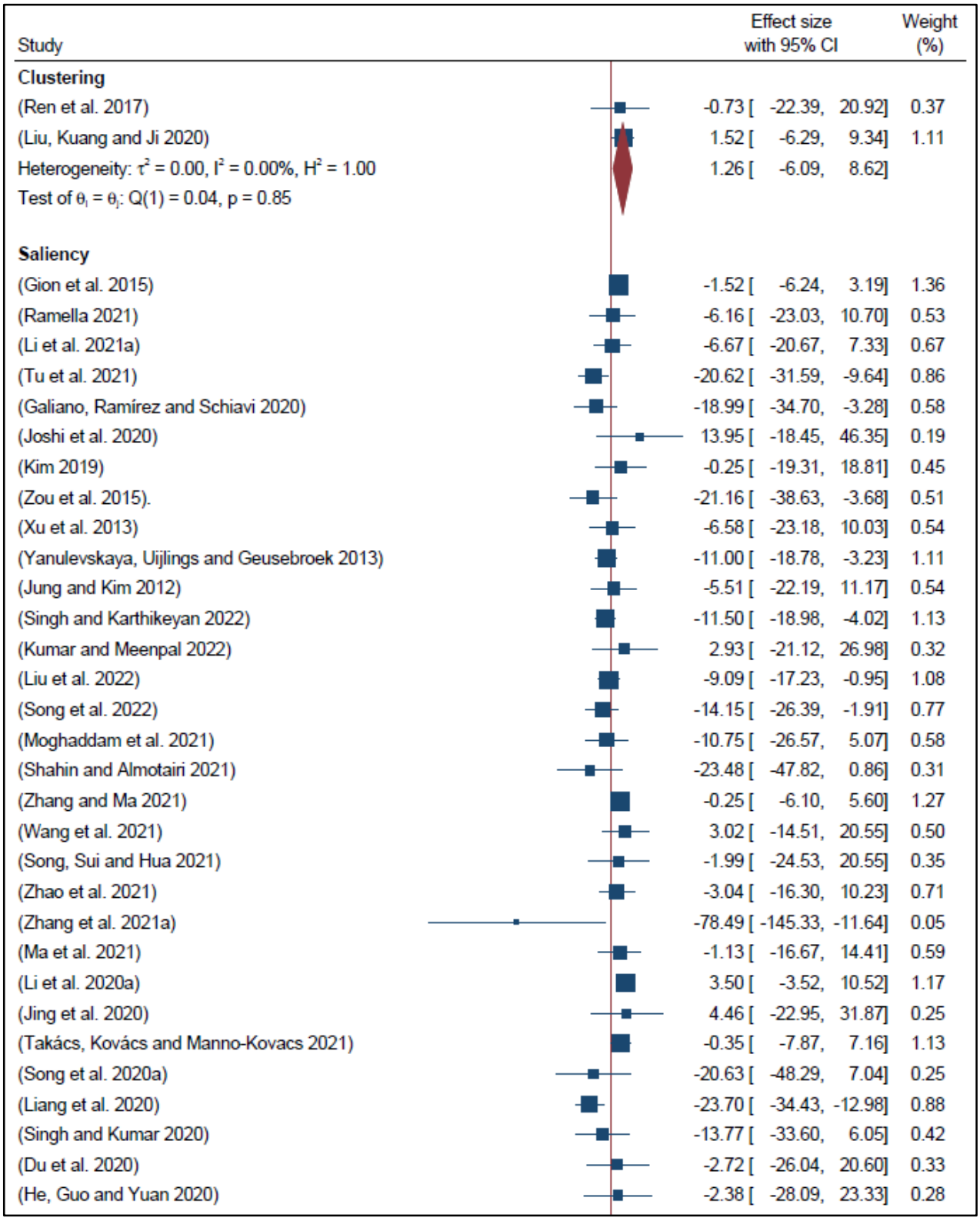
Study
Effect size with 95% CI
Weight (%)
Clustering
(Ren et al. 2017) -0.73 [-22.39, 20.92] 0.37
(Liu, Kuang and Ji 2020) 1.52 [-6.29, 9.34] 1.11
Heterogeneity: τ^2 = 0.00, I^2 = 0.00%, H^2 = 1.00 1.26 [-6.09, 8.62]
Test of $\theta_i = \theta_j$: Q(1) = 0.04, p = 0.85
Saliency
(Gion et al. 2015) -1.52 [-6.24, 3.19] 1.36
(Ramella 2021) -6.16 [-23.03, 10.70] 0.53
(Li et al. 2021a) -6.67 [-20.67, 7.33] 0.67
(Tu et al. 2021) -20.62 [-31.59, -9.64] 0.86
(Galiano, Ramírez and Schiavi 2020) -18.99 [-34.70, -3.28] 0.58
(Joshi et al. 2020) 13.95 [-18.45, 46.35] 0.19
(Kim 2019) -0.25 [-19.31, 18.81] 0.45
(Zou et al. 2015). -21.16 [-38.63, -3.68] 0.51
(Xu et al. 2013) -6.58 [-23.18, 10.03] 0.54
(Yanulevskaya, Uijlings and Geusebroek 2013) -11.00 [-18.78, -3.23] 1.11
(Jung and Kim 2012) -5.51 [-22.19, 11.17] 0.54
(Singh and Karthikeyan 2022) -11.50 [-18.98, -4.02] 1.13
(Kumar and Meenpal 2022) 2.93 [-21.12, 26.98] 0.32
(Liu et al. 2022) -9.09 [-17.23, -0.95] 1.08
(Song et al. 2022) -14.15 [-26.39, -1.91] 0.77
(Moghaddam et al. 2021) -10.75 [-26.57, 5.07] 0.58
(Shahin and Almotairi 2021) -23.48 [-47.82, 0.86] 0.31
(Zhang and Ma 2021) -0.25 [-6.10, 5.60] 1.27
(Wang et al. 2021) 3.02 [-14.51, 20.55] 0.50
(Song, Sui and Hua 2021) -1.99 [-24.53, 20.55] 0.35
(Zhao et al. 2021) -3.04 [-16.30, 10.23] 0.71
(Zhang et al. 2021a) -78.49 [-145.33, -11.64] 0.05
(Ma et al. 2021) -1.13 [-16.67, 14.41] 0.59
(Li et al. 2020a) 3.50 [-3.52, 10.52] 1.17
(Jing et al. 2020) 4.46 [-22.95, 31.87] 0.25
(Takács, Kovács and Manno-Kovacs 2021) -0.35 [-7.87, 7.16] 1.13
(Song et al. 2020a) -20.63 [-48.29, 7.04] 0.25
(Liang et al. 2020) -23.70 [-34.43, -12.98] 0.88
(Singh and Kumar 2020) -13.77 [-33.60, 6.05] 0.42
(Du et al. 2020) -2.72 [-26.04, 20.60] 0.33
(He, Guo and Yuan 2020) -2.38 [-28.09, 23.33] 0.28

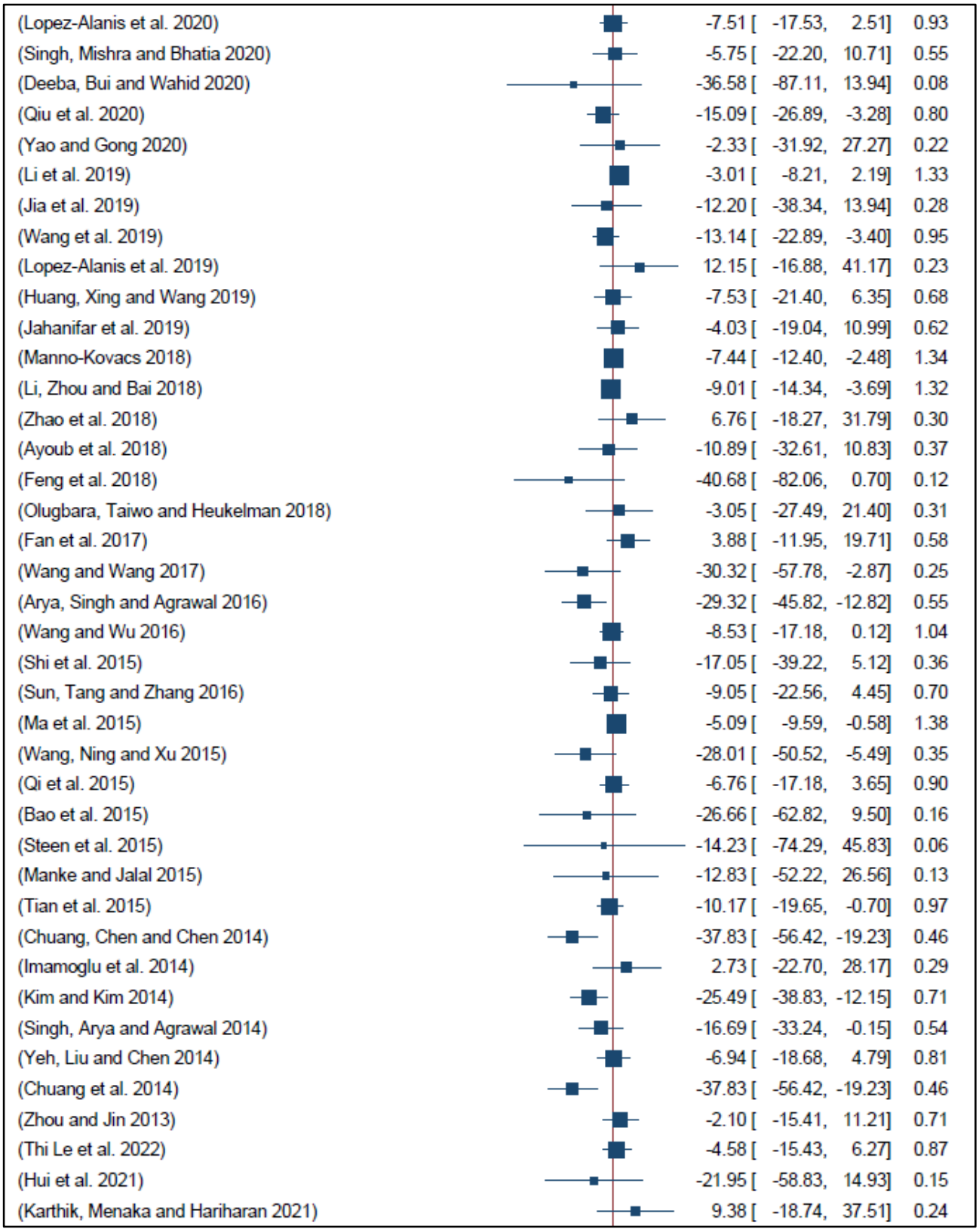
(Lopez-Alanis et al. 2020) -7.51 [-17.53, 2.51] 0.93
(Singh, Mishra and Bhatia 2020) -5.75 [-22.20, 10.71] 0.55
(Deeba, Bui and Wahid 2020) -36.58 [-87.11, 13.94] 0.08
(Qiu et al. 2020) -15.09 [-26.89, -3.28] 0.80
(Yao and Gong 2020) -2.33 [-31.92, 27.27] 0.22
(Li et al. 2019) -3.01 [-8.21, 2.19] 1.33
(Jia et al. 2019) -12.20 [-38.34, 13.94] 0.28
(Wang et al. 2019) -13.14 [-22.89, -3.40] 0.95
(Lopez-Alanis et al. 2019) 12.15 [-16.88, 41.17] 0.23
(Huang, Xing and Wang 2019) -7.53 [-21.40, 6.35] 0.68
(Jahanifar et al. 2019) -4.03 [-19.04, 10.99] 0.62
(Manno-Kovacs 2018) -7.44 [-12.40, -2.48] 1.34
(Li, Zhou and Bai 2018) -9.01 [-14.34, -3.69] 1.32
(Zhao et al. 2018) 6.76 [-18.27, 31.79] 0.30
(Ayoub et al. 2018) -10.89 [-32.61, 10.83] 0.37
(Feng et al. 2018) -40.68 [-82.06, 0.70] 0.12
(Olugbara, Taiwo and Heukelman 2018) -3.05 [-27.49, 21.40] 0.31
(Fan et al. 2017) 3.88 [-11.95, 19.71] 0.58
(Wang and Wang 2017) -30.32 [-57.78, -2.87] 0.25
(Arya, Singh and Agrawal 2016) -29.32 [-45.82, -12.82] 0.55
(Wang and Wu 2016) -8.53 [-17.18, 0.12] 1.04
(Shi et al. 2015) -17.05 [-39.22, 5.12] 0.36
(Sun, Tang and Zhang 2016) -9.05 [-22.56, 4.45] 0.70
(Ma et al. 2015) -5.09 [-9.59, -0.58] 1.38
(Wang, Ning and Xu 2015) -28.01 [-50.52, -5.49] 0.35
(Qi et al. 2015) -6.76 [-17.18, 3.65] 0.90
(Bao et al. 2015) -26.66 [-62.82, 9.50] 0.16
(Steen et al. 2015) -14.23 [-74.29, 45.83] 0.06
(Manke and Jalal 2015) -12.83 [-52.22, 26.56] 0.13
(Tian et al. 2015) -10.17 [-19.65, -0.70] 0.97
(Chuang, Chen and Chen 2014) -37.83 [-56.42, -19.23] 0.46
(Imamoglu et al. 2014) 2.73 [-22.70, 28.17] 0.29
(Kim and Kim 2014) -25.49 [-38.83, -12.15] 0.71
(Singh, Arya and Agrawal 2014) -16.69 [-33.24, -0.15] 0.54
(Yeh, Liu and Chen 2014) -6.94 [-18.68, 4.79] 0.81
(Chuang et al. 2014) -37.83 [-56.42, -19.23] 0.46
(Zhou and Jin 2013) -2.10 [-15.41, 11.21] 0.71
(Thi Le et al. 2022) -4.58 [-15.43, 6.27] 0.87
(Hui et al. 2021) -21.95 [-58.83, 14.93] 0.15
(Karthik, Menaka and Hariharan 2021) 9.38 [-18.74, 37.51] 0.24

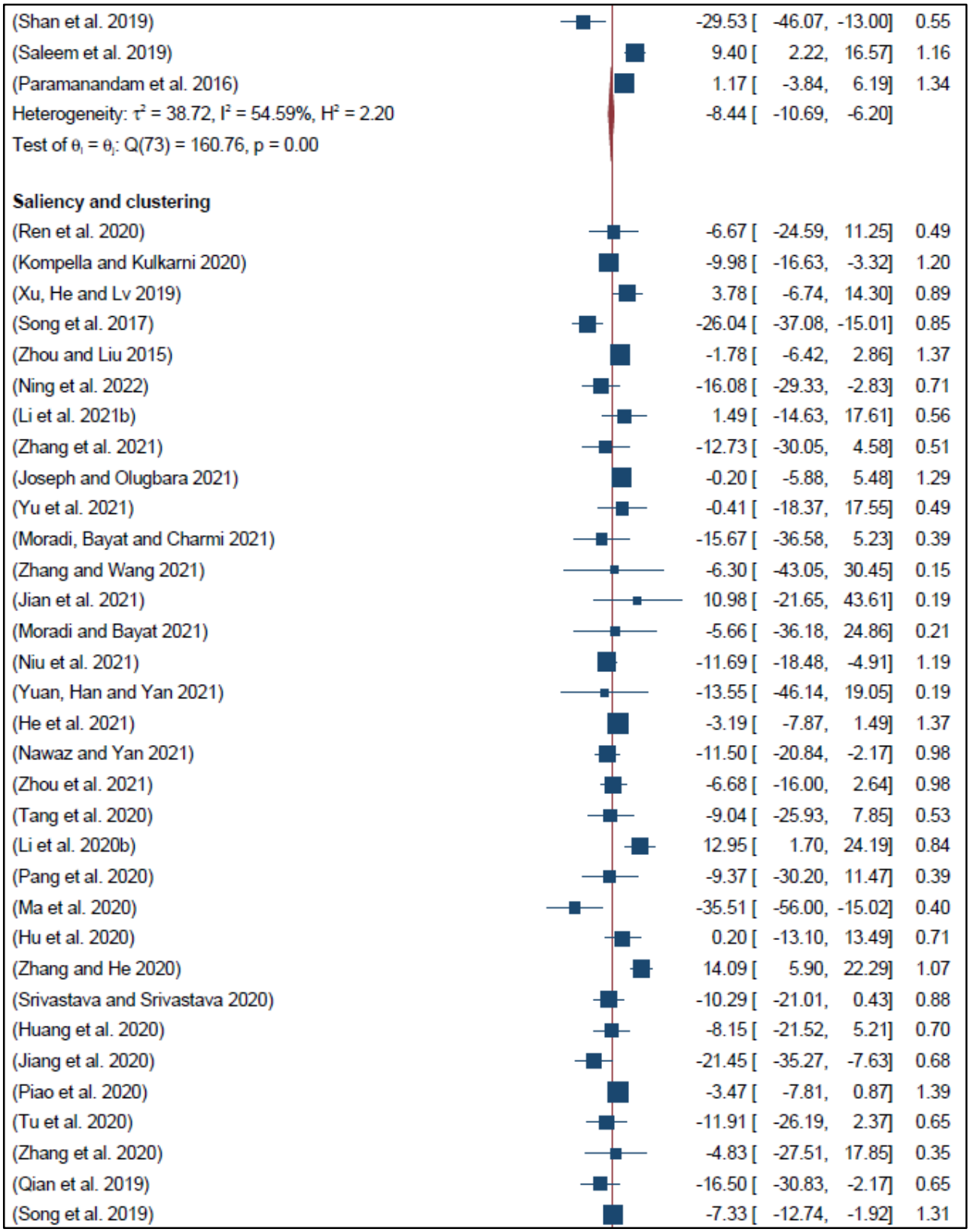
(Shan et al. 2019) -29.53 [-46.07, -13.00] 0.55
(Saleem et al. 2019) 9.40 [2.22, 16.57] 1.16
(Paramanandam et al. 2016) 1.17 [-3.84, 6.19] 1.34
Heterogeneity: τ^2 = 38.72, I^2 = 54.59%, H^2 = 2.20 -8.44 [-10.69, -6.20]
Test of $\theta_i = \theta_j$: Q(73) = 160.76, p = 0.00
Saliency and clustering
(Ren et al. 2020) -6.67 [-24.59, 11.25] 0.49
(Kompella and Kulkarni 2020) -9.98 [-16.63, -3.32] 1.20
(Xu, He and Lv 2019) 3.78 [-6.74, 14.30] 0.89
(Song et al. 2017) -26.04 [-37.08, -15.01] 0.85
(Zhou and Liu 2015) -1.78 [-6.42, 2.86] 1.37
(Ning et al. 2022) -16.08 [-29.33, -2.83] 0.71
(Li et al. 2021b) 1.49 [-14.63, 17.61] 0.56
(Zhang et al. 2021) -12.73 [-30.05, 4.58] 0.51
(Joseph and Olugbara 2021) -0.20 [-5.88, 5.48] 1.29
(Yu et al. 2021) -0.41 [-18.37, 17.55] 0.49
(Moradi, Bayat and Charmi 2021) -15.67 [-36.58, 5.23] 0.39
(Zhang and Wang 2021) -6.30 [-43.05, 30.45] 0.15
(Jian et al. 2021) 10.98 [-21.65, 43.61] 0.19
(Moradi and Bayat 2021) -5.66 [-36.18, 24.86] 0.21
(Niu et al. 2021) -11.69 [-18.48, -4.91] 1.19
(Yuan, Han and Yan 2021) -13.55 [-46.14, 19.05] 0.19
(He et al. 2021) -3.19 [-7.87, 1.49] 1.37
(Nawaz and Yan 2021) -11.50 [-20.84, -2.17] 0.98
(Zhou et al. 2021) -6.68 [-16.00, 2.64] 0.98
(Tang et al. 2020) -9.04 [-25.93, 7.85] 0.53
(Li et al. 2020b) 12.95 [1.70, 24.19] 0.84
(Pang et al. 2020) -9.37 [-30.20, 11.47] 0.39
(Ma et al. 2020) -35.51 [-56.00, -15.02] 0.40
(Hu et al. 2020) 0.20 [-13.10, 13.49] 0.71
(Zhang and He 2020) 14.09 [5.90, 22.29] 1.07
(Srivastava and Srivastava 2020) -10.29 [-21.01, 0.43] 0.88
(Huang et al. 2020) -8.15 [-21.52, 5.21] 0.70
(Jiang et al. 2020) -21.45 [-35.27, -7.63] 0.68
(Piao et al. 2020) -3.47 [-7.81, 0.87] 1.39
(Tu et al. 2020) -11.91 [-26.19, 2.37] 0.65
(Zhang et al. 2020) -4.83 [-27.51, 17.85] 0.35
(Qian et al. 2019) -16.50 [-30.83, -2.17] 0.65
(Song et al. 2019) -7.33 [-12.74, -1.92] 1.31

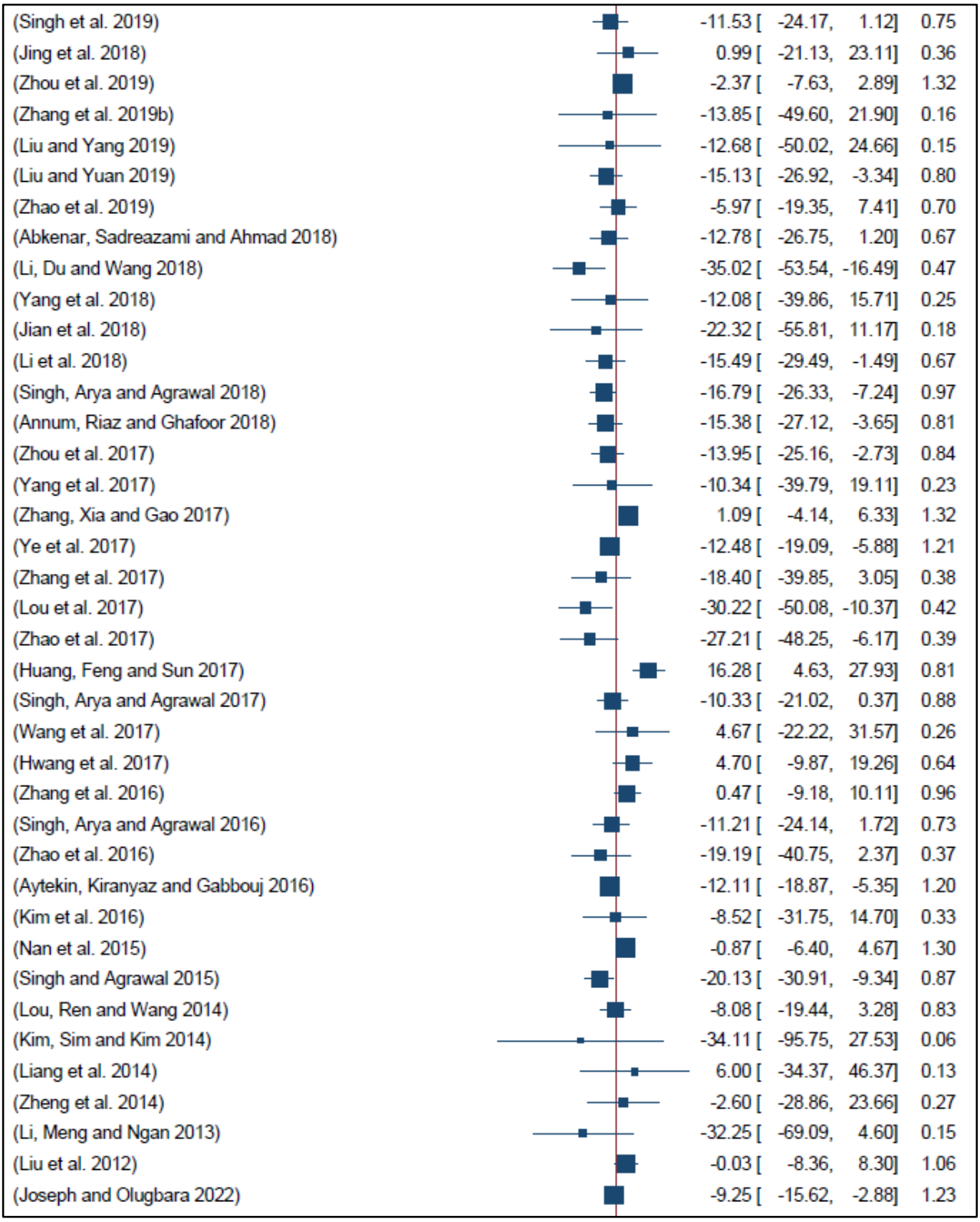
(Singh et al. 2019) -11.53 [-24.17, 1.12] 0.75
(Jing et al. 2018) 0.99 [-21.13, 23.11] 0.36
(Zhou et al. 2019) -2.37 [-7.63, 2.89] 1.32
(Zhang et al. 2019b) -13.85 [-49.60, 21.90] 0.16
(Liu and Yang 2019) -12.68 [-50.02, 24.66] 0.15
(Liu and Yuan 2019) -15.13 [-26.92, -3.34] 0.80
(Zhao et al. 2019) -5.97 [-19.35, 7.41] 0.70
(Abkenar, Sadreazami and Ahmad 2018) -12.78 [-26.75, 1.20] 0.67
(Li, Du and Wang 2018) -35.02 [-53.54, -16.49] 0.47
(Yang et al. 2018) -12.08 [-39.86, 15.71] 0.25
(Jian et al. 2018) -22.32 [-55.81, 11.17] 0.18
(Li et al. 2018) -15.49 [-29.49, -1.49] 0.67
(Singh, Arya and Agrawal 2018) -16.79 [-26.33, -7.24] 0.97
(Annum, Riaz and Ghafoor 2018) -15.38 [-27.12, -3.65] 0.81
(Zhou et al. 2017) -13.95 [-25.16, -2.73] 0.84
(Yang et al. 2017) -10.34 [-39.79, 19.11] 0.23
(Zhang, Xia and Gao 2017) 1.09 [-4.14, 6.33] 1.32
(Ye et al. 2017) -12.48 [-19.09, -5.88] 1.21
(Zhang et al. 2017) -18.40 [-39.85, 3.05] 0.38
(Lou et al. 2017) -30.22 [-50.08, -10.37] 0.42
(Zhao et al. 2017) -27.21 [-48.25, -6.17] 0.39
(Huang, Feng and Sun 2017) 16.28 [4.63, 27.93] 0.81
(Singh, Arya and Agrawal 2017) -10.33 [-21.02, 0.37] 0.88
(Wang et al. 2017) 4.67 [-22.22, 31.57] 0.26
(Hwang et al. 2017) 4.70 [-9.87, 19.26] 0.64
(Zhang et al. 2016) 0.47 [-9.18, 10.11] 0.96
(Singh, Arya and Agrawal 2016) -11.21 [-24.14, 1.72] 0.73
(Zhao et al. 2016) -19.19 [-40.75, 2.37] 0.37
(Aytekin, Kiranyaz and Gabbouj 2016) -12.11 [-18.87, -5.35] 1.20
(Kim et al. 2016) -8.52 [-31.75, 14.70] 0.33
(Nan et al. 2015) -0.87 [-6.40, 4.67] 1.30
(Singh and Agrawal 2015) -20.13 [-30.91, -9.34] 0.87
(Lou, Ren and Wang 2014) -8.08 [-19.44, 3.28] 0.83
(Kim, Sim and Kim 2014) -34.11 [-95.75, 27.53] 0.06
(Liang et al. 2014) 6.00 [-34.37, 46.37] 0.13
(Zheng et al. 2014) -2.60 [-28.86, 23.66] 0.27
(Li, Meng and Ngan 2013) -32.25 [-69.09, 4.60] 0.15
(Liu et al. 2012) -0.03 [-8.36, 8.30] 1.06
(Joseph and Olugbara 2022) -9.25 [-15.62, -2.88] 1.23

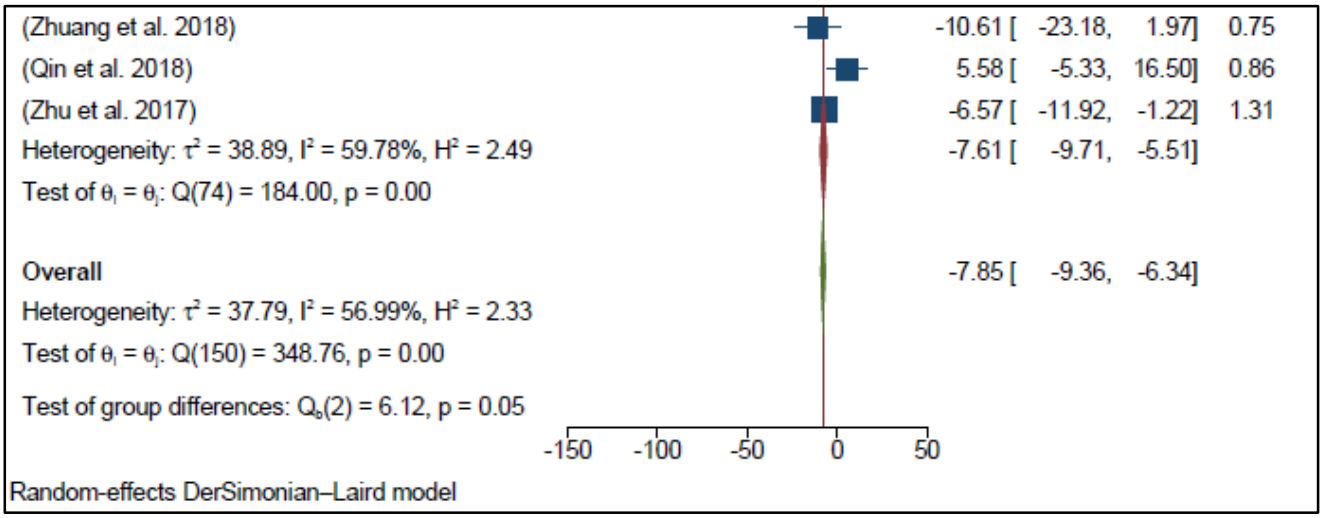

Figure 2-5 Forest plot derived from subgroup analysis-based segmentation method

2.6.3 Meta-regression

The subgroup analysis presents evidence of heterogeneity. The variables such as the year of study publication, pre-preprocessing, number of datasets, and number of images were observed as moderators in the meta-regression model to examine the parameters that caused the heterogeneity. The significant overall heterogeneity can be based on various sources such as the number of datasets and images used for evaluation, preprocessing, and year of study publication. The meta-regression results summarized in Tables 2-6 represent the sources of heterogeneity. The moderator, number of images was statistically significant at $p<0.05$ and it revealed that the estimated effect size has been impacted by the number of images used for segmentation performance evaluation.

Table 2-6 Meta-regression model to assess the source of heterogeneity

Sources of heterogeneity	Estimates	Std. Error	95% CI	p-value
Year	0.384	0.305	[0.031 0.219]	0.211
Preprocessing	1.792	1.818	[-0.435 0.681]	0.326
Number of Datasets	0.263	0.619	[-0.396 0.008]	0.671
Number of images	-0.000	0.000	[-0.000 0.000]	0.025*
Constant	-782.037	616.068	[-448.341 -70.145]	0.206

*p<0.05

Following the meta-regression with the continuous moderators of publication year and image number, a bubble plot (Figures 2-6 and 2-7) is used to show the relationship between the effect size and the relevant moderator. The graph is a scatter plot, commonly denoted by bubbles, where each bubble denotes study and is positioned in accordance with the moderator under analysis (x-axis) and its

parameter estimate (y-axis). The size of bubbles varies depending on the weight given to the parameter estimation. The meta regression analysis (coefficient 0.384, 95% CI: 0.031 0.219 and p=0.211) showed an insignificant correlation between the publication year and the segmentation performance. The bubble plot in Figure 2-6 illustrates this insignificant positive relationship between the performance of segmentation methods and publication year.

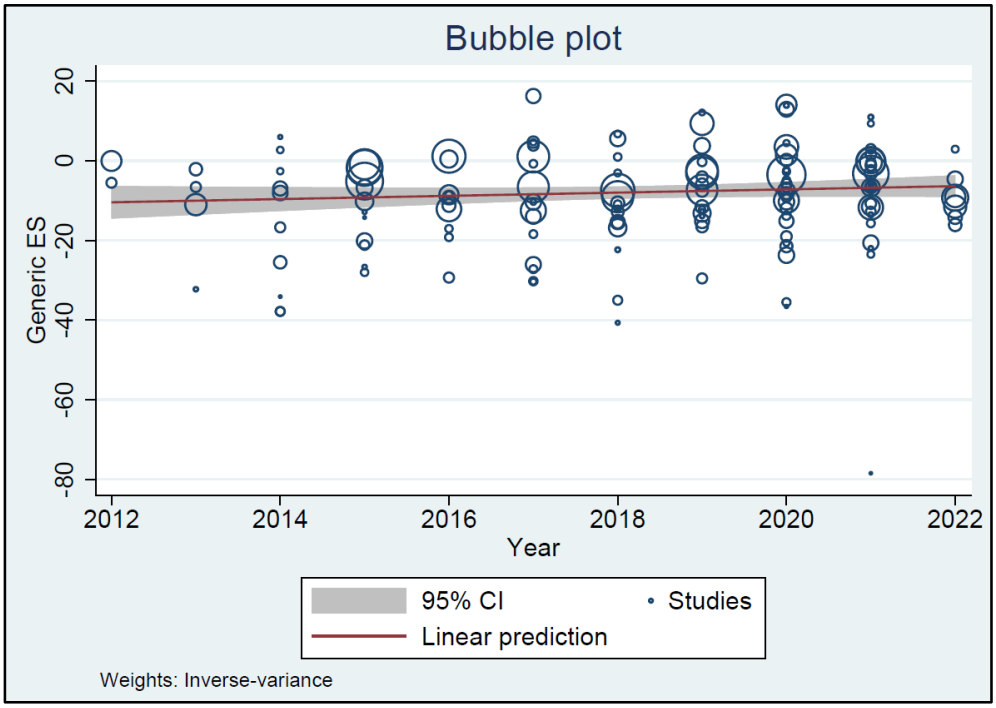

Figure 2-6 Meta-regression based on year of publication

The results of the meta-regression analysis showed a significant relationship (coefficient -0.00003, 95% CI: -.0005753 -.0001084, and P =0.025) between the number of images and the performance of image segmentation. These data reveal a strong pattern of declining segmentation performance with more images, as shown by the regression line in Figure 2-7. Additionally, the regression line provides a good fit to the data because the majority of studies are relatively close to it.

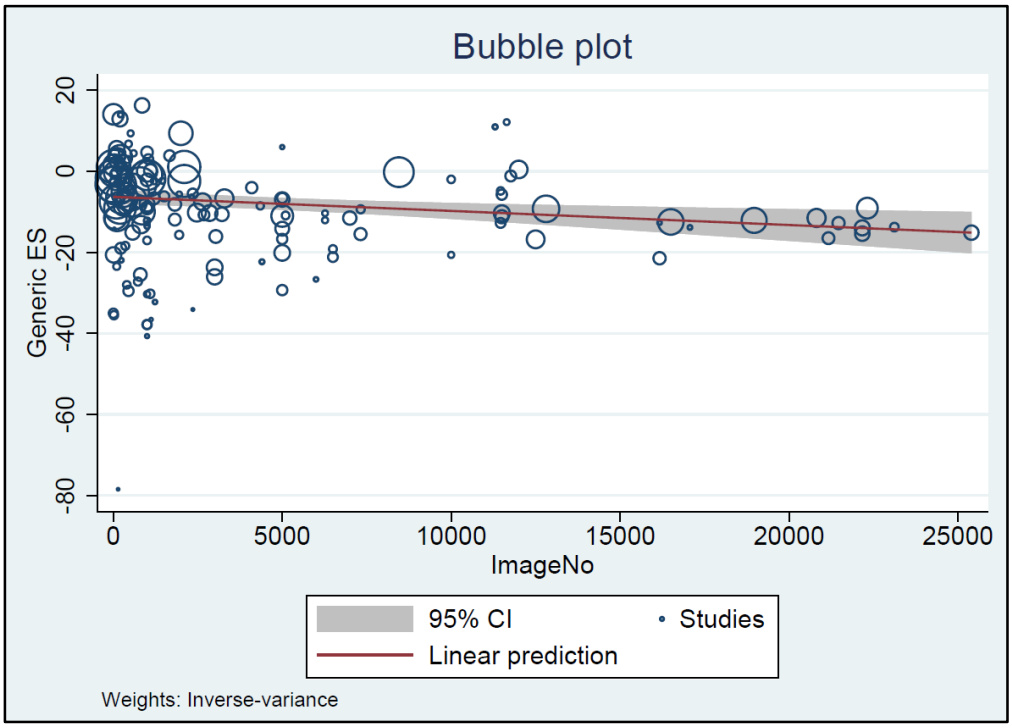

Figure 2-7 Meta-regression based on number of images

2.6.4 Publication bias

The asymmetrical distribution of the studies depicted in the funnel plot (Figure 2-8) is a sign of publication bias (Crocetti 2016). Pooled effect size and the 95% confidence interval is represented by the vertical and diagonal lines respectively. The presence of a smaller portion of studies outside the triangular region indicates evidence of publication bias.

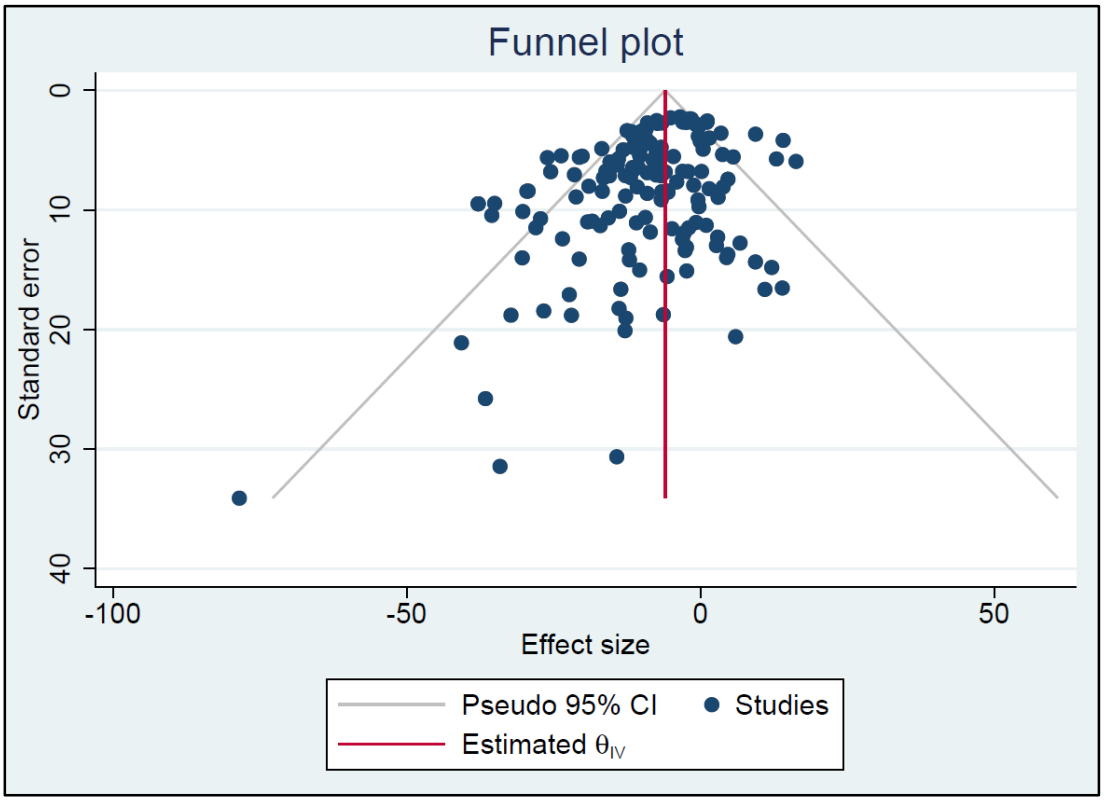

Figure 2-8 Funnel Plot with Pseudo 95% confidence limits indicating publication bias

Egger statistical test was performed to report the publication bias among the studies that were taken into account to overcome the subjectivity caused by the visual interpretation of the funnel plot. The Egger test aims to ascertain whether the intercept of the association between the estimate of effect size and the standard error is noticeably different from zero at $p<0.001$. The results reported in Table 2-7 affirm an insignificant publication bias with a p-value of 0.038 confirming the impact of the inclusion and exclusion criteria in abolishing bias.

Table 2-7 Egger test for examining publication bias

Parameter	Estimate	Std. err	t	p	95% conf. interval	
Slope	-0.780	0.203	-3.85	0.002	-1.181	-0.379
Bias	-2.987	1.427	-2.09	0.038	-5.807	-0.168

2.7 Discussion of findings

The meta-analysis conducted is based on 151 studies that met the inclusion and exclusion criteria, selected from several studies published from 2012 to 2022. This is an attempt to perform a meta-analysis on image segmentation methods with a special focus on clustering and saliency. The meta-analysis using the random effect model has shown that there is statistical heterogeneity in the

effect sizes of the examined studies. The Galbraith plot showed that only 7% of the studies were outside the shaded area, which is evidence of weak heterogeneity. It is determined that the primary source of heterogeneity is the number of images used for performance evaluation. There was a significant difference in the number of images used by each study for validating the segmentation performance with one study using 2 images and another using 25399 images to validate the segmentation results. This shows the importance of examining the number of images used for evaluation before concluding the quality of segmentation performance (Monteiro and Campilho 2006). Two subgroup analyses conducted respectively based on the image segmentation approach and methods demonstrate the evidence of heterogeneity and the explanation of this variation is based on the sample size used by the individual authors to evaluate the developed image segmentation algorithm.

The publication bias is investigated by considering the various reasons that can attribute biases in the included studies. The findings by funnel plot show evidence of publication bias in this study, but additional statistical analysis based on the Egger test has demonstrated that the publication bias is not significant. This supports the effectiveness of the inclusion and exclusion criteria used for selecting the relevant studies for analysis. This finding also supports that the asymmetry in the funnel plot is not always due to the publication bias but rather to other factors such as the sample size (Rothstein, Sutton and Borenstein 2006).

2.7.1 Characteristics of primary studies

The general characteristics of all 151 included studies are depicted in Appendix A. Figure 2-9 illustrates the publication trends of 151 articles reviewed using PRISMA. Recent years have witnessed marked resurgence popularity of segmentation models as shown in Figure 2-9. The data revealed an increasing trend in the use of saliency and clustering for image segmentation from 2012, especially with a high increase in 2017 and 2020.

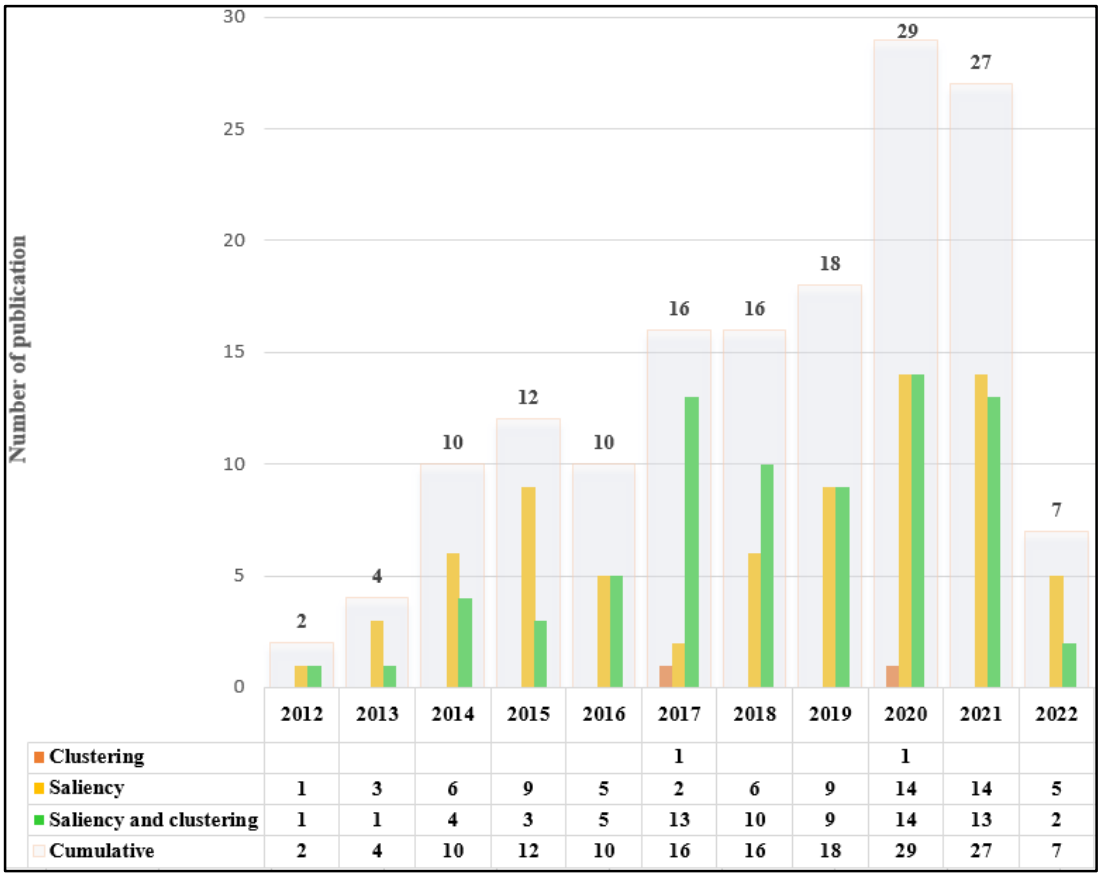

	2012	2013	2014	2015	2016	2017	2018	2019	2020	2021	2022
Clustering						1			1		
Saliency	1	3	6	9	5	2	6	9	14	14	5
Saliency and clustering	1	1	4	3	5	13	10	9	14	13	2
Cumulative	2	4	10	12	10	16	16	18	29	27	7

Figure 2-9 Number of relevant publications per segmentation method and year

Articles published in the scientific journal were the main source of information. In total, the papers reviewed here were published in 75 different journals representing the extent to which various disciplines use image segmentation methods. Only journals that published more than three studies related to image segmentation are presented in Figure 2-10. Most of these papers (68%) were obtained from 26 peer-reviewed journals as presented in Figure 2-10, while the rest are from a variety of journals. Multimedia Tools (8%) and Applications and IEEE Transactions on Image Processing (7%) were the top 2 journals with articles related to image segmentation methods.

Figure 2-10 The number of relevant publications per literature source

In Figure 2-11 it can be distinguished that the geographical coverage of the published papers is mainly from China. Countries with three or more publications are China (97), India (16), Korea (6), Hong Kong (4), Iran (3), and South Africa (3).

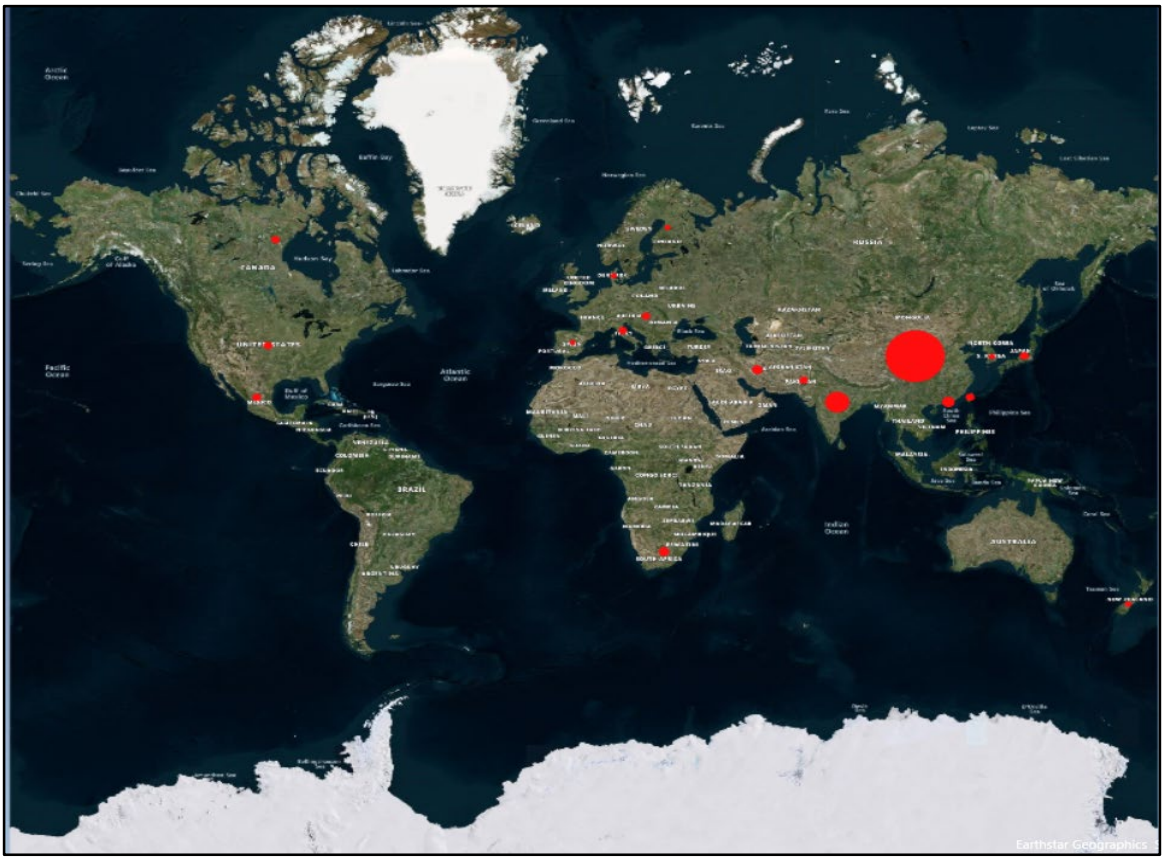

Figure 2-11 Spatial distribution of research institutions. The total number of publications from each study is represented by the bubble size.

2.7.2 Image segmentation methods

This systematic review of the included studies demonstrated the evidence of using both supervised and unsupervised methods for image segmentation. Generally, supervised segmentation methods exhibit better results compared to unsupervised methods. In a supervised approach, a large number of training data with extensive parameter tuning and high segmentation performance are directly proportional. Due to the requirement of parameter tuning, the demand for immense manual labels, and the convolution model training, supervised methods are expensive in terms of computation and memory, hence these methods are not feasible for real-time applications (Liang, Liu and Ma 2019). In contrast, unsupervised methods are not dependent on training datasets and are more applicable to extensive image classes. Of the 151 articles reviewed in this study, 105 studies (70%) adopted the unsupervised approach while 46 studies (30%) utilized the supervised approach as shown in Figure 2-12. This supported the finding of Wang *et al.* (2022a) that the wide application of the supervised methods is limited by the requirement of pixel-level for the model training. The higher percentage of unsupervised methods is principally related to the wide application of unsupervised approaches in

image segmentation because of their computational efficiency and robustness. This supports the finding by Ullah *et al.* (2020) that due to the complexity and difficulty of generating large training datasets for supervised methods, researchers are encouraged to use unsupervised methods for image segmentation.

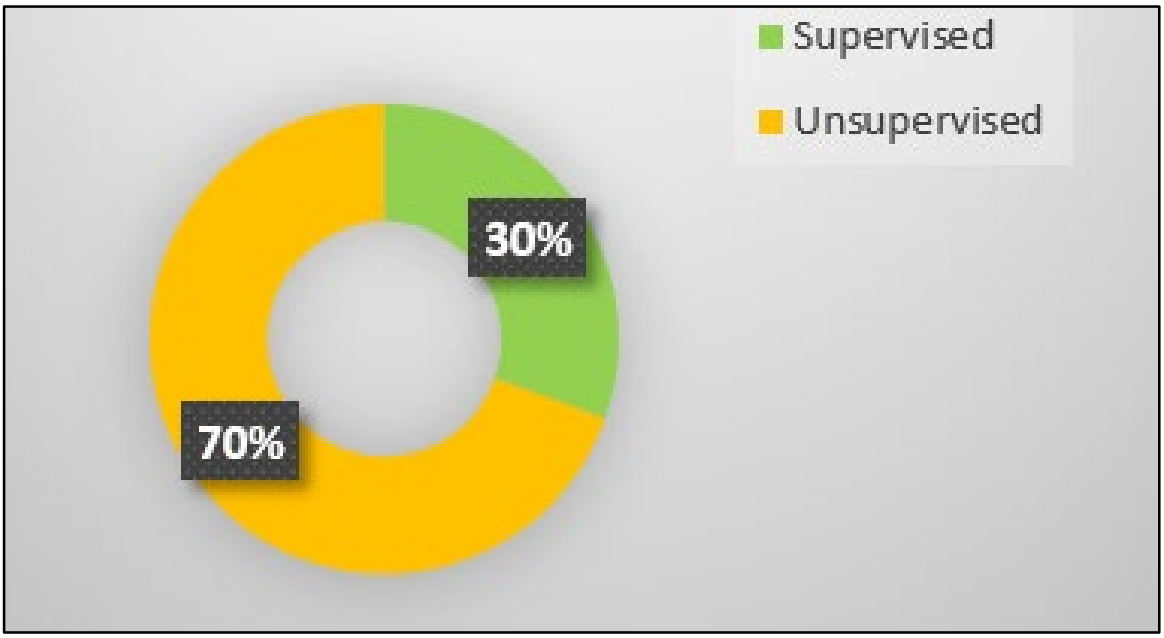

Figure 2-12 Distribution of supervised and unsupervised approaches

Segmentation methods from the included studies are categorized into clustering, saliency, and saliency and clustering. Figure 2-13 shows the distribution of papers that employed these segmentation methods. It is worth noting that saliency-based image segmentation methods are by far the most frequently used in the reviewed studies. 74 studies (49%) were based on saliency and 75 studies (50%) utilized saliency and clustering methods to retrieve the region of interest. Two studies applied on clustering method. This is surprisingly a low number, however, the ability of the saliency methods to detect the region of interest is easily attributed to the use of combining saliency and clustering in image segmentation. Especially, in unsupervised approaches, the segmentation methods based on saliency and clustering are higher (56 studies) than the saliency-based methods (47 studies) as shown in Figure 2-14. This shows the popularity of saliency and clustering in unsupervised image segmentation methods and the extended implementation of saliency in supervised segmentation methods.

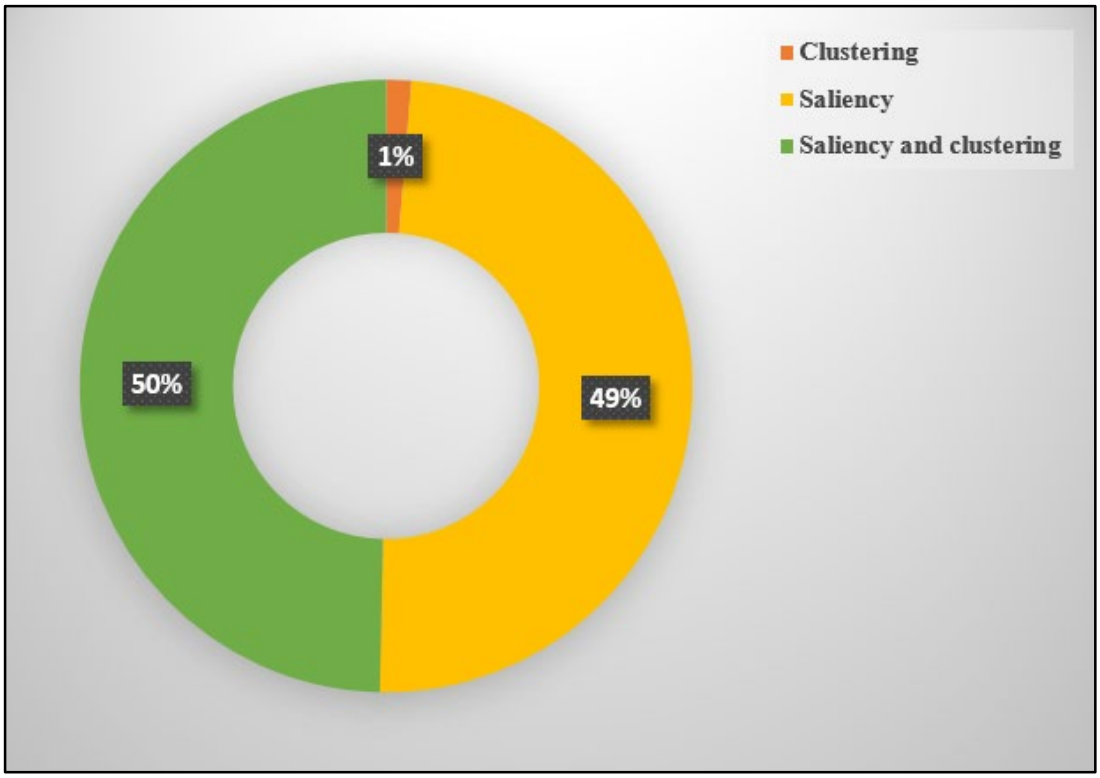

Figure 2-13 Distribution of image segmentation methods

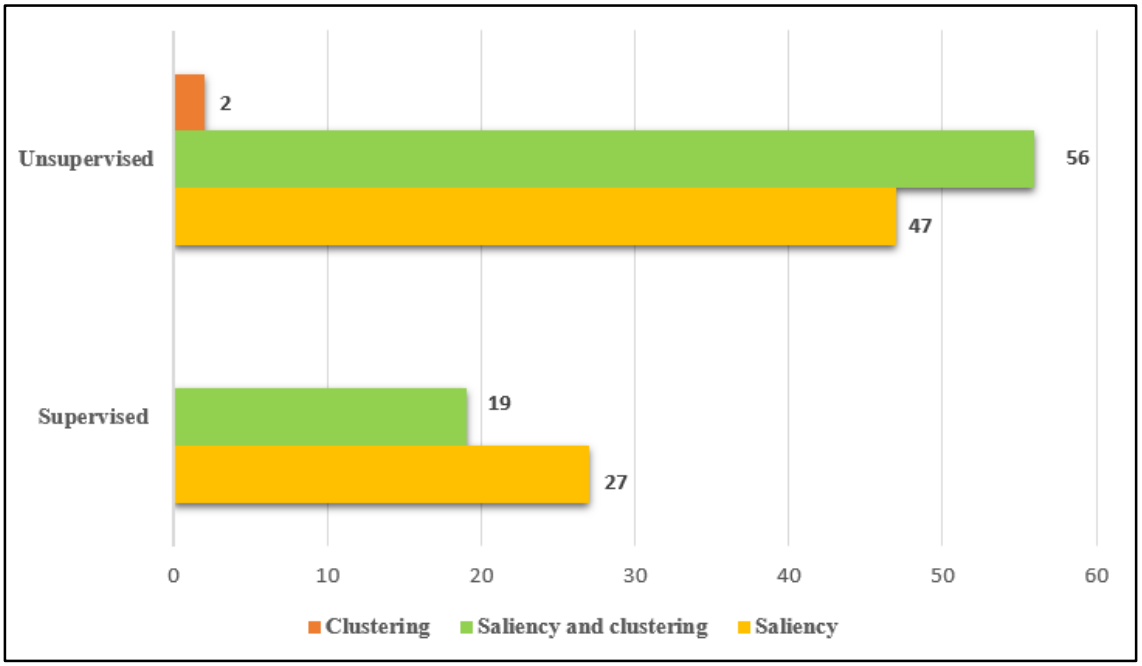

Figure 2-14 Distribution of image segmentation methods per segmentation approach

The accurate segmentation of the region of interest is often affected by the presence of heterogeneous properties inherent in the input image. Mostly, these heterogeneous properties are addressed by the majority of the existing segmentation methods with the help of preprocessing methods. Hence preprocessing phase is generally considered an effective way of accelerating segmentation results. However, the segmentation algorithms that use preprocessing phases to enhance the segmentation accuracy are adversely affected by the extra computational time (Joseph and Olugbara 2022b). An appropriate segmentation method can address the heterogeneous properties inherent in the input image and thereby elude the demand for preprocessing and computational complexity. Of the 46 supervised image segmentation methods, 11 studies (24%) applied the preprocessing step to circumvent the undesirable artifacts inherent in the input image. Similarly, 24 studies (23%) from unsupervised segmentation methods used the preprocessing stage as illustrated in Figure 2-15. This indicates that most of the reviewed studies elude the preprocessing phase.

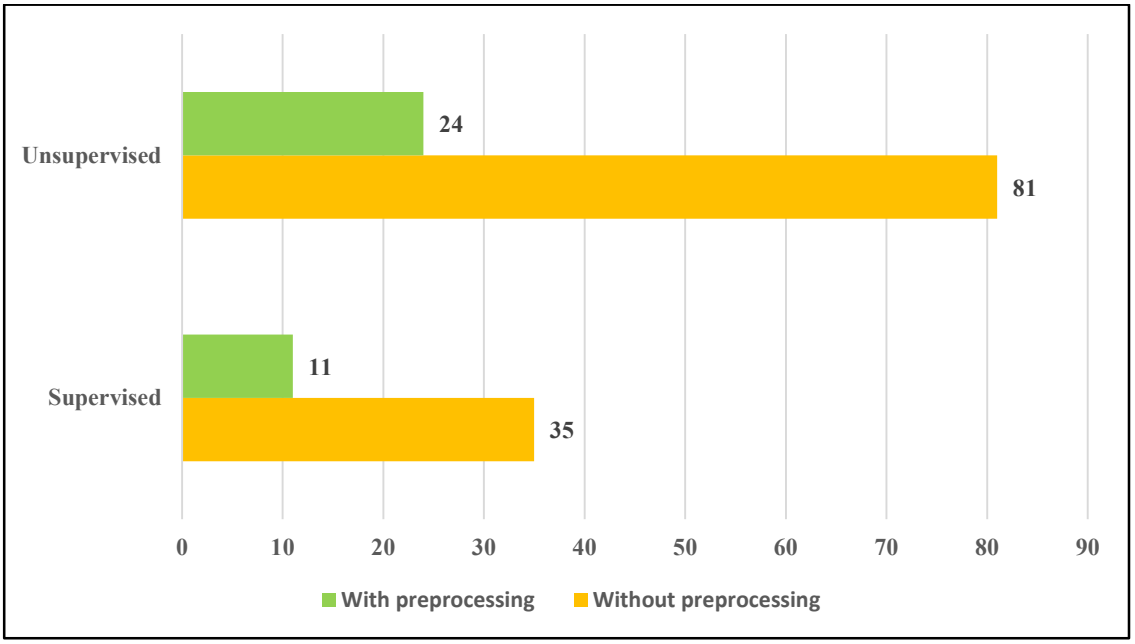

Figure 2-15 Studies with and without image preprocessing

2.7.3 Regional granularity for image abstraction

Regional granularity for image abstraction is considered an important stage in image processing to reduce computational complexity. Researchers have proposed the concept of integrating pixels rather than directly operating on individual pixels to enhance the computational efficiency of the image segmentation method. A region of similar pixels or superpixels representation has the advantage of reducing the image primitives compared to the pixel level representation (Jia *et al.* 2019b). The methods

that used group of pixels considered non-overlapping patches (Gion *et al.* 2015; Li, Zhou and Bai 2018; Kim 2019; Li *et al.* 2021a; Kumar and Meenpal 2022) or homogenous clusters (Liu *et al.* 2012; Zhou and Liu 2015; Singh, Arya and Agrawal 2017; Song *et al.* 2017; Jahanifar *et al.* 2019; Joseph and Olugbara 2021; Moradi, Bayat and Charmi 2021; Yu *et al.* 2021b; Zhang and Wang 2021; Zhang *et al.* 2021c; Ning *et al.* 2022) as the image elements for further processing of image segmentation. Literature showed evidence of using different approaches to group the pixels as illustrated in Figure 2-16. The importance of using a group of pixels to reduce the computational efficiency is visible in the reviewed studies as only 49 studies (32%) used the pixel instead group of pixels whereas 102 studies (68%) applied the group of pixels to reduce the computational complexity. For the group pixels, there are 83 studies (55%) used regions and 19 studies (13%) used the patch-based approach for grouping similar pixels. Patch-based methods use fixed-size patches or blocks to represent a group of pixels. However, patch-based methods produce fuzzy segmentation results because of the irregular statistical features of the patches and the presence of both background and foreground objects in the regular patches. The model proposed by Jia *et al.* (2019a) aimed to solve the issues related to patch-based models and employed a mean-shift clustering algorithm to segment the input into uniform regions of non-overlapping patches.

The concept of a group of pixels as an alternate method to represent the image into homogenous regions for image abstraction has been used in many studies. Various methods such as K-Means clustering (Singh, Arya and Agrawal 2017; Qian *et al.* 2019; Singh *et al.* 2019), histogram clustering (Devi, Singh and Laskar 2020; Inbarani and Azar 2020), Mean shift clustering (Liu *et al.* 2012; Zhou and Liu 2015), spectral clustering (Song *et al.* 2017; Ning *et al.* 2022), texture segmentation (Saleem *et al.* 2019; Srivastava and Srivastava 2020), feature clustering (Zhuang *et al.* 2018) and Simple linear Iterative Clustering (SLIC) (Abkenar, Sadreazami and Ahmad 2018; Liu and Yang 2019; Xu, He and Lv 2019; Zhou *et al.* 2019; Hu *et al.* 2020; Huang *et al.* 2020; Kompella and Kulkarni 2020; Zhang and He 2020; He *et al.* 2021b; Jian *et al.* 2021; Moradi and Bayat 2021; Moradi, Bayat and Charmi 2021; Niu *et al.* 2021; Yu *et al.* 2021b; Li *et al.* 2022) approaches have been adapted by researchers to generate the regions. In recent times, myriads of image segmentation models have employed the superpixel approach to divide the input image into perceptually homogenous regions. However, the main limitation of these models is that the isolated or cluttered pixels cannot be grouped correctly due to the constraint of spatial domain connectivity (Singh, Kumar and Singh 2020). Another inevitable problem with the superpixel-based model is the determination of an optimum number of superpixels. An inadequate number of superpixels can lead to the non-uniform highlighting of salient regions (Tang and Wu 2016).

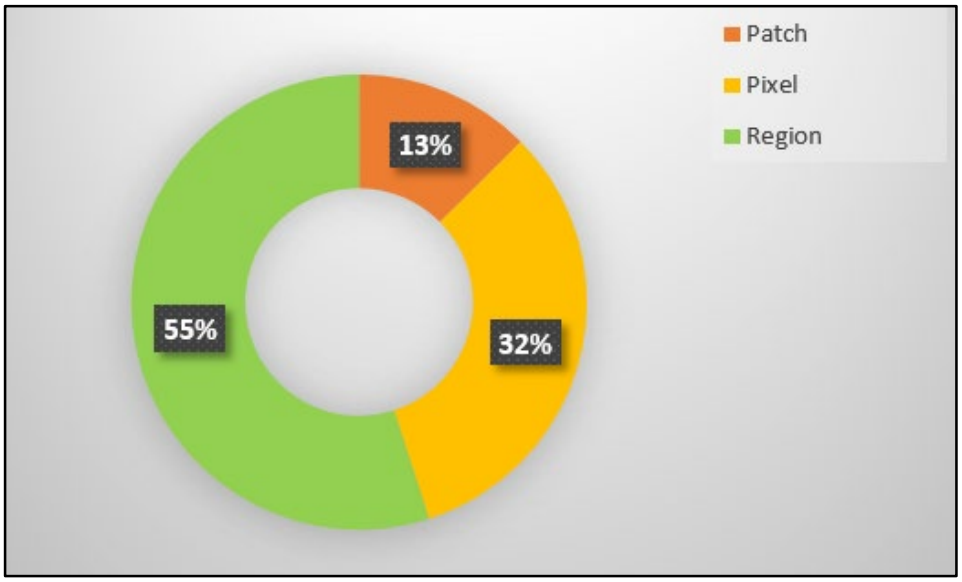

Figure 2-16 Unit of processing

2.7.4 Public image segmentation datasets

Myriads of image datasets were used by the reviewed studies to evaluate the segmentation performance. Many studies used multiple datasets and the datasets that were included in at least five studies are shown in Figure 2-17 and the description of these popular datasets is illustrated in Table 2-8. Of the 151 studies reviewed, 34 studies (23%) used the MSRA5K dataset, 31 studies (18%) used ECSSD, and 27 studies used (18%) the PASCAL image dataset.

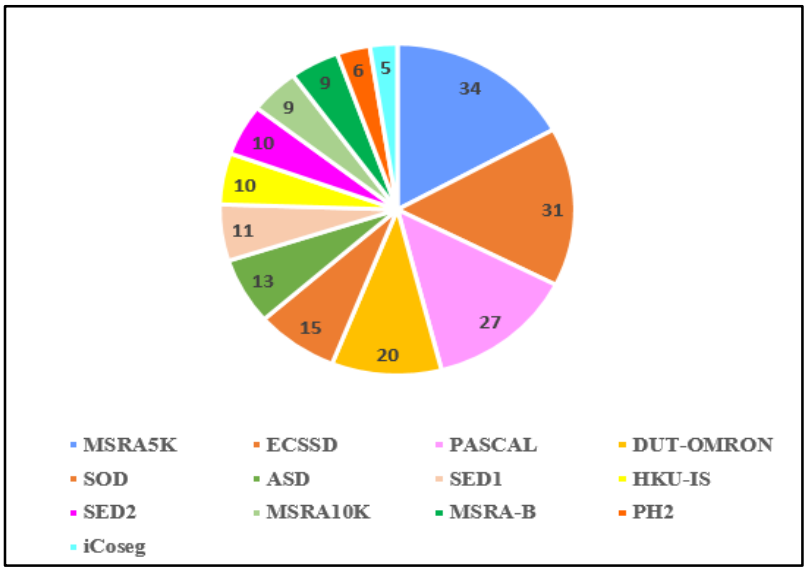

Figure 2-17 Image datasets used

Table 2-8 Description of image datasets

Dataset	Number of images	Description
MSRA5K(Jiang *et al.* 2011; Liu *et al.* 2011)	5000	Microsoft Research Asia dataset with pixel-wise object level annotation. Single objects with a simple and clean background.
ECSSD (Shi *et al.* 2015)	1000	Extended complex scene saliency dataset with semantically meaning full objects with the complex and challenging background.
PASCAL-S (Li *et al.* 2014)	850	Image segmentation dataset with 20 categories of multiple objects and complex scenes.
DUT-OMRON (Yang *et al.* 2013)	5168	Image dataset with one or multiple small objects with high image content variants and complex backgrounds. Contain pixel-wise object level annotation.
SOD (Movahedi and Elder 2010; Arbelaez *et al.* 2011)	300	A subset of Berkeley segmentation image dataset with multiple low contrasts objects to background and object touching the image boundary.
ASD (Achanta *et al.* 2009)	1000	A subset of MSRA10K and this dataset contains single easily detectable centrally located objects in a clean and simple background.
SED1 (Alpert *et al.* 2011)	100	This segmentation evaluation dataset contains one object with a simple background.
HKU-IS (Li and Yu 2015)	4447	Dataset with multiple disconnected low contrast objects touching the image boundary.
SED2 (Alpert *et al.* 2011)	100	This segmentation evaluation dataset contains two objects with complex backgrounds.
MSRA10K (Liu *et al.* 2011)	10000	Image dataset with pixel-wise annotation
MSRA-B (Liu *et al.* 2011)	5000	General image dataset with bounding box-based object annotation. Contains general images with a simple background and easily recognizable objects of interest. This dataset is biased towards image centers.
PH2 (Mendonça *et al.* 2013)	200	Dermoscopic images of melanocytic lesions with their corresponding ground truths performed by expert dermatologists
iCoseg (Batra *et al.* 2010)	643	Image dataset of 38 groups pixel-wise hand-annotated ground truth.

2.8 Conclusion

The meta-analysis conducted in this chapter was motivated by the popularity of image segmentation methods. Information from 151 scientific articles was used to create a database with 15 fields relating to image segmentation algorithms, which served as the foundation for the meta-analysis. Several conclusions were then drawn as a result.

i. The unsupervised segmentation approach remained the most frequently used approach as compared to the supervised segmentation approach. Unsupervised segmentation approaches frequently used saliency and clustering-based segmentation methods because of their ability to simulate visual attention mechanisms.

ii. Due to the computational complexity of image preprocessing, more studies excluded the image preprocessing stage in the image segmentation process. This shows the popularity of image segmentation methods that are independent of the image preprocessing stage.

iii. The concept of a region of pixels or superpixels for image abstraction is extensively used by many studies to reduce computational complexity. This highlighted the importance of generating an adequate method to automatically detect the homogenous regions as the segmentation results are highly dependent on the regional granularity of the homogeneous regions.

iv. There was a significant variance in the number of images used by each study to confirm the segmentation performance. This leads to 56.99% variability in the effect size estimate. The findings of the meta regression analysis demonstrated that the identified between-study variation is explained by the number of images used for segmentation evaluation.

2.9 Chapter summary

The meta-analysis performed in this chapter helps to highlight the advances in image segmentation methods. The review confirms that clustering and saliency-based image segmentation methods play an important role in image segmentation. The meta-analysis assists to present transparent, objective, and replicable summaries of the image segmentation methods based on clustering and saliency. This powerful meta-analysis assists to understand the emerging trends in image segmentation.

CHAPTER THREE: THEORETICAL FOUNDATION

This chapter presents the fundamental principle of image segmentation, image processing units, and stages involved in a typical image segmentation process to improve the segmentation quality. The approaches for image preprocessing, color models, and image segmentation with a focus on clustering and saliency methods were also presented in this chapter. Conventional clustering methods and saliency models used in image segmentation were also described. The clustering of the foreground and background regions as well as post-processing methods for enhancing the segmentation outcomes were further discussed.

3.1 Image segmentation principle

The main objective of image segmentation is to represent the image as a group of meaningfully connected regions. This is achieved through the analysis of image features in terms of pixel characteristics such as color, texture, intensity, and location. The process of image segmentation partitions an image into several distinguished regions with a special meaning based on pixel properties. Hence image segmentation can be viewed as a process that partitions the given data into subregions. Let R represents the image spatial region, and the segmentation process subdivides R into n subregions R_1, R_2 , …, R_n met the following conditions (Gonzalez and Woods 2018):

i. $\bigcup_{i=1}^{n} R_i = R$

ii. $R_i \text{ is a connected set for } i = 1,2,...,n$

iii. $R_i \cap R_j = \phi \text{ for all } i \text{ and } j, i \neq j$

iv. $Q(R_i) = TRUE \text{ for } i = 1,2,...,n$

v. $Q(R_i \cup R_j) = FALSE \text{ for any adjascent regions } R_i \text{ and } R_j$

Condition (i) indicates that the segmentation should be complete means that every pixel must be assigned to a region. Condition (ii) says that pixels in a region must be connected based on some predefined characteristics. Condition (iii) indicates that all regions should be disjoint. $Q(R_i)$ is the logical predicate that defines the pixel properties, hence condition (iv) deals with properties that must be satisfied by all pixels in a segmented region. Finally, condition (v) says that two adjacent regions

R_i and R_j must be dissimilar based on the logical predicate. Hence the basic principle of image segmentation is partitioning the images into elemental parts or objects that contain pixels with uniform and similar features. Image segmentation applications are interested to extract the most salient region with a unique characteristic in the image. Since image segmentation has a wide range of applications and the level of segmentation depends on the application, there is no universal theory of image segmentation (Ming 2010; Ramesh *et al.* 2021).

Clustering is a process of segregating and labeling data based on similarity measures. Image segmentation is typically defined as a complete partitioning of input images into homogeneous regions in terms of color, intensity, texture, or spatial features of image pixels. The main objective of image segmentation is the recognition of homogeneous regions as distinct and belonging to different objects within the image. Fundamentally image segmentation is the clustering of image pixels based on certain criteria. The fundamental task in image segmentation is to distinguish between foreground and background regions, hence the process of image segmentation can be considered as a clustering problem, where the image pixels are analyzed to cluster into homogenous groups based on some characteristics (Bong and Rajeswari 2011; Abd Elaziz *et al.* 2021; Mittal *et al.* 2021; Zhong and Shih 2021). Feature extraction is a major stage to assign the pixels to a corresponding region hence one or more features of the input image are considered to produce a new salient feature based on the goal of image segmentation (Bong and Rajeswari 2011). Since salient regions are extremely different from the background regions, salient detection methods are employed as a two-class clustering problem to cluster foreground and background regions (Hu *et al.* 2016). Salient features can discriminate an image region from other regions, and the measure of saliency is widely applied in image segmentation (Hu *et al.* 2020; Joshi *et al.* 2020; Lin and Fan 2020; Ramadan, Lachqar and Tairi 2020; Ren *et al.* 2020; Song *et al.* 2020a; Yao and Gong 2020; Ramella 2021; Joseph and Olugbara 2022b; Joseph and Olugbara 2022a; Ning *et al.* 2022).

3.2 Image segmentation processing unit

Image segmentation algorithms usually consider either pixels or groups of pixels or regions as a unit of processing in image segmentation. Image pixels are the basic unit of processing in traditional image segmentation algorithms (Wang, Qi and Shen 2020) and it demands a huge amount of computational time to process images with high resolution (Ren and Malik 2003). For pixel-based methods, pixels are considered as an independent image element to extract the features such as color

differences, edge information, and spatial cues. Pixels are considered as a discrete representation of images rather than a natural entity, hence the concept of superpixels which preserve the structure necessary for image segmentation is introduced by (Ren and Malik 2003; Chen, Li and Huang 2017). The concept of superpixels or a cluster of pixels that agglutinates similar pixels has been widely accepted by researchers to replace the pixels (Zou *et al.* 2015; Chen, Li and Huang 2017; Jahanifar *et al.* 2019; Zhou *et al.* 2019; Abd Elaziz *et al.* 2021; Ning *et al.* 2022). Pixels are grouped based on similarity in terms of color, contrast, or spatial features and attained the information redundancy of images. The abstraction of an image into different groups of pixels with similar properties has a significant role in reducing the computation time by considering each region as a unit of processing.

3.3 Image segmentation stages

Image preprocessing, segmentation of input images into homogenous regions, and post-processing are the three stages generally included in a segmentation process for an accurate segmentation result (Shivhare and Gupta 2015). The stage of preprocessing is comprised of noise reduction and color model transformation to enhance the quality of the input image. Cluster generation, region of interest or foreground detection, and the separation of foreground and background regions are the main steps of image segmentation. Finally, post-processing operations are applied to improve the segmentation results.

Segregation of the region of interest from the background region is not adequate to generate quality segmentation results because of the heterogeneous properties of images. The segmented image is the basis for image understanding and the accuracy of image segmentation is critical as it determines the quality of the image analysis tasks such as pattern recognition and classification. The segmentation results regardless of applied segmentation methods can be enriched by integrating additional procedures before and after the segmentation stage. Agglutination of image preprocessing, color model transformation and post-processing stages can further improve the performance of image segmentation. The preprocessing stage optimally prepares the input image for the segmentation process by artifact removal (Palus 2005; Vocaturo, Zumpano and Veltri 2018; Zafar *et al.* 2020; Henke *et al.* 2021), and color model transformation allows a better segmentation (Henke *et al.* 2021) and the post-processing stage improves the segmentation results by noise reduction (Wang and Cao 2019a; Hafeez, Yan and Guoliang 2021). Hence the process of image segmentation is typically performed with a series of stages as depicted in Figure 3-1. The segmentation stages are explained in depth in the sections that follow.

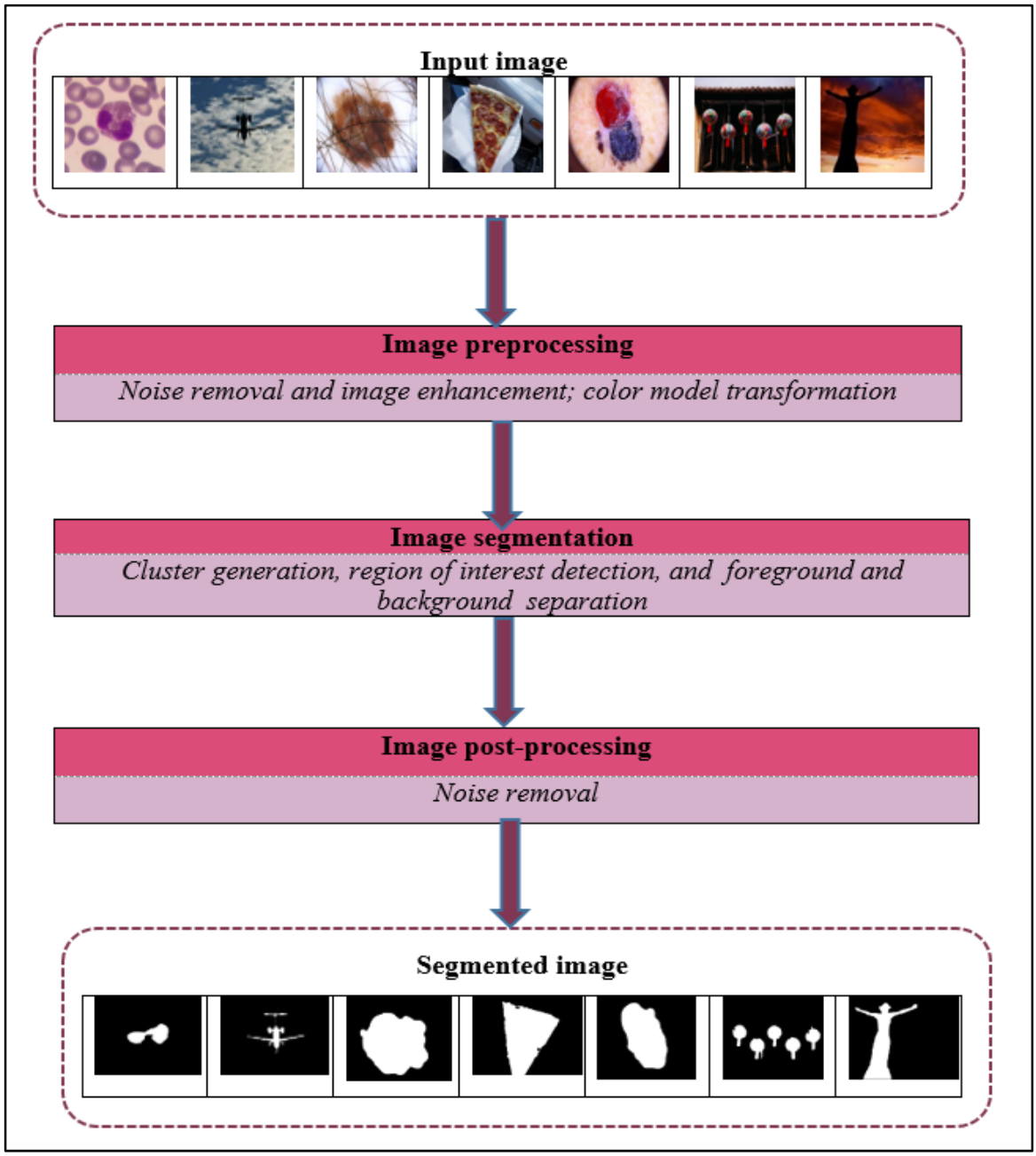

Figure 3-1 Stages of the image segmentation process

3.4 Image preprocessing

Preprocessing stage is considered an important stage in image segmentation for noise removal and to enrich the quality of the input image for many image segmentation applications. The accurate segmentation of the region of interest is often prejudiced by the heterogeneous properties inherent in the input image. These heterogeneous properties include the presence of undesirable artifacts, illumination variation, and contrast imbalances. The objective of the preprocessing stage can mainly be

achieved by image enhancement, image restoration, and artifact removal (Hoshyar, Jumaily and Hoshyar 2014) as in Figure 3-2.

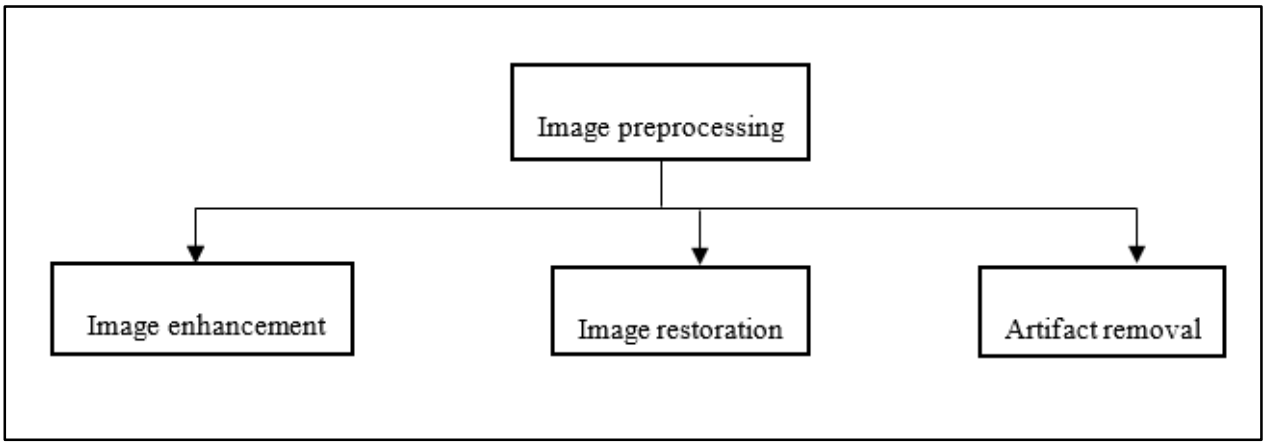

Figure 3-2 Image preprocessing

Image scaling, color model transformation, and contrast enhancement are the three basic categories of image enhancement used in image segmentation. Image scaling is applied to get a standard size of input image because of the various methods and devices used for image acquisition. Since color information has a crucial role in extracting image features for segmentation, the transformation to a suitable color model has paramount importance in image processing.

Image enhancement methods enable the correction of non-uniform illumination and the low contrast nature of the input image. These enhancement methods are based on intensity or contrast adjustment (Garnavi *et al.* 2011; Guarracino and Maddalena 2019), filtering (Emre Celebi *et al.* 2008; Garnavi *et al.* 2011; Agarwal *et al.* 2017; Jahanifar *et al.* 2017; Khan *et al.* 2019), Adaptive Histogram Equalization (AHE) (Hoshyar, Jumaily and Hoshyar 2014; Pennisi *et al.* 2016) and Contrast Limited Adaptive Histogram Equalization (CLAHE) (Okuboyejo, Olugbara and Odunaike 2014; Premaladha and Ravichandran 2016; Jaisakthi, Chandrabose and Mirunalini 2017; Ibraheem and Elmogy 2020). Contrast enhancement improves the image quality by image border sharpening and accentuating the brightness difference between the foreground and background regions. Histogram Equalization (HE) is a global contrast enhancement method for adjusting image intensity levels by a uniform distribution of pixel intensity. Adaptive histogram equalization is the modified version of HE where region-wise contrast enhancement is computed based on the intensity of neighborhood pixels. The noise problem in AHE because of the high contrast difference between the regions, is resolved using histogram equalization by contrast limiting. Hence CLAHE is the modified version of AHE to limit the artifacts

(Singh and Dixit 2015). CLAHE is an effective and excellent method broadly applied to contrast enhancement for both natural and medical images (Pizer *et al.* 1987; Pizer *et al.* 1990; Premaladha and Ravichandran 2016).

The restoration process enhances the image appearance and is one of the challenging steps in image processing as it relates to the feature extraction from the imperfect image which is in contrast to image enhancement (Maru and Parikh 2017). The process is used to restore the corrupted or degraded image like that of the original image. The main objective of the restoration process is to recover the original image by identifying the type of noise and applying the inverse of it to get the original image (Kaur and Singh 2014).

Similarly, many artifact removal algorithms are based on thresholding (Emre Celebi et al. 2008; Jahanifar et al. 2017; Guarracino and Maddalena 2019), morphology (Pennisi et al. 2016; Nida et al. 2019), filtering (Premaladha and Ravichandran 2016; Agarwal et al. 2017; Guarracino and Maddalena 2019; Majumder and Ullah 2019), and the most known DullRazor (Garnavi et al. 2011; Ahn et al. 2015; Bi et al. 2016; Ahn et al. 2017; Vocaturo, Zumpano and Veltri 2018; Javed et al. 2019; Khan et al. 2019; Majumder and Ullah 2019; Ünver and Ayan 2019; Hu et al. 2020) have been developed to address the issues of occlusion due to the artifacts. The artifact removal and image enhancement methods are generally executed before the segmentation process as demonstrated in Figure 3-1.

3.5 Color transformation

Color transformation is an integral step in image segmentation since color plays an important role in representing the information of digital images for computer vision. Color models are used to specify the colors in a more general and standardized way. A color model is a geometric specification of a tridimensional coordinate system and a subspace within which color is represented by a unique point (Garcia-Lamont *et al.* 2018). Color models provide a balanced approach to specifying, manipulating, ordering, and displaying the color components of objects (Plataniotis and Venetsanopoulos 2013). Color models help to understand the color features of a particular device or digital file (Bora, Gupta and Khan 2015). Color features simplify image segmentation, and the results of image segmentation are influenced by the choice of color models and features. Identification and extraction of objects become simpler while using color features. The most common color models employed for image segmentation are RGB, HSV, HSI, L∗a∗b∗, L∗u∗v∗, YUV, and YCbCr (Garcia-Lamont *et al.* 2018), and these color models are summarized in Table 3-1.

Table 3-1 Common color models employed for image segmentation

Color model	Advantages	Disadvantages
RGB (red, green, and blue): This color model is based on the Cartesian coordinate system and each color is represented by spectral components of red, green, and blue.	• More computationally practical • easy to implement • More convenient in image acquisition and display • Base color model for many applications as no need for transformation on the screen	• No removable singularities, • Sensitive to non-uniform illumination • Non-linear with visual perception • Not suitable for object recognition and classifications applications • device dependent
HSV (hue, saturation, value), HSI (hue, saturation, intensity): the color is represented with hue, saturation, and value and S and V components emulate the human perception of color. In HSI, colors are specified using three components, Hue (H), saturation (S) and intensity (I) in cylindrical coordinates and very similar to HSV.	• Robust on non-uniform illumination • based on human color perception • suitable for image processing application • The segmentation process can be achieved fast with a single component, hue.	• Not uniform • Nonremovable singularities • do not supply insight for color manipulation
CIE L*a*b*, CIE L*u*v: These are the uniform color models derived from CIE XYZ space. L*a*b color model is perceptually uniform, and the L component approximates the human perception of lightness and the a and b channels closely match the human chromatic opponent system. In CIE L*u*v, lightness is represented by L, u* and v* represent the correlates of chroma and hue.	• Efficiency in measuring small color differences • Perceived as uniform	• Non-linear transformation • Device-independent • Suffer from unintuitive • Singularity problem
YUV, YCbCr: These color models are employed to standardize television images. YUV is the standard for color coding for National Television Standard Committee (NTSC) and YCbCr is for digital television. In this model, the luminance channel (Y) is separated from the chromatic channels U (Cb) and V(Cr) to reduce the effect of lighting variations	• Suitable for image compression and coding color for TV signals • Performance can be improved by separating the chromaticity components	• Dependent on RGB primaries • Correlation between channels due to a linear transformation

Color transformation is the process of conversion of the color components from one color model to another. According to Gonzalez and Woods (2008), the color transformation is modeled using the expression

$$g(x, y) = T\,[f(x, y)]$$

$where\ f(x, y)$ is a color input image and $g(x, y)$ is then transformed color output image and T is the operator on f over a spatial neighborhood of (x, y). Most of the image acquisition devices are employed to represent the colors in the RGB color model. It is significant to map the color components into other spaces to utilize the color features specified by such models. Each color model has its components and feature space with the ability of mapping from one color model to another using standard formula. The nature of the applications and the color model characteristics are highly correlated. Color features have paramount importance in detecting regions of interest in images hence, the selection of appropriate color models has an impact on the quality of image segmentation.

3.6 Image clustering

The clustering of an input image is generally accomplished by applying the techniques of clustering. Clustering methods have the advantage of accomplishing unsupervised image segmentation without labels and multichannel image segmentation because of the ability to classify high-dimensional data (Lei *et al.* 2020). The process of image segmentation groups the pixels in an image into different clusters that exhibit similar characteristics such as color, intensity, or texture (Bora and Gupta 2014; Matta 2014) and is considered the foreground and background separation problem. Hence myriads of clustering techniques have been proposed in the literature to segment the foreground regions from the image background (Ren *et al.* 2017 ; Abdalla *et al.* 2019; Khan, Yang and Zheng 2019; Fan *et al.* 2021; Nagaraju *et al.* 2021).

According to Jain, Murty and Flynn (1999), feature selection or feature extraction from patterns, selection of proximity measures, and the grouping of patterns are the three mandatory stages involved in the clustering process. This also includes a feedback loop as shown in Figure 3-3 (Jain, Murty and Flynn 1999).

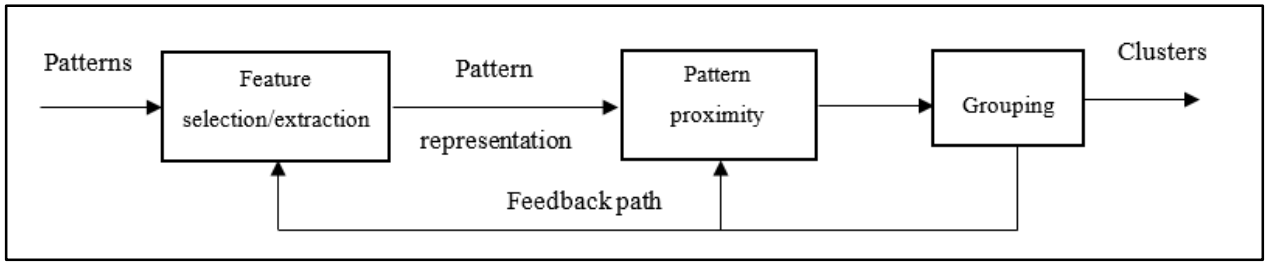

Figure 3-3 Stages in clustering

Feature selection is the identification of the most effective set of features from a set of patterns or classes that need to be used in clustering. While feature extraction deals with the transformation of original features into new salient features. Both are very vital in the clustering procedure as the identification of features should be useful to distinguish the patterns or data objects belonging to different clusters. In image segmentation, pixel characteristics such as color (Joseph and Olugbara 2021), intensity (Olugbara, Adetiba and Oyewole 2015), or texture (Oskouei *et al.* 2021) are used for feature representation (Bora and Gupta 2014; Matta 2014) to cluster similar image pixels. Pattern proximity is the stage that deals with the construction of criteria based on appropriate proximity measures to establish the relationship between the patterns. The conceptual similarity of patterns is typically represented by a distance function that measures it. The grouping stage deals with the division of patterns into different groups and the grouping is dependent on the type of clustering techniques. For instance, in hard clustering, the patterns are strictly associated with one cluster or none and in soft clustering, patterns are concurrently associated with more than one cluster. The fast, reliable, and consistent performance characteristics and the unsupervised nature of clustering algorithms promote the overwhelming use of clustering in image segmentation applications (Dubey *et al.* 2013; Kirati and Tlili 2014; Ren *et al.* 2017; Oskouei *et al.* 2021).

3.7 Conventional clustering methods

In clustering-based image segmentation, the data objects are image pixels and the image is partitioned into a group of similar pixels known as clusters (Lei *et al.* 2016; Wazarkar and Keshavamurthy 2018) with the objective of grouping the unlabeled pixels into homogenous regions that exhibit maximum intra-class similarity and minimum inter-class similarity. The simplicity and accuracy of clustering algorithms ameliorated the popularity of employing clustering approaches in diverse image processing applications (Dubey *et al.* 2013; Kirati and Tlili 2014). A variety of clustering-based algorithms have been developed and practiced by researchers to improve the success rate of image processing applications. Literature shows various types of classification of general clustering methods based on their characteristics.(Xu and Tian 2015; Saxena *et al.* 2017; Wazarkar and Keshavamurthy 2018). Clustering algorithms used in image segmentation are classified into hierarchical (Johnson 1967; Fahad *et al.* 2014; Saxena *et al.* 2017; Shafii 2018; Ghosal *et al.* 2020; Mittal *et al.* 2021), partitional (Fahad *et al.* 2014; Xu and Tian 2015; Saxena *et al.* 2017; Shafii 2018; Ghosal *et al.* 2020; Mittal *et al.* 2021), density based (Ester *et al.* 1996; Fahad *et al.* 2014; Ghosal *et al.*

2020), grid-based (Fahad *et al.* 2014; Ghosal *et al.* 2020) and model-based (Fahad *et al.* 2014; Shafii 2018; Ghosal *et al.* 2020) as illustrated in Figure 3-4 (Ghosal *et al.* 2020).

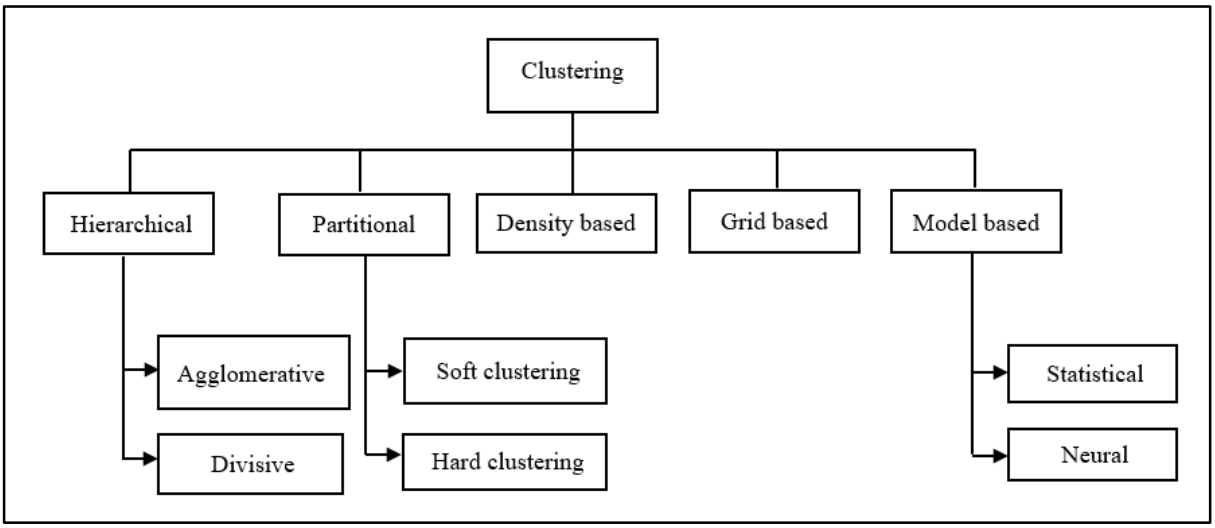

Figure 3-4 Classification of clustering algorithms

3.7.1 Hierarchical clustering

The fundamental idea of hierarchical clustering algorithms is to create a hierarchical relationship among the data objects to generate the clusters (Johnson 1967). Hierarchical clustering methods create nested sequences of clusters called a dendrogram, with a single cluster formed at the higher level and child clusters that represent individual points at the lower levels (Sisodia *et al.* 2012; Cohen-Addad *et al.* 2018; Benabdellah, Benghabrit and Bouhaddou 2019). The dendrogram is a tree structure with each leaf representing a data object and the internal node representing a data cluster with its successor leaves (Cohen-Addad *et al.* 2018; Chehreghani 2020; Krestanova *et al.* 2020). Descendant level clusters are combined to form each of the intermediate nodes in hierarchical clustering. Hierarchical methods generate a structure of partitions with one main cluster holding all of the given data objects placed on one side and single-element clusters positioned on the other (Krestanova *et al.* 2020).

The agglomerative (bottom-up) and divisive (top-down) techniques are the two categories of hierarchical clustering methods (Fahad *et al.* 2014; Ramesh and Nandhini 2017; Sharma, López and Tsunoda 2017; Cohen-Addad *et al.* 2018; Chehreghani 2020). In an agglomerative approach, the individual data objects are aggregated together to build the candidate dendrogram bottom-up. In this method, each data object is initially assumed to be a singleton cluster and two adjacent clusters are fused simultaneously based on their similarity. Agglomeration of clusters continues until the desired

number of clusters is achieved or all data objects are clustered into one single cluster (Islam and Ahmed 2013).

The divisive approach is based on the partition of a single large cluster split into two clusters based on minimal similarity and constructing the candidate dendrogram top-down. In this method, initially, all data objects are combined as a single cluster and partitioned into two clusters at each iteration. The process is continued by the successive division of clusters and it repeats until all the clusters encompass one single data object. The concept of these algorithms in image segmentation is to build a dendrogram signifying nested grouping of patterns i.e. pixels in images (Islam and Ahmed 2013).

3.7.2 Partitional clustering

Due to the computational efficiency, partitional clustering is more popular and preferred over hierarchical clustering, especially for a large dataset (Mittal *et al.* 2021). In the partitional clustering approach, K clusters are formed by partitioning a set of N data objects, and clusters are represented by the cluster centers (Sisodia *et al.* 2012; Ramesh and Nandhini 2017). In this approach, the given data is divided into several clusters based on the cluster centers which can be mean, medoid, or mode (Gupta and Panda 2018), and data objects are assigned to the cluster by optimizing the criterion function. Euclidean distance is the most common criterion function and data objects are assigned to the cluster with minimum distance (Saxena *et al.* 2017; Mittal *et al.* 2021). Prompt determination of clusters is the main characteristic of this approach and similar to hierarchical clustering, cluster counts need to be found in advance for an optimum number of cluster formations. Hard and soft clustering are two subcategories of partition-based clustering (Petrus 2019; Ghosal *et al.* 2020; Mittal *et al.* 2021).

Hard and soft clustering use different approaches for computing the membership function to designate the data points to the clusters. In hard clustering, the data points are strictly associated with one cluster or none. Hence each data point is associated with exactly one cluster and the clusters are mutually disjoint (Mittal *et al.* 2021). Typical examples of hard clustering algorithms used in image segmentation tasks are K-Means, K-Medoid, Clustering LARge Applications (CLARA), PICA and Histogram-based clustering. Soft clustering methods assign each data point to more than one cluster based on a degree of membership that illustrates the level of association among data (Mittal *et al.* 2021). Due to the concurrent association of data objects in more than one cluster, the generated clusters can all overlap and the right partition is achieved by choosing the cluster with the highest membership per

data point. FCM is a classic example of a soft clustering technique that allows one data point to belong to more than one cluster different from hard clustering methods(Chen *et al.* 2015; Saxena *et al.* 2017)

K-Means is a popular unsupervised simplest and benchmarked iteratively and heuristic clustering algorithm introduced by MacQueen (1967). In K-Means clustering, the centroid of a cluster is computed by calculating the mean of all data objects in the corresponding cluster. The algorithm is comprised of two phases: define the centroid for each cluster and associate each data point with its nearest cluster based on Euclidean distance (Nazeer and Sebastian 2009; Dhanachandra, Manglem and Chanu 2015; Arora and Varshney 2016). Cluster centroids are updated after each addition of data objects that have a minimum distance to the cluster. Each cluster is well-defined by its member data objects and its centroids by sustaining the minimum total within-cluster variance which is calculated as follows (Renjith, Sreekumar and Jathavedan 2020):

$Total\ within\ cluster\ \ va\ riance = \sum_{k=1}^{K} \sum_{E_i \in C_k} (E_i - \mu_k)^2$ k, represents the cluster count and E_i, is the data objects in the cluster, C_k with the centroid μ_k.

Generally, this category of partitioning algorithm includes all methods inspired by the K-Means algorithm. Typical examples of partitioning-based clustering algorithms inspired by the K-Means algorithms are K- Medoids (Yerpude and Dubey 2012)and CLARA (Rousseeuw and Kaufman 1990).

Pixel Intensity Clustering Algorithm (PICA) is a multi-level partition-based clustering technique developed by Olugbara, Adetiba and Oyewole (2015). The algorithm utilizes the image pixel intensity set, the desired cluster count, and a Forgy-based linear partitioning method for the stable initialization of cluster centroids. The occurrence probability of specified pixel intensity is utilized to apply the linear partition scheme. Unallocated pixel intensities are assigned to the suitable clusters by applying the maximization of cluster variance. Between clusters, variance is the notion of distance measures utilized in PICA to identify the closest cluster centroid. This eliminates common problems such as the dead center problem and incorrect allocation of pixels to clusters embedded in conventional clustering algorithms. Cluster weight and centroids are updated after assigning pixel intensities to the respective clusters. Simplicity, robustness, and computational cost-effectiveness are the major highlights of PICA.

Histogram-based clustering, image pixels are grouped according to the intensity values in the image. A set of optimal threshold values are used for histogram partition and resulted in the grouping of image

pixels in different clusters (Mittal *et al.* 2021). In this approach, the probability distribution of i^{th} intensity level of an image with N number of pixels each having an intensity level from (0, 1,2,…, L-1) is defined and is used for calculating the mean intensity value of the image. The grouping of image pixels into *n* clusters is based on the identification of n-1 threshold levels, and the allocation of the pixels into each cluster is based on the intensity levels by considering the maximization of inter-class variance (Mittal *et al.* 2021). The histogram properties of the image can be considered for the automatic selection of several clusters hence, this method has been widely used for the automatic determination of cluster count required for many image segmentation applications (Khan *et al.* 2017; Basar *et al.* 2020; Devi, Singh and Laskar 2020; Lei *et al.* 2020; Sharma and Singhai 2020).

Fuzzy C-Means (FCM) is a widely used iterative soft clustering technique introduced by Dunn (1973) and later improved by Peizhuang (1983). In conventional FCM, the initial cluster centers are arbitrarily selected and clusters are formed based on the similarity between data objects and the cluster centers. Each data object is concurrently belonging to more than one cluster up to a certain degree instead of exclusively fitting into only one cluster and the aggregate membership value of a data object in all clusters should be one (Siddique *et al.* 2018). The degree of membership of each data object in clusters directly proportional to the closeness between data objects and the cluster centroids

The multiple fuzzy membership grade allows more flexibility for FCM especially dealing with many clusters (Ganesh, Naresh and Arvind 2017). FCM algorithms are well-suited to handle the problems associated with recognizing pattern ability, data with noises, and mixed media information (Sun *et al.* 2016). However, FCM possesses very high time complexity and the sophistication of the Fuzzy C-Means algorithm is higher than K-Means. Fuzzy c-means clustering is widely applied for image segmentation. However, there are downsides to this approach, including sensitivity to initial values, being trapped in local optima, and finding it challenging to distinguish objects with identical color intensities (Mohammdian-Khoshnoud *et al.* 2022). In a codicil, FCM is not suitable for images with strong homogeneity and noises because spatial information is discarded in the objective function (Namburu, Samayamantula and Edara 2017; Zheng *et al.* 2017; Aljebory and Mohammed 2018). Modification of FCM objective functions with spatial information is proposed by researchers (Zheng *et al.* 2017; Aljebory and Mohammed 2018; ShanmugaPriya and Valarmathi 2018) to ameliorate the performance of conventional FCM.

3.7.3 Density-based clustering

Density-based clustering is developed by Ester *et al.* (1996) for determining clusters in spatial databases. In these algorithms, the data points are grouped based on density region, connectivity, and region boundary (Fahad *et al.* 2014; Benabdellah, Benghabrit and Bouhaddou 2019). Clusters are related dense component that grows in the direction of density and the density of points within a cluster will be greater than those outside of it (Sarmah and Bhattacharyya 2012). Density Based Spatial Clustering of Applications with Noise (DBSCAN), Mean Shift (MS) and spectral-based clustering are the three popular density-based clustering algorithms used in image segmentation. DBSCAN is a notable density-based clustering algorithm that locates the region of high density that are separated by a region of low density (Dhua *et al.* 2015). In DBSCAN a new cluster is formed based on two parameters known as epsilon (Eps) which is the radius of the cluster and a minimum number of points ($MinPts$) within the cluster. MS is non parametric density-based clustering algorithm introduced by Fukunaga and Hostetler (1975) to discover maxima of a density function for feature space analysis. Comaniciu and Meer (2002) extended this algorithm to detect image nodes resulting in homogenous region centers. It can be used for clustering any arbitrarily shaped object without prior knowledge of cluster numbers (Dhua *et al.* 2015).

3.7.4 Grid-based clustering

In grid-based clustering the data space is divided into fixed cell counts to form the grid structure and on which multi-resolution clustering is performed (Sarmah and Bhattacharyya 2012; Ramesh and Nandhini 2017; Benabdellah, Benghabrit and Bouhaddou 2019). Wave cluster is a grid-based clustering algorithm developed by Sheikholeslami, Chatterjee and Zhang (2000). This technique creates a standard two-dimensional grid on the data to represent the data points in each cell. These algorithms aim to detect a set of clusters from a given set of spatial objects, $O_{j,}1 \leq i \leq N$. Data is summarized into a grid structure by applying multi-dimensional grid structure on the data space.

3.7.5 Model-based clustering

In the model-based technique mixture of a probability distribution is used to generate the data and clusters are formalized based on this probability distribution (Ramesh and Nandhini 2017). Multivariate normal distribution with unknown parameters and class labels are used to generate the clusters and parameters are repeatedly adjusted to achieve an improved fit between the data points and

model (Wehrens *et al.* 2004). Statistical and Neural Networks are the two common methods employed in model-based clustering techniques (Benabdellah, Benghabrit and Bouhaddou 2019). In the statistical approach, clusters are determined using probability measures. A neural network uses a set of inputs and output units with interconnected weights. Expectation-Maximization and Self-Organizing Maps are the example for statistical and Neural Network based approaches respectively.

Expectation-Maximization (EM) is an iterative approach proposed by (Dempster, Laird and Rubin 1977) to compute the maximum-likelihood estimates. EM is one of the popular algorithms used for density estimation of data points in unsupervised clustering (Naik and Shah 2014). EM finds the maximum likelihood estimate of parameters in a statistical model of a given data set where the model depends on the unobserved latent variables. It iteratively estimates the unknown model parameters in two steps, the Expectation (E) and the Maximization (M) (Fahad *et al.* 2014; Naik and Shah 2014; Dhanachandra and Chanu 2017). A Self-Organizing Map (SOM) is a type of neural network suitable for the unsupervised learning method developed by Kohonen (1990). SOM combines competitive learning with dimension reduction by smoothing the clusters to a priori grid (Chebbout and Merouani 2012). Self-Organizing means the neural network learns itself through unsupervised learning without any supervision and Map means SOM networks try to map their weights to match the given input data (Kohonen 1990).

3.8 Generating clusters in image segmentation

Generating clusters for image abstraction is an important step to reduce the computational complexity of image segmentation. Many pixel-level image segmentation methods endure high computational complexity and the exclusion of spatial information causes an inaccurate segmentation resulting in many inconsistent regions (Jing, Jin and Xiang 2022). Various levels of image abstraction have been used in image segmentation to tackle these issues. The concept of a group of pixels, known as superpixel is introduced by Ren and Malik (2003) as an alternate method for dividing the image into perceptually homogenous regions. Pixel groupings are based on intra-region and inter-region similarity. The former indicates that the pixels in a region are similar in terms of color, intensity, or texture, that pixels in different regions are dissimilar and the latter emphasis that the pixels of different regions dissimilar. Owing to the merit of mitigation of computational complexity and the consideration of spatial information, aggregation of pixels is employed to provide the cluster cues to guide the segmentation of the region of interest. The clustering process partitions the image pixels into regions

of pixels or superpixels to represent the digital image in a more simpler and abstract format for an easier and more precise analysis (Ghosal *et al.* 2020). Hence many clustering techniques such as K-Means (Singh, Arya and Agrawal 2017; Qian *et al.* 2019; Singh *et al.* 2019), FCM (Wu *et al.* 2020), DBSCAN (Wang and Zhang 2021), Mean Shift (Liu *et al.* 2012; Zhou and Liu 2015), and histogram-based clustering(Joseph and Olugbara 2021) methods have been widely employed to aggregate pixels for image abstraction.

Simple Linear Iterative Clustering (SLIC) based on the K-Means technique proposed by Achanta *et al.* (2010) is a representative superpixel algorithm widely used for image abstraction because of its simplicity. This approach adapts the K-Means clustering and the local clustering of pixels is achieved by combining color similarity and image plane space. However, finding an optimum superpixel granularity is a challenging task for this approach as the efficiency and robustness of segmentation are highly dependent on the superpixel granularity (Abd Elaziz *et al.* 2021; Jing, Jin and Xiang 2022). Linear Spectral Clustering (LSC) is a superpixel algorithm developed by Chen, Li and Huang (2017) based on weighted K-Means clustering that maps each image pixel to weighted points in ten-dimensional feature space by kernel functions to generate the patches of homogenous pixels.

Recently Wang and Zhang (2021) applied DBSCAN to aggregate pixels based on a minimum contour density to generate clusters of images for image abstraction. Density Peaks clustering (DPC) based on DBSCAN is a widely accepted image superpixel generation (Abd Elaziz *et al.* 2021; Wang and Zhang 2021). Cluster centers are selected based on a decision graph that shows the local density of each data point and the distance from points with higher density. Points with the highest peaks of density than the others in their neighbors are considered as the cluster centers and assumed that the cluster center is far from other cluster centers. The remaining points are allocated to the nearest highest density points. Regardless of the efficiency of this method, the manual determination of cluster centers, determination of cut of distance, and the inability to handle clusters with more than one high-density point are the limitation of this approach (Yuan *et al.* 2021).

Jia *et al.* (2019a) adapted the Mean shift clustering algorithm to generate homogenous regions for image representation. In this approach modes of color or intensity of the image, and pixels are identified by an iterative mode-seeking procedure for locating the local maxima of a density function (Wang *et al.* 2017c). Wu *et al.* (2020) applied Fuzzy C-Means clustering to generate superpixels by integrating the local spatial information to the objective function of FCM. Clustering methods such as

K-Means, Fuzzy C-Means, DBSCAN, and Mean Shift have been extensively utilized to divide an image into multiple regions or superpixels. Region generation based on these classic clustering methods has suffered from high computational complexity because of multiple iterations and they are not adequate for diversified classes of images (Lou *et al.* 2020; Zhang *et al.* 2020e). Identification of an optimum cluster count for an accurate and stable segmentation is the limitation of many of the clustering techniques and the manual determination of the initial luster count cause instability and subjectivity in segmentation results (Jing, Jin and Xiang 2022). The automatic detection of region count is a difficult problem because of the diversity in color images. Moreover, the number of homogenous regions in an image is unknown.

3.9 Region of interest detection

Homogenous regions in an image can be clustered more precisely by including salient features of the image pixels. Salient object detection models attempt to extract visually distinguishable points and regions from a visual scene. The saliency measure indicates the distinction of objects to their background by forming a saliency map that states how a pixel or region pops out from its background (Wang *et al.* 2016; Ye *et al.* 2017; Wu *et al.* 2021). The saliency model classifies the image pixels into foreground and background, so saliency detection is considered a two-class clustering.

It is evident from the literature that a plethora of saliency models (Itti, Koch and Niebur 1998; Harel, Koch and Perona 2007; Hou and Zhang 2007; Zhang *et al.* 2008; Achanta *et al.* 2009; Seo and Milanfar 2009; Rahtu *et al.* 2010; Duan *et al.* 2011; Liu *et al.* 2011; Murray *et al.* 2011; Tavakoli, Rahtu and Heikkilä 2011; Goferman, Zelnik-Manor and Tal 2012; Erdem and Erdem 2013; Jiang *et al.* 2013a; Li *et al.* 2013b; Yang, Zhang and Lu 2013; Yang *et al.* 2013; Lou, Ren and Wang 2014; Cheng *et al.* 2015; Mohammadpour and Mozaffari 2015; Sun, Lu and Liu 2015; Wang *et al.* 2015; Zhou *et al.* 2015; He, Lau and Yang 2016; Kim *et al.* 2016; Yang and Yang 2017; Olugbara, Taiwo and Heukelman 2018; Wu *et al.* 2018; Liu and Yang 2019; Lopez-Alanis *et al.* 2019; Lou *et al.* 2020; Zhang *et al.* 2020e; Joseph and Olugbara 2021; Wu *et al.* 2021; Li *et al.* 2022) have been proposed by researchers in the past two decades. Among these models, bottom-up saliency detection models are ubiquitous because of their simplicity and computational effectiveness.

3.9.1 Bottom-up saliency detection

Bottom-up saliency detection models are inspired by the human visual system and are solely directed by the image properties. These fast and saliency models can be categorized into eye fixation prediction models (Itti, Koch and Niebur 1998; Harel, Koch and Perona 2007; Han *et al.* 2015), and Salient Object Detection (SOD) models (Lou, Ren and Wang 2014; Kim *et al.* 2016; Ji *et al.* 2019; Liu and Yang 2019; Tang *et al.* 2019; Lou *et al.* 2020; Xia *et al.* 2020). These two types of models are based on the definition of saliency as "where people look" or "which objects stand out" (Borji 2014). The former model focuses on predicting the location where the people are freely seeing natural scenes, while the latter aims to detect and segment the salient objects. SOD has become more popular than eye fixation models due to its capability in recognizing the features of salient objects than only predicting their locations (Singh, Kumar and Singh 2020; Umeki *et al.* 2020). SOD models target finding the salient regions which attract human attention and extract it from the background by exploiting contrast in the various features such as color, texture, and location. Usually, salient regions are regarded as perceptually distinct image components that contrast with their backgrounds (Gupta *et al.* 2020). This dissimilarity, rarity, or uniqueness has been comprehensively investigated in SOD by exploring mainly the contrast features of the image elements such as pixels or groups of pixels. Several advancements have been achieved in bottom-up SOD models by exploring heuristic features such as contrast, texture, and location for saliency detection (Gupta *et al.* 2020; Ullah *et al.* 2020). Contrast features have become more prominent among these because they are a better reflection of how the human visual system prioritizes high contrast areas. Methods based on contrast prior are employed either locally or globally.

Local contrast-based methods assess the rarity of image units (pixels, blocks, superpixels, or regions) in their immediate neighborhood or surrounding regions. In the model proposed by Harel, Koch and Perona (2007) local uniqueness maps from various feature channels are nonlinearly integrated to highlight the most attractive region. Center-surround local contrast using the difference of mean filter for the detection of the salient region was proposed by Achanta *et al.* (2008). In this approach, the Euclidean distance between the average feature vectors of the center and the surrounding regions is used to compute the center-surround color contrast. A center-surround model that computes pixel-level saliency using the self-resemblance metric was proposed by Seo and Milanfar (2009). This method employs local steering kernels and matrix cosine similarity-based nonparametric kernel density to distinguish a pixel from its surroundings. A pixel-wise center-surrounds local saliency model was proposed by Rahtu *et al.* (2010) using a probabilistic framework merged with illumination features and

color contrast and optical flow to formulate the saliency measures of each pixel. This method uses a sliding window to analyze the entire image to calculate the pixel level saliency. According to experimental findings, this method produces consistent results on specific datasets. The method, however, struggles to distinguish objects from the background when there is a lack of clear visual contrast between the background and foreground pixels. Murray *et al.* (2011) presented a local central surround contrast-based saliency map employing inverse wavelet transform for each color channel at a multi-spatial scale. Tavakoli, Rahtu and Heikkilä (2011) presented a center-surround method that uses kernel density estimation and sparse sampling to compute saliency by combining center bias with local color contrast information. The model proposed by Zhou *et al.* (2015), integrated compactness prior and local contrast with the diffusion process employing manifold ranking.

The diffusion process was employed to mitigate the limitation of local contrast that emphasizes the object borders rather than the entire region. The improper suppression of salient regions, particularly on images with varied salient object attributes, can result from considering only the local relevance of surrounding regions (Luo *et al.* 2018). Lou *et al.* (2017) proposed a local contrast-based method for detecting small targets by calculating the contrast between the targeted small regions and the surrounding area. Large salient regions can be easily removed from the local contrast-based methods because of the limited spatial neighborhood consideration (Gupta *et al.* 2020). Further, the challenges linked to low saliency at the object interior and the high saliency at the object boundaries lead to a significant increase in the salient object detection models based on global contrast features.

Global contrast-based methods are proficient in uniformly emphasizing the entire salient region by allocating equivalent salient values across similar salient regions and have been widely used in salient object detection. The frequency-tuned global contrast-based method is proposed by Achanta *et al.* (2009) using the Euclidean difference between pixel features and the mean color feature in the L*a*b* color model to compute the pixel level saliency. Cheng *et al.* (2015) introduced color histogram as global contrast and used Gaussian Mixture Model to describe the weighted sum of the color difference of the contrast of the region to other image regions. According to Cheng *et al.* (2015) high contrast to a neighborhood region exhibits greater saliency than high contrast to distant regions. Hence to increase the effect of surrounding regions they integrated the spatial relationship of regions to compute saliency. An essential complement to the contrast feature is the distribution of spatial compactness (Zhou *et al.* 2015).

Despite the significance of contrast-based techniques for saliency detection, these models are nonetheless susceptible to significant drawbacks. For example, attenuated object saliency values are the main constraint of local contrast-based methods. However, this problem is alleviated in global contrast-based methods, yet highlighting the salient region uniformly is still a problem faced by global contrast-driven methods. Another issue of global contrast-based methods is that they incorrectly highlight the background area more than the salient object, especially in images with complicated backgrounds or huge salient objects (Li *et al.* 2018a). Recently Lou *et al.* (2020) used global color cues based on statistics and contrast of color names to get beyond the restriction of simply utilizing the surroundedness cue. The main flaw in this method is its inability to recognize the salient objects connected with the image borders.

Recently methods integrating local and global features have been suggested to improve the detection of salient regions. For example, the context-aware saliency detection model was introduced by Goferman, Zelnik-Manor and Tal (2012) that integrates local and global features to compute the saliency of the patches. Liu and Wang (2015) proposed a model that combined both local and global methods for computing saliency. The authors used local contrast difference features to get the attention map based on the block variance map and then global color contrast is calculated based on attended and non-attended regions. Then the local and global contrast features are used to compute the saliency. A learning-based method that combines both global and local saliency features is proposed by Kim *et al.* (2016). Global saliency is computed using high dimensional color transform by linearly combining RGB, L*a*b*, and HSV color models. The color contrast between the superpixels and the relative location of the superpixels are further utilized for local saliency computation. Ishikura *et al.* (2018) proposed a salient object detection model that employs multiscale extrema of local perceptual color difference combined with global measure rarity and global center bias to distinguish large salient objects.

It is important to note that the contrast prior models perform well on images with substantial color contrast differences between foreground and background regions. However, when there is no obvious visual contrast between the foreground and background regions, these models struggle to distinguish objects from the background (Liu and Wang 2015). Hence it is essential to include more information on foreground and background regions to get a model that is suitable for diverse image categories. The application of appropriate prior knowledge to detect saliency has achieved greater importance and different saliency methods define the prior knowledge from a diverse perspective. Saliency detection

can perform better with appropriate prior knowledge, but the results are not accurate on images with complicated backgrounds and salient objects with variable shape, size, location, and appearance. For instance, when the background is framed close to the image center or when salient objects are close to the image boundary, center prior models are inadequate to track the salient objects (Zhou *et al.* 2015; Afzali *et al.* 2018; Li *et al.* 2018a; Zhou *et al.* 2018b).

Methods that take advantage of background and connectivity priors suffer from the improper suppression of salient objects that significantly touch the image boundaries (Jiang *et al.* 2013a; Zhang, Zhang and Guo 2016; Zhou *et al.* 2018b; Xia *et al.* 2020). Some methods are ineffective at detecting larger salient objects that overlap the foreground and background because they treat the larger objects as background and achieve low saliency detection accuracy (Ishikura *et al.* 2018). Color contrast prior is inadequate to effectively detect low contrast salient objects from complex background scenes. This stresses that although there has been noticeable progress, salient object recognition is still a difficult problem because of the variation, inherent complexity, and unpredictability of salient regions in the image (Zhou and Yang 2014; Zhang, Zhang and Guo 2016; Pahuja *et al.* 2019).

3.9.2 Top-down saliency detection

Deep learning-based methods are the leading top-down salient object detection methods. For example, the saliency detection method proposed by Yan *et al.* (2020) aggregated the DNN sparse labeling and dense labeling schemes to extract the hybrid image features by multiscale kernels. Nasiripour, Farsi and Mohamadzadeh (2019) proposed a salient object detection method using K-Means Singular-Value Decomposition (K-SVD) training and sparse coding by combining the top-down and bottom-up image features based on superpixel abstraction. In the model proposed by Li *et al.* (2017b) a deep neural network namely LCNN that embedded high-level features captured using CNN and contrast and spatial information-based low-level features for detecting the saliency. And the final saliency score is computed using the confidence score generated by SVM discriminative learning method.

A deep network and aggregation saliency prediction model that exploits the in-network feature hierarchy of a convolutional network is proposed by Liang, Liu and Ma (2019). And Stochastic Gradient Descent (SGD) is used for training the network. A deep learning-based saliency model that modeled the semantic features of the salient objects using a Fully Convolutional Neural Network (FCNN) is developed by Li *et al.* (2016). This data-driven approach used non-linear regression to refine

the final saliency map. A multi-context deep learning framework that integrates global and local contexts using convolutional neural networks is proposed by Zhao *et al.* (2015b). The use of semantic information and prior knowledge of the scene helps to achieve superior performance by these models but, increased computational complexities because of the extensive training and testing time are the major challenges of deep learning-based models (Cai *et al.* 2020). Construction of a large-labeled dataset for saliency detection is a strenuous task and also deep learning-based models require high-performance computing devices for training and testing which are retrained these models from using in real-time applications (Wang *et al.* 2021b; Zhang and Wang 2021; Wang *et al.* 2022a).

3.10 Clustering by thresholding

The thresholding effect clusters the segmented image into two clusters of foreground and background (Jain, Murty and Flynn 1999) and has been widely used in the image segmentation process to separate the foreground and background regions (Ananthi and Balasubramaniam 2016; Wang and Cao 2019b; Hafeez, Yan and Guoliang 2021). One of the most popular techniques for thresholding is Otsu thresholding (Otsu 1979) which has been exploited by the segmentation methods because of its simplicity, adaptability and robustness (Sheng *et al.* 2016; Fan *et al.* 2017; Zhang *et al.* 2018a; He, Guo and Yuan 2020; Hu *et al.* 2020; Makem and Tiedeu 2020; Qiu *et al.* 2020; Chen *et al.* 2021). The Otsu method performs non-parametric, unsupervised, and automatic global thresholding for image segmentation by considering foreground and background classes of pixels (Bangare *et al.* 2015).

In the Otsu technique, the pixels of a given image are represented in gray levels, $L = [1,2,..,L]$ and the number of pixels at level i is denoted by n_i, and the total number of pixels, $N = \sum_{i=1}^{L} n_i$. The gray level histogram is normalized and represented by the probability distribution as below:

$$p_i = n_i / N$$

An optimum threshold level k is selected by maximizing the between-class variance to cluster the pixels into two classes C_0 and C_1 (foreground and background or vice versa) where C_0 and C_1 denoted pixels with levels $L = [1,2,...,k]$ and $L = [k+1, k+2,...,L]$ respectively. The threshold value is calculated based on the zeroth and the first-order cumulative moments of the gray level (Otsu 1979). The intrinsic benefit of Otsu thresholding is that since it applies thresholding on image intensity, the geometric properties of an image object have no impact on its performance (Goh *et al.* 2018).

3.11 Image post-processing

Post-processing is a crucial stage in image segmentation to improve the quality of segmentation by eliminating the undesirable artifacts that may be developed during the segmentation process (Furtado 2021). Generally, it uses simple mathematical morphological operations to remove imperfections and noisy pixels. The concepts of mathematical morphology were introduced by Georges Matheron and Jean Serra in the mid-sixties (Serra 1986; Matheron and Serra 2002). Set theory is the language of mathematical morphology and is based on sets, integral geometry and mesh algebra (Serra 1986). It has gradually developed into a powerful tool for image analysis and has been broadly used for image processing and analysis (Garnavi *et al.* 2011; Bi *et al.* 2016; Agarwal *et al.* 2017; Jahanifar *et al.* 2017; Olugbara, Taiwo and Heukelman 2018; Patiño, Avendaño and Branch 2018; Ross-Howe and Tizhoosh 2018; Zhang *et al.* 2018a; Guarracino and Maddalena 2019; Khan *et al.* 2019; Li *et al.* 2019b; Ünver and Ayan 2019; Devi, Singh and Laskar 2020; Hu *et al.* 2020; Lou *et al.* 2020).

The process of morphology is defined in terms of sets and image processing it is performed with the sets of pixels of objects and the sets of pixels of a structuring element. A structuring element is a shape defined in terms of coordinates of a set of discrete points relative to some origin and the morphological operations are controlled by the shape of the structuring element. Normally objects are represented by the foreground pixels and the structuring element is by both foreground and background pixels (Gonzalez and Woods 2018). Morphological transformation is well known for eradicating isolated individual pixels, background noise and filling holes or disparate pixels (Setitra and Larabi 2014). In image processing, the morphological transformation of an image is performed with the image being processed and the structuring element with two basic operations, erosion and dilation.

Erosion is the morphological transformation that combines two sets by Minkowski subtraction of set elements. Thus the erosion of an image, 'A' by a structuring element, B is the set of all points, z such that B translated by z is contained in A and this process is defined as in Equation 3.1. Erosion shrinks the foreground objects while increasing the size of the background region.

$$A \ominus B = \{z|(B)_z \subseteq A\} \tag{3.1}$$

Dilation combines the two sets by Minkowski's addition of set elements. Thus the dilation of an image, 'A' by a structuring element, B is defined as in Equation 3.2. The dilation of A by B is the set of all displacement z such that the foreground element of B overlaps with at least one element of A.

$$A \oplus B = \{z | (B)_z \cap A \neq \emptyset\} \quad (3.2)$$

The combination of dilation and erosion can produce more complex morphological transformations. These can be used to recover objects with connected components of comparable intensity values while simultaneously maintaining information such as contour features, shape, and intensity and eliminating background noise (Vincent 1993; Zhang *et al.* 2018a). Opening and closing are the two most widely used operations and are defined in terms of erosion and dilation. An opening operation (Equation 3.3) is defined as an erosion followed by dilation using the same structuring element for both dilation and erosion. Opening operations are generally employed to smoothen the object counters, break narrow lines and remove thin protrusions. Closing operation (Equation 3.4) is the reverse of opening and it eliminates tiny holes and fills in gaps by merging tune breaks and thin gulfs as a result of a dilation followed by erosion. This operation helps to brighten the small objects and fill the small holes while maintaining the shape and size of the original objects. The opening and closing operations are defined using Equations 3.3 and 3.4 respectively.

$$A^{\circ}B = (A \ominus B) \oplus B \quad (3.3)$$

$$A \cdot B = (A \oplus B) \ominus B \quad (3.4)$$

A post-processing stage separates the classes into connected regions and removes all artifacts that occurred during the segmentation process.

3.12 Chapter summary

This chapter explores fundamental principles of segmentation, provides in-depth information on several methods used in image segmentation, and covers the key phases of the segmentation process. A comprehensive explanation of common techniques used for image preprocessing, color model transformation, segmentation methods based on clustering and saliency and the post-processing operations were also presented. The methods and materials used to accomplish the research objectives of this study will be covered in the following chapter.

CHAPTER FOUR: METHODS AND MATERIALS

This chapter presents the methods and materials used for obtaining the study objectives stated in chapter 1. The primary method proposed in this study is the color histogram clustering algorithm which determines the optimum cluster count and integrates color contrast, contrast prior, center prior, and spatial features for efficiently segmenting the salient region from diverse classes of images. The proposed image segmentation algorithm is presented in terms of a flowchart, mathematical formulation, and algorithmic explanation. Further, the statistical method used to investigate the image preprocessing effects on algorithm performance is presented. The evaluation tools, image datasets, and evaluation metrics that were used to rate the effectiveness of the proposed algorithm are then discussed.

4.1 Methods

The newly created segmentation algorithm, which makes use of the cooperation of clustering and saliency, is the main method used in this work. The proposed segmentation algorithm and the approaches used for the investigation of the effect of preprocessing on the proposed algorithm are also explained in this section.

4.1.1 Color histogram clustering method

The novel regional Color Histogram Clustering (CHC) method is presented in this study for the detection and segmentation of salient objects in Red, Green, and Blue (RGB) images. The histogram-based clustering algorithm uses the Quantized RGB (QRGB) color image as the input to decrease the number of colors in the input image. The several color models used in salient object detection and segmentation methods comprise RGB (Li *et al.* 2013b; Kim *et al.* 2016; Zheng *et al.* 2018; Hu *et al.* 2020; Huang *et al.* 2020; Lou *et al.* 2020), HSV (Zheng *et al.* 2018; Feng *et al.* 2020), HSI (Sheng *et al.* 2016), L*a*b* (Lou, Ren and Wang 2014; Sun, Lu and Liu 2015; Wang *et al.* 2015; Yadav, Bansal and Sunkaria 2015; Sethy, Negi and Bhoi 2017; Zhou *et al.* 2017; Ishikura *et al.* 2018; Wu *et al.* 2018; Liu and Yang 2019; Lopez-Alanis *et al.* 2019; Xu, He and Lv 2019; Kompella and Kulkarni 2020; Jian *et al.* 2021; Oskouei *et al.* 2021) and combination of color models (Abdul-Nasir, Mashor and Mohamed 2013; Li *et al.* 2013b; Kim *et al.* 2016; Wang *et al.* 2017b; Zheng *et al.* 2018; Ndayikengurukiye and Mignotte 2022). The L*a*b* color model was utilized in this study to extract color features due to its perceptual homogeneity, while the QRGB color model was used for clustering (Lou, Ren and Wang 2014; Cheng *et al.* 2015; Han *et al.* 2017).

Literature has shown that quantization in the RGB color model generally outperformed quantization in the L*a*b* color model (Zhou *et al.* 2018a). Instead of using the quantized RGB, the original RGB color model was converted into the L*a*b* color model to reduce the impacts of quantization error. Due to its inherent benefits of perceptual homogeneity, the L*a*b* color model was chosen for color feature extraction in the range of [0, 1] to reduce the impact of any potential dominant colors (Sun, Lu and Liu 2015; Nouri, Kazemi and Danyali 2018). The proposed algorithm efficiently calculates pixel-level saliency scores by utilizing color contrast, contrast ratio, spatial feature, and center before regional color and spatial features. The method is encompassed four essential steps of input image segmentation into regions using color histogram clustering, calculation of region saliency scores, silhouette object segmentation, and post-processing of the computed saliency map. Figure 4-1 illustrates the outline of the proposed algorithm for detecting and segmenting salient objects.

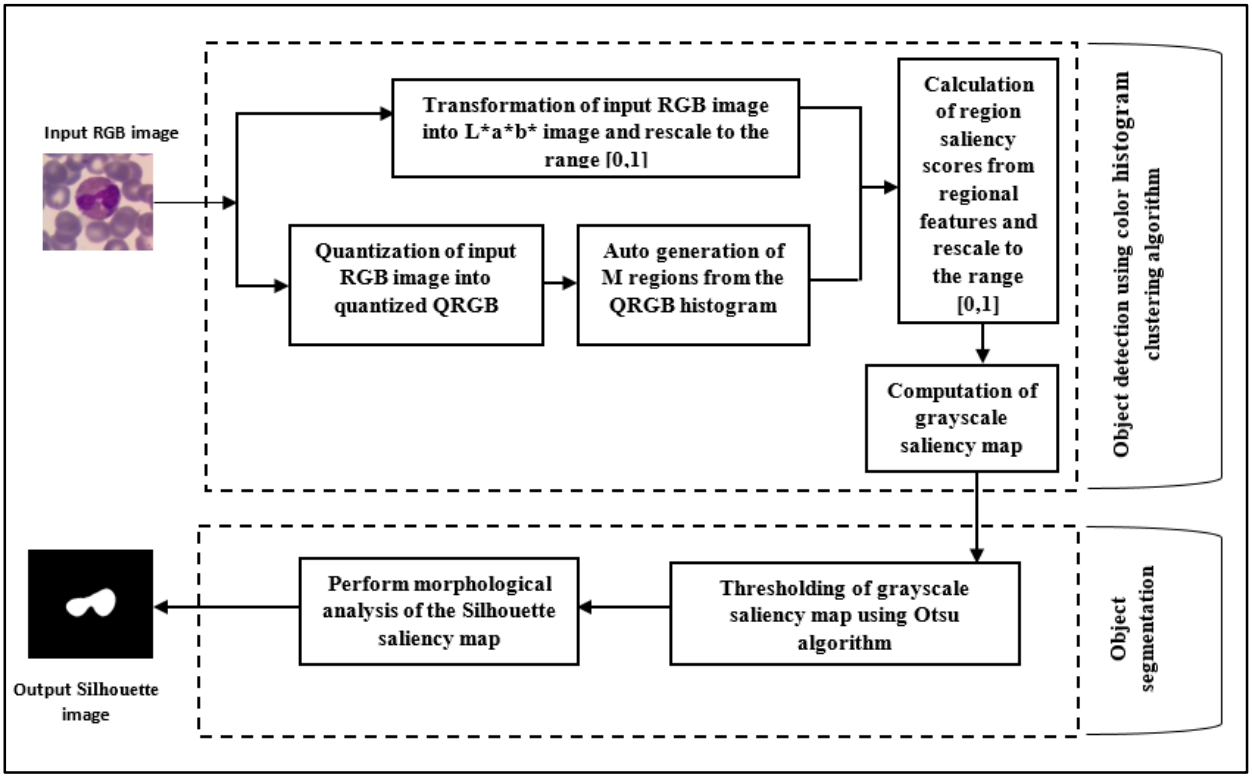

Figure 4-1 Flowchart of the proposed image segmentation algorithm

4.1.2 Segmentation of input image

An acceptable step in a saliency detection process is the segmentation of an image into regions of similar pixels. The purpose is to minimize the computational complexity of the image data because pixels in a region have similar color characteristics (Zhang, Zhang and Guo 2016). It is common

practice to divide an image into multiple regions using a multilevel segmentation method including superpixel-based clustering, K-Means clustering, DBSCAN, and mean-shift clustering. Among these methods, superpixel-based segmentation is frequently employed (Jiang *et al.* 2013a; Li *et al.* 2013b; Yang, Zhang and Lu 2013; Zhou *et al.* 2015; Jiang, Zhong and Lin* 2017; Hu *et al.* 2018; Zhou *et al.* 2018b; Ji *et al.* 2019; Liu and Yang 2019; Xu, He and Lv 2019; Kompella and Kulkarni 2020; Jiang *et al.* 2021; Wu *et al.* 2021). Superpixel-based segmentation methods, however, have suffered from high computational costs due to repeated iterations and thus are inadequate for a variety of image classes (Liu and Yang 2019; Zhang *et al.* 2020e). The calculation of the ideal number of superpixels is a further unavoidable issue with the superpixel-based methods. Due to the diversity of color images and information, the automatic detection of region count is a challenging problem. The quantity of homogenous regions in an image is also unclear. Small and large region counts may cause under, and over-segmentation of the images, which may result in uneven highlighting of the salient regions. The characteristics of the color histogram to generate homogenous regions served as inspiration for the regional color histogram clustering proposed in this study. Due to its ability to offer global statistics of color images that define the proportion of various color features, a color histogram is frequently employed in computer vision algorithms (Liu *et al.* 2019). The segmentation approach is accomplished by the subprocesses of color quantization and region generation.

4.1.2.1 Color Quantization

The true-color image has a maximum set of $256^3 = 16{,}777{,}216$ colors that are typically more than the total number of pixels in an image (Márquez-de-Silva, Felipe-Riverón and Fernández 2008; Feng *et al.* 2015). Less dominant colors can be omitted from saliency detection because extremely infrequent colors are insignificant for emphasizing salient locations (Lou, Ren and Wang 2014). Color quantization is a popular technique for combining less prominent colors with dominant colors to significantly reduce the computational complexity of image processing (Feng *et al.* 2015; Cheng and Wei 2019). The minimum variance method (Lou, Ren and Wang 2014) or pixel intensity clustering algorithm (Olugbara, Adetiba and Oyewole 2015) can be successfully applied to achieve color quantization. However, the 'imquantize*'* built-in color quantization function in MATLAB (2019a, The MathWorks, Inc., Natick, Massachusetts, United States) was successfully employed to get the prominent colors of the input RGB image. The function quantizes an input image into the desired number of colors using the multilevel image thresholding method of Otsu. The individual color channels of red (R), green (G), and blue (B) of the RGB color model was quantized into QR, QG, and

QB at the level of 8 to realize a maximum of 512 colors. This figure represents the maximum number of 512 possible regions in a color image. Using Equation 4.1, the quantized intensity levels are combined to provide the index (Q_{RGB}) of a quantized RGB color in the color palette.

$$Q_{RGB} = w_r * Q_r + w_g * Q_g + w_b * Q_b \tag{4.1}$$

where $w_r = 8$, $w_g = 64$, and $w_b = 1$ are the respective weights of R, G, and B colors. The human visual system is more sensitive to the color green than other colors, hence the green channel was given the highest weight value (Yu, Zhang and Wang 2015).

4.1.2.2 Color Histogram

Based on the quantized RGB color model, a global color histogram with bins is calculated utilizing each pixel in the input image. By weighing the trade-off between performance and computational complexity, the 8 × 8 × 8 quantization system with 512 bins is ideal (Lee, Xin and Westland 2005). Following this line of reasoning, it has been decided that the parameter "q=8" is adequate for successful color quantization. The global histogram was employed to generate regional clustering for image abstraction. The histogram bins with pixels are chosen as representative regions, and the bins without pixels are rejected. As a result, a data structure with 'M' entries is created to hold the features of the pixels that belong to each region. This method indicates that each region is characterized by a feature vector that contains the average color pixel intensity, average color pixel coordinates, and distance between the regional center and the image screen center.

4.1.3 Calculation of region saliency

The global color contrast $CC(r_i)$ of a region r_i is determined in terms of the region weight W_i and color difference of a region to all other regions in the image as in Equation (4.2).

$$CC(r_i) = \sum_{j=1}^{M} W_j \left\| (L_i, a_i, b_i) - (L_j, a_j, b_j) \right\|_2 \tag{4.2}$$

where (L, a, b) is the color value of the region in L*a*b* color model, $\| . \|_2$ indicates the L_2 norm, and M is the number of regions automatically detected. There will be a maximum of 8 colors in an image, assuming each image channel of the image has 2 distinct intensity levels. The number, M of

the possible colors or regions in a quantized color image, will lie in the range of [8, 512]. The regional weight function $W=(W_1,...,W_M)$ is integrated into the region saliency calculation process. The weight function will account for the contribution of high saliency by larger regions than by the smaller ones. The weight of a region is calculated based on the relative probability of the pixels in the region to emphasize the color contrast of larger regions (Lou, Ren and Wang 2014; Cheng *et al.* 2015), as defined by Equation (4.3).

$$W_i = \frac{f_i}{f} \tag{4.3}$$

where f_i is the frequency of the pixels occupied in each region r_i and f is the total number of pixels in the image. The spatial contrast function $SC(r_i)$ integrates the global color contrast with the spatial feature and color ratio of a region (r_i) as follows in Equation (4.4):

$$SC(r_i) = W_i CC(r_i) + \sum_{j=1}^{M} W_j \phi(r_i, r_j) \exp(-DS(r_i, r_j)) \tag{4.4}$$

In sharp contrast to the work of Lou, Ren and Wang (2014) utilized regional saliency differences as a weighting coefficient to suppress the effect of non-salient regions, the proposed algorithm utilizes a more resilient function, $\phi(r_i, r_j)$ based on the contrast ratio given by Equation (4.5). The contrast ratio is an important aspect of image quality that measures the difference between the maximum and minimum brightness of an image. In the context of this study, it measures the difference between the maximum and minimum brightness of regions in an image.

$$\phi(r_i, r_j) = \left(\frac{CC(r_i) + 0.05}{CC(r_j) + 0.05} \right) \tag{4.5}$$

The significance of center prior in saliency detection as given by Equation (4.6) has been highlighted in literature following the fundamental assumption that salient objects are framed near the image center while background pixels are distributed at the image borders (Lou, Ren and Wang 2014; Zhou *et al.* 2015; Jiang, Zhong and Lin* 2017; Afzali *et al.* 2018; Liu and Yang 2019). It is usually formulated and extensively used in literature as a Gaussian distribution (Li *et al.* 2013b; Yang, Zhang and Lu 2013; Lou, Ren and Wang 2014; Zhou *et al.* 2015; Ishikura *et al.* 2018). The region saliency score $CS(r_i)$ is obtained in terms of spatially weighted color contrast and the Euclidean distance

between the region spatial center and the image screen center. This is to integrate the center prior with color contrast, contrast ratio, and spatial feature using Equation (4.6).

$$CS(r_i) = SC(r_i) * \exp(-DS(S(r_i), C)/\alpha^2) \tag{4.6}$$

where $S(r_i)$ is the spatial center of a region and C = (0.5, 0.5) is the image screen center. Since salient objects are always not positioned at the image center, the concept of center prior can lead to the exclusion of salient objects located at the image boundary or inclusion of the background region (Li *et al.* 2013b; Lou, Ren and Wang 2014; Fareed *et al.* 2018). This can occur, especially when an object possesses multiple colors such that object colors at the image center are different from those in the background. The parameter $\alpha \in [0.1, 1.0]$ is incorporated into the function to strengthen the center prior. Even though the function can compute a low saliency score for a region around the boundary, an appropriate value α can make adequate salient objects more salient, regardless of their positions. In addition to the color contrast features, spatial features play a significant role in human attention, and the use of spatial coherence in saliency computation is widely accepted by many researchers (Duan *et al.* 2011; Lou, Ren and Wang 2014; Cheng *et al.* 2015; Zhou *et al.* 2015; Kim *et al.* 2016; Liu and Yang 2019). The spatial distance $DS(r_i, r_j)$ between two regions is computed using Equation (4.7).

$$DS(r_i, r_j) = \left\| \left(C_i^x, C_i^y\right) - \left(C_j^x, C_j^y\right) \right\|_2 \tag{4.7}$$

where $\left(C_i^x, C_i^y\right)$ is the spatial center of a region r_i that is computed by averaging the x and y coordinates of pixels in the region. The regional saliency score generated is normalized to the range of [0, 1] before assigning the pixel level saliency. The saliency score of each pixel is assigned by the saliency score of the respective region to obtain the saliency map, C_{Map} as shown in Equation (4.8). The assignment is based on the assertion that pixels belonging to the same region have the same saliency.

$$C_{Map} = CS(r_i) \tag{4.8}$$

4.1.4 Segmentation of silhouette objects

The Otsu thresholding technique is integrated to segment the silhouette objects from the grayscale saliency map. The MATLAB implementation of the Otsu thresholding is applied in this study

to complement the functioning of the color histogram clustering algorithm. In the segmentation process, the Otsu method applies nonparametric, unsupervised, and automatic global thresholding. A discriminant criterion selects the ideal threshold to optimize the separability of the resulting clusters in a grayscale image. The approach finds the best threshold by using the zeroth-order and first-order cumulative moments of a grayscale histogram. A Silhouette image is generated by dichotomizing the pixels of the input grayscale image into two clusters at a specific scale.

4.1.5 Post-processing of silhouette objects

The post-processing stage is performed to abolish unwanted artifacts that may be present at the saliency detection stage by the quantization error. In this study, morphological reconstruction is used for post-process. A morphological reconstruction is an excellent method for locating objects with connected components that have comparable intensity values while retaining details like contour, shape, and intensity while simultaneously suppressing background noise (Vincent 1993; Zhang *et al.* 2018a). Morphological reconstruction can also reduce the intensity of salient objects by retaining non-black pixels in the background that are not obtrusive (Lou *et al.* 2020). Binary morphological operations of fill and dilation with a disk-shaped structural element of radius 3 are applied to the silhouette map generated by Otsu thresholding of the grayscale saliency map. The image regions with an isolated area lesser than 30% are eliminated because of the basic assumption that the region of interest are naturally the largest objects in an image.

4.2 Color histogram clustering algorithm

Color Histogram Clustering Algorithm (CHC) depicted in Algorithm 1(Joseph and Olugbara 2022b) provides a complete algorithmic description of the essential steps for segmenting the salient object. The algorithm is generic and usable for other image segmentation tasks. Index, Palette, and Cluster are the important variables used in the algorithm. The Index variable, which has dimensions M by N, holds the index value between 1 and 512 related to the quantized input image. The height and width of the input image are represented by the parameters M and N, respectively. The average L*a*b* color features, average spatial coordinates, and count of homogeneous pixels in a region of the input image are stored by a Palette of dimensions 512 by 5. A cluster is a variable with K by 9 dimensions that stores regional characteristics of a cluster as well as the non-zero elements in the Palette, where K lies in the closed range [8, 512]. The input image quantization process is implemented in Step 2. Steps

3 through 24 implement the regional feature extraction process. The process covers the conversion of the input RGB image to the L*a*b* color image normalized to values in [0, 1]. In step 25, the empty clusters caused by fewer colors determined are eliminated. The computation of the cluster saliency score starts from step 26 to step 50 while the clusters are rescaled to [0, 1] in step 50. Steps 51 to 55 are used to complete the task of assigning the saliency score for each image pixel. Steps 56 and 57 respectively executed the Otsu Silhouette thresholding and binary morphological analysis. The MATLAB (2019a, The MathWorks, Inc., Natick, MA, USA) norm function used in steps 30 and 44 implements the Euclidean distance. The mathematical formulation provided in section 4.1.2 and 4.1.3 serve as the foundation for this algorithmic description of the algorithm.

Algorithm 1 Color Histogram Clustering

Input: M × N × 3 RGB color image (Input), distance scaling parameter (n) such that $0.1 \leq n \leq 1.0$
Output: $M \times N$ Silhouette image (Output), number of clusters automatically detected (K)

```
% Constant parameters
NIC=3; % number of image components
IQL=8; % image quantization level
NCD=IQL^3; % maximum number of desired colors
LCL=1; % lab color light
LCA=2; % lab color A
LCB=3; % lab color B
PXC=4; % pixel x-coordinate
PYC=5; % pixel y-coordinate
PDC=6; % pixel distance to image center
CPC=7; % cluster pixel count
CPL=8; % cluster pixel label
CCC=8; % cluster color contrast
CSS=9; % cluster saliency score
1.      K=0;
2.      Index=ImageQuantization(Input, IQL);
3.      Input=rgb2lab(Input);
4.      Input=rescaleImage(Input, [0,1]);
5.      for x = 1 to M do
6.        for y = 1 to N do
7.          Palette(index(x, y), CPC)=Palette(index(x, y),CPC)+1;
8.          Palette(index(x, y), LCL)=Palette(index(x, y), LCL)+Input(x, y), LCL);
9.          Palette(index(x, y), LCA)=Palette(index(x, y), LCA)+Input(x, y), LCA);
10.         Palette(index(x, y), LCB)=Palette(index(x, y), LCB)+Input(x, y), LCB);
11.         Palette(index(x, y), PXC)=Palette(index(x, y), PXC)+x;
12.         Palette(index(x, y), PYC)=Palette(index(x, y), PYC)+y;
13.       end for
14.     end for
15.     for z=1 to NCD
16.       if Palette(z, CPC) > 0
17.         K=K+1;
```

```
18.             Palette(z, CPL)=K;
19.             Palette(z, PXC)=Palette(z, PXC)/M;
20.             Palette(z, PYC)=Palette(z, PYC)/N;
21.             Palette(z, 1:PYC)=Palette(z,1:PYC)/Palette(z, CPC);
22.             Cluster(K, 1:CPC)=Palette(z, 1:CPC);
23.           end if
24.       end for
25.       Cluster(K+1:NCD, :)=[ ];
26.       Wr=Cluster(:, CPC)/(M*N);
27.       for x = 1 to K
28.          Cluster(x, CCC)=0;
29.          for y = 1 to K
30.              Cluster(x,CCC)=Cluster(x,CCC)+Wr(y)*norm(Cluster(x,1:NIC)-Cluster(y, 1:NIC));
31.          end for
32.       end for
33.       for x = 1 to M
34.         for y = 1 to N
35.           Cluster(Palette(Index(x,y),CPL),PDC)=Cluster(Palette(Index(x,y),CPL),PDC)+(x/M-0.5)^2+(y/N-
          0.5)^2;
36.         end for
37.       end for
38.       for z = 1 to K
39.         Cluster(z, PDC)=Cluster(z, PDC)/( n * n *Cluster(z, CPC));
40.       end for
41.       for x = 1 to K
42.           Cluster(x, CSS)=0;
43.           for y = 1 to K
44.               Ds=norm(Cluster(x, PXC:PYC)-Cluster(y, PXC:PYC));
45.               Phixy=(Cluster(x, CCC)+0.05)/(Cluster(y, CCC)+0.05);
46.               Cluster(x, CSS)=Cluster(x, CSS)+Wr(y)* Phixy*exp(-Ds);
47.           end for
48.           Cluster(x,CSS)=exp(-Cluster(x,PDC))*(Wr(x)*Cluster(x, CCC)+ Cluster(x, CSS));
49.       end for
50.       Cluster(:, CSS)=rescale(Cluster(:, CSS));
51.       for x = 1 to M
52.          for y = 1 to N
53.              Input(x, y, LCL)=Cluster(Palette(Index(x, y), CPL), CSS);
54.          end for
55.       end for
56.       Output=OtsuThresholding(Input(:, :, LCL));
57.       Output=BinaryMorphology(Output);
end Algorithm
```

4.3 Preprocessing effects on algorithm performance

The preprocessing effect on the performance of the color histogram clustering algorithm was investigated using a paired t-test which is regarded as a suitable technique for assessing the significant

difference between the means of two distributions (Kothari 2004; Xu *et al.* 2017). The statistical significance of the means of the preprocessed and non-preprocessed performance distributions of the proposed algorithm was therefore estimated using the two-tailed paired t-test. A *p*-value less than 0.05 ($p < 0.05$) is considered to declare a hypothesis statistically significant or not. The first pair involves the accuracy score obtained from the proposed algorithm without any preprocessing step, while the second pair represents the accuracy scores of the proposed algorithm with the preprocessing step. Table 4-1 shows the summary of steps used in the evaluation of determining the effect of preprocessing.

Table 4-1 Summary of preprocessing effects

Without preprocessing	**With preprocessing**
Color Histogram clustering	Preprocessing using DullRazor to remove artifacts or preprocessing using adaptive histogram equalization contrast enhancement.
Detection of the region of interest using CHC	Color Histogram clustering
Segmentation of region of interest	Detection of the region of interest using CHC Segmentation of region of interest.

The assertion made in the statistical analysis of the performance of the CHC algorithm is explained in the manner as below. The performance of the CHC algorithm for image segmentation has been significantly amplified by including a preprocessing stage in the segmentation method at a 5% significance level. Based on this assertion, the null hypothesis (Ho) and alternate hypothesis (Ha) are formulated as follows.

Ho: There is no statistically significant improvement in the performance of the CHC algorithm in segmenting salient regions by incorporating a preprocessing stage.

Ha: There is a statistically significant improvement in the performance of the CHC-Otsu algorithm in segmenting salient regions by incorporating a preprocessing stage.

4.4 Materials

Materials used in this study include the experimental image datasets, tool for algorithm implementation, and performance evaluation metrics.

4.4.1 Image datasets

The study used images with various salient properties such as location (center or boundary), object sizes (salient objects that overlap center and boundary regions), number of salient objects (multiple objects), color contrast (low contrast), and background complexity. The image datasets of MSRA10K (Liu *et al.* 2011), ASD (Achanta *et al.* 2009), SED2 (Alpert *et al.* 2011), ImgSal (Li *et al.* 2012), DUT OMRON (Yang *et al.* 2013), ECSSD (Shi *et al.* 2015), HKU-IS (Li and Yu 2015), and SOC (Fan *et al.* 2018) are used for selecting images with aforementioned properties because they have been extensively used for evaluating salient object detection and segmentation methods (Li *et al.* 2013b; Lou, Ren and Wang 2014; Borji *et al.* 2015; Ren *et al.* 2017; Zhou *et al.* 2018b; Liang, Liu and Ma 2019; Liu and Yang 2019; Jiang *et al.* 2020; Pang *et al.* 2020b; Singh, Mishra and Bhatia 2020; Singh and Kumar 2020; Singh, Kumar and Singh 2020; Zhang *et al.* 2020f; Jian *et al.* 2021; Ma *et al.* 2021a; Moradi, Bayat and Charmi 2021; Nawaz and Yan 2021; Yuan, Han and Yan 2021; Zhang and Wang 2021; Zhang *et al.* 2021c; Liu *et al.* 2022).

The MSRA10K is a descendent of the Microsoft Research Asia (MSRA) dataset and many of the images in this collection frequently feature a single prominent object against a simple and plain background (Li *et al.* 2017c; Niu, Su and Guo 2018). The ASD is a portion of the MSRA dataset that has a single foreground and simple backdrop with ground truth region annotation (Xia and Zhang 2018). These two datasets were primarily used to choose center located, boundary located, foreground or background overlapped, and low contrast images. Multiple salient objects with highly complicated backgrounds can be found in the SED2, ImgSal, and DUT-OMRON datasets (Jiang, Zhong and Lin* 2017; Niu, Su and Guo 2018; Nouri, Kazemi and Danyali 2018; Zhu *et al.* 2018). These three datasets were used to choose the images that had a variety of salient objects and intricate backgrounds.

In addition, the images were chosen to demonstrate the potential use of the proposed algorithm in various classes of images including obstacles found in real-world settings such as cluttered backgrounds and objects with properties representing occlusion. The ability of the proposed algorithm to handle complicated images was tested by selecting images from the ECSSD dataset (Shi *et al.* 2015). The ECSSD dataset contains 1000 images with salient items that have colors that are influenced by background areas and salient objects with varied colors, sizes, and position features, creating significant ambiguity for salient object detection methods. Fundamentally, the ECSSD dataset is regarded as being difficult for performance comparisons (Kim *et al.* 2016; Oh *et al.* 2017a; Oh *et al.* 2017b; Niu, Su and

Guo 2018; Wu *et al.* 2018; Liu and Yang 2019; Lopez-Alanis *et al.* 2019). The HKU-IS dataset contains 4447 complicated scenes with several disconnected items that are strikingly comparable to the background regions and have a varied spatial distribution (Li and Yu 2015; Wang *et al.* 2022a). A recent dataset created by Fan *et al.* (2018) called Salient Objects in Clutter (SOC) is a subset of the Common Objects in Contexts (COCO) dataset (Lin *et al.* 2014). The SOC dataset was created to test CNN-based salient object detection techniques. It contains challenging salient objects with properties that mimic occlusion, background clutter, and challenges in real-world scenarios. The proposed algorithm is not based on the CNN approach and is not featured for distinguishing salient items from obscured or cluttered backgrounds. Nevertheless, the capacity of the proposed algorithm to detect salient objects in real-world settings was tested using 1500 images from the SOC dataset.

Since the medical images are different from natural images and the noise and artifacts present in the medical images are typically a challenging case for accurate segmentation (Liu *et al.* 2021). Four more publicly available medical image datasets namely, PH2, ISIC2018, HAM10000, and Raabin-WBC were incorporated in this study to deepen the application of the proposed algorithm and to prove its generalization ability. Pedro Hispano hospital image dataset (PH2) (Mendonça *et al.* 2013) is a publicly available dataset with 200 dermoscopy images of melanocytic lesions and their corresponding ground truth. The International Skin Imaging Collaboration (ISIC) is the largest public dermoscopy image archive available. The ISIC2018 challenge (Codella *et al.* 2019) supplied a dataset with 2594 images and their equivalent ground truth for melanoma skin lesion segmentation. HAM10000 (Human Against Machine with 10000 training images") (Tschandl, Rosendahl and Kittler 2018) dataset contains 10015 dermatoscopic images, recently released for training deep learning methods and are publicly available through the ISIC archive. This dataset has been widely used in many studies (Sae-Lim, Wettayaprasit and Aiyarak 2019; Afza *et al.* 2021; Khan *et al.* 2021; Varalakshmi *et al.* 2021) for skin lesion classification and the literature shows no evidence of segmentation performance on this multi-source dermatoscopic image dataset. This study has incorporated HAM10000 for evaluating skin lesion segmentation to see the performance of the proposed algorithm on the huge dataset. Raabin-WBC (Kouzehkanan *et al.* 2021) is a large publicly available health dataset of white blood cells from peripheral blood samples that were recently published in 2021. All images from these datasets except Raabin-WBC are used further to evaluate the image preprocessing effects of the proposed algorithm. All datasets used in this study are summarized in Table 4-2.

Table 4-2 Datasets used to evaluate the proposed algorithm

Dataset	Remarks	Available at
MSRA10K	Dataset of images with a single prominent object and a plain background.	https://mmcheng.net/msra10k/
ASD	Dataset of images with annotated ground truth regions, a single salient object, and simple background.	https://www.epfl.ch/labs/ivrl/research-/saliency/frequency-tuned-salient-region-detection/
SED2	Image dataset with multiple objects and complex background.	https://www.wisdom.weizmann.ac.il/~vision/Seg_E-valuation_DB/dl.html
ImgSal	Image dataset with multiple salient objects with complex background.	https://qualinet.github.io/databases/image/imgsal_mc-gill_database_for_saliency_detection/
DUT OMRON	Image dataset with multiple small objects with high content variation and complex background.	http://saliencydetection.net/dutomron/
ECSSD	Image dataset with objects of various colors, sizes, and spatial characteristics.	https://www.cse.cuhk.edu.hk/leojia/projects/hsaliency/dataset.html
HKU-IS	Contains intricate scenes with many dispersed objects that are closely related to the background and have a varied spatial distribution.	https://i.cs.hku.hk/~yzyu/research/deep_saliency.html
SOC	It features images of noticeable objects from daily object categories. Each salient image has features that reflect typical difficulties in real-world scenarios in addition to object category annotations.	http://dpfan.net/SOCBenchmark/
ISIC2018	International skin imaging collaboration 2018 (ISIC2018), and it is the largest publicly available dermoscopic image dataset for the ISIC2018 challenge.	https://challenge.isic-archive.com/data
HAM10000	The HAM10000 dataset is a sizable collection of dermatoscopic pictures of typical pigmented skin lesions from various sources. The ISIC Archive has recently made it available for use in deep learning training.	https://doi.org/10.7910/DVN/DBW86T
PH2	Dermoscopic images of melanocytic lesions were manually segmented and identified, along with the related ground truth annotation, by skilled dermatologists.	https://www.fc.up.pt/addi/ph2%20database.html
Raabin-WBC	A substantial and publicly accessible dataset of white blood cells from typical peripheral blood samples.	https://raabindata.com/free-data/

4.4.2 Evaluation tools

MATLAB (2019a, The MathWorks, Inc., Natick, Massachusetts, United States) and Stata software (StataCorp. 2021, College Station, StataCorp LLC) of version 17 are the two tools mainly used in this study. MATLAB is a powerful language and robust interactive environment for developing algorithms in technical computing (Gonzalez, Woods and Eddins 2004) and it has been widely used in

the field of object detection and segmentation (Nikbakhsh, Baleghi and Agahi 2021; Oskouei *et al.* 2021; Shahin and Almotairi 2021; Tu *et al.* 2021; Yu *et al.* 2021b; Yuan *et al.* 2021; Jing, Jin and Xiang 2022; Wang *et al.* 2022a). Hence the implementation and the evaluation of the proposed algorithm were carried out using MATLAB on a computer with an Intel(R) Core (TM) i7-8650U CPU @ 1.90GHz 2.11 GHz, and 8 GB random access memory. Stata is general-purpose statistical software that offers hundreds of basic and advanced commands for statistical modeling (Leckie and Charlton 2013). Hence in this study, the statistical evaluation of the effect of preprocessing was performed using Stata software.

4.4.3 Evaluation metrics

The obtained segmentation results were evaluated using different evaluation metrics such as accuracy, specificity, sensitivity/recall, precision, F-Measure, Mean Absolute Error (MAE), Overlap Ratio (OR), Dice similarity index, and Jaccard index. These metrics have been considered the most common metrics for the evaluation of the segmented images (Li *et al.* 2013a; Borji *et al.* 2015; Zhou *et al.* 2015; Pennisi *et al.* 2016; Bi *et al.* 2017; Nouri, Kazemi and Danyali 2018; Olugbara, Taiwo and Heukelman 2018; Wu *et al.* 2018; Youssef *et al.* 2018; Liu and Yang 2019; Sae-Lim, Wettayaprasit and Aiyarak 2019; Ünver and Ayan 2019; Kompella and Kulkarni 2020; Salih and Viriri 2020; Okuboyejo and Olugbara 2021; Rajput, Tanwar and Raman 2021; Li *et al.* 2022; Liu *et al.* 2022). These evaluation metrics are computed based on the parameters, True Positive (TP), False Positive (FP), True negative (TN), and False Negative (FN). TP and FP respectively are the number of foreground pixels that are correctly identified as a region of interest and the amount of non-object pixels that are incorrectly predicted as foreground region. While TN and FN are the amounts of non-object pixels that are accurately identified as background region and the amount of non-object pixels incorrectly predicted as foreground region.

i. Accuracy

Accuracy refers to the degree to which the foreground objects are predicted correctly (Kaur and Kaur 2018) and is mathematically estimated as in Equation 4.9

$$Accuracy = \frac{TP + TN}{TP + TN + FP + FN} \tag{4.9}$$

The better performance is indicated by the higher values of accuracy.

ii. Specificity

Specificity or True Negative Rate (TNR) is the proportion of accurately identified non-object regions and is mathematically represented as in equation (4.10)

$$Specificity = \frac{TN}{TN + FP} \tag{4.10}$$

The better performance is indicated by the higher values of specificity.

iii. Precision

Precision is the ratio of the number of correctly identified foreground pixels to the total number of pixels in the segmented image (Jiang *et al.* 2018; Olugbara, Taiwo and Heukelman 2018; Nawaz and Yan 2020) and is defined as in equation (4.11)

$$Precision = \frac{TP}{TP + FP} \tag{4.11}$$

The better performance is indicated by the higher values of precision.

iv. Recall or Sensitivity

Recall or Sensitivity or True Positive Rate (TPR) is the degree of the correctly identified salient regions to the total number of salient object pixels in the ground truth (Jiang *et al.* 2018; Olugbara, Taiwo and Heukelman 2018; Nawaz and Yan 2020) and is mathematically represented as, in Equation (4.12)

$$Recall = \frac{TP}{TP + FN} \tag{4.12}$$

A higher value indicates better performance.

v. F-Measure

F-Measure is computed as a weighted harmonic mean of precision and recall and is defined as in Equation (4.13) (Achanta *et al.* 2009 ; Li *et al.* 2013a)

$$F_\beta = \frac{(1+\beta^2)\,\mathrm{Pr}ecision \times \mathrm{Re}call}{\beta^2 \times \mathrm{Pr}ecision + \mathrm{Re}call} \tag{4.13}$$

where, the value of β^2 is set to 0.3 as recommended by (Achanta *et al.* 2009; Lou, Ren and Wang 2014; Borji *et al.* 2015; Zhang *et al.* 2017b; Liu and Yang 2019) to weigh precision more than recall. The better performance is indicated by the higher values of F-Measure.

vi. Mean Absolute Error

The successfully identified non-object pixels i.e. the true negative value is not considered either by precision or recall. This affects the methods that correctly identify the non-object pixels but failed to correctly detect the salient object pixels (Perazzi *et al.* 2012; Sikha, Kumar and Soman 2018). This study also computes the Mean Absolute Error (MAE) between the saliency map and the ground truth for a balanced evaluation to consider this effect into account. The MAE is a common metric to measure the dissimilarity between the estimated and the actual values (Li *et al.* 2017c) and is defined as the average of absolute error between the continuous saliency map (S) and the ground truth (GT) as in Equation (4.14)

$$MAE = \frac{1}{W \times H} \sum_{x=1}^{W} \sum_{=1}^{H} \left| S(x,y) - GT(x,y) \right| \tag{4.14}$$

where W and H are respectively the width and height of the image. The lower the value of MAE indicates the better performance.

vii. Overlapping Ratio

The Overlapping Ration (OR), is the ratio of overlapping between the binarized segmented image, S' and the group truth, GT (Niu, Chen and Guo 2018) and is defined as in Equation 4.15

$$OR = \frac{\left| S' \cap GT \right|}{\left| S' \cup GT \right|} \tag{4.15}$$

The better performance is indicated by the higher values of OR.

viii. Dice similarity index

The dice similarity measures the association between the segmentation output and ground truth (Dice 1945) and is represented mathematically as in Equation 4.16.

$$Dice = \frac{2TP}{FP + 2TP + FN} \tag{4.16}$$

ix. Jaccard index

Jaccard Coefficient is one of the common similarity indices used for evaluating the segmentation results and is defined as the count of common pixels in the saliency map and the ground truth over their union and is defined as in equation 4.17 (Jaccard 1912; Taha and Hanbury 2015; Nawaz and Yan 2021).

$$Jaccard = \frac{TP}{TP + FN + FP} \tag{4.17}$$

4.5 Chapter summary

This chapter provided in-depth information regarding the methods and tools used in this study. The segmentation algorithm developed in this study is to solve the problem of detecting optimum cluster count for image segmentation and to ensure the application of the algorithm on a wide range of images. The histogram clustering based on the quantized RGB image is used for the automatic detection of the optimum clusters. Color contrast, contrast ratio, spatial features, and center prior are integrated to enable an effective and efficient segmentation of regions of interest from a diverse class of images. This chapter also included a presentation of the statistical approach used to examine the impact of preprocessing on the effectiveness of the proposed algorithm. Details of image datasets, evaluation tools, and the evaluation metrics used for assessing the efficacy of the proposed algorithm for segmenting salient objects from diverse classes of images were also explained.

CHAPTER FIVE: EXPERIMENTAL RESULTS

This chapter intends to explain the experiments carried out in this study to fulfill the study objectives outlined in chapter 1. Selection of an optimum number of cluster count is a decisive process as the incorrect cluster number can lead to over or under-segmentation of color images and cause non-uniform detection of salient regions. In this study, color histogram clustering is applied for the selection of an optimum cluster count for the region granularity and agglutinates color contrast, contrast ratio, spatial feature, and center before efficient and effective segmentation of salient objects. The first set of experiments was conducted to evaluate the ability of the proposed algorithm to automatically detect the optimum clusters for the detection of salient objects from the diverse class of images. Further, the performance of the proposed algorithm on six categories of images against 30 state-of-the-art saliency detection methods and seven deep learning-based methods was experimentally analyzed. Experiments were undertaken in the succeeding section using seven image datasets with various image properties to validate the performance of the proposed algorithm across a variety of images. The image preprocessing effect of the proposed algorithm was further investigated in the subsequent section. Experiments were also conducted to demonstrate the run-time computational analysis of the proposed algorithm against the state-of-the-art methods. The last section of this chapter summarized the optimal cluster counts generated by the proposed algorithm.

5.1 Experiments

This study employed the properties of salient objects to classify various images into distinct groups to give a more comprehensive experimental analysis of the proposed segmentation algorithm to detect the salient region. The position of salient objects (center or boundary), object size (salient items that overlap center and boundary regions), number of salient objects (multiple salient objects), color contrast (low contrast), and complex background are the salient object attributes depicted in Figure 5-1. Seven top-down deep learning-based methods and thirty modern bottom-up methods were used to compare the performance of the proposed algorithm. Five bottom-up saliency methods and deep learning methods were removed from the comparison of six categories of images because the source codes were not available. The central bias weight, α, is the only parameter that was used in the proposed algorithm and was experimentally selected $\alpha \in [0.1,1.0]$.

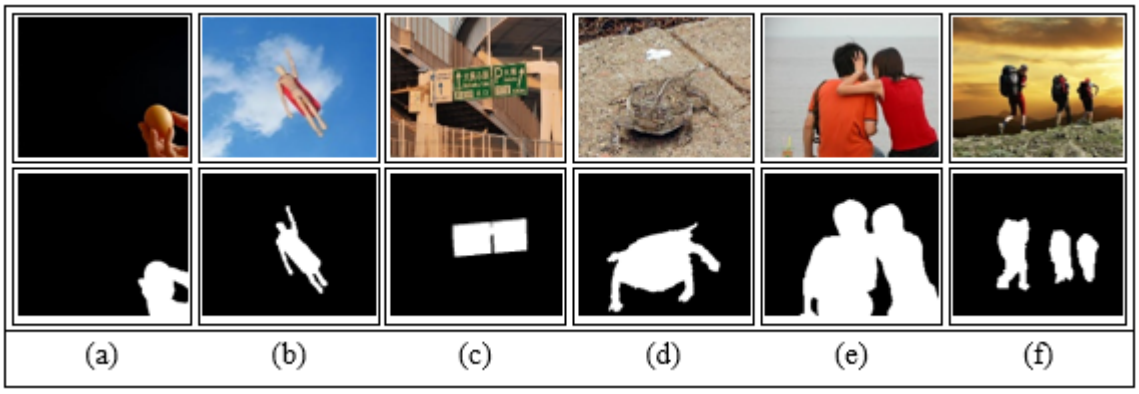

Figure 5-1 Category of images: (a) boundary; (b) center; (c) complex background; (d) low contrast; (e) overlap; (f) multiple objects

5.1.1 Methods comparison

The details of the methods used for comparison are illustrated in Table 5-1. A combination of different pixel-based and region-based bottom-up saliency models that are based on various approaches such as global contrast, graph-based, learning-based, center surroundedness, prior knowledge, and top-down models are used for comparison.

In numerous studies, most of these bottom-up saliency detection techniques have been extensively benchmarked (Lou, Ren and Wang 2014; Borji *et al.* 2015; Singh, Arya and Agrawal 2016; Wang *et al.* 2016; Singh, Arya and Agrawal 2017; Annum, Riaz and Ghafoor 2018; Nouri, Kazemi and Danyali 2018; Singh, Arya and Agrawal 2018; Wu *et al.* 2018; Jia *et al.* 2019b; Jiang *et al.* 2020; Lou *et al.* 2020; Nawaz and Yan 2020; Singh, Mishra and Bhatia 2020; Singh and Kumar 2020; Zhang *et al.* 2020d). In addition, this study has included the CNS (Lou *et al.* 2020) and RPC (Lou, Ren and Wang 2014) because of their similarity to the proposed algorithm. Since deep learning-based top-down methods have been the subject of many recent high-end advancements, this study compared the proposed algorithm with seven of them.

Table 5-1 Methods compared for salient objects detection

Bottom-Up Saliency Methods			
No	**Method**	**Approach and Prior Knowledge**	**Unit of Processing**
1	FES (Tavakoli, Rahtu and Heikkilä 2011)	Center-surroundedness contrast, center prior	Pixel
2	IT (Itti, Koch and Niebur 1998)	Center-surroundedness, intensity, color, and orientation contrast	
3	GB (Harel, Koch and Perona 2007)	Graph-based, center-surroundedness activation map	
4	SeR (Seo and Milanfar 2009)	Local steering kernel features and color features	
5	SEG (Rahtu *et al.* 2010)	Local feature contrast, boundary prior	

6	SR (Hou and Zhang 2007)	Spectral residual approach	
7	AC (Achanta *et al.* 2008)	Center surroundedness color contrast prior	Patch/Block
8	CA (Goferman, Zelnik-Manor and Tal 2012)	Global, and local features, context prior, center Prior	
9	SWD (Duan *et al.* 2011)	Center prior, color dissimilarity, spatial distance	
10	COV (Erdem and Erdem 2013)	Local color contrast, center prior	
11	SUN (Zhang *et al.* 2008)	The local intensity and color features, feature space	
12	MRBF (Ma *et al.* 2021b)	Boundary connectivity, foreground prior	Region by SLIC algorithm
13	DCLC (Zhou *et al.* 2015)	Diffusion-based using manifold ranking, compactness local contrast, center prior	
14	MCVS (Zhang and Wang 2021)	Background prior, foreground prior, and contrast features	
15	CSV (Singh, Kumar and Singh 2020)	Global color spatial distribution, object position prior	
16	HDCT (Kim *et al.* 2016)	Learning-based approach, global and local color contrast features, location, histogram, texture, and shape features	
17	FCB (Liu and Yang 2019)	Foreground and background cues, center prior	
18	MC (Jiang *et al.* 2013a)	Boundary prior, graph-based, Markov random walk	
19	MR (Yang *et al.* 2013)	Boundary prior, graph-based manifold ranking	
20	DGL (Wu *et al.* 2018)	Graph-based, boundary prior	
21	FBSS (Wang *et al.* 2021a)	Boundary, texture, color, and contrast priors	
22	DSR (Li *et al.* 2013b)	Background prior	
23	MAP (Sun, Lu and Liu 2015)	Boundary prior, graph-based, Markov absorption probabilities	
24	BGFG (Wang *et al.* 2015)	Background and foreground prior	
25	GR (Yang, Zhang and Lu 2013)	Convex-hull-based center prior, contrast and smoothness prior, graph-based	
26	BPFS (Ding *et al.* 2020)	Global color contrast, background prior, and foreground seeds	
27	RPC (Lou, Ren and Wang 2014)	Color contrast, center prior	Regions by graph-based segmentation
28	DRFI (Jiang *et al.* 2013b)	Color and texture contrast features, backgrounds features	
29	CNS (Lou *et al.* 2020)	Surroundedness and global color contrast cues	Regional histogram of color name space
30	SIM (Murray *et al.* 2011)	Center surroundedness color contrast	Spatial scale
31	CHC(Method proposed in this study)	Color contrast, contrast ratio, spatial feature, and central prior	Regional color histogram clustering
	Deep-learning-based top-down saliency methods		
1	MSNSD (Liang, Liu and Ma 2019)		
2	MSNSD-A (Liang, Liu and Ma 2019)		
3	TSL (Yan *et al.* 2020)		
4	LCNN (Li *et al.* 2017b)		
5	DS (Li *et al.* 2016)		
6	MCDL (Zhao *et al.* 2015a)		
7	(Nasiripour, Farsi and Mohamadzadeh 2019)		

The default parameters provided by the authors were used in this study to execute the source code for the models AC, BGFG, CNS, DCLC, DGL, DRFI, GB, GMR, HDCT, IT, MAP, MR, and RPC to obtain the saliency map. The saliency map of CA, COV, DSR, FES, GR, MC, SEG, SeR, SR, SUN, and SWD is obtained using the implementation of the salient object detection benchmark released by Borji *et al.* (2015) and retains the default parameters set by the authors. Due to the lack of access to the code of the rest of the models, they were excluded from the visual comparison, computational time complexity, and comparison with the six categories of images. Based on the visual saliency results provided by the authors of FCB it was considered for overlap image category and the ECSSD dataset.

5.1.2 Performance evaluation

Both qualitative and quantitative evaluations were used to verify the performance of the proposed algorithm. The qualitative analysis enables visual comparison of saliency maps with the ground truth annotation. This makes it easier to assess the degree of closeness of saliency maps with the ground truth. Qualitative evaluation is more subjective and compared to this, quantitative evaluation is more accurate. Hence this study quantitatively assessed the proposed algorithm using the common evaluation metrics such as Precision, Recall, F-measure, Means Absolute Error (MAE), and Overlapping Ratio (OR) (Li *et al.* 2013a; Borji *et al.* 2015; Zhou *et al.* 2015; Kim *et al.* 2016; Singh, Arya and Agrawal 2016, 2017; Annum, Riaz and Ghafoor 2018; Niu, Chen and Guo 2018; Singh, Arya and Agrawal 2018; Wu *et al.* 2018; Jia *et al.* 2019b; Liu and Yang 2019; Lou *et al.* 2020; Nawaz and Yan 2020; Singh, Mishra and Bhatia 2020; Singh and Kumar 2020; Moghaddam *et al.* 2021; Shahin and Almotairi 2021; Yu *et al.* 2021b; Zhang and Ma 2021; Zhang *et al.* 2021c; Kumar and Meenpal 2022; Liu *et al.* 2022; Song *et al.* 2022). This study used these assessment metrics to compare the performance of the proposed algorithm to the selected models. Precision-recall values were determined by comparing the binary equivalent of the saliency map with the ground truth image. The saliency map was bipartite using a fixed threshold value between 0 and 255, and pairs of Precision and Recall values were calculated for each threshold to depict the performance in various cases (Li *et al.* 2013a; Borji *et al.* 2015).

5.2 Qualitative results

The visual performance of the investigated methods is demonstrated in Figure 5-2. The Color Histogram Clustering (CHC) algorithm developed in this study highlighted the salient regions with

well-formed edge information and suppress the non-salient pixels. The effectiveness of CHC in detecting the salient items accurately and uniformly in many classes of images is noteworthy when compared to several of the existing methods shown here in Figure 5-2. The qualitative findings showed that the majority of the methods in use were successful in producing positive outcomes for image categories that consisted of single or homogenous object images that were quite simple. Multiple salient objects, low contrast, and complex background image categories continue to be challenging for existing methods. As seen in Figure 5-2a, methods that used background or boundary prior, such as BGFG, DGL, DSR, MC, MR, and MAP, were unable to detect or consistently highlight objects near the image boundary. In contrast, the salient items that touch the image boundaries have been successfully recognized and consistently highlighted by the CHC. This showed that, regardless of where the salient items are located in the images, CHC can efficiently suppress the background while highlighting the region of interest with distinct edges.

On images with salient objects in the center, methods that took advantage of the center prior performed well. When a salient and a non-salient object (a strawberry and a bowl) appear in the center of a picture, as in Figure 5-2(b2), methods that exploit the center prior did not perform well. As a result, these methods concomitantly identified both items as salient regions. However, methods like RPC, DCLC, GR, CNS, and HDCT that use color contrast have been successful in highlighting actual salient objects. Boundary prior methods, including MC, MR, MAP, and DGL, were unable to recognize the correct salient object in this category of images because they mistakenly identified the white bowl as a salient object while misinterpreting the image boundary areas as background. The CHC has proven strength in recognizing salient objects, regardless of variation in sizes, as in Figure 5-2(b1) (small salient object) and Figure 5-2(b3) (large salient object). This made the performance of the proposed algorithm for this category of images highly praiseworthy. Several existing methods, including DCLC, GR, MAP, MC, MR, and RPC, have been unable to uniformly highlight the entire salient regions because of the varied features in terms of color and appearance of the salient object, as seen in Figure 5-2(b3). Instead of highlighting all salient regions, these methods have only been able to do so partially. The CHC, in contrast, produced outstanding results that are almost similar to the ground truth images.

Figure 5-2c depicted a visual comparison of the selected methods against a complicated background. The findings demonstrated the effectiveness of the CHC in distinguishing salient objects from varied and complicated backgrounds, while all other methods performed relatively poorly. Due to the use of multi-level pre-segmentation maps and the addition of color and texture cues to identify

multi-invariant objects, DRFI performed significantly better than the other methods. For contrast-based and graph-based approaches, salient objects with low contrast to the background are seen as the problematic case. Figure 5-2d showed the visual representation of the low contrast image category and it is important to note that, except for the CHC method, none of the other methods did particularly well in this category of images. The DGL method introduced a deformed smoothness constraint to address this issue with graph-based methods. However, DGL experienced failures, as shown in Figure 5-2(d3), where it was unable to handle low-contrast objects correctly. Due to the usage of feature extraction using contrast vectors, the result in Figure 5-2(d3) demonstrated that the efficacy of DRFI is not free from the restriction of contrast-based cues. DSR performed substantially better than the other methods, but the results did not eliminate background noise, as seen in Figure 5-2 (d3). Poor performance on low-contrast objects was also seen with the regional contrast-based RPC method that used low-level color contrast features.

Comparing the results of CHC to the listed methods, RPC has shown promising outcomes. Due to the heterogeneous nature of objects, as shown in Figure 5-2e, it is still difficult for many recent methods to regularly highlight salient objects in the category of multiple objects. The findings of Figure 5-2(e1) showed that numerous approaches, including CNS, DGL, DSR, MAP, MC, and MR, can only detect one salient object. The CHC has once more proven that it is capable of successfully detecting heterogeneous objects from this class of images. For this category of images, only CHC and DRFI displayed significantly better results. As shown in Figure 5-2f, the images that fall under the overlapped category are typically larger and overlap both the image boundary and the image center. Similar to the preceding categories, the CHC exhibited exceptional performance for images in this category. In addition, the graph-based approaches or diffusion-based methods like DGL, MR, MC, and MAP have generated good outcomes on the overlapping image categories. DSR has performed poorly on overlapped images, in contrast to its good performance on low contrast images, because the method erroneously allocated all image boundaries as a background template. As shown in Figure 5-2, the methods AC, COV, FES, IT, GB, SeR, SUN, SWD, and SIM consistently showed difficulties in highlighting salient objects from all the mentioned categories of images.

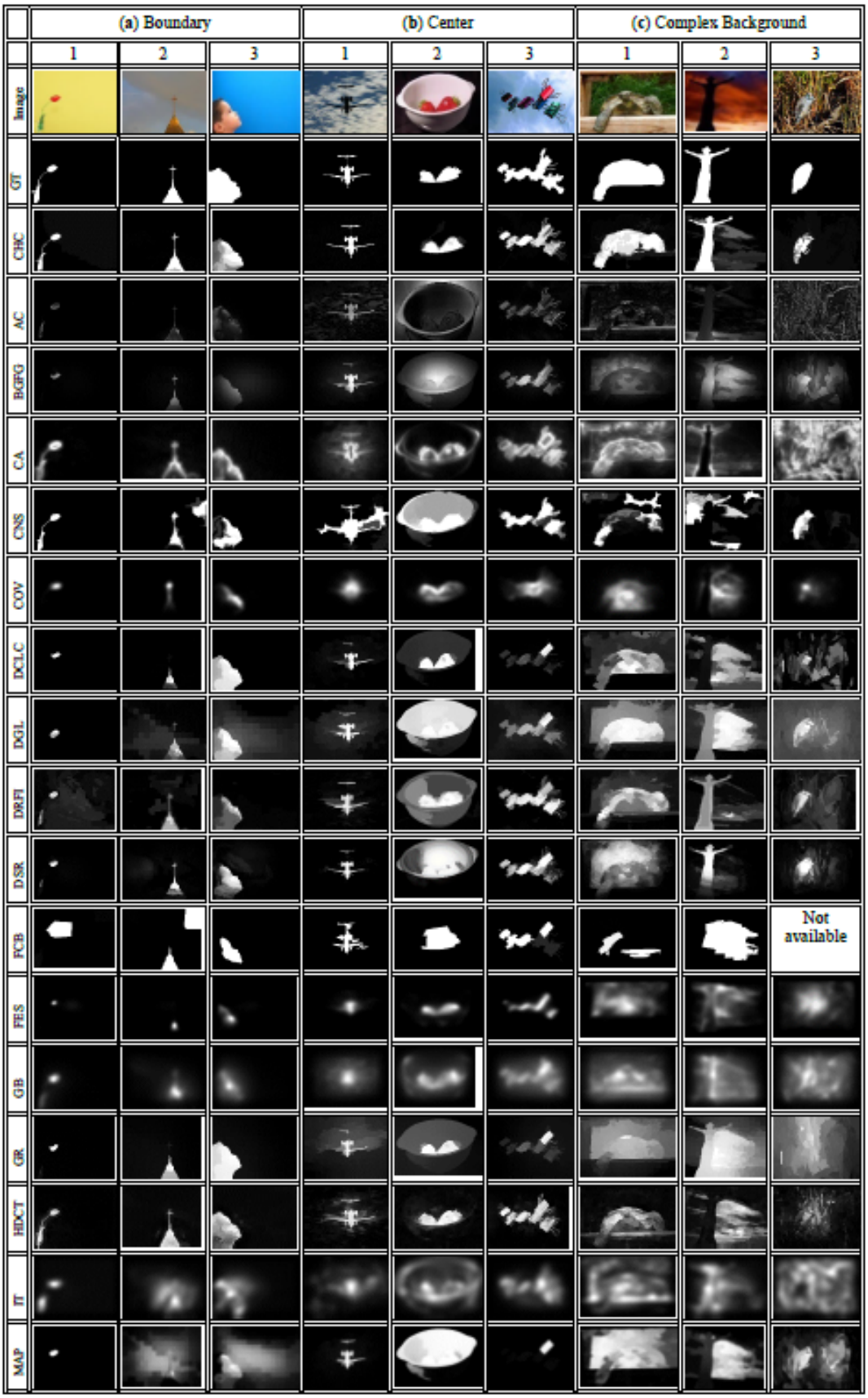
(a) Boundary
(b) Center
(c) Complex Background
1
2
3
1
2
3
1
2
3
Image
GT
CHC
AC
BGFG
CA
CNS
COV
DCLC
DGL
DRFI
DSR
FCB
FES
GB
GR
HDCT
IT
MAP
Not available

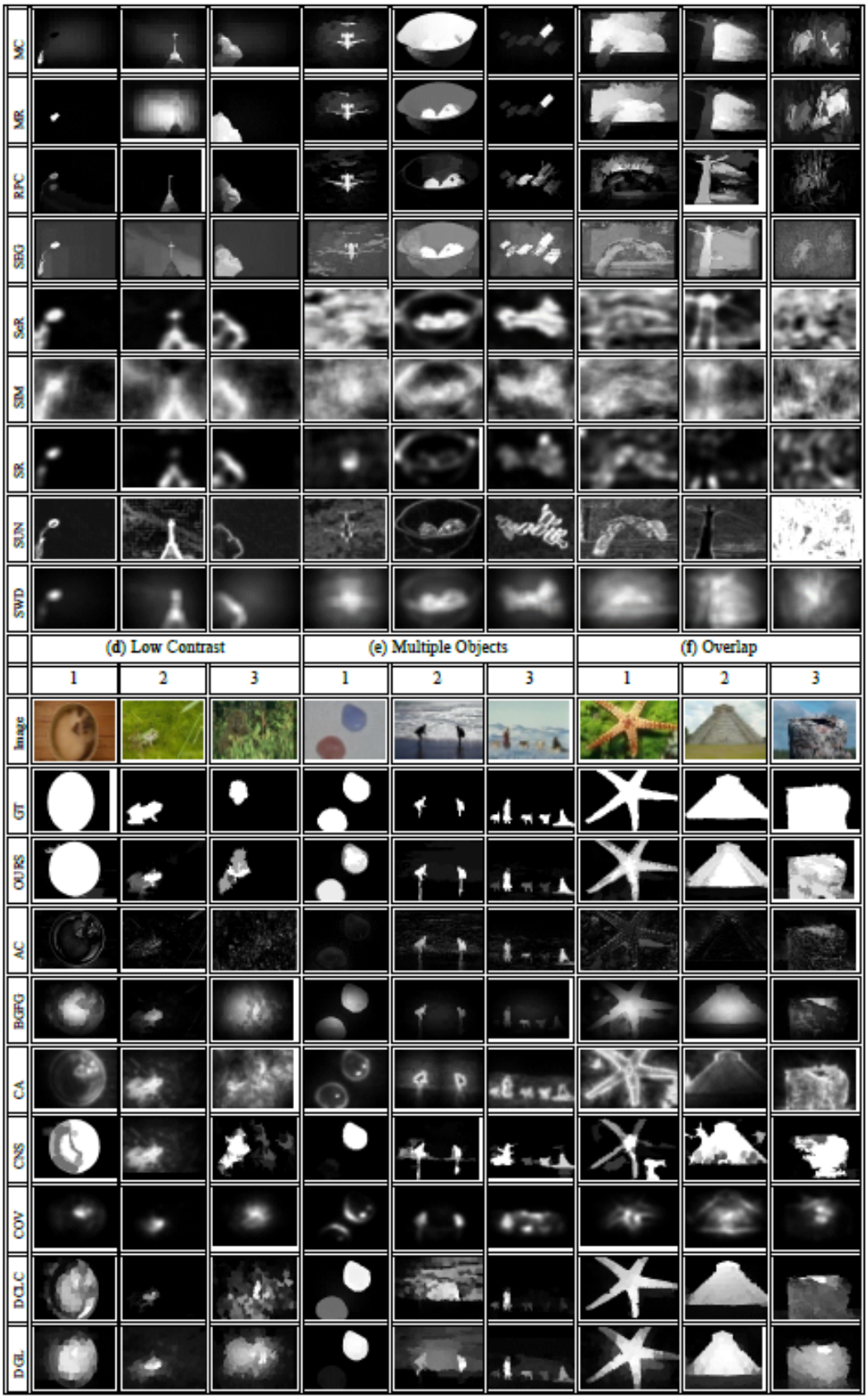
MC
MR
RPC
SRG
SeR
SIM
SR
SUN
SWD
(d) Low Contrast
(e) Multiple Objects
(f) Overlap
1
2
3
1
2
3
1
2
3
Image
GT
OURS
AC
BGFG
CA
CNS
COV
DCLC
DGL

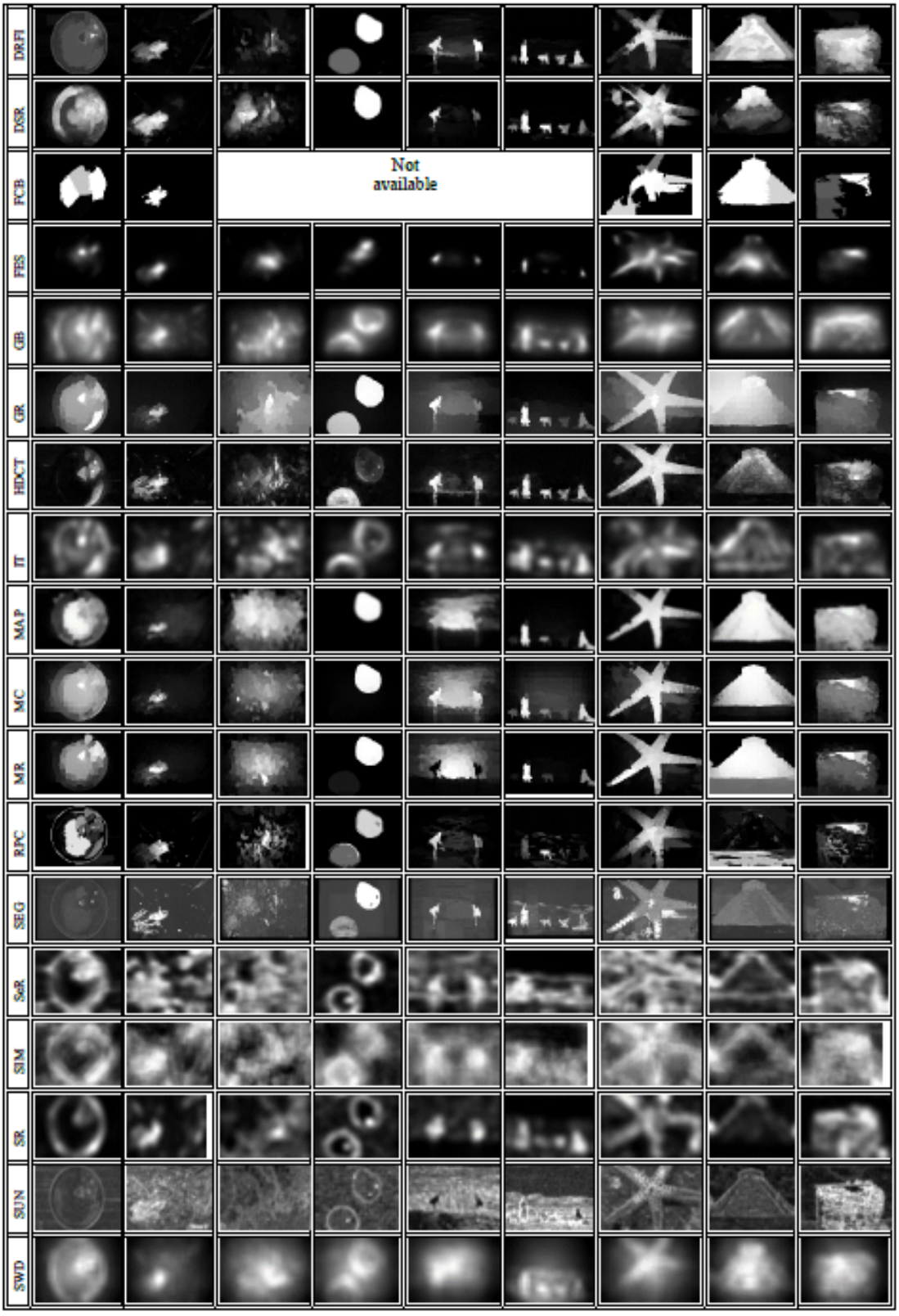

Figure 5-2 Visualized performances of the selected methods on six categories of images: (a) Boundary; (b) Center; (c) Complex Background; (d) Low Contrast; (e) Multiple Objects; (f) Overlap

5.3 Quantitative results

The effectiveness of the proposed algorithm was evaluated using the evaluation metrics presented in chapter 4. A quantitative comparison of the CHC and the existing methods is provided in Table 5-2 in terms of the metrics of precision, recall, F-measure, MAE, and OR to objectively assess the effectiveness of the CHC on various categories of images.

Table 5-2 The performance metrics for six different image categories. The highest values are shown in bold. The up arrow ↑ denotes greater performance at higher values, and the down arrow ↓ denotes better performance at lower values.

(a)	Metric	CHC	AC	BGFG	CA	CNS	COV	DCLC	DGL	DRFI	DSR	FES	GB	GR
Boundary (350)[1]	Precision↑	**0.945**	0.698	0.807	0.621	0.800	0.580	0.928	0.909	0.867	0.846	0.765	0.578	0.924
	Recall↑	0.891	0.692	0.782	0.843	0.825	0.561	0.887	0.859	**0.932**	0.868	0.677	0.774	0.898
	F-measure↑	**0.932**	0.697	0.801	0.661	0.805	0.576	0.918	0.897	0.882	0.851	0.743	0.614	0.918
	MAE↓	0.062	0.133	0.111	0.140	0.071	0.130	**0.057**	0.073	0.080	**0.057**	0.110	0.152	0.095
	OR↑	**0.844**	0.541	0.659	0.545	0.700	0.387	0.832	0.794	0.808	0.747	0.551	0.480	0.837
	Metric		**HDCT**	**IT**	**MAP**	**MC**	**MR**	**RPC**	**SEG**	**SeR**	**SIM**	**SR**	**SUN**	**SWD**
	Precision↑		0.878	0.532	0.804	0.884	0.900	0.860	0.873	0.531	0.562	0.536	0.58	0.627
	Recall↑		0.927	0.705	0.799	0.808	0.841	0.797	0.624	0.787	0.529	0.701	0.578	0.648
	F-measure↑		0.888	0.564	0.803	0.865	0.886	0.844	0.799	0.574	0.554	0.567	0.58	0.632
	MAE↓		0.077	0.179	0.092	0.104	0.070	0.097	0.274	0.191	0.325	0.154	0.233	0.219
	OR↑		0.816	0.417	0.691	0.741	0.785	0.698	0.588	0.452	0.337	0.425	0.408	0.446
	Metric	**CHC**	**AC**	**BGFG**	**CA**	**CNS**	**COV**	**DCLC**	**DGL**	**DRFI**	**DSR**	**FES**	**GB**	**GR**
Center (370)[1]	Precision↑	**0.949**	0.633	0.854	0.606	0.819	0.733	0.910	0.906	0.862	0.856	0.772	0.664	0.913
	Recall↑	0.889	0.543	0.850	0.655	0.903	0.699	0.915	0.909	**0.933**	0.888	0.734	0.765	0.866
	F-measure↑	**0.934**	0.610	0.853	0.617	0.837	0.725	0.911	0.906	0.877	0.863	0.763	0.685	0.901
	MAE↓	0.067	0.184	0.112	0.204	**0.058**	0.147	0.063	0.063	0.075	0.062	0.136	0.183	0.122
	OR↑	**0.846**	0.420	0.727	0.435	0.768	0.520	0.838	0.830	0.804	0.762	0.589	0.511	0.801
	Metric		HDCT	IT	MAP	MC	MR	RPC	SEG	SeR	SIM	SR	SUN	SWD
	Precision↑		0.859	0.549	0.874	0.896	0.908	0.839	0.808	0.505	0.474	0.507	0.500	0.742
	Recall↑		0.925	0.618	0.899	0.906	0.892	0.795	0.568	0.559	0.259	0.521	0.336	0.649
	F-measure↑		0.873	0.564	0.88	0.898	0.904	0.828	0.736	0.516	0.398	0.510	0.450	0.719
	MAE↓		0.091	0.218	0.063	0.079	0.061	0.109	0.279	0.273	0.381	0.214	0.319	0.230
	OR↑		0.794	0.386	0.796	0.82	0.818	0.686	0.527	0.344	0.171	0.330	0.245	0.475
	Metric	**CHC**	**AC**	**BGFG**	**CA**	**CNS**	**COV**	**DCLC**	**DGL**	**DRFI**	**DSR**	**FES**	**GB**	**GR**
Complex background (210)[1]	Precision↑	**0.933**	0.404	0.774	0.550	0.768	0.670	0.847	0.875	0.856	0.827	0.629	0.598	0.762
	Recall↑	0.753	0.317	0.697	0.405	0.747	0.554	0.793	0.810	**0.827**	0.774	0.595	0.537	0.531
	F-measure↑	**0.885**	0.380	0.755	0.508	0.763	0.639	0.834	0.859	0.849	0.814	0.621	0.583	0.692
	MAE ↓	**0.120**	0.253	0.179	0.311	0.130	0.195	0.133	0.135	0.138	0.127	0.200	0.259	0.260
	OR↑	0.710	0.22	0.568	0.295	0.623	0.418	0.700	**0.726**	0.721	0.657	0.438	0.384	0.490
	Metric		**HDCT**	**IT**	**MAP**	**MC**	**MR**	**RPC**	**SEG**	**SeR**	**SIM**	**SR**	**SUN**	**SWD**
	Precision↑		0.824	0.482	0.828	0.821	0.819	0.695	0.683	0.334	0.287	0.416	0.381	0.708
	Recall↑		0.780	0.362	0.803	0.769	0.774	0.601	0.310	0.180	0.055	0.273	0.123	0.376
	F-measure↑		0.814	0.448	0.822	0.808	0.809	0.671	0.535	0.279	0.146	0.371	0.257	0.588
	MAE↓		0.160	0.303	0.131	0.164	0.139	0.185	0.341	0.439	0.454	0.318	0.430	0.321
	OR↑		0.666	0.254	0.694	0.669	0.670	0.485	0.285	0.131	0.045	0.197	0.102	0.310
	Metric	**CHC**	**AC**	**BGFG**	**CA**	**CNS**	**COV**	**DCLC**	**DGL**	**DRFI**	**DSR**	**FES**	**GB**	**GR**
Low contrast (165)[1]	Precision↑	**0.908**	0.539	0.787	0.614	0.717	0.710	0.844	0.837	0.843	0.814	0.738	0.672	0.792
	Recall↑	0.715	0.365	0.653	0.510	0.628	0.545	0.715	0.721	**0.753**	0.710	0.545	0.600	0.501
	F-measure↑	**0.854**	0.486	0.751	0.586	0.694	0.663	0.810	0.807	0.820	0.788	0.682	0.654	0.698
	MAE↓	**0.122**	0.227	0.178	0.248	0.155	0.193	0.146	0.159	0.148	0.134	0.187	0.224	0.233
	OR↑	**0.659**	0.278	0.538	0.38	0.516	0.423	0.625	0.631	0.654	0.599	0.445	0.436	0.457
	Metric		**HDCT**	**IT**	**MAP**	**MC**	**MR**	**RPC**	**SEG**	**SeR**	**SIM**	**SR**	**SUN**	**SWD**
	Precision↑		0.805	0.585	0.804	0.827	0.820	0.730	0.740	0.461	0.499	0.537	0.467	0.731
	Recall↑		0.685	0.491	0.720	0.710	0.720	0.572	0.249	0.370	0.219	0.441	0.238	0.452
	F-measure↑		0.774	0.560	0.783	0.797	0.795	0.686	0.508	0.437	0.385	0.511	0.382	0.640
	MAE↓		0.173	0.252	0.156	0.175	0.153	0.182	0.310	0.340	0.388	0.261	0.371	0.274
	OR↑		0.578	0.348	0.606	0.613	0.61	0.466	0.233	0.257	0.175	0.316	0.198	0.364
	Metric	**CHC**	**AC**	**BGFG**	**CA**	**CNS**	**COV**	**DCLC**	**DGL**	**DRFI**	**DSR**	**FES**	**GB**	**GR**
Multiple objects (160)[1]	Precision	**0.876**	0.640	0.735	0.576	0.752	0.537	0.84	0.834	0.807	0.790	0.633	0.556	0.86
	Recall	0.786	0.567	0.696	0.592	0.743	0.535	0.748	0.762	**0.818**	0.759	0.587	0.644	0.666
	F-measure	**0.853**	0.621	0.726	0.580	0.750	0.537	0.812	0.816	0.810	0.783	0.621	0.574	0.806
	MAE↓	**0.836**	0.921	0.888	0.958	0.840	0.911	0.850	0.860	0.842	0.839	0.896	0.955	0.909

	OR	**0.695**	0.425	0.528	0.371	0.582	0.331	0.652	0.656	0.663	0.614	0.410	0.382	0.599
	Metric		**HDCT**	**IT**	**MAP**	**MC**	**MR**	**RPC**	**SEG**	**SeR**	**SIM**	**SR**	**SUN**	**SWD**
	Precision		0.801	0.536	0.741	0.813	0.820	0.741	0.771	0.427	0.422	0.506	0.442	0.583
	Recall		0.791	0.586	0.733	0.741	0.714	0.666	0.381	0.469	0.245	0.537	0.259	0.464
	F-measure		0.799	0.547	0.739	0.795	0.793	0.723	0.624	0.436	0.362	0.513	0.380	0.550
	MAE↓		0.864	0.967	0.866	0.878	0.851	0.883	1.032	1.047	1.124	0.960	1.091	1.021
	OR		0.638	0.338	0.574	0.619	0.619	0.521	0.352	0.255	0.141	0.314	0.176	0.295
	Metric	**CHC**	**AC**	**BGFG**	**CA**	**CNS**	**COV**	**DCLC**	**DGL**	**DRFI**	**DSR**	**FCB**	**FES**	**GB**
	Precision↑	**0.986**	0.703	0.969	0.738	0.881	0.815	0.981	0.969	0.975	0.949	0.968	0.853	0.777
	Recall↑	0.767	0.344	0.593	0.442	0.638	0.395	**0.804**	0.767	0.756	0.661	0.615	0.478	0.461
	F-measure↑	0.925	0.567	0.845	0.639	0.810	0.654	**0.934**	0.913	0.924	0.862	0.855	0.722	0.671
	MAE↓	0.134	0.313	0.217	0.280	0.148	0.285	0.130	**0.105**	0.130	0.157	0.140	0.260	0.274
	OR↑	0.757	0.313	0.581	0.381	0.609	0.358	**0.790**	0.755	0.768	0.641	0.603	0.447	0.402
Overlap (250)[1]	**Metric**	**GR**	**HDCT**	**IT**	**MAP**	**MC**	**MR**	**RPC**	**SEG**	**SeR**	**SIM**	**SR**	**SUN**	**SWD**
	Precision↑	0.96	0.967	0.666	0.96	0.963	0.971	0.956	0.782	0.622	0.515	0.644	0.671	0.872
	Recall↑	0.658	0.747	0.361	0.712	0.702	0.767	0.568	0.216	0.38	0.104	0.365	0.293	0.370
	F-measure↑	0.868	0.906	0.557	0.889	0.887	0.915	0.826	0.487	0.542	0.269	0.547	0.517	0.664
	MAE↓	0.178	0.154	0.304	0.136	0.147	0.114	0.225	0.321	0.311	0.389	0.307	0.326	0.287
	OR↑	0.65	0.728	0.305	0.697	0.690	0.755	0.556	0.214	0.312	0.092	0.304	0.260	0.342

[1] Number of images.

5.3.1 Salient objects located at image boundary

Based on the standard evaluation metrics, Table 5-2 displays detailed results for the investigated methods. In comparison to the learning-based approaches of HDCT and DRFI, the results demonstrated that CHC achieved the best precision (0.945), F-measure (0.932), and OR (0.844), with a marginally lower recall. The DCLC and DSR both scored 0.057, while the CHC recorded the second-best MAE result of 0.062. The performances of DCLC and GR are discernible in addition to the performance of CHC. GR employed a convex hull to estimate salient objects and the centroid of the convex hull as the center prior instead of the image center to favor the identification of salient objects farther away from the image center. In contrast to other diffusion-based approaches like MC and MR, which regarded the nodes that touch the image boundary as background seeds, the DCLC ranked saliency based on foreground seeds acquired through local contrast and succeeded well in this category. For all other evaluation metrics, SIM displayed the worst performance, while the SeR had the lowest precision (0.531). Regardless of the inclusion of a center prior, careful parameter selection has allowed CHC to generate a reliable detection of salient objects placed far from the image center. The average precision, recall, F-measure, MAE, and OR for all the methods under investigation are shown in Figure 5-3 for the border image category.

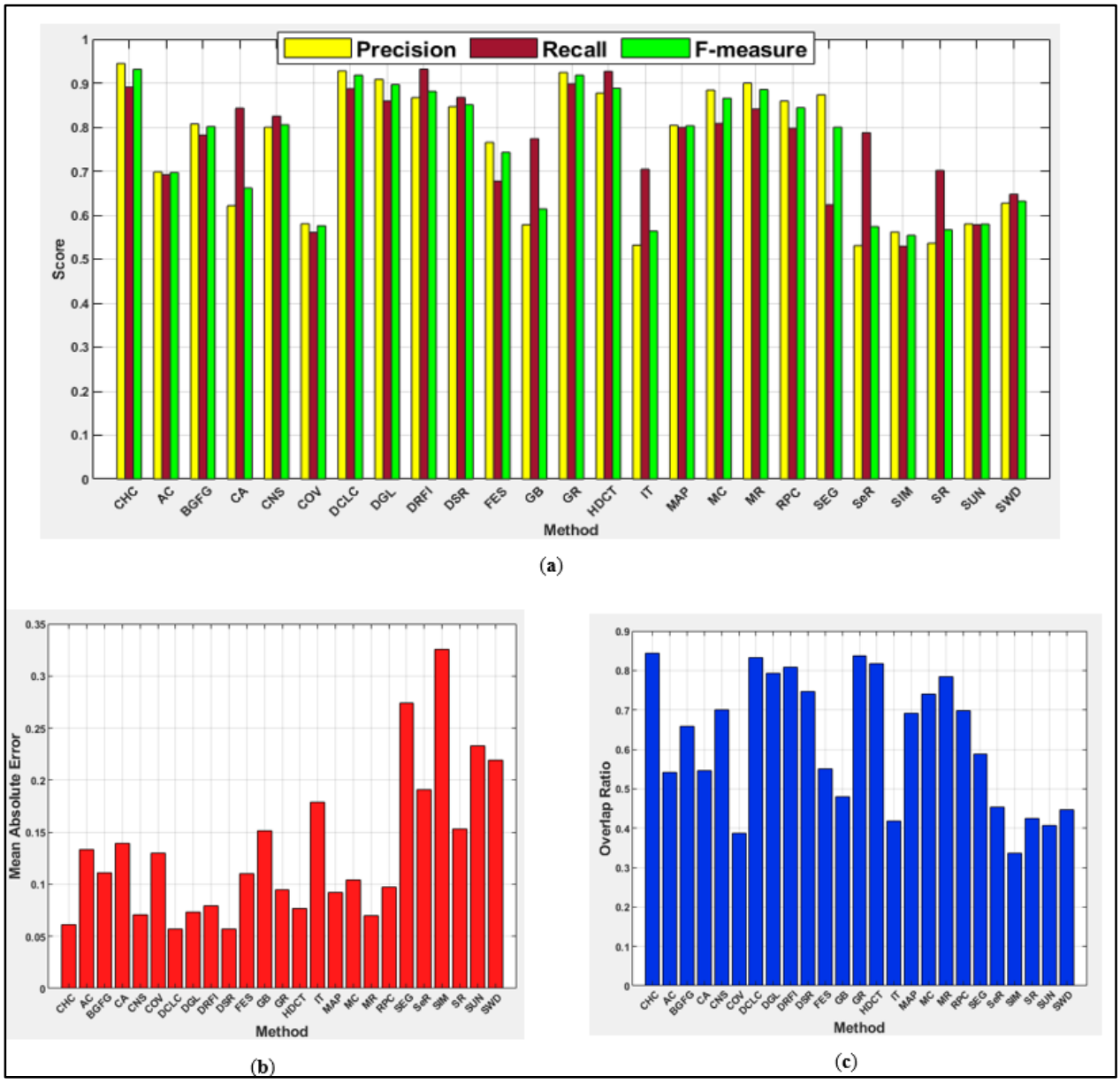

Figure 5-3 (a) F-measure; (b) MAE and (c) OR on image category: boundary

5.3.2 Salient objects located at image center

For the category of salient objects located at the center of the image, the CHC obtained the highest precision (0.949), F-measure (0.934), and OR (0.846). The CNS scored the lowest MAE score of 0.058, followed by MR and DSR with values of 0.061 and 0.062, respectively, and the CHC with a MAE score of 0.067. The DRFI had the highest recall score (0.933). On the center category of images, the DGL exhibited better F-measure and OR results than on the boundary category of images, with SIM being the last. The results also showed that the images with objects that are positioned far from the image boundary and toward the image center, support methods that reap the benefits of the location

prior. This group of images is comparatively simpler. Center prior-based methods like FES, COV, and SWD performed significantly better than the boundary image category. The precision values for

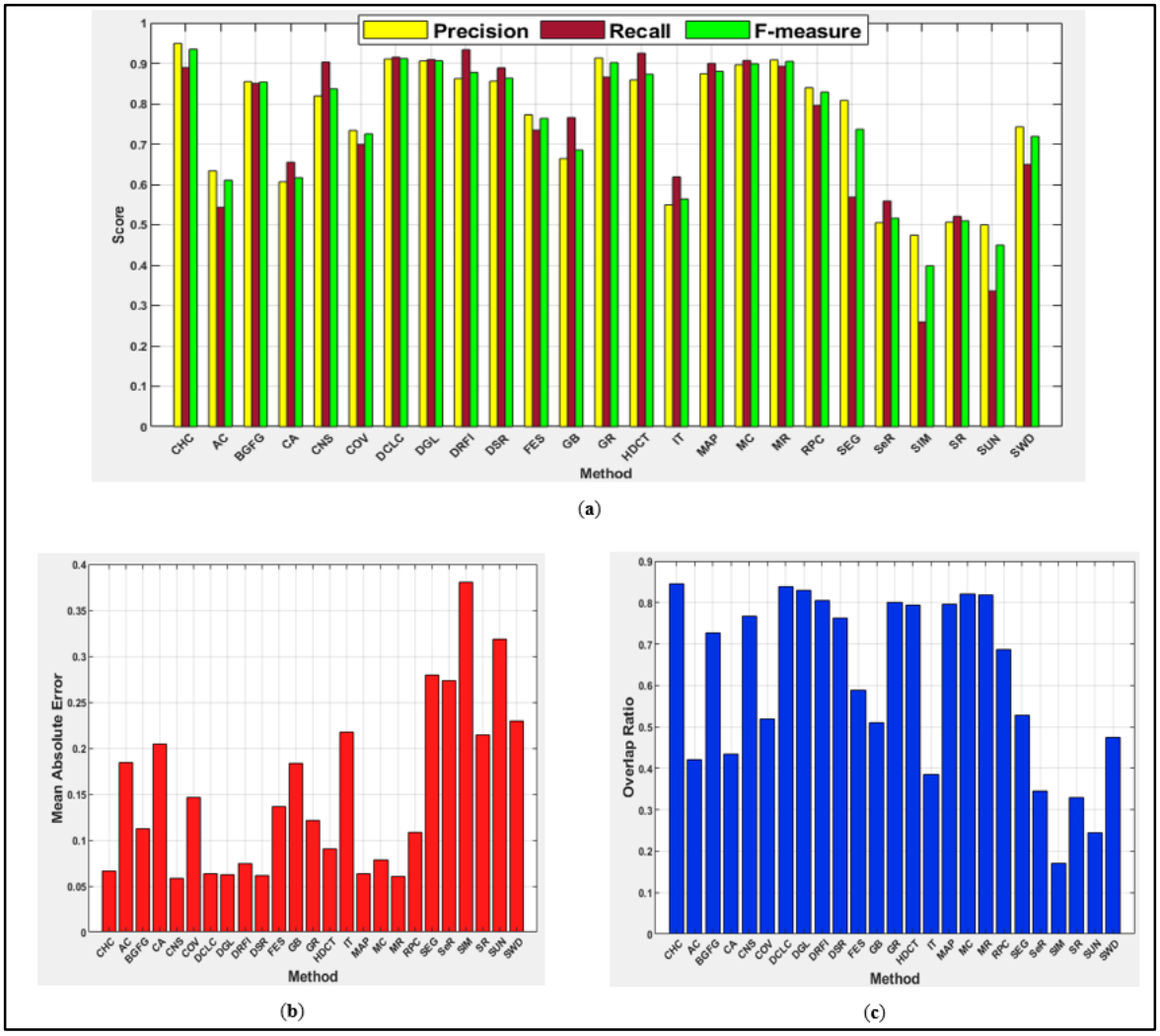

Figure 5-4 (a) F-measure; (b) MAE and (c) OR on image category: center

methods like DCLC, DGL, GR, and MR range between 0.9 and 1.0, whereas average F-measure, MAE, and OR have shown that CHC is superior to the other methods as shown in Figure 5-4.

5.3.3 Salient objects with complex background

The results of the methods under investigation demonstrated that it is typically challenging to detect salient objects in this image category. However, CHC showed a strong ability to accurately identify salient objects, and it is the only method to achieve a precision score above 0.900 with a maximum F-measure of 0.885. Additionally, CHC obtained the best MAE score of 0.120. Surprisingly, DCLC achieved poor results for this category of images while achieving good results for the boundary

and center image categories. DGL and DRFI, on the other hand, enhanced their results for this group of images. In comparison to other manifold ranking-based methods like MR, the deformed smoothness constraint-based manifold ranking approach used by the DGL method has helped to increase performance for this image category. Results for MR showed reduced performance on complex background images as compared to other categories of images, as reported by Ma *et al.* (2021b). Again, the SIM performed poorly with this category of images. For all the methods under investigation, Figure 5-5 displayed the averages for precision, recall, F-measure, MAE, and OR. The outcomes demonstrated the ability of CHC to handle images with complicated backgrounds and established its superiority over the other methods analyzed.

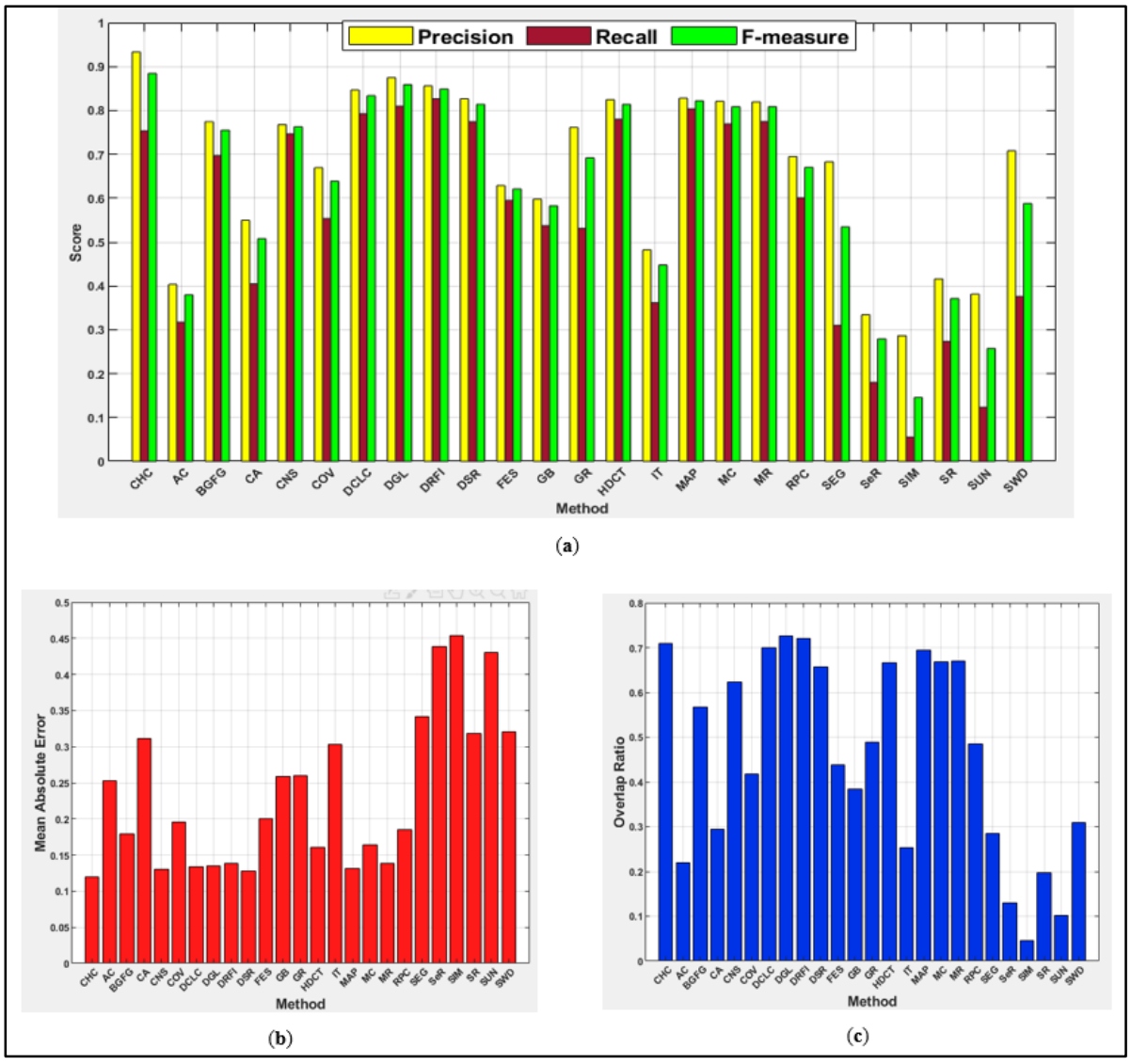

Figure 5-5 (a) F-measure; (b) MAE and (c) OR on image category: complex background

5.3.4 Salient objects with low color contrast

Similar to other image categories, CHC demonstrated the strength in efficiently detecting salient objects from the low contrast object category. Except for recall, it received the highest rankings for the majority of the performance metrics. CHC received a recall value of 0.715 whereas the maximum recall values on images in this category range between 0.7 and 0.8. This study clearly shows that when an object has a similar color contrast to background regions, it is challenging to distinguish salient regions using the currently available methods. This also applies to learning-based methods, as the performance of both HDCT and DRFI on images in this category is not promising. Additionally, when compared to other image categories, contrast prior-based methods including DCLC, GR, CNS, and RPC have shown the lowest performances. Similar to the outcomes of other categories, SIM once more received the lowest values for all the performance metrics. The average precision, recall, F-measure, MAE, and OR of all the approaches are shown in Figure 5-6, where the CHC outperforms the other methods in handling salient objects with low color contrast to the background.

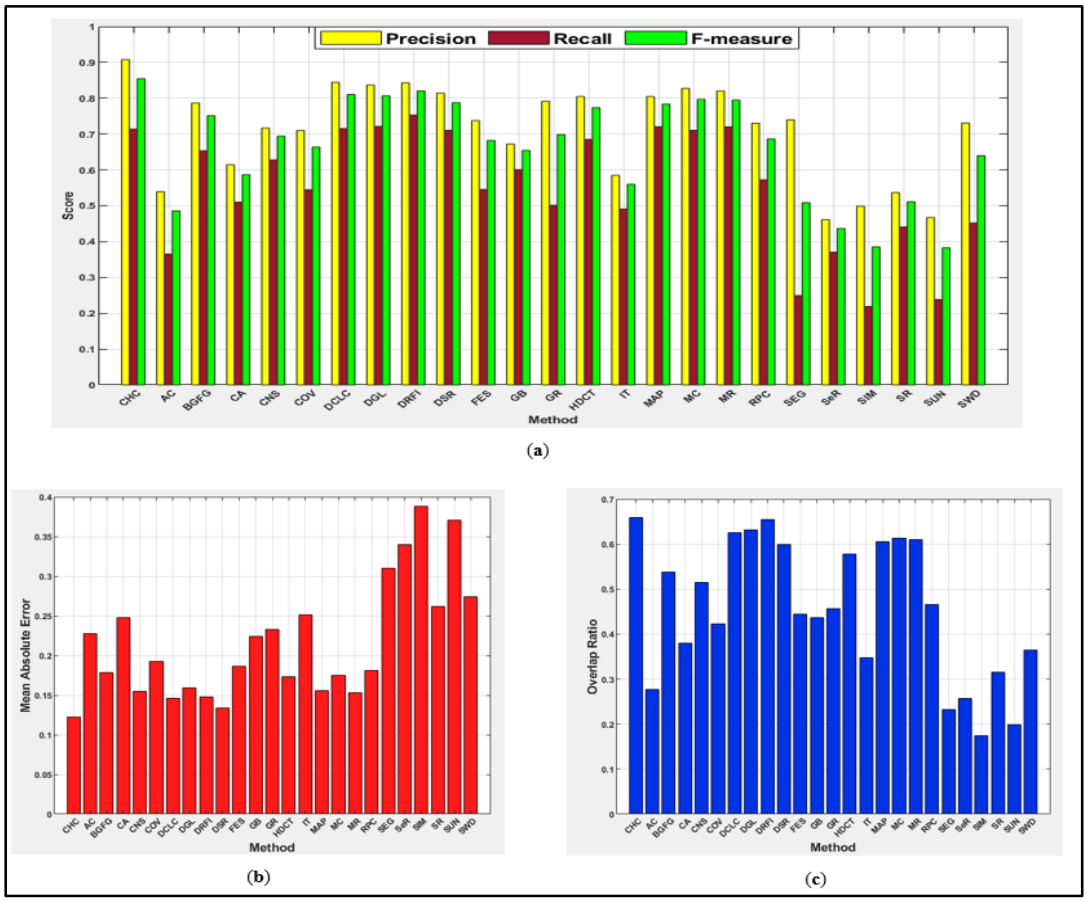

Figure 5-6 (a) F-measure; (b) MAE and (c) OR on image category: low contrast

5.3.5 Multiple salient objects

When salient objects present heterogeneous characteristics in terms of position, color, size, and number, it is challenging to accurately identify them. This image category includes many objects with different positions, sizes, numbers, and colors. However, the performance of CHC was impressive with the highest values for precision (0.876), F-measure (0.853), MAE (0.836), and OR (0.695). The best recall values were achieved by the learning-based DRFI (0.818) and HDCT (0.791), whereas CHC scored the third highest value (0.786). The results from the other methods demonstrated that it was challenging to find multiple salient objects with heterogeneous attributes. All methods displayed comparatively worse MAE performance for this group of images.

Aside from CHC, DGL also demonstrated respectably good performance, with the second-highest values for F-measure (0.834) and OR (0.656). These results demonstrated the shortcoming of COV in detecting multiple salient objects, as it performed comparably poorly to other image categories. This is as a result of taking into account the spatial coincidence assumption in multiscale saliency calculation (Erdem and Erdem 2013). In this category of images, the SIM method once again performed poorly. The average precision, recall, F-measure, MAE, and OR of all the methods examined on the image category with multiple objects are shown in Figure 5-7. The outcomes illustrate the capacity of CHC to handle salient objects with diverse position, count, and size properties.

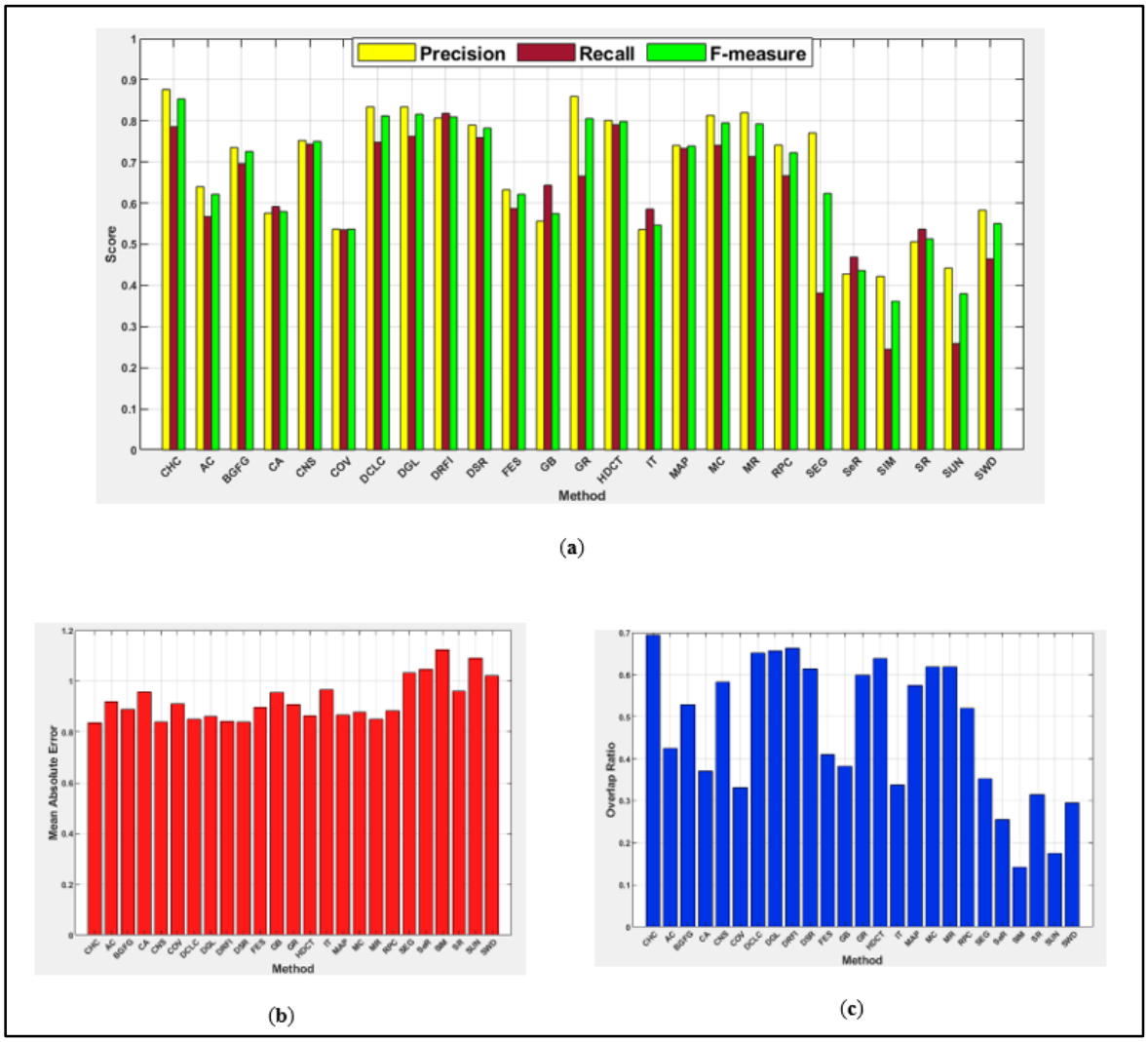

Figure 5-7 (a) F-measure; (b) MAE and (c) OR on image category: multiple salient objects

5.3.6 Overlapped salient objects

Figure 5-8 shows the average precision, recall, F-measure, MAE, and OR scores attained for the overlapped image category. The DCLC obtained the highest recall (0.804), OR (0.790), and F-measure (0.934) in this group of images, making it the top overall performer. With an F-measure of 0.925, CHC is very competitive with DCLC and has the greatest precision value of 0.986. Interestingly, SIM and SUN scored poorer MAE values of 0.389 and 0.326, whereas the graph-based methods of DGL (0.105) and MR (0.114) achieved the best MAE scores. The SIM approach also had the worst performance in this group of images.

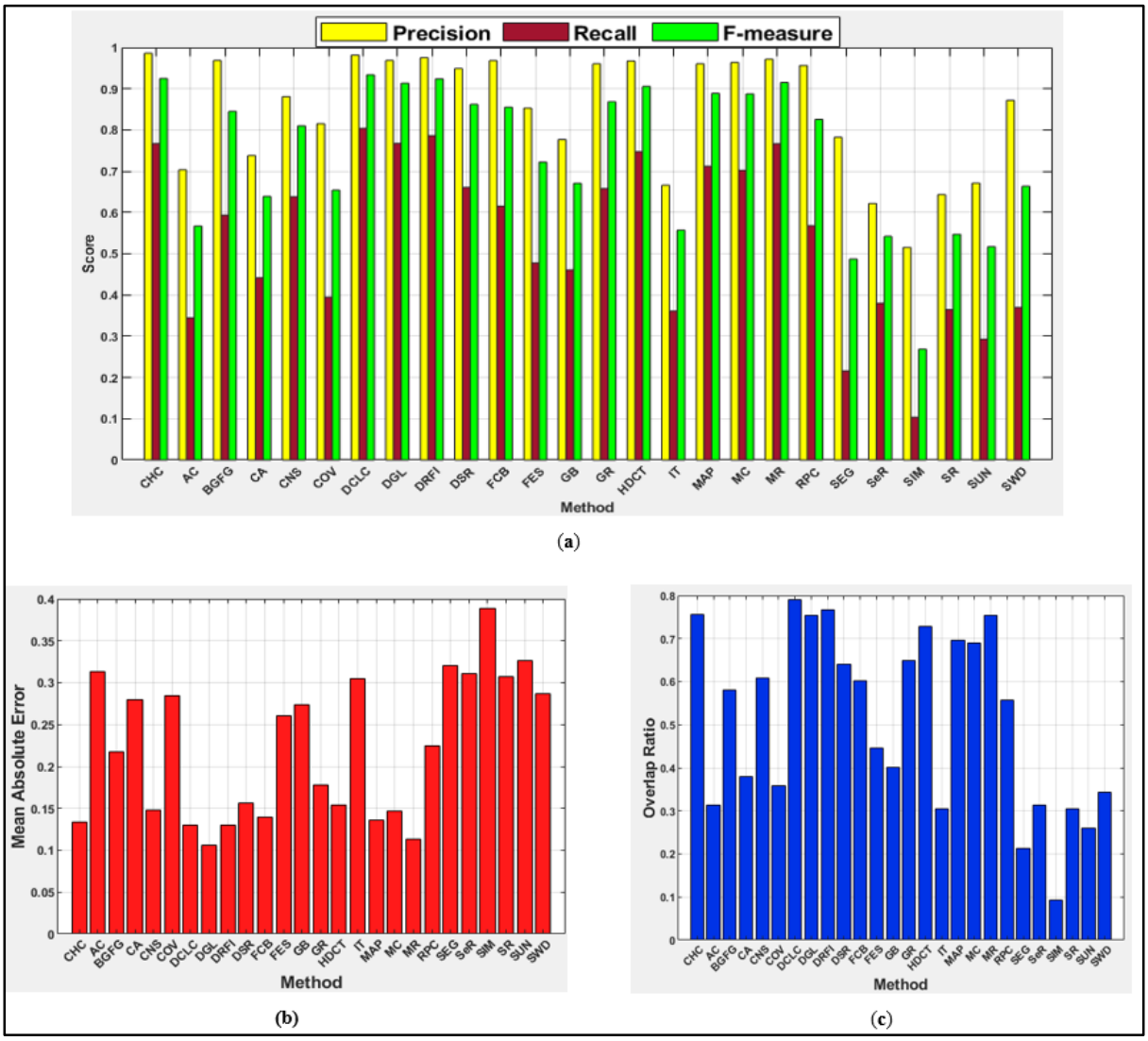

Figure 5-8 (a) F-measure; (b) MAE and (c) OR on image category: overlapped salient objects

5.4 Comparison of algorithms on different image datasets

Seven datasets with various image attributes were chosen to test the effectiveness of the proposed algorithm across various images. These datasets include ECSSD (Shi *et al.* 2015), HKU-IS (Li and Yu 2015), SOC (Fan *et al.* 2018), PH2 (Mendonça *et al.* 2013), ISIC2018 (Codella *et al.* 2019), HAM10000 (Tschandl, Rosendahl and Kittler 2018) and Raabin-WBC (Kouzehkanan *et al.* 2021). A total of 1000 images comprised the ECSSD dataset, which is renowned for its salient objects with varied attributes and occluded backgrounds. HKU-IS is a dataset of 4447 images of complex scenes with numerous dispersed heterogeneous objects that are visually similar to the background and have a varied spatial distribution. Fan *et al.* (2018) recently released a dataset called Salient Objects in Clutter (SOC), which is a subset of the common objects in contexts (COCO) dataset (Lin *et al.* 2014). The SOC dataset was

created to test CNN-based salient object recognition techniques. It contains challenging salient objects with properties that mimic occlusion, background clutter, and challenges in real-world scenarios. Since CHC is not based on the CNN method, it is not equipped to recognize salient objects from occluded or cluttered backgrounds. It was also tested against 1500 images from the SOC dataset to ascertain its capacity to recognize salient objects in real-world settings.

Further, the proposed algorithm was evaluated on dermoscopic and leukocyte image datasets. Dermoscopy is a non-invasive technique for the visual evaluation of a substructure of skin to aid in the analysis of amelanotic lesions, (Emre Celebi *et al.* 2008; Jain and Pise 2015). Early detection of melanoma in skin lesions is strongly advised to reduce complications and the high mortality rates brought on by skin cancer (Jamil *et al.* 2016; Sreelatha, Subramanyam and Prasad 2019). Numerous segmentation methods have been used for the detection and segmentation of skin lesions due to the importance of lesion segmentation in the diagnosis of malignant melanoma (Emre Celebi *et al.* 2008; Garnavi *et al.* 2011; Okuboyejo, Olugbara and Odunaike 2014; Ahn *et al.* 2015; Bi *et al.* 2016; Pennisi *et al.* 2016; Bi *et al.* 2017; Ashour *et al.* 2018; Ali *et al.* 2019; Guarracino and Maddalena 2019; Khan *et al.* 2019; Salih and Viriri 2020; Tan, Zhang and Lim 2020; Li *et al.* 2021b). Hence this study incorporated three dermoscopic image datasets, PH2, ISIC2018, and HAM10000 to assess the performance of CHC in skin lesion segmentation. 200 dermoscopic images of melanocytic lesions comprise the small PH2 dataset.

The ISIC2018 is the largest publicly available dermoscopic image dataset that contains 2594 images and associated ground truths for the study of skin lesions to identify melanoma. Many studies have used small datasets like PH2 extensively (Ahn *et al.* 2015; Bozorgtabar, Abedini and Garnavi 2016; Pennisi *et al.* 2016; Premaladha and Ravichandran 2016; Ahn *et al.* 2017; Bi *et al.* 2017; Fan *et al.* 2017; Olugbara, Taiwo and Heukelman 2018; Patiño, Avendaño and Branch 2018; Youssef *et al.* 2018; Javed *et al.* 2019; Khan *et al.* 2019; Ünver and Ayan 2019; Hu *et al.* 2020; Salih and Viriri 2020; Okuboyejo and Olugbara 2021; Rajput, Tanwar and Raman 2021), while the huge HAM10000 (Tschandl, Rosendahl and Kittler 2018) is a huge dataset of 10015 images of highly complex multisource dermatoscopic images. Although the dataset is frequently used to classify skin lesions, there is no more extensive evidence in the literature on the performance of the images for segmentation (Sae-Lim, Wettayaprasit and Aiyarak 2019; Afza *et al.* 2021; Khan *et al.* 2021; Varalakshmi *et al.* 2021).

The computer-aided analysis of leukocytes for error-free illness diagnosis has been made possible by recent advancements in medical imaging, and these techniques are typically paired with those of image processing and pattern recognition, respectively, for segmentation and classification of leukocytes (Andrade *et al.* 2019). Image segmentation has been suggested in digital hematology as a key tool for carrying out reliable, accurate, and automatic examination of leukocytes. For the diagnosis of diseases and determining the severity of diseases, the detection and segmentation of leukocyte nuclei are essential (Huang, Hung and Chan 2012; Andrade *et al.* 2019; Al-Dulaimi *et al.* 2020; Chen *et al.* 2021). This study used the Raabin-WBC (Kouzehkanan *et al.* 2021) a sizable public health dataset of white blood cells published in 2021 to aid in the experimental comparison and evaluation of approaches for classes of different images, for validating the segmentation performance of the proposed algorithm. Therefore, this study analyzed this newly released dataset of 1145 leukocyte images with ground truth annotation.

A comprehensive evaluation based on both qualitative and quantitative approaches was carried out to validate the performance of the CHC algorithm proposed in this study. The following section illustrates the experimental comparison of the proposed algorithm against the state-of-the-art methods on a wide range of image datasets.

5.4.1 Qualitative comparison of sample images

The qualitative results based on the evaluation of complex and real-world image datasets such as ECSSD, HKU-IS, and SOC are presented in the following section. The visual representation of the results generated by CHC and 26 modern techniques on the ECSSD dataset is shown in Figure 5-9. On images from this dataset, CHC has once more shown astounding results. In this dataset, learning-based techniques like HDCT and DRFI have performed better. The outcomes demonstrated the advantages of CHC over a broad range of image categories, and, when compared to current modern approaches, its output is more trustworthy with outcomes that are practically identical to the ground truth.

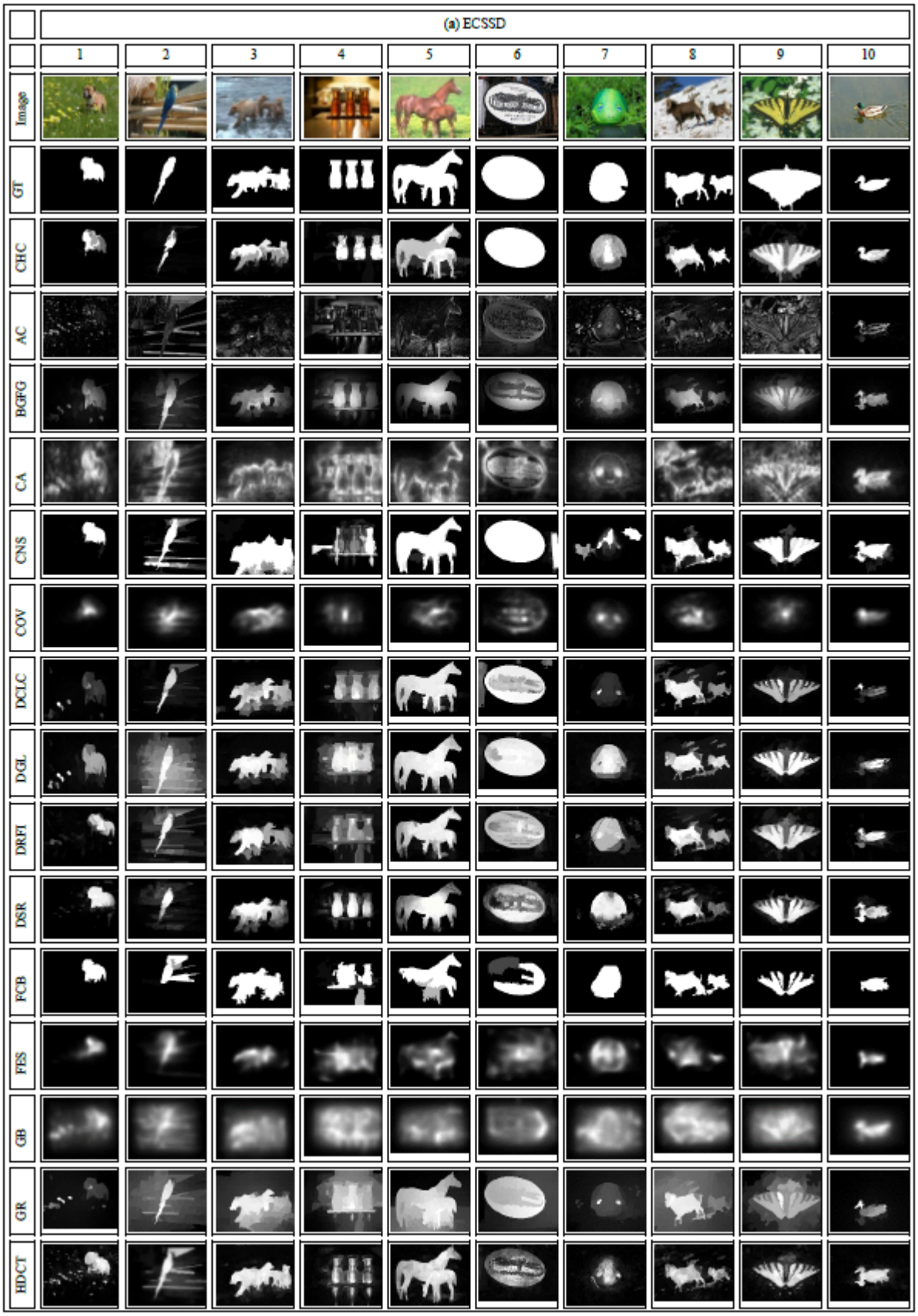
(a) ECSSD
1
2
3
4
5
6
7
8
9
10
Image
GT
CHC
AC
BGFG
CA
CNS
COV
DCLC
DGL
DRFI
DSR
FCB
FES
GB
GR
HDCT

Figure 5-9 Qualitative performance of the investigated methods on the ECSSD dataset

The qualitative performance of CHC on the difficult HKU-IS and SOC datasets was compared to the best-performing methods as in Figure 5-10. The HKU-IS is recognized for its numerous, disjointed salient objects that exhibit a strong resemblance to the background regions. A greater representation of real-world scenes can be found in the SOC image dataset. Results of the CHC and six other methods that generally performed well for the category of multiple objects are visually presented in Figure 5-10. On these two difficult datasets, the CHC performed well, with the results nearly matching the ground truth. When a salient object is surrounded by multiple non-salient objects, as in Figure 5-10(a2), CHC highlighted the salient object to match the image from the ground truth, while other methods identified all of the objects on the table. According to the visual comparison shown in Figure 5-10, many of the available methods struggled to distinguish salient items with heterogeneous features, such as illumination, size, position, and quantity, from a background that is cluttered and representative of a real-world scene. Nevertheless, despite the complexity of these images, CHC performed admirably.

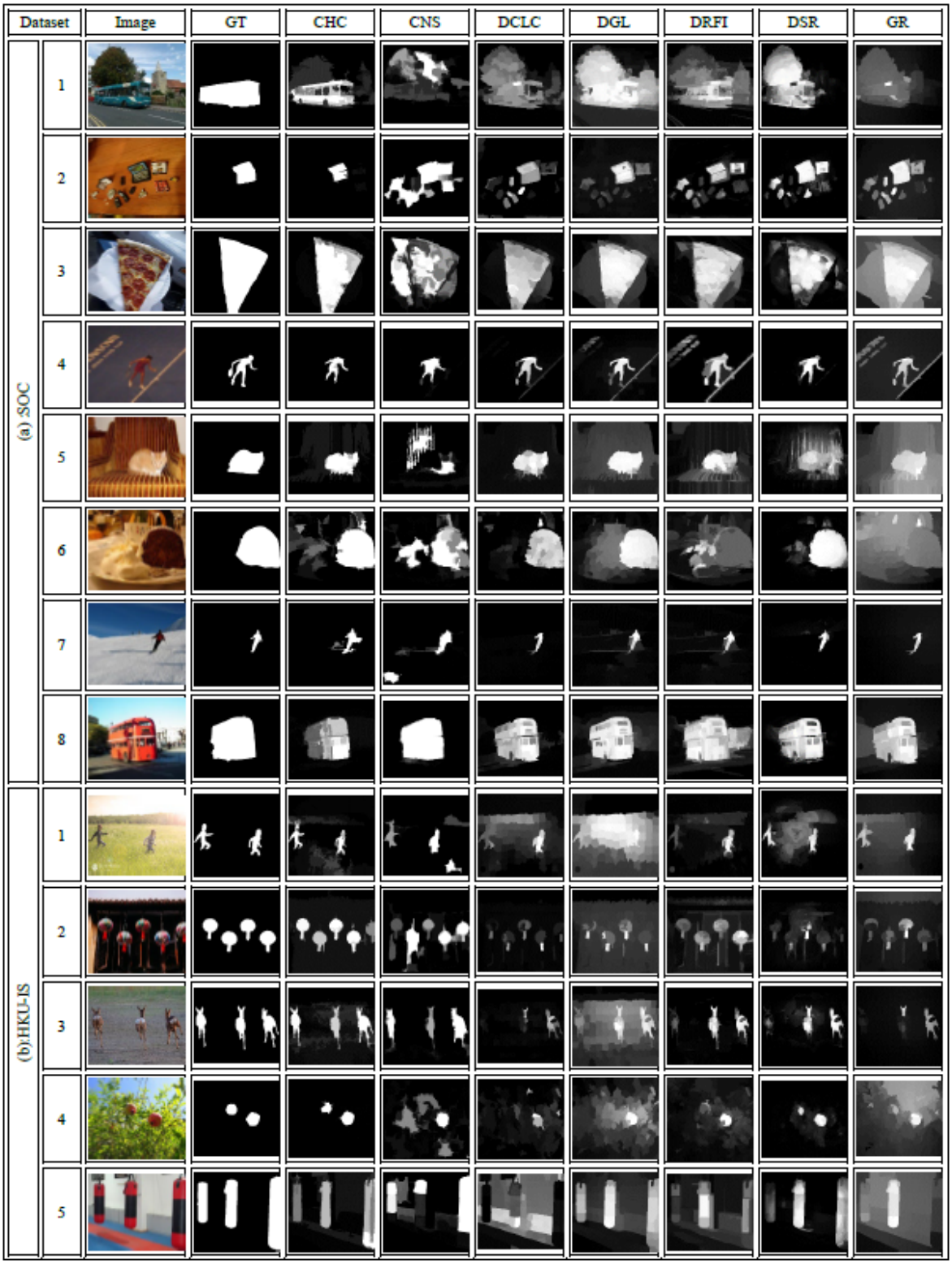
Dataset
Image
GT
CHC
CNS
DCLC
DGL
DRFI
DSR
GR
(a) SOC
1
2
3
4
5
6
7
8
(b)HKU-IS
1
2
3
4
5

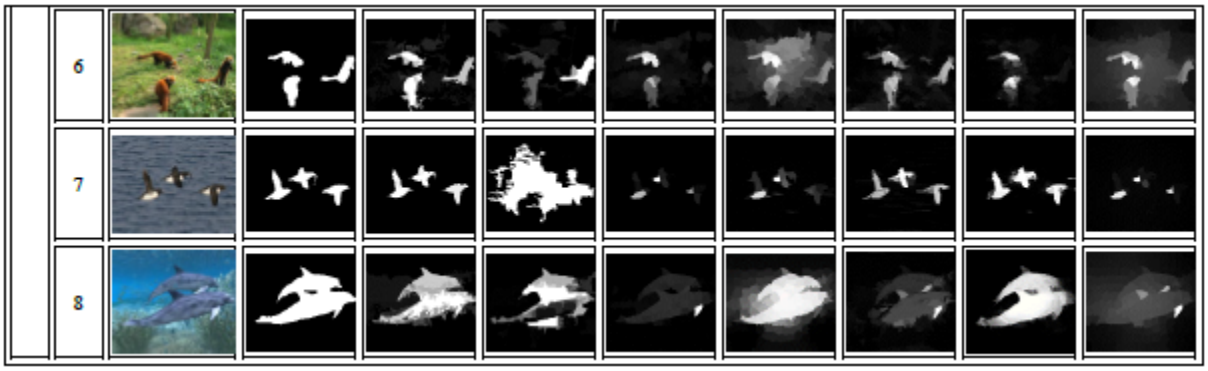

Figure 5-10 Qualitative performance of the proposed algorithm on SOC and HKU-IS datasets

For the experimental comparison of the dermoscopic image datasets of PH2, ISIC2018, and HAM100015, this study included a set of supervised and unsupervised segmentation methods. These include the leading supervised methods: SPCA (Bi *et al.* 2016), (Youssef *et al.* 2018), RU-Net and R2U-Net (Alom *et al.* 2018), YOLO (Ünver and Ayan 2019), R2AU-Net (Zuo, Chen and Wang 2021), (Li *et al.* 2021b) and unsupervised methods: SSLS (Ahn *et al.* 2015), ASLM (Pennisi *et al.* 2016), (Patiño, Avendaño and Branch 2018), SDI (Guarracino and Maddalena 2019), (Salih and Viriri 2020), and (Rajput, Tanwar and Raman 2021). The details of these methods are given in Table 5-3. For the methods of SDI+ and SPCA, the segmentation results were obtained using the source code with the default parameters recommended by the authors. It is important to note that the source code of the rest of the methods are not available, hence this study relied on the statistics published in the original references or the literature for quantitative evaluation and these methods were excluded from the visual comparison on PH2, ISIC2018 and HAM10000.

Table 5-3 Segmentation methods used for comparison in dermoscopic image datasets

No	Study	Approach	Segmentation method
1	SSLS (Ahn *et al.* 2015)	Unsupervised	Clustering and saliency
2	ASLM (Pennisi *et al.* 2016)	Unsupervised	Color region merging and thresholding
3	SPCA(Bi *et al.* 2016)	Supervised	Clustering and Cellular automata
4	(Youssef *et al.* 2018)	Supervised	Semantic segmentation based on deep learning encoder and decoder
5	(Patiño, Avendaño and Branch 2018)	Unsupervised	Superpixel clustering and thresholding
6	R2U-Net (Alom *et al.* 2018)	Supervised	Recurrent, Residual convolutional neural network
7	YOLO (Ünver and Ayan 2019)	Supervised	Deep convolutional network and Grabcut
8	SDI+ (Guarracino and Maddalena 2019)	Unsupervised	Thresholding
9	(Salih and Viriri 2020)	Unsupervised	Stochastic region-merging
10	(Li *et al.* 2021b)	Supervised	Semantic segmentation based on u-Net
10	R2AU-Net (Zuo, Chen and Wang 2021)	Supervised	Recurrent residual convolutional neural network with attention gate connection
12	(Rajput, Tanwar and Raman 2021)	Unsupervised	Clustering and partially order homomorphic Permutation Ordered Binary (POB) number system

Some examples of the segmentation results of the proposed algorithm versus state-of-the-art methods are illustrated in Figures 5-11 to 5-13. The first row shows the original images, the second row is the ground truth images, and rows 3 to 5 respectively represent the segmentation results of CHC, SPCA, and SDI+. Figure 5-11 demonstrates the visual performance achieved from the PH2 dataset. The PH2 dataset contains extreme cases when lesions touch the multiple image boundaries as in Figure 5-11 (1-5) and normal cases where the lesion is within the image as in Figure 5-11(6-10) (Ahn *et al.* 2017). It is worth noting that, CHC segmented the region of interest with a high resemblance to the corresponding ground truth regardless of the skin lesion location and the characteristics of surrounding regions.

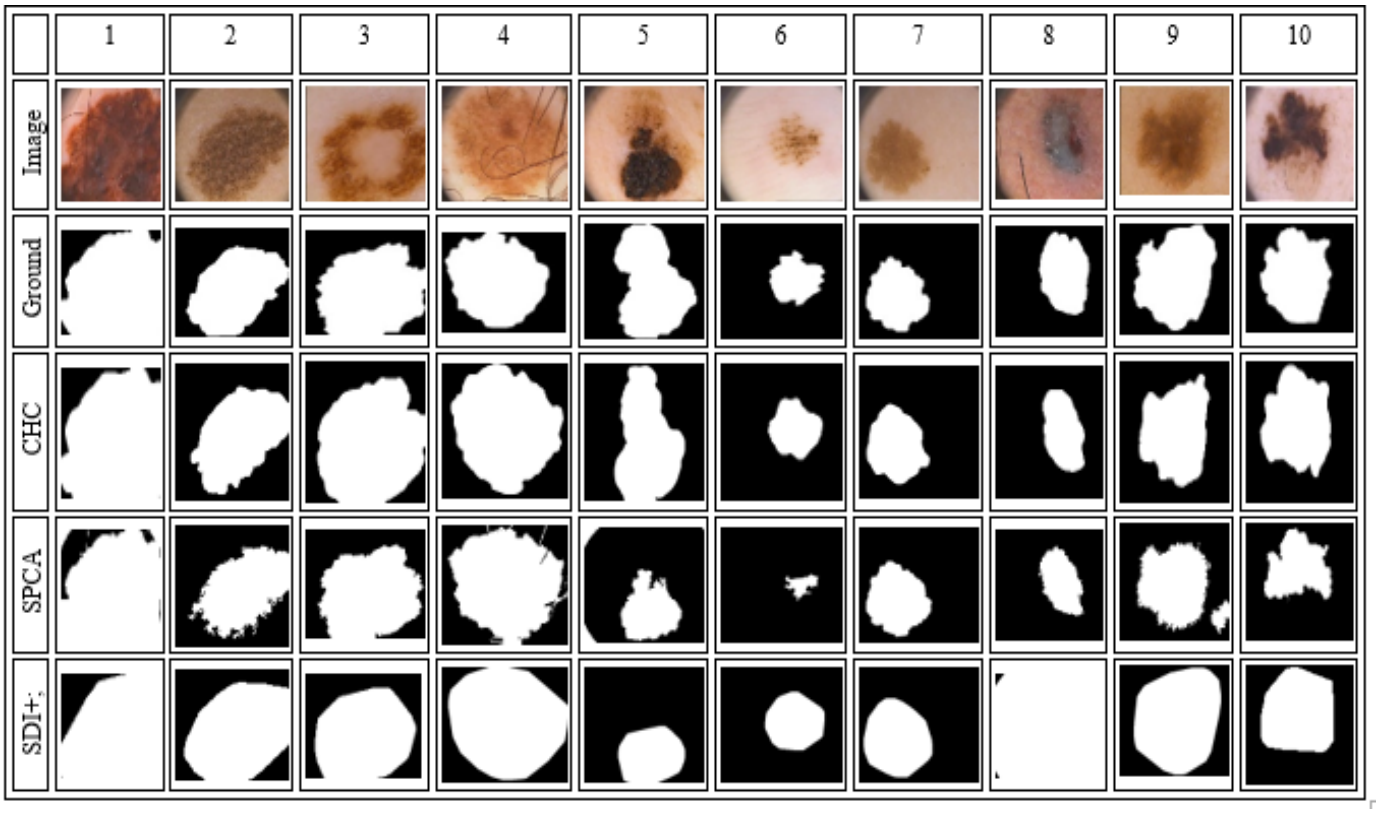

Figure 5-11 Qualitative results on PH2 dataset

Similarly, Figure 5-12 displays the sample of segmentation results from the ISIC2018 dataset. All methods reasonably performed well on images as illustrated in Figure 5-12 (b, c, g, and h) where the dermoscopy images are free from complex artifacts. However, the performance of these methods on the rest of the images presented in Figure 5-12 declined because of the various types of artifacts. In contrast, the proposed algorithm performed well on all images irrespective of the artifacts such as hair, marker, vignette noise/dark frame, ruler marks, marker ink, and bubbles.

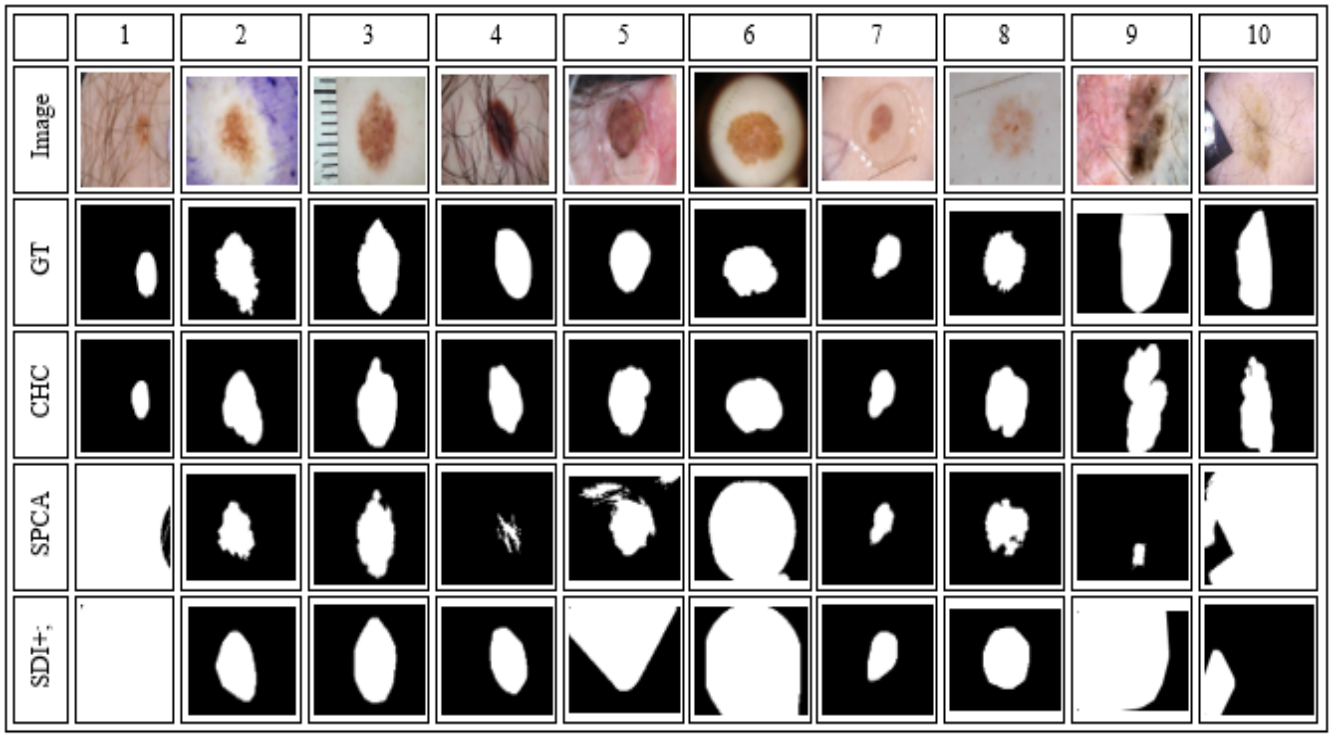

Figure 5-12 Qualitative results on ISIC2018

CHC successfully managed to produce consistent segmentation results on the HAM10000 dataset as shown in Figure 5-13. However, the segmentation quality of the rest of the methods is strongly decreased especially on images with artifacts such as the presence of hair (Figure 5-13 (5, 8, 9)), and irregular borders (Figure 5-13 (1-3)). The segmentation results of CHC on all images in Figures 5-11 to 5-13 show its ability to produce quality results regardless of the artifacts, presence of irregular borders, and heterogeneity of skin lesions. The application of histogram clustering and appropriate integration of color and spatial features has contributed greatly to the outstanding performance of the proposed algorithm.

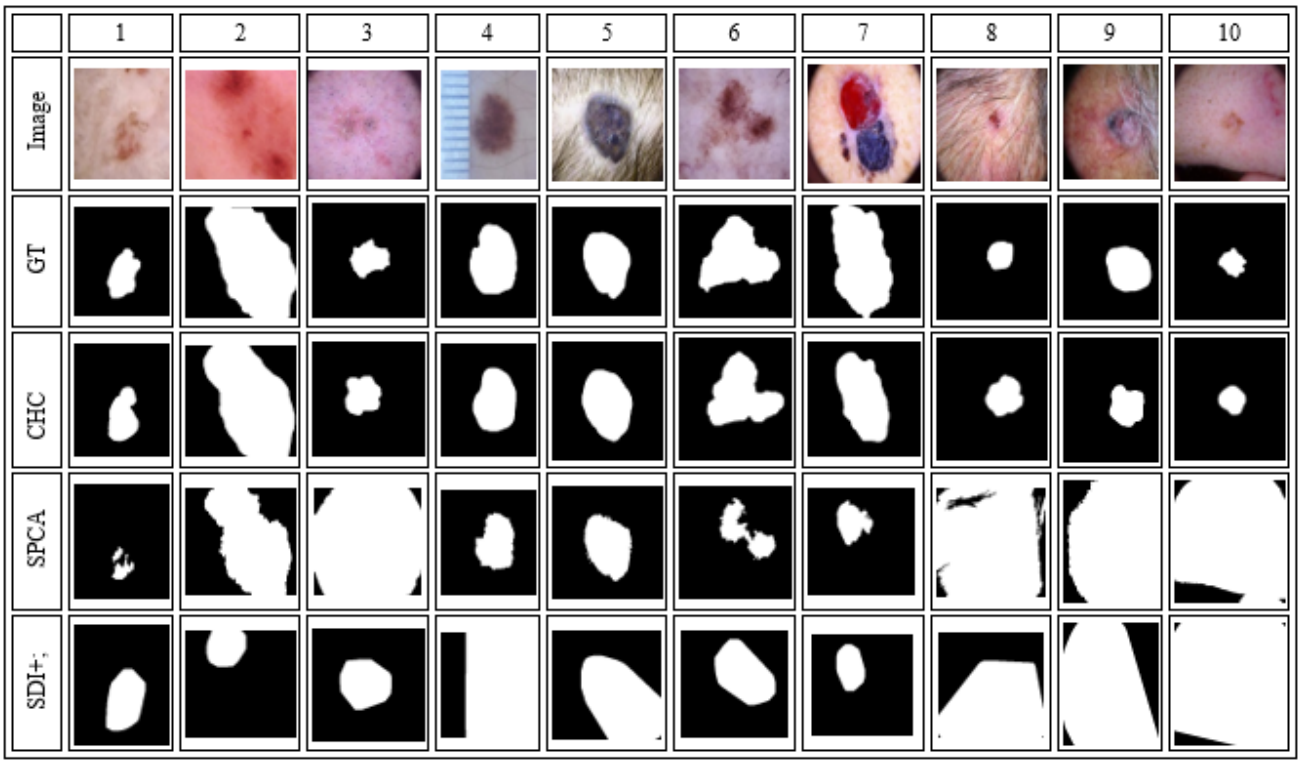

Figure 5-13 Qualitative results on HAM10000 dataset

The visual observation of the segmentation outcomes of the leukocyte image dataset, Raabin-WBC, against the ground truth annotation was assessed using qualitative analysis. The 10 modern saliency models that integrated center prior, background prior, or border prior have been empirically examined for segmenting leukocyte nuclei in this work, which was driven by the notion that leukocyte nuclei are typically positioned in the center. Figure 5-14 confirmed the visual comparison outcomes of the chosen methods on the Raabin WBC dataset. Here the CHC indicates the saliency map and the CHC* represents the binary map after the inclusion of Otsu thresholding for the two-class binary segmentation.

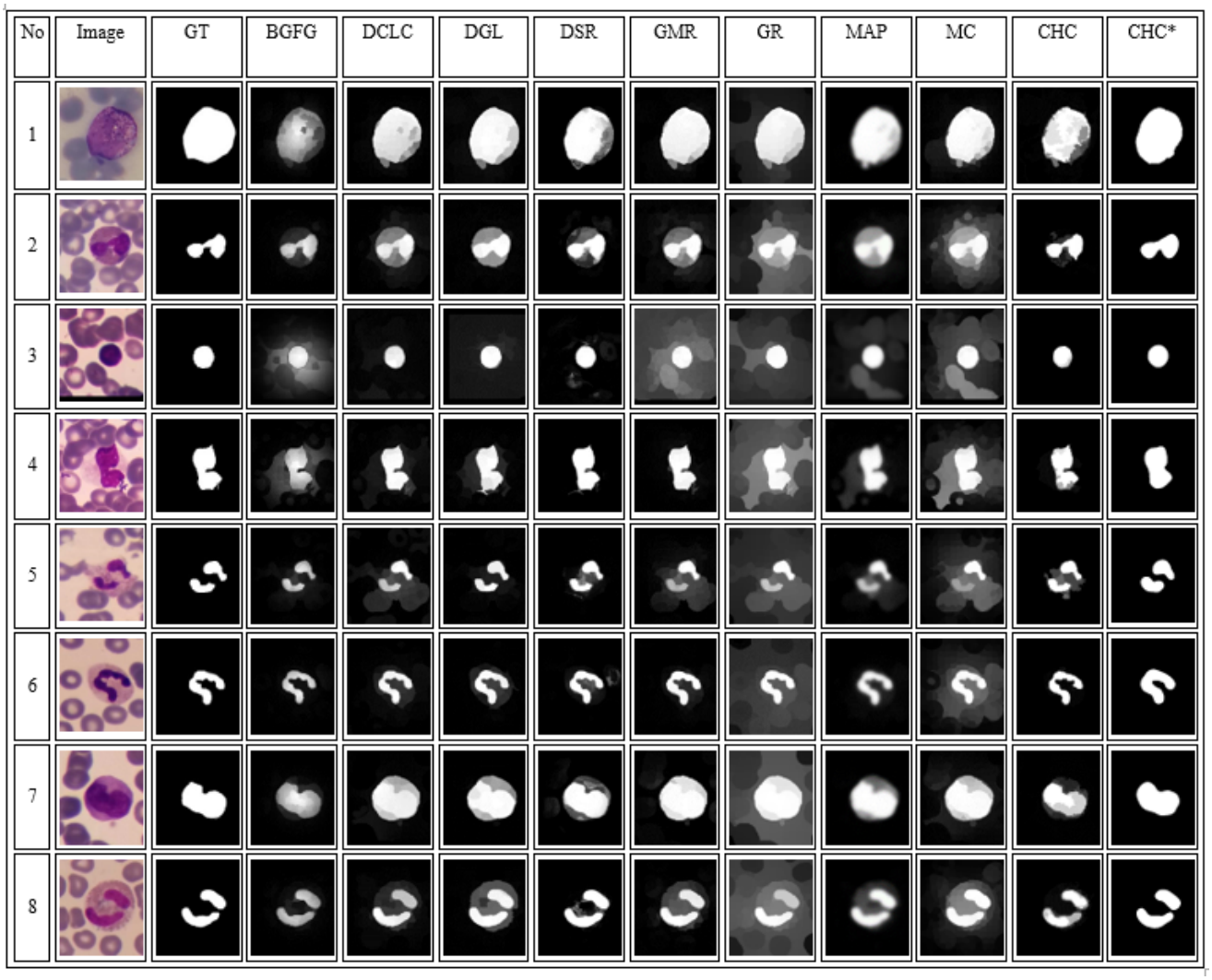

Figure 5-14 Qualitative results on the Raabin-WBC dataset

It is evident from the results that most of the methods are functioning well in recognizing the salient region with well-formed edges regardless of the kind of leukocyte nuclei. This is due to the utilization of intrinsic cues such as center prior, background, and border priors. However, Otsu thresholding combined with morphological operations favors the CHC* to give segmentation results that closely resemble the ground truth images.

5.4.2 Quantitative comparison of complex scene image datasets

Images of ECSSD, HKU-IS, and SOC were further used for the quantitative evaluation of the proposed algorithm. On the ECSSD dataset, the CHC results were evaluated against all 30 bottom-up saliency methods as shown in Table 5-4 and Figure 5-15. The ECSSD dataset is well recognized for including complex images, but CHC is superior because it has attained the best precision (0.853), F-

measure (0.790), MAE (0.163), and OR values (0.573). The high recall value of 0.820 was achieved by BPFS. The graph-based methods of DGL, FBSS, and MRBF as well as the learning-based method of DRFI also produced superior results; nevertheless, only the CHC was able to attain precision above 0.800. The foreground and backgrounds seed selection methods, such as MRBF and FBSS, have also outperformed the background and foreground seed selection method, BGFG, in terms of MAE scores. The DCLC that outperformed and demonstrated excellence in the overlap image category saw a fall in performance on the ECSSD dataset. Except for the MAE, the SIM approach displayed the lowest value for most performance indicators, whereas the SUN method comparatively displayed the lowest value for MAE. These experiments have successfully demonstrated the capability of CHC to detect salient objects across a broad range of image categories.

Table 5-4 Performance statistics on ECSSD dataset (1000 images) in terms of precision (↑), recall (↑), F-measure (↑), MAE (↓), and OR (↑). The top outcomes are shown by bold values. The up arrow, ↑ denotes greater performance at higher values, and the down arrow, ↓ denotes better performance at lower values.

Method	Precision	Recall	F-measure	MAE	OR	Method	Precision	Recall	F-measure	MAE	OR
CHC	**0.853**	0.635	**0.790**	**0.163**	**0.573**	GR	0.714	0.391	0.600	0.283	0.348
AC	0.439	0.300	0.396	0.210	0.263	HDCT	0.767	0.640	0.733	0.198	0.519
BGFG	0.723	0.606	0.692	0.208	0.467	IT	0.570	0.406	0.521	0.289	0.285
BPFS	0.660	**0.820**	0.690	0.166		MAP	0.758	0.661	0.733	0.185	0.534
CA	0.532	0.374	0.485	0.310	0.266	MC	0.768	0.652	0.738	0.202	0.531
CNS	0.708	0.600	0.680	0.166	0.480	MCVS	0.780	0.540	0.700	0.170	
COV	0.679	0.527	0.636	0.215	0.388	MR	0.767	0.647	0.736	0.186	0.525
CSV	0.760	0.650	0.740	0.210		MRBF	0.780	0.670	0.760	0.177	
DCLC	0.769	0.636	0.734	0.182	0.530	RPC	0.629	0.489	0.590	0.218	0.372
DGL	0.785	0.655	0.750	0.191	0.548	SEG	0.662	0.230	0.462	0.340	0.212
DRFI	0.794	0.698	0.769	0.170	0.572	SeR	0.366	0.207	0.311	0.404	0.144
DSR	0.753	0.647	0.726	0.171	0.517	SIM	0.365	0.078	0.197	0.433	0.062
FBSS	0.770	0.560	0.709	0.169		SR	0.460	0.302	0.411	0.311	0.212
FCB	0.721	0.515	0.660	0.173	0.422	SUN	0.384	0.102	0.235	0.437	0.087
FES	0.672	0.545	0.638	0.212	0.404	SWD	0.704	0.354	0.573	0.318	0.283
GB	0.629	0.519	0.600	0.263	0.364						

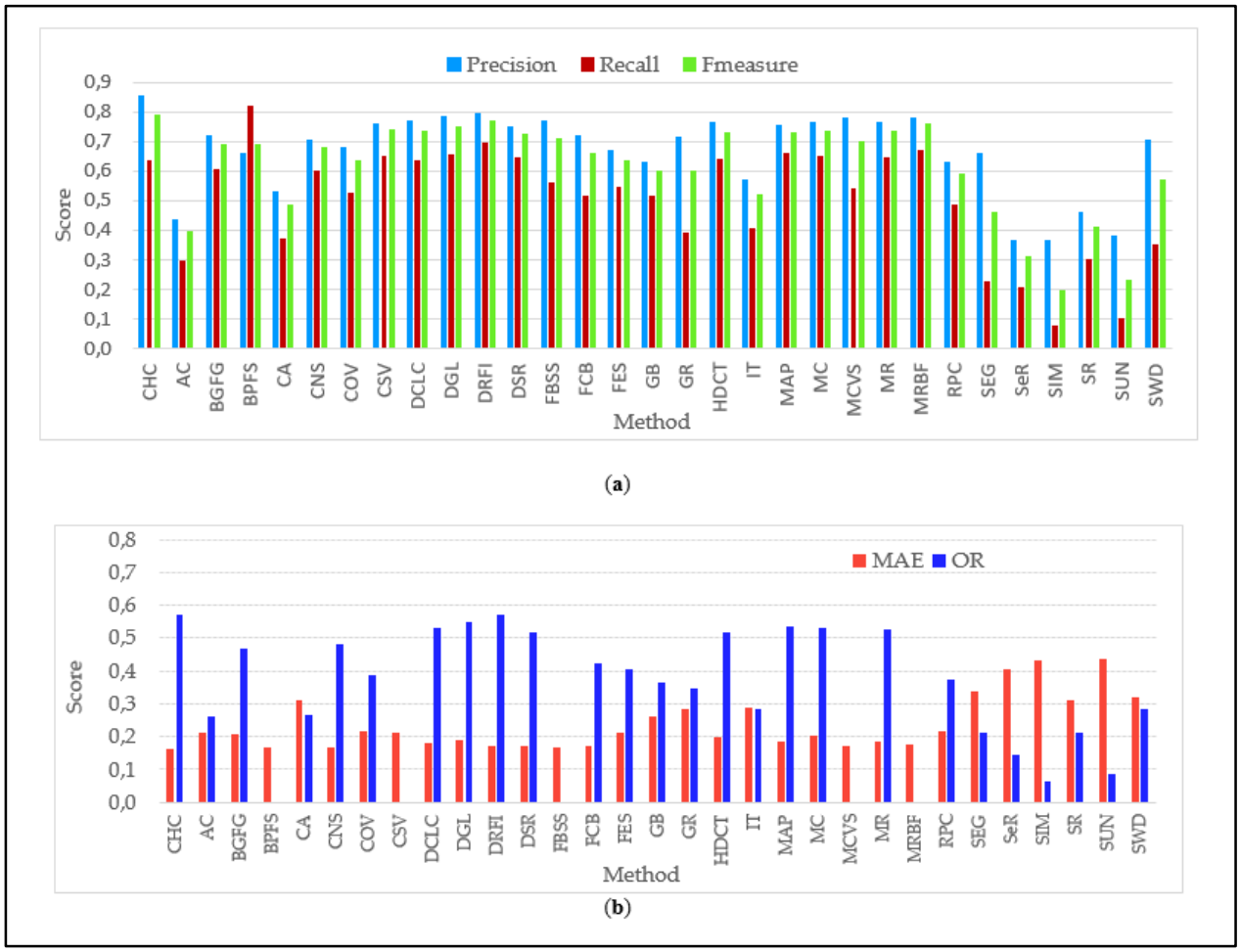

Figure 5-15 (a) F-measure; (b) MAE and OR on ECSSD dataset

The proposed algorithm, CHC is not related to top-down or deep-learning-based methods. Although CHC is not connected to top-down or deep-learning-based approaches, this study has expanded the quantitative comparison to seven deep-learning-based top-down saliency detection methods on the ECSSD dataset to show the superiority of the CHC. Bottom-up saliency methods have recently faced some difficulties due to the performance of deep learning-based top-down methods (Ding *et al.* 2020). However, the effectiveness of CHC has shown that bottom-up saliency detection methods may successfully compete with deep-learning-based top-down, methods. Table 5-5 compared CHC with deep learning methods using the F-measure and MAE values given by the original references. Despite the complexity of the ECSSD dataset, the CHC has the highest F-measure (0.790) when compared to deep-learning-based methods. The deep learning method of DS has a relatively best MAE value of 0.160, but the MAE value of CHC is 0.163, which is a very competitive outcome. This outcome demonstrated that CHC is even more competitive versus deep-learning-based top-down methods.

The performance of the deep-learning-based MSNSD-A and MSNSD methods, respectively, scored the second and third best F-measure values and higher than those of other bottom-up methods, including the graph-based and learning-based methods listed in Table 5-4, as shown by the F-measure and MAE scores in Tables 5-4 and 5-5. Deep learning techniques of DS (0.160) and LCNN (0.162) received the highest values in terms of MAE scores, demonstrating that their saliency maps are reasonably close to the ground truth. The effectiveness of these methods, however, heavily relies on supervised learning based on labeled training data (Zhang and Wang 2021). Deep learning methods are constrained from using real-time and various categories of images because of their great sensitivity to and dependence on training datasets (Gupta *et al.* 2020; Wang *et al.* 2021a).

Table 5-5 Comparison of deep learning methods using the F-measure (↑) and MAE (↓) on the ECSSD dataset. Bold is used to highlight the best outcomes.

Method	F-Measure	MAE
MSNSD-A (Liang, Liu and Ma 2019)	0.777	0.171
MSNSD (Liang, Liu and Ma 2019)	0.774	0.179
DS (Li *et al.* 2016)	0.759	**0.160**
LCNN (Li *et al.* 2017b)	0.715	0.162
(Nasiripour, Farsi and Mohamadzadeh 2019)	0.430	0.255
TSL (Yan *et al.* 2020)	0.737	0.178
MCDL (Zhao *et al.* 2015a)	0.732	
CHC	**0.790**	0.163

The performance of the investigated methods in terms of precision, recall, F-measure, MAE, and OR on HKU-IS and SOC datasets are summarized in Table 5-6. The methods of DCLC, DGL, and DRFI were taken into consideration in the comparison using two datasets because they demonstrated comparably strong performances on all selected categories of images. The HKU-IS is well known for images with several salient objects, and these methods are among the best performing methods, notably for the category of images with multiple objects. Additionally, the F-measure and MAE scores stated in the original references were used to compare three deep learning methods MSNSD-A, MSNSD, and MCDL on the HKU-IS dataset. Due to the lack of access to their source codes, this study did not compare any other deep learning techniques on the SOC dataset. On the HKU-IS dataset, CHC achieved the second-highest F-measure (0.776), while the deep learning methods MSNSD-A and MSNSD scored the highest F-measure (0.837) and lowest MAE (0.071). Furthermore, CHC achieved the highest precision (0.813) and OR results (0.578). On the SOC dataset, all methods generally performed poorly. On realistic images with obscured and cluttered backgrounds, it was noted in the literature that existing saliency detection algorithms often performed poorly, with an F-measure of less than 0.45 (Fan *et al.* 2018). The experimental findings of this study proved that the performance of the investigated methods declined in this dataset. Surprisingly, DCLC, DGL, and DRFI got 0.543, 0.552, and 0.561

correspondingly, whereas CHC achieved an F-measure of 0.618. Additionally, CHC achieved comparably the best scores for MAE (0.202) and OR (0.389).

Table 5-6 Precision (↑), recall (↑), F-Measure (↑), MAE (↓), and OR (↑) of the proposed algorithm against others on HKU-IS and SOC datasets. The best results are highlighted in bold.

Datasets	**HKU-IS**					**SOC**				
Metrics	**Precision**	**Recall**	**F-Measure**	**MAE**	**OR**	**Precision**	**Recall**	**F-Measure**	**MAE**	**OR**
DCLC	0.724	0.653	0.707	0.160	0.517	0.558	0.499	0.543	0.215	0.236
DGL	0.725	0.672	0.712	0.189	0.528	0.568	0.505	0.552	0.263	0.244
DRFI	0.753	**0.755**	0.754	0.144	0.577	0.560	**0.563**	0.561	0.219	0.356
MSNSD-A	-	-	**0.837**	**0.071**	-	-	-	-	-	-
MSNSD	-	-	**0.837**	**0.071**	-	-	-	-	-	-
MCDL	-	-	0.743	0.093	-	-	-	-	-	-
CHC	**0.813**	0.673	0.776	0.144	**0.578**	**0.650**	0.531	**0.618**	**0.202**	**0.389**

5.4.3 Quantitative comparison on dermoscopic image datasets

Based on the commonly used performance measures of accuracy, sensitivity, specificity, and dice similarity, the segmentation results on dermoscopic image datasets were evaluated to the top supervised and unsupervised methods to assess the performance of CHC. The findings in Table 5-7 showed that CHC had the highest specificity value. The accuracy score of 0.92 attained by CHC was extremely competitive with that of the YOLO supervised deep learning method, which recorded the greatest accuracy score of 0.93. The CHC successfully predicted the non-lesion pixels, as evidenced by the high specificity score of 0.98. The CHC and the algorithm provided in (Patiño, Avendaño and Branch 2018) recorded the second-best Dice score of 0.89, which is very near to the maximum Dice score of 0.90 by (Salih and Viriri 2020). These results demonstrated the efficiency of CHC in extracting a significant amount of skin lesion pixels from the non-lesion pixels. Despite the 95% specificity score, the SPCA recorded the lowest sensitivity score of 73%.

Table 5-7 Performance comparison of the proposed algorithm against leading algorithms on the PH2 dataset (200 images)

Method	**Accuracy**	**Sensitivity**	**Specificity**	**Dice**
SSLS (Ahn *et al.* 2015)[a]	0.85	0.75	**0.98**	0.78
ASLM (Pennisi *et al.* 2016)[a]	0.90	0.80	0.97	0.83
(Youssef *et al.* 2018)[b]	0.89	**0.92**	0.87	0.87
(Rajput, Tanwar and Raman 2021) [a]	0.86	0.83	0.92	0.88
(Patiño, Avendaño and Branch 2018)[a]	0.90	0.91	0.89	0.89
SDI+ (Guarracino and Maddalena 2019)[a]	0.91	**0.92**	0.90	0.85
(Salih and Viriri 2020)[a]	0.92	0.84	0.96	**0.90**
SPCA (Bi *et al.* 2016) [b]	0.87	0.73	0.95	0.80
YOLO (Ünver and Ayan 2019)[b]	**0.93**	0.84	0.94	0.88
CHC [a]	0.92	0.85	**0.98**	0.89

[a] unsupervised method; [b] supervised method.

On the ISIC2018 dataset, the CHC received the highest specificity value (0.99), as shown in Table 5-8. The highest accuracy score of 0.93 and Dice score of 0.87 was achieved by the supervised methods (Li *et al.* 2021b) and Attention ResU-Net (Zuo, Chen and Wang 2021). The method proposed by Li *et al.* (2021b) and SDI+ (Guarracino and Maddalena 2019) obtained the greatest sensitivity score of 0.87. Despite having a specificity score of almost 90%, SPCA had the lowest sensitivity score (0.59), which was relatively low. These findings showed that CHC is competent because it achieved the best specificity score of 0.99 and the second-highest accuracy score of 0.92.

Table 5-8 Performance comparison of the proposed algorithm against leading algorithms on the ISIC2018 dataset (2594 images)

Methods	Accuracy	Sensitivity	Specificity	Dice
SDI+ (Guarracino and Maddalena 2019)[a]	0.87	**0.87**	0.89	0.75
SPCA (Bi *et al.* 2016)[b]	0.84	0.59	0.92	0.62
(Li *et al.* 2021b)[b]	**0.93**	**0.87**	0.97	**0.87**
RU-Net(Alom *et al.* 2018)[b]	0.88	0.79	0.93	0.68
R2U-Net(Alom *et al.* 2018)[b]	0.90	0.73	0.97	0.69
Attention ResU-Net (Zuo, Chen and Wang 2021)[b]	0.92	0.84	0.95	0.85
R2AU-Net (Zuo, Chen and Wang 2021)[b]	**0.93**	0.82	0.97	**0.87**
CHC[a]	0.92	0.78	**0.99**	0.81

[a] unsupervised method; [b] supervised method

In addition to the performance evaluation of the results using the PH2 and ISIC2018 datasets, which have been extensively used by the numerous existing skin lesion segmentation methods, this study included the large dataset of HAM10000 for the analysis of skin lesion segmentation results (Table 5-9). On the HAM10000 dataset, the segmentation results of CHC were compared with SPCA and SDI+ because of the unavailability of the computer source codes of the other selected methods. CHC reported the highest accuracy (0.91) and specificity (0.99) scores. The maximum Dice score of 0.83 obtained by SDI+ (Guarracino and Maddalena 2019) is not far off from the Dice score (0.82) recorded by CHC. With a sensitivity score of 0.88, the SDI+ dataset performed similarly to the PH2 and ISIC2018 datasets. The results obtained by CHC have demonstrated the superiority of the algorithm over other top methods on this enormous collection of dermoscopic images.

Table 5-9 Performance comparison of the proposed algorithm against leading algorithms on the HAM10000 dataset (10015 images)

Methods	Accuracy	Sensitivity	Specificity	Dice
SDI+ (Guarracino and Maddalena 2019)[a]	0.90	**0.88**	0.94	**0.83**
SPCA (Bi *et al.* 2016)[b]	0.85	0.62	0.96	0.70
CHC (proposed) [a]	**0.91**	0.77	**0.99**	0.82

[a] unsupervised method; [b] supervised method.

5.4.4 Quantitative comparison on leukocyte image dataset

Using the common assessment criteria of accuracy (Acc), sensitivity (Sen), specificity (Spe), Dice (Dice), and Jaccard (Jacc), the competency of the comparative saliency methods was quantitatively assessed further on the Raabin-WBC dataset. These evaluation metrics are universally used for assessing leukocyte nuclei segmentation results (Ananthi and Balasubramaniam 2016; Al-jaboriy *et al.* 2019; Wang and Cao 2019b; Makem and Tiedeu 2020; Chen *et al.* 2021). Table 5-10 presents the results of the evaluation metrics of accuracy, specificity, sensitivity, Dice, and Jaccard. The segmentation results for each type of leukocyte and their average values are shown in this table. The highest average accuracy was attained by methods like BGFG, DCLC, DGL, DSR, CHC, and CHC*. Except for GR, all center prior-based methods achieved accuracy scores of 99.00%, proving the basic evidence that these methods are more effective at finding items that are located at the image center. The convex-hull-based center bias proposed in GR was not able to reach the maximum benchmark accuracy of 99.00 percent compared to other center-prior-based methods. This confirms earlier research showing that GR underperformed for objects in the center of the image (Joseph and Olugbara 2021). Due to the incorporation of deformed smoothness-based manifold ranking, only DGL outperformed the other boundary prior-based approaches in terms of accuracy (99.00%), although at the expense of computational complexity. The results generated using background prior-based techniques also demonstrated successful detection of the leukocyte nuclei.

Table 5-10 Segmentation results of the proposed algorithm on images from the Raabin-WBC dataset (1145 images)

Method	Leukocyte type	Acc	Sen	Spe	Dice	Jacc	Method	Leukocyte type	Acc	Sen	Spe	Dice	Jacc
BGFG	Basophil[a]	0.96	0.81	1.00	0.89	0.80	GR	Basophil[a]	0.99	0.93	1.00	0.96	0.92
	Eosinophil[b]	0.99	0.93	1.00	0.94	0.88		Eosinophil[b]	0.96	0.97	0.96	0.81	0.72
	Lymphocyte[c]	0.99	0.92	1.00	0.94	0.90		Lymphocyte[c]	0.99	0.97	0.99	0.94	0.90
	Monocyte[c]	0.99	0.93	1.00	0.95	0.92		Monocyte[c]	0.99	0.97	0.99	0.95	0.92
	Neutrophil[c]	0.99	0.89	1.00	0.93	0.86		Neutrophil[c]	0.98	0.95	0.99	0.89	0.82
	Average	**0.99**	**0.89**	**1.00**	**0.93**	**0.87**		**Average**	**0.98**	**0.96**	**0.99**	**0.91**	**0.85**
DCLC	Basophil[a]	0.98	0.92	1.00	0.95	0.91	MAP	Basophil[a]	0.98	0.91	1.00	0.95	0.90
	Eosinophil[b]	0.98	0.97	0.98	0.87	0.80		Eosinophil[b]	0.97	0.99	0.97	0.84	0.74
	Lymphocyte[c]	1.00	0.97	1.00	0.96	0.92		Lymphocyte[c]	1.00	0.98	1.00	0.97	0.94
	Monocyte[c]	0.99	0.97	0.99	0.96	0.93		Monocyte[c]	0.99	0.98	0.99	0.96	0.93
	Neutrophil[c]	0.99	0.95	0.99	0.90	0.83		Neutrophil[c]	0.98	0.99	0.98	0.87	0.78
	Average	**0.99**	**0.95**	**0.99**	**0.93**	**0.88**		**Average**	**0.98**	**0.97**	**0.99**	**0.92**	**0.86**
DGL	Basophil[a]	0.98	0.91	1.00	0.95	0.90	MC	Basophil[a]	0.98	0.91	1.00	0.95	0.91
	Eosinophil[b]	0.98	0.98	0.98	0.86	0.78		Eosinophil[b]	0.95	0.98	0.95	0.77	0.66
	Lymphocyte[c]	1.00	0.96	1.00	0.96	0.93		Lymphocyte[c]	0.99	0.97	1.00	0.96	0.92
	Monocyte[c]	0.99	0.97	1.00	0.96	0.93		Monocyte[c]	0.99	0.97	0.99	0.95	0.92
	Neutrophil[c]	0.99	0.95	0.99	0.90	0.83		Neutrophil[c]	0.97	0.97	0.97	0.85	0.77
	Average	**0.99**	**0.95**	**0.99**	**0.93**	**0.88**		**Average**	**0.98**	**0.96**	**0.98**	**0.90**	**0.83**
DSR	Basophil[a]	0.98	0.89	1.00	0.94	0.88	CHC	Basophil[a]	0.96	0.79	1.00	0.88	0.79
	Eosinophil[b]	0.99	0.96	0.99	0.90	0.84		Eosinophil[b]	0.99	0.92	1.00	0.94	0.90
	Lymphocyte[c]	1.00	0.96	1.00	0.96	0.92		Lymphocyte[c]	0.99	0.90	1.00	0.95	0.90
	Monocyte[c]	0.99	0.96	1.00	0.96	0.93		Monocyte[c]	0.99	0.93	1.00	0.96	0.92
	Neutrophil[c]	0.99	0.93	0.99	0.91	0.84		Neutrophil[c]	0.99	0.91	1.00	0.93	0.88
	Average	**0.99**	**0.94**	**0.99**	**0.93**	**0.88**		**Average**	**0.99**	**0.89**	**1.00**	**0.93**	**0.88**
GMR	Basophil[a]	0.99	0.92	1.00	0.95	0.91	CHC*	Basophil[a]	0.97	0.85	1.00	0.92	0.85
	Eosinophil[b]	0.97	0.97	0.97	0.83	0.74		Eosinophil[b]	0.99	0.96	0.99	0.94	0.89
	Lymphocyte[c]	0.99	0.96	1.00	0.95	0.91		Lymphocyte[c]	1.00	0.95	1.00	0.97	0.94
	Monocyte[c]	0.99	0.97	0.99	0.96	0.93		Monocyte[c]	0.99	0.95	1.00	0.96	0.92
	Neutrophil[c]	0.99	0.95	0.99	0.89	0.82		Neutrophil[c]	0.99	0.97	0.99	0.90	0.83
	Average	**0.98**	**0.95**	**0.99**	**0.92**	**0.86**		**Average**	**0.99**	**0.94**	**1.00**	**0.94**	**0.89**

[a] 218 images; [b] 201 images; [c] 242 images

Sensitivity values for the BGFG and CHC methods were the lowest, while the CHC*, an enhanced version of the CHC, increased the sensitivity rating by 5.00 % to achieve the sensitivity score of 94.00%. The only saliency detection method to achieve 100% specificity were BGFG, CHC, and CHC*. The outcome demonstrated that these methods are capable of successfully highlighting the leukocyte nuclei and accurately detecting non-salient regions. The average specificity for MC was 0.98, which was the lowest. The CHC* achieved the greatest Jaccard index of 0.89 and the MC achieved the lowest value of 0.83, with all saliency detection methods scoring above the average of 0.83 for the Jaccard index. CHC* received the highest Dice score of 0.94, while MC received the lowest score of 0.90. This demonstrated the capability of CHC* to generate segmentation results that are closely matched to ground truth images. In general, all methods exhibited good performance results to highlight the

capability of saliency detection methods to distinguish the leukocyte nuclei from the surrounding background pixels.

5.5 Preprocessing effects on algorithm performance

This section focuses on the experimental findings from analyzing the effects of DullRazor and CLAHE preprocessing methods on the performance of the proposed algorithm, CHC. The presentation of the experimental findings in this part is divided into three sections: preprocessing effects by visualization, preprocessing effects by statistical testing, and runtime analysis of preprocessing effects. The dermoscopic images showed a variety of heterogeneous features, which are summarized in Table 5-11.

Table 5-11 The description of the heterogeneous characteristics seen in dermoscopic images

Image property	Property description
1	Images with irregular skin lesion shape
2	A large skin lesion that connects multiple image boundaries
3	Skin lesion with low contrast to the surrounding skin
4	Skin lesion with color chart artifact
5	Skin lesion with hair artifact
6	Skin lesion with marker ink artifact
7	Skin lesion with ruler artifact
8	Skin lesion with blood vessel artifact
9	Skin lesion with gel bubble artifact
10	Image with vignette noise artifact
11	Skin lesion with multiple artifacts
12	Skin lesion with multiple shades of color intensity
13	Small skin lesion

5.5.1 Preprocessing effects by visualization

The simplest and fastest way to demonstrate the efficacy of segmentation techniques is through visual inspection. Conventionally, dermoscopic images with undesirable heterogeneous features were employed to graphically illustrate how preprocessing affects the performance of a segmentation algorithm. The segmentation outcomes from the selected dermoscopic images using CHC with and without the implementation of preprocessing techniques are shown in Figures 5-16 to 5-18 for the PH2, ISIC2018, and HAM10000 datasets, respectively. Since the images of the PH2 dataset do not adequately address most of the undesirable heterogeneous features stated in Table 5-11, Figure 5-16 only shows the image categories that are currently accessible from the PH2 dataset. The use of DullRazor and CLAHE preprocessing tools for artifact removal and contrast enhancement has generally led to substantial improvements. However, the findings have shown that the proposed algorithm is

capable of eliminating unwanted artifacts and properly highlighting skin lesions without the requirement for preprocessing.

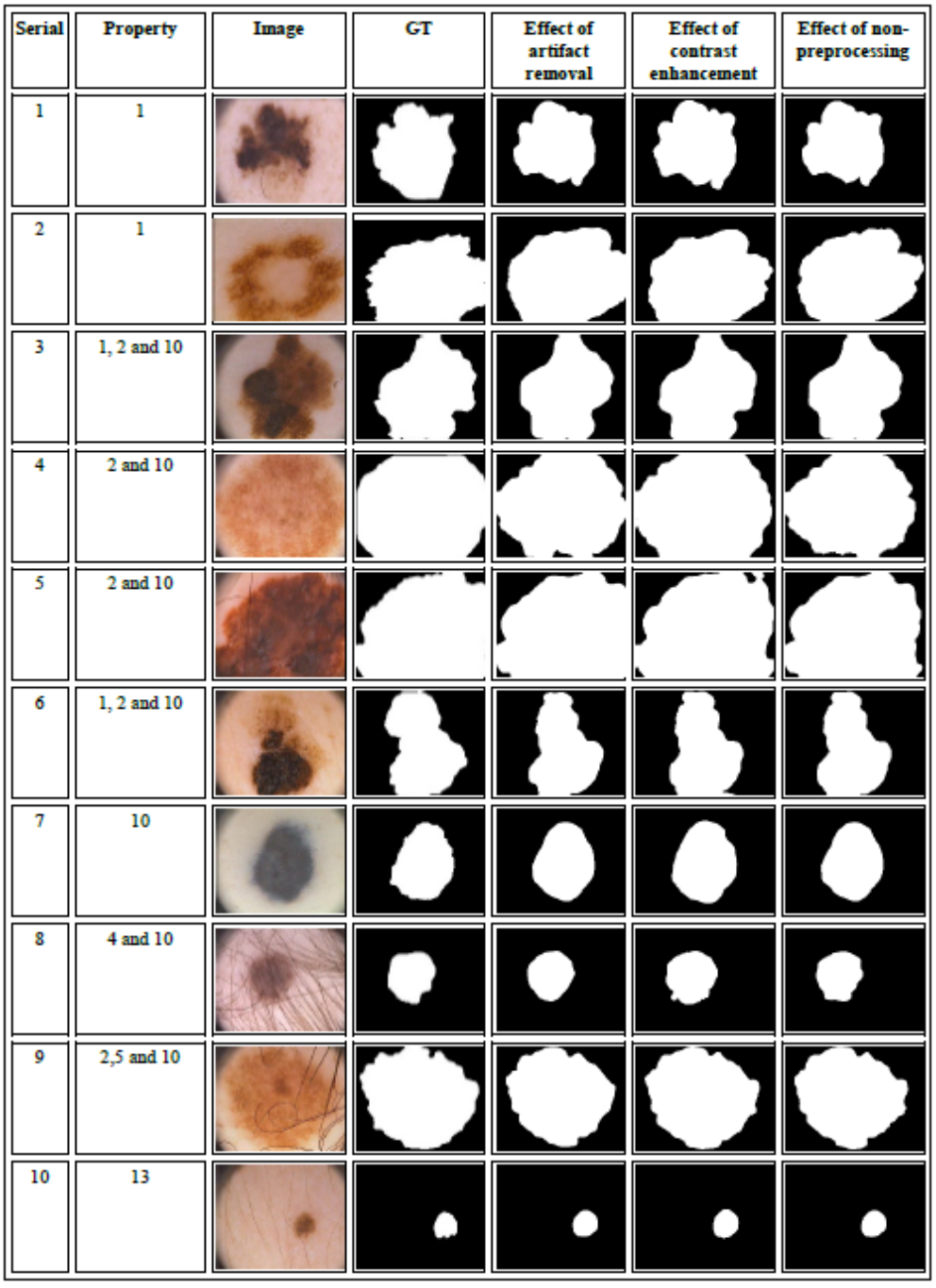

Figure 5-16 The visual effects of preprocessing on the PH2 dataset

As seen in Figure 5-17, the ISIC2018 is a complicated dataset with images of undesired heterogeneous features. Figure 5-17 illustrates the appropriateness of the proposed algorithm to manage

these heterogeneous features. The contrast enhancement preprocessing has a negative impact on the segmentation outputs of the images with serial numbers 10 and 12.

Serial	Property	Image	GT	Effect of artifact removal	Effect of contrast enhancement	Effect of non-preprocessing
1	1	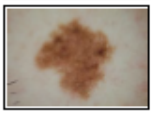				
2	2					
3	3	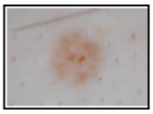				
4	4 and 5					
5	5					
6	6	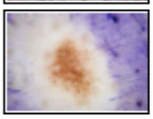				
7	7	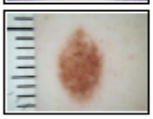				
8	8	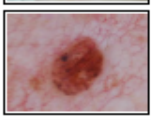				
9	9					
10	10					
11	11					
12	12					
13	13					

Figure 5-17 The visual effects of preprocessing on the ISIC2018 dataset

As demonstrated in Figure 5-18, the addition of contrast enhancement preprocessing significantly decreased the segmentation performance on images with serial numbers 3, 9, 7, 10, 11, and 12. The findings provided in Figures 5-16 to 5-18 make it abundantly clear that the proposed algorithm is capable of accurately segmenting skin lesions despite their diverse features.

Serial	Property	Image	GT	Effect of artifact removal	Effect of contrast enhancement	Effect of non-preprocessing
1	1 and 3					
2	2 and 3	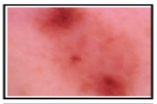				
3	3 and 10	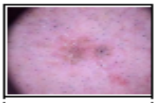				
4	5	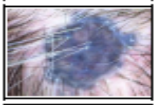				
5	6	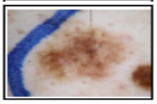				
6	7	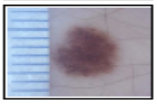				
7	8					
8	9					
9	10					
10	5 and 10					
11	7 and 12					
12	13					

Figure 5-18 The visual effects of preprocessing on the HAM10000 dataset

5.5.2 Preprocessing effects by statistical testing

The impacts of preprocessing on the saliency segmentation of skin lesions were investigated using statistical performance evaluation measures of accuracy and dice similarity. The statistically significant evidence of the difference between the means of the non-preprocessed and preprocessed segmentation findings shown in Tables 5.12–5.14 was ascertained using the paired t-test statistic. The accuracy and Dice scores for the segmentation performances with and without artifact removal preprocessing are shown in pairs 1 and 3, respectively. Pairs 2 and 4 illustrate the segmentation performance without preprocessing and with image enhancement preprocessing, respectively, in terms of accuracy and Dice scores. Without artifact removal preprocessing, the mean accuracy value for the PH2 dataset is noticeably higher. However, the accuracy is greatly improved with a p-value less than 0.05 when image enhancement preprocessing is used for the PH2 dataset. The proposed algorithm without the use of DullRazor preprocessing produced a higher value for Dice similarity, but the increase is not statistically significant. In divergence, the incorporation of image enhancing preprocessing is to provide a statistically significant difference in the accuracy and Dice scores with a p-value of 0.000<0.05 to accept the alternative hypothesis.

Table 5-12 Paired samples test for preprocessing effects using PH2 dataset.

Variable			Mean	Std. Err.	Std. dev.	[95% CI]	t-value	df	Sig[a]
Accuracy	Pair 1	Without preprocessing	0.921	0.009	0.127	0.903 - 0.939	2.043	199	0.042
		With artifact removal	0.919	0.009	0.130	0.901 - 0.938			
	Pair 2	Without preprocessing	0.921	0.009	0.127	0.903 - 0.939	-3.9213	199	0.000
		With image enhancement	0.933	0.008	0.118	0.917 - 0.950			
Dice	Pair 3	Without preprocessing	0.893	0.007	0.105	0.878 - 0.908	0.953	199	0.342
		With artifact removal	0.891	0.008	0.106	0.876 - 0.906			
	Pair 4	Without preprocessing	0.893	0.007	0.105	0.878 - 0.908	-4.0814	199	0.000
		With image enhancement	0.909	0.007	0.942	0.896 - 0.922			

Std. Err. = standard error; Std dev. = standard deviation; Sig = significance; [a] (2-tailed); CI=confidence interval; df=degrees of freedom.

According to the findings in Table 5-13 for the ISIC2018 dataset, the addition of artifact removal or image enhancement preprocessing had no statistically significant impact on the segmentation

outcomes. Despite the accuracy and Dice scores being better for results produced without preprocessing than for results acquired with artifact removal preprocessing, the improvement in results is not statistically significant. However, the segmentation quality according to the Dice score is shown to be significantly improved by the proposed algorithm without the application of image enhancement preprocessing.

Table 5-13 Paired samples test for preprocessing effects using ISIC2018 dataset

Variable			Mean	Std. Err.	Std. dev.	[95% CI]	t-value	df	Sig[a]
Accuracy	Pair 1	Without preprocessing	0.923	0.002	0.113	0.918 - 0.927	1.777	2593	0.076
		With artifact removal	0.921	0.002	0.114	0.917 - 0.926			
	Pair 2	Without preprocessing	0.923	0.002	0.113	0.918 - 0.927	-0.096	2593	0.924
		With image enhancement	0.923	0.002	0.112	0.918 - 0.927			
Dice	Pair 3	Without preprocessing	0.813	0.004	0.179	0.806 - 0.820	0.651	2593	0.515
		With artifact removal	0.812	0.003	0.178	0.806 - 0.819			
	Pair 4	Without preprocessing	0.813	0.004	0.179	0.806 - 0.820	4.953	2593	0.000
		With image enhancement	0.803	0.004	0.189	0.795 - 0.810			

Std. Err. = standard error; Std dev. = standard deviation; Sig = significance; [a] (2-tailed); CI=confidence interval; df=degrees of freedom.

Despite the diverse characteristics of the dermoscopic images, the segmentation results for the HAM10000 dataset in Table 5-14 demonstrate the capacity of the proposed algorithm to segment skin lesions accurately without preprocessing support. The proposed algorithm was able to increase accuracy and Dice scores significantly without using artifact removal preprocessing. Without using image-enhancing preprocessing, the average Dice score was enhanced significantly.

Table 5-14 Paired samples test for preprocessing effects using HAM10000 dataset

Variable			Mean	Std. Err.	Std. dev.	[95% CI]	t-value	df	Sig[a]
Accuracy	Pair 1	Without preprocessing	0.910	0.001	0.105	0.908 - 0.912	4.765	10014	0.000
		With artifact removal	0.909	0.001	0.106	0.907 - 0.911			
	Pair 2	Without preprocessing	0.910	0.001	0.105	0.908 - 0.912	-0.7440	10014	0.000
		With image enhancement	0.914	0.001	0.103	0.912 - 0.916			
Dice	Pair 3	Without preprocessing	0.824	0.002	0.153	0.821 - 0.827	6.339	10014	0.000
		With artifact removal	0.821	0.002	0.157	0.818 - 0.824			
	Pair 4	Without preprocessing	0.824	0.002	0.153	0.821 - 0.827	3.801	10014	0.000
		With image enhancement	0.820	0.002	0.169	0.817 - 0.823			

Std. Err. = standard error; Std dev. = standard deviation; Sig = significance; a (2-tailed); CI=confidence interval; df=degrees of freedom

5.5.3 Runtime analysis of preprocessing effects

Figure 5-19 reports the computational running times of the proposed algorithm on the selected datasets with and without preprocessing. According to the runtime per image of each dataset, preprocessing makes the segmentation algorithm more time-consuming than anticipated. Using the DullRazor and CLAHE preprocessing methods on the PH2 dataset, it can be seen that the running times correspondingly increase to 0.50 seconds and 0.54 seconds. Since each image in the HAM10000 dataset has a dimension of 256 x 256 rather than the 400 x 300 used for images in the PH2 and ISCI 2018 datasets, the running time per image in the HAM10000 dataset is significantly lower than that of the other datasets. The average running time for preprocessing using the CLAHE approach recorded the worst average running time, as shown in Figure 5-20, which also shows the average time for each method across the datasets.

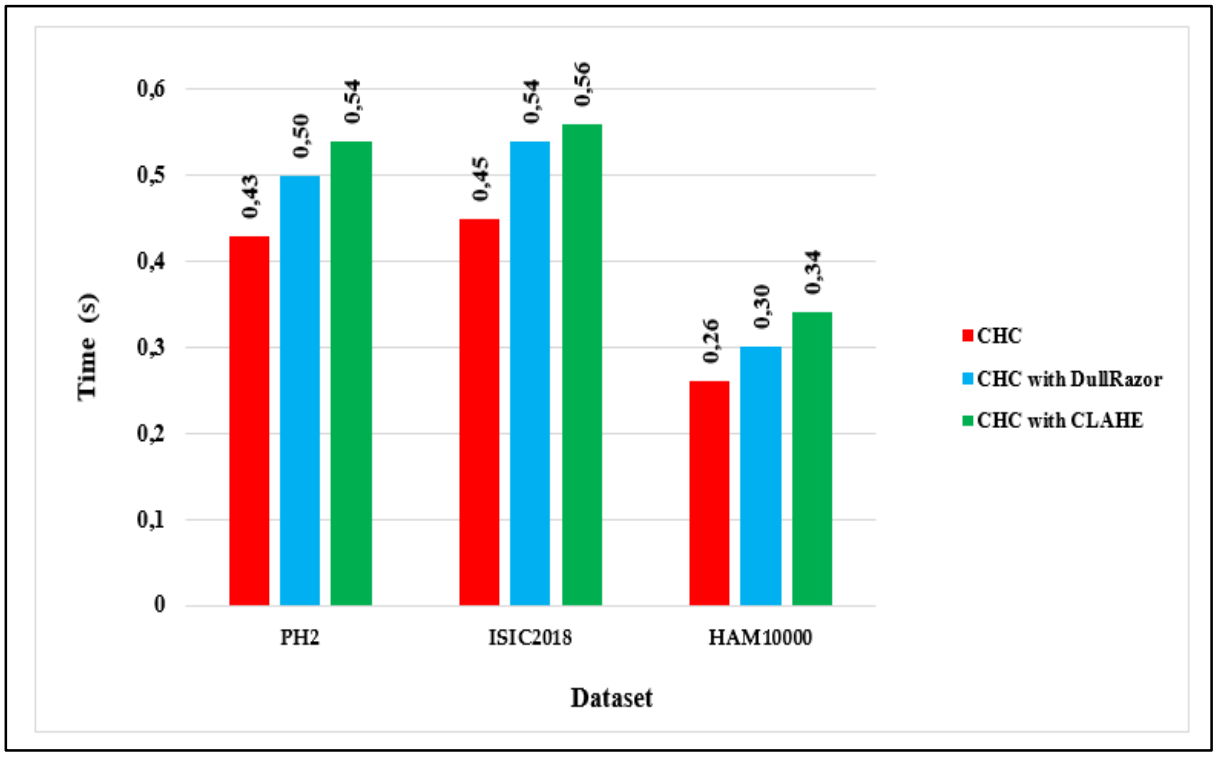

Figure 5-19 Computation time per dermoscopic image dataset

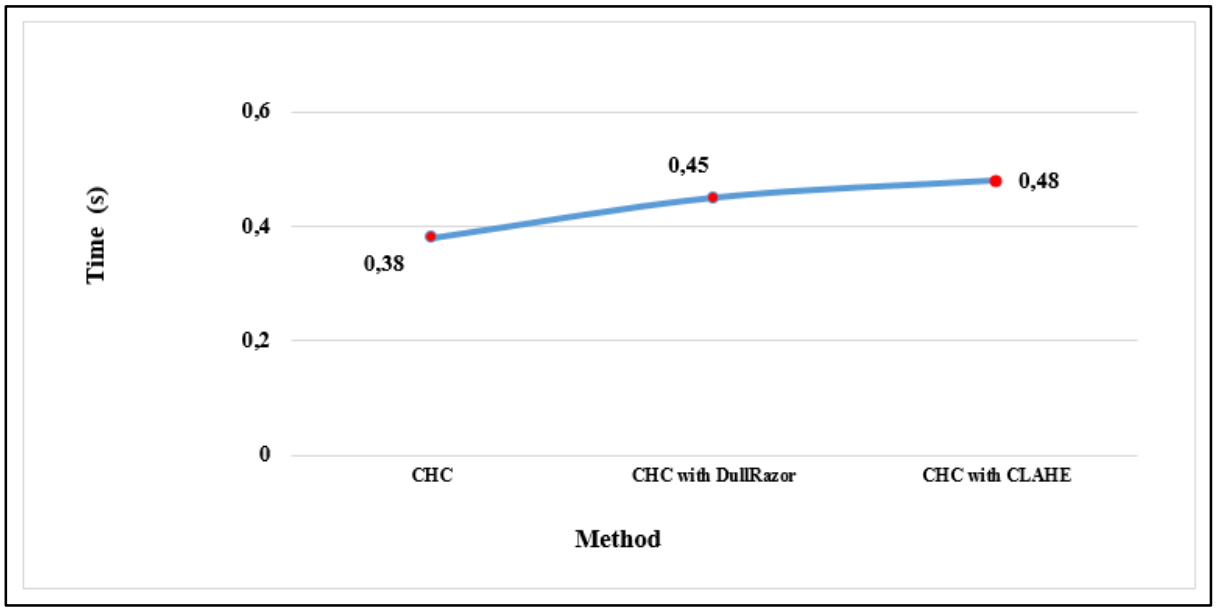

Figure 5-20 The average running time per method

5.6 Runtime analysis of algorithm

Salient object detection methods should make image analysis less computationally complex by effectively identifying regions of interest. Fast and accurate detection of the most important regions is crucial because this is an intelligent preprocessing stage of computer vision tasks. Most methods used in real-time applications are constrained by computational complexity. Due to their computational complexity, deep learning-based approaches are inherently constrained by this issue. This study included runtime computational analysis to experimentally demonstrate the effectiveness of CHC. Due to the absence of access to the source codes, several methods were not included in the runtime analysis. A computer with an Intel(R) Core(TM) i7-8650U CPU @ 1.90GHz 2.11GHz and 8 GB of random access memory was used to experiment. The running times of 25 methods on the ECSSD dataset are listed in Table 5-15. Apart from MAP, FES, SR, and SWD, CHC performed significantly better than the majority of the other methods. The worse performance of FES, SR, and SWD, regardless of computational efficiency, was demonstrated in quantitative and qualitative analysis. The methods that CHC competes with, like DCLC, DGL, and DRFI, are computationally more expensive, as seen in Table 5-15. The CA experienced considerable computational complexity, which was mostly brought on by the adoption of the K-nearest neighbor algorithm to identify the closest patches. Due to the longer feature extraction times required by the traditional learning-based HDCT and DRFI methods, they are also computationally costly. The sample size parameter employed in the computation of the attention map is the primary factor affecting the longer running time of the most recent CNS method. The computational cost of the DGL is higher than that of other graph-based techniques like GR, MAP, MC, and MR.

Table 5-15 Average running time of 25 algorithms on ECSSD dataset. Best results are highlighted in bold

Method	**CHC**	**AC**	**BGFG**	**CA**	**CNS**	**COV**	**DCLC**	**DGL**	**DRFI**	**DSR**	**FES**	**GB**	**GR**
Time Time (S)	**0.23**	80.33	5.56	15.15	11.34	4.29	0.47	1.33	6.16	1.82	**0.21**	0.52	0.36
Method	HDCT	IT	**MAP**	MC	MR	RPC	SEG	SeR	SIM	**SR**	SUN	**SWD**	
Time Time (S)	4.17	0.26	**0.21**	0.24	0.54	2.08	1.91	0.51	0.39	**0.12**	2.39	**0.12**	

Further to the time analysis performed on the salient object detection, this study also performed the time analysis on the segmentation performance of CHC on the Raabin-WBC dataset (Table 5-16).

The MC and CHC algorithms exhibited the best performance with an average running time of 0.11 seconds per image. Only BGFG and DSR, with run times of 3.89 and 1.39 seconds, respectively, exhibited comparably low performance. Although MC is computationally efficient, it performed poorly across all evaluation metrics except for sensitivity. Notably, CHC has demonstrated strong performance on all evaluation measures, except sensitivity, and minimal computational runtime complexity. The improved version, CHC*, addressed the drawback of CHC in obtaining high sensitivity score and achieved the best results while preserving an effective run time of 0.24s per image. By properly integrating color contrast, contrast ratio, spatial characteristics, and the center prior, the proposed algorithm was able to accurately locate leukocyte nuclei. Fast and effective detection of leukocyte nuclei is paramount in the clinical diagnosis of leukocytes.

Table 5-16 Average running time of 10 algorithms on Raabin-WBC dataset. Best results are highlighted in bold

Method	BGFG	DCLC	DGL	DSR	GMR	GR	MAP	MC	CHC	CHC*
Time Time (S)	3.89	0.48	0.93	1.39	0.41	0.27	0.15	**0.11**	**0.11**	0.24

5.7 Optimum cluster generation

Determination of an optimum number of clusters for regional granularity is an inevitable problem in many of the existing clustering-based image segmentation methods. The systematic literature review performed in chapter 2 has revealed the use of the superpixel approach for image abstraction by many of the existing methods. The identification of an ideal number of superpixels is the fundamental issue with the superpixel-based methods. Small and large superpixel counts may, respectively, result in under and over-segmentation of images, which may cause salient regions to be highlighted unevenly (Tang and Wu 2016). The automatic determination of the cluster count is the main attraction of the proposed algorithm and the following table (Table 5-17) summarizes the cluster count generated for each of the image datasets used in this study.

Table 5-17 Optimum clusters generated by the proposed algorithm

Image category/dataset	No of images	Minimum cluster count	Maximum cluster count	Most frequently used cluster count
Boundary	350	11	310	78
Center	370	8	289	139
Complex	210	54	359	96
Lowcontrast	165	20	230	97
Multiple objects	160	22	316	88
Overlap	250	22	402	117
ECSSD	1000	8	415	116
HKU-IS	4447	8	400	110
SOC	1500	8	403	124
PH2	200	37	100	57
ISIC2018	2594	26	164	60
HAM100015	10015	18	132	33
Raabin-WBC	1145	33	184	55

It is worth noticing that the range of cluster count generated is highly dependent on the image type. The highest four cluster counts of 415, 403, 402, and 400 were generated respectively for ECCSSD, SOC, overlap image category, and HKU-IS datasets. The most frequently used cluster count is between 33 and 139.

This study also analyzed the effect of a smaller and larger number of superpixel counts on well-known saliency models such as DCLC, GMR, MAP, and MC. Few experiences were performed with superpixel counts of 50 and 250 on these models and the results are illustrated in Figure 5-21. For instance, in Figure 5-21(2) the performance of all these methods is solely dependent on the selection of superpixel counts. MC managed to segment the center object effectively with superpixel 50, but the same salient object is not highlighted correctly with 250 superpixels. In Figure 5-21(4) the GMR is favored by a larger number of superpixel count for accurate detection, while Figure 5-21 (6) comparatively produced a better result with a smaller number of superpixels. Similarly, the performance of DCLC and MAP are also based on the superpixel count as illustrated in Figure 5-21. It is obvious that the selection of superpixel count has a strong impact on the segmentation results and it is always depending on the input image. The visual representation of the segmentation results showed that for some images, a lower number of superpixels is enough for accurate segmentation, while some images require a larger number of images, and this varies from method to method.

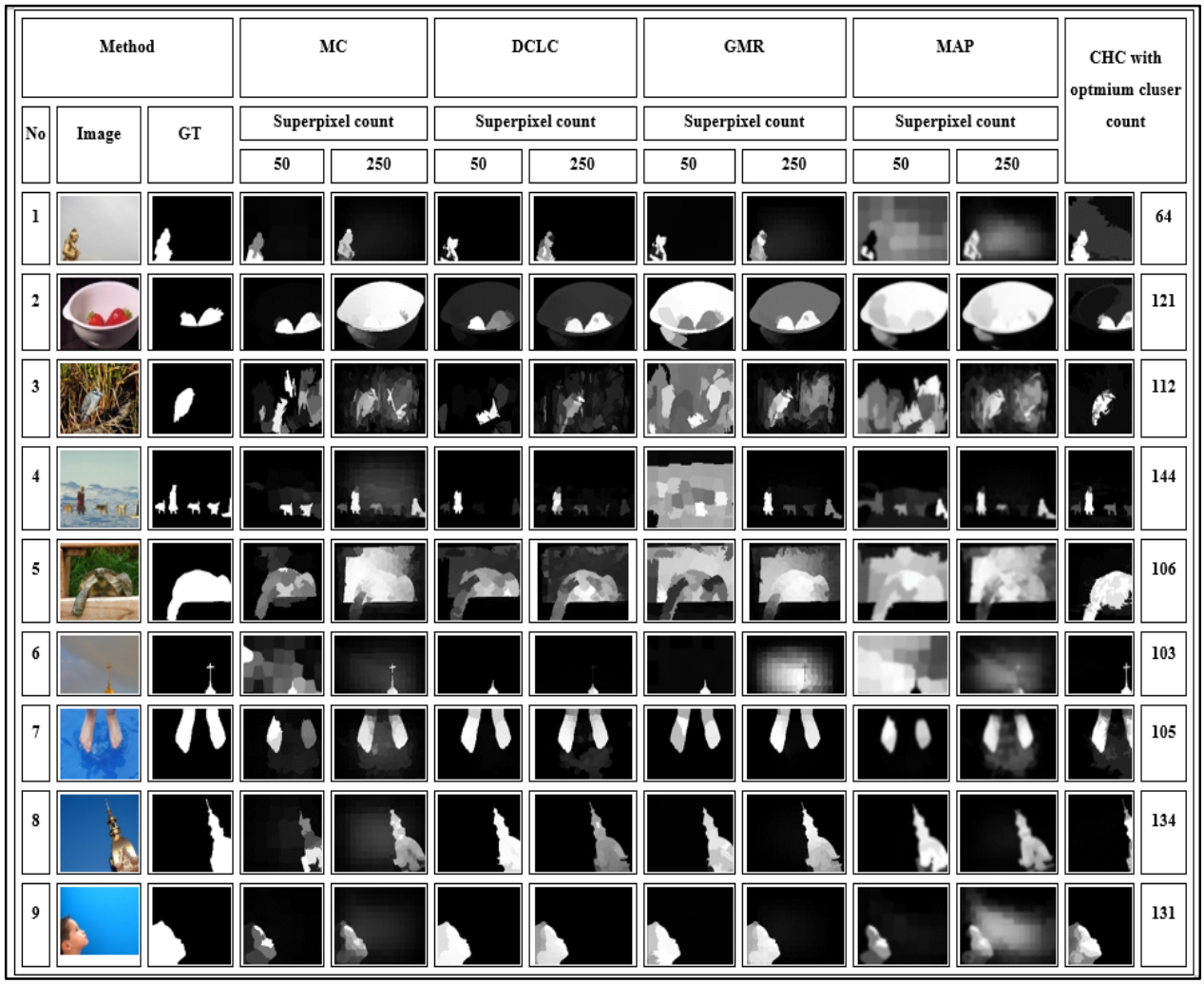

Figure 5-21 Visual comparison of different superpixel counts

The results shown in Figure 5-21 corroborate the findings by Liu and Yang (2019) which show how saliency detection performance is impacted by superpixel granularity. The algorithm proposed in this study can produce accurate segmentation results consistently irrespective of the type of images. The results are shown in Figure 5-21 and 5-22 reported the segmentation results and the optimum cluster count automatically determined by the CHC segmentation algorithm for selected images.

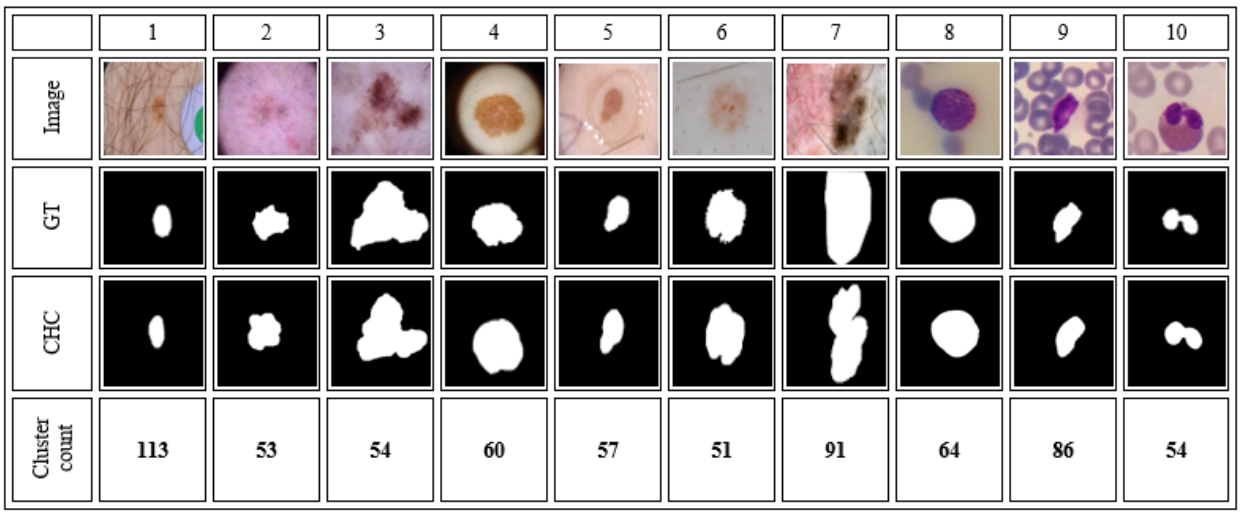

Figure 5-22 Medical images segmentation output with the optimum cluster count

In Figure 5-22, the original images are represented by the first row, while the ground truth images are by the second row. The last two rows represent respectively the segmentation results and the cluster count obtained by the proposed algorithm. The cluster count generated by the color histogram algorithm is varied based on the image characteristics.

5.8 Chapter summary

This chapter detailed the experimental comparisons conducted to validate the performance of the proposed segmentation algorithm. The effectiveness of the proposed algorithm is thoroughly compared to deep learning and state-of-the-art methods on six categories of images and seven image datasets. Additionally, the preprocessing effects on the proposed algorithm in segmenting the region of interest were examined. The computational efficiency of the proposed algorithm was further demonstrated through an experimental runtime analysis. The main draw of the proposed algorithm is the automatic cluster count determination, and this chapter also provided the cluster counts generated for each of the image datasets used in this study. The experimental results showed that the agglutination of color contrast, contrast ratio, center prior and the spatial features, the ability to determine the optimum cluster, and the preprocessing free approach intensified the successful application of the proposed algorithm on a wide gamut of images. The next chapter will present the findings and discussions based on the study results obtained in this chapter.

CHAPTER SIX: DISCUSSION

This chapter discusses the results achieved based on the second and third study objectives outlined in chapter 1. The first section explicates the performance of the proposed algorithm on six categories of images against 30 state-of-the-art saliency detection methods and seven deep learning-based methods. The performance of the proposed algorithm on seven additional image datasets is discussed in greater detail in the section that follows. The sections dispassionately interpret the significance of the study results relative to the findings of the comparative methods to accomplish the second study objective. In the subsequent section, the image preprocessing effects of the proposed algorithm are covered to reach the third study objective. The latter two sections discussed, the computational efficiency of the proposed algorithm and the resultant optimum cluster counts.

6.1 Performance of the proposed algorithm on different image categories

The outstanding performance of the proposed algorithm for image segmentation is perceptible in the visual and quantitative comparisons provided in chapter 5. The capability of the proposed algorithm in addressing the detection and segmentation of salient objects over the various categories of images was impressive. The proposed algorithm consistently outperformed all categories of images given in Figure 5-1 in terms of precision and F-measure, while the MAE and OR values always rank in the top three, as shown in Table 5-2. The supervised learning method DRFI achieved good recall values for all image categories except overlap, and HDCT was also quite competitive with DRFI in terms of attaining better recall values. However, both supervised learning methods scored high recall values at the expense of low precision and F-measure. With a rise in the recall value, the pixel-based approaches of GB, IT, SeR, and SR saw a decrease in precision across the categories of boundary and center objects. The MAP approach recorded better recall values, but the Markov absorption probability determines the generalized initial saliency map. This can make it difficult to detect salient objects that are close to the image boundary, and it is clear from the experimental results that MAP did not perform well in terms of recall for the boundary, overlap, and multiple object categories. The high recall value is typically not regarded as a good option for evaluating segmentation results, because the recall score could be increased by highlighting the entire image region. A high recall value with a low precision indicates the detection of the salient regions with noisy pixels (Chuang, Chen and Chen 2014). In other words, high recall values can be achieved at the cost of reducing precision and vice-versa (Perazzi *et al.* 2012; Banerjee, Mitra and Shankar 2018). As a result, it is more reasonable to validate the performance of

the segmentation results using the F-measure, which is the harmonic mean of precision and recall (Tang *et al.* 2019; Singh and Kumar 2020; Wang and Tian 2020).

In addition to achieving the maximum F-measure on the boundary, center, complex background, low contrast, and multiple objects, the proposed algorithm also achieved more balanced precision and recall values. DCLC recorded the highest F-measure for the overlapped image category, and the proposed algorithm had the second-best F-measure. On a few image categories, including center and complex background, the CNS method performed well in terms of MAE. However, due to the consideration of low-level features like color and surroundedness cues, CNS has not been able to attain the best MAE on the boundary, overlapping, and low contrast image categories (Lou *et al.* 2020). The DSR method also produced lower MAE for boundary images, however, the proposed algorithm performed best for complicated categories such as complex backgrounds, low contrast, and multiple objects. Since salient objects are usually not found near the image center, algorithms that take advantage of the center prior principle can discard salient items that touch the image boundary (Li *et al.* 2018a). However, the proposed algorithm is still capable of demonstrating remarkable performance in the category of boundary images with the appropriate integration of color contrast, contrast ratio, spatial characteristics, and center prior.

The DGL method can handle different categories of images than other graph-based methods, albeit at the expense of computational complexity. In comparison to the graph-based methods of GB, GR, MC, MR, and MAP, DGL is computationally more complex, as shown by the runtime analysis results presented in Table 5-15. GR technique applied a convex-hull-based center bias to address the typical drawback of the center prior map, which inadvertently suppresses the salient objects further from the image center. The accuracy of salient objects that are close to the image boundary has been enhanced by the convex-hull center prior, however, this method performed poorly for objects that are located at the center of the image. DRFI approach employed a 35-dimensional feature vector of geometric, appearance, color, texture, and background information for describing a region. These characteristics, combined with multi-level segmentation, have allowed the DRFI approach to perform well on a variety of image types. Regardless of the usage of color contrast characteristics, the results obtained by DRFI are free from the constraints of contrast-based methods. However, the performance of DRFI in the boundary image category can be impacted by the assumption that a thin image border serves as a pseudo background. Another inherent problem with this method is computational complexity as reported in Table 5-15. When compared to the category of images with salient objects at

the image center, the methods DGL, MR, MAP, and MC that exploited the boundary prior have demonstrated relatively poor performance in the category of boundary images. This demonstrated the main problem with boundary prior based method is that it treats boundary regions as backgrounds and is ineffective when salient objects are close to the image boundary.

The performance of contrast prior-based algorithms like CNS, DCLC, RPC, and GR has been relatively poor when applied to low contrast images. This is because contrast prior works best with images that clearly distinguish between foreground and background regions in terms of color contrast. In terms of a unit of processing, the region-based methods listed in Table 5-1 demonstrated comparatively better performance than the pixel or patch-based methods regardless of the methods used for image abstraction. Hence the results of this study strengthen the existing finding that the segmentation performance can be increasingly improved through image abstraction by clustering similar image pixels (Filali, Allili and Benblidia 2016; Shan *et al.* 2019; Zhang, You and Wu 2019).

The results of investigated algorithms, as given in Table 5-2, suggest that salient object properties such as count, location, size, color contrast, or background complexity have a significant impact on the efficacy of an algorithm. Further, these algorithms are influenced by the ideal conditions that favor the prior knowledge integrated, but the effectiveness of these methods is diminished once they are applied to images with heterogeneous properties. As a result, a majority of these algorithms only perform well when applied to a certain type of image and fail miserably when used on a wide variety of images. Singh and Kumar (2020) proposed a new framework named saliency bagging where the saliency map is computed by integrating saliency maps from five famous saliency models such as DRFI(Jiang *et al.* 2013b), DSR (Li *et al.* 2013b), GMR (Yang *et al.* 2013), MC(Jiang *et al.* 2013a) and RBD(Zhu *et al.* 2014) to address this issue. Contrarily, the proposed algorithm has consistently outperformed existing algorithms in most image categories, regardless of the numerous object characteristics and complexity of the background. The combination of color contrast, contrast ratio, spatial feature, and center prior information in the proposed algorithm has successfully separated salient regions from non-salient regions and uniformly highlighted salient objects. Due to its success in detecting salient objects in a variety of images, the proposed algorithm is almost universally applicable. Additionally, the quantitative comparison of the proposed algorithm has demonstrated its superiority over the investigated methods, and the performance of the proposed algorithm when compared to top-down deep-learning methods is astounding.

6.2 Algorithm performance on different image datasets

Achieving a high segmentation accuracy of images with simple and homogenous backgrounds is not a challenging task for many of the existing methods. The results demonstrated in the previous sections highlighted that the category of images where the objects are located near the image center or boundary with a uniform background is an ideal case for many of the existing methods to produce quality segmentation results. However, obtaining a consistent performance on images with complex structures is a challenging task for many of the existing methods. The performance evaluation of the proposed algorithm on different image datasets with complex image structures is discussed in the following sections.

6.2.1 Complex scene image datasets

Despite the challenging images of ECSSD with single and multiple salient objects on a noisy and complicated background, the proposed algorithm showed a remarkable performance with precision above 85% and an F-Measure close to 80%. The results in Tables 5-4 and 5-5 proved the challenges that all the compared methods, including deep learning methods, encountered. The precision and F-measure score were both below 80% on this dataset. The proposed algorithm scored the best values for all evaluation metrics except recall. These high values of precision, F-measure, MAE, and OR showed the contribution of this newly developed algorithm in handling images of different natures. The method BPFS scored the highest recall value across images from the ECSSD dataset but at the cost of low precision and low F-measure as shown Table 5-4.

The extended evaluation of the proposed algorithm on the HKU-IS and SOC datasets has further demonstrated the strength of the algorithm in processing images from various datasets. HKU-IS dataset is widely recognized for the complex scene with low contrast and multiple salient objects with appearance changes as illustrated in Figure 5-10. On this dataset, it is obvious that the deep learning methods MSNSD-A and MSNSD scored the best in terms of F-measure and MAE, however, the outcome of the proposed algorithm is quite close to these best values. The efficacy of the proposed algorithm is better and commendable when compared to the other investigated bottom-up methods. The results obtained for investigated methods on the SOC dataset were in contrast to the findings of Fan *et al.* (2018), where the authors indicated that present saliency methods show poor results with an F-measure less than 0.45 on images that are closer to the real-world scenes. Conversely, the proposed

algorithm scored comparatively best F-Measure of 0.618 on SOC, whereas all other investigated methods, DCLC, DGL, and DRFI respectively scored the F-Measure above 0.543, 0.552, and 0.561. The F-measure of above 60% by the proposed algorithm on this complicated dataset reinforced the application of the proposed algorithm on a wide range of images. However, neither the proposed algorithm nor the bottom-up methods performed very well in identifying salient objects in the cluttered and obscured background. This supports the finding of Borenstein and Ullman (2002) that the salient objects from cluttered and obscured images cannot be meaningfully detected using simple image features like color, contrast, and texture. Incorporating high-level features can improve the ability to detect objects against a cluttered and obscured background (Borenstein and Ullman 2002; Bravo and Farid 2004).

6.2.2 Dermoscopic image datasets

The segmentation results achieved by the proposed algorithm on the selected dermoscopic image datasets is further proving the strength of this algorithm. The performance of the compared methods varied on different datasets. Despite the inclusion of preprocessing stage, the results obtained by ASLM (Pennisi *et al.* 2016) on images from the PH2 dataset were noticeably inferior to those computed by the proposed algorithm. On the PH2 image dataset, the YOLO supervised segmentation method developed by Ünver and Ayan (2019) has the highest segmentation accuracy. However, this deep learning method is largely dependent on preprocessing and the provision of a large training dataset to increase confidence in the deep learning model. As a result, the primary limitations of supervised approaches are their intrinsic computational complexity and their excessive reliance on annotated datasets of excellent quality. The SPCA supervised learning approach using cellular automata and superpixels proposed by Bi *et al.* (2016) had the lowest sensitivity score. Additionally, SPCA performs quite poorly in comparison to the other supervised learning techniques given in Table 5-7 The maximum sensitivity score was recorded by the SDI+ method (Guarracino and Maddalena 2019) and it is important to note that high sensitivity is insufficient to measure the actual performance because a 100% sensitivity score could be attained by labeling every image pixel as a region of interest. The ability to extract additional structural data from superpixels allowed the method developed by Majumder and Ullah (2019) to achieve reasonably excellent accuracy and sensitivity results on the PH2 dataset without any preprocessing phase. Nevertheless, superpixel-based methods are severely constrained by the best choice of superpixel granularity, their reliance on single value superpixel granularity could result in unsatisfactory segmentation results (Filali, Allili and Benblidia 2016). Moreover, this method does not

successfully identify non-lesion pixels because its specificity score is only 0.89. In divergence, the proposed algorithm provides really impressive segmentation results and is well-designed to automatically determine the best region granularity.

On the ISIC2018 dataset, the deep learning methods of R2AU-Net (Zuo, Chen and Wang 2021) and the method proposed by Li *et al.* (2021b) had the highest accuracy of 93%. The proposed algorithm performs excellently on this dataset, obtaining the second-highest accuracy score of 92%, which is extremely close to the level of accuracy attained by supervised methods. On images from the ISIC2018 dataset compared to the PH2 dataset, it is evident that the performance of all comparing algorithms for Dice similarity is decreasing. It demonstrates the complexity of the images included in this dataset as well as the challenges that all comparing methods faced in achieving segmentation outcomes that were more in line with the ideal ground truth. The proposed algorithm recorded a Dice score of 0.81 while the deep learning methods (Li *et al.* 2021b) and R2AU-Net (Zuo, Chen and Wang 2021) recorded the highest Dice scores of 0.87. The SPCA showed the worst performance on this dataset except for the specificity score. As the ISCI 2018 dataset contains images of several undesired heterogeneous properties as described in Table 5-11, the SPCA and SDI+ perform considerably worse on the ISIC2018 data than on the PH2 dataset. The results obtained by these two methods clearly showed that the segmentation results were not sufficiently improved by DullRazor and multiple preprocessing, as applied, respectively, by the SPCA and SDI+ algorithms. Only a few undesired artifacts, such as hair, specular lights, dark areas, and marker ink, were addressed by the preprocessing technique utilized by SDI+ (Guarracino and Maddalena 2019). Despite the addition of preprocessing, the presence of additional artifacts such color calibration charts, and dark corners seemed to be a difficult case for SDI+. The authors of SDI+ noted the significance of a preprocessing phase to deal with many kinds of undesired artifacts.

The deep learning methods, as shown in Table 5-8, consistently display promising results in ISIC2018 dataset but with the extra demands for computing resources. Higher confidence in the deep learning architecture and the necessity for a large training dataset are directly correlated. As a result, there is always a trade-off between the computational complexity and effectiveness of deep learning methods. Moreover, a substantial training dataset must be available for deep learning algorithms to perform well. The proposed algorithm, however, performs unexpectedly well on the ISIC2018 dataset with a straightforward yet efficient segmentation approach, although the dataset contains complex images. The segmentation results obtained have proven the resilience of the algorithm for segmenting

skin lesions in dermoscopic images from a large dataset. The suggested method did outperform other algorithms on images from the HAM10000 dataset. This emphasized the ability of the proposed algorithm to segment the region of interest from a huge dataset with heterogeneous image properties.

6.2.3 Leukocyte image dataset

The experimental comparison performed on the Raabin-WBC dataset showed the power of saliency and clustering methods to segment the region of interest from the leukocyte image dataset. Overall, this image dataset yielded good results for all the saliency detection algorithms that were chosen. The inclusion of center prior, which is based on the fundamental presumption that objects close to the image center are more prominent, enabled center-prior-based algorithms like DCLC, GR, CHC, and CHC* to obtain good segmentation results. Leukocyte nuclei are typically located far from the image boundary, which favors algorithms that take advantage of location priors such as background and boundary. Considering this, this work demonstrated that leukocyte nuclei can be detected and gave good segmentation results using saliency detection methods that include center-prior, background prior, or boundary prior. These saliency detection algorithms are more successful and efficient at detecting the leukocyte nuclei due to the usage of location priors such as center, boundary, and background.

6.3 Image preprocessing effects

The results of the proposed algorithm with and without preprocessing were compared, and it was shown that there was no statistically significant difference between these two results. According to the results of the preprocessing effects analysis, the DullRazor preprocessing may successfully correct skin lesions that are surrounded by undesired artifacts including hair, color chart, ruler, and marker ink. However, as seen in Figures 5.16–5.18, the proposed algorithm produced better results without the addition of artifact removal preprocessing. It is significant to note that the segmentation outcomes of the images represented by serial numbers 10 and 12 in Figure 5-17 and the images with serial numbers 3, 7, 9–12 in Figure 5-18 were significantly degraded by the inclusion of the CLAHE image enhancement preprocessing.

The qualitative findings displayed in Figures 5-16 to 5-18 are further supported by the t-test statistical analysis results provided in Tables 5-12 to 5-14. As shown in Tables 5-12 to 5-14, the inclusion of artifact removal preprocessing did not result in a statistically significant improvement in segmentation accuracy or Dice similarity. The performance scores across datasets for the CHC method

without preprocessing were higher than those for the method with preprocessing by DullRazor. Without preprocessing the images from the HAM10000 dataset, the CHC method gave noticeably better segmentation results. On the PH2 and HAM10000 datasets, however, the addition of image enhancement preprocessing revealed some statistically significant effects on segmentation accuracy with a p-value of $0.000 < 0.05$. The conclusion drawn from these findings is that image enhancing preprocessing boosts skin lesion segmentation outcomes. The impact of the image enhancing preprocessing, however, was not statistically significant when images from the complex ISIC2018 dataset were used. Except for the PH2 dataset, the CHC method without preprocessing statistically yielded considerably higher Dice scores than the segmentation with image enhancement preprocessing. However, PH2 is a small dataset that does not provide a sufficient volume of images with diverse heterogeneous qualities in comparison to the ISIC2018 and HAM10000 datasets. This assertion highlighted the appropriateness of the CHC algorithm to address heterogeneous properties of dermoscopic images.

Despite the existence of undesired artifacts such as ruler markings, hair, color charts, pen marks, vignette, noise, fuzzy borders, and numerous shades of color, the analysis of preprocessing effects has demonstrated that the CHC algorithm is capable of segmenting skin lesions effectively without preprocessing. This contradicts the findings of studies, which showed that preprocessing is necessary for a thorough and effective detection of skin lesions in dermoscopic pictures (Garnavi *et al.* 2011; Filali, Abdelouahed and Aarab 2019; Li *et al.* 2021b). Numerous studies have demonstrated the enormous influence of preprocessing in greatly improving the results of segmentation (Premaladha and Ravichandran 2016; Pathan, Prabhu and Siddalingaswamy 2018; Ross-Howe and Tizhoosh 2018; Vocaturo, Zumpano and Veltri 2018; Filali, Abdelouahed and Aarab 2019; Guarracino and Maddalena 2019; Zafar *et al.* 2020; Khan *et al.* 2021; Li *et al.* 2021b; Okuboyejo and Olugbara 2021). Conversely, the results of this study are consistent with the findings of Palus (2005) who stated that the preprocessing effect is influenced by the employment of segmentation and post-processing methods. An effective segmentation method can avoid the additional requirements of preprocessing and reduce its computing cost. This avowal has been proven in this study that the precise segmentation of skin lesions in dermoscopic images was greatly aided by the seamless application of color histogram clustering and a comprehensive mechanism combining color contrast, contrast ratio, and spatial feature with center prior. Preprocessing can be removed from image segmentation, which can significantly reduce the inherent computational complexity.

The computation efficiency of the CHC algorithm is demonstrated by the running times reported in Figures 5-19 and 5-20. The need for more computing time is one of the apparent drawbacks of using the preprocessing phase, as is clear from the findings presented. The use of preprocessing increased the computing time of CHC. Preprocessing phases used by segmentation algorithms to increase accuracy are adversely affected by the increased computing time, with multi-level preprocessing techniques having more severe ramifications. The segmentation results are generally impeded by the undesirable heterogeneous properties inherent in the dermoscopic images. Most of the known skin lesion segmentation algorithms take care of these heterogeneous qualities with the aid of a suitable choice of parameter signatures and preprocessing techniques. The widespread applicability of these methods is severely constrained by their dependence on preprocessing techniques (Bi *et al.* 2017). Except for those methods proposed by Salih and Viriri (2020) and Patiño, Avendaño and Branch (2018) the majority of the comparative methods examined in this work rely heavily on the preprocessing and parameter tuning choices. The method proposed by Patiño, Avendaño and Branch (2018) is freed of preprocessing but it may be limited in its ability to segment skin lesions in dermoscopic images with various features, such as large areas, irregular boundaries, and undesirable artifacts, because of its dependence on single-scale superpixel granularity. According to the findings of this study, the CHC algorithm can segment skin lesions precisely without being constrained by preprocessing. The results of this study showed that further preprocessing requirements can be eliminated if a segmentation method is sufficient to handle the complexity of images.

6.4 Computational efficiency

Generally, image segmentation accuracy and computing complexity are always tradeoffs. However, this is not the case with the proposed algorithm, as shown in Tables 5-15 and 5-16, where CHC has obtained the best performance while maintaining an effective run time of 0.23s per image in the ECSSD image dataset and 0.24s in the Raabin-WBC dataset. The fundamental benefit of region-based segmentation methods over pixel-based ones is their computational efficiency. The effect of region-based approaches is further emphasized by the color histogram clustering algorithm proposed in this work. The proposed algorithm not only determines the optimum cluster count but also reduces the computation complexity. Therefore, the segmentation algorithm proposed in this work is a suitable solution for effective and efficient segmentation results.

6.5 Selection of optimum cluster count

The ideal choice of optimum cluster count has a significant impact on the accuracy of salient object detection and segmentation (Filali, Allili and Benblidia 2016). The segmentation of the regions of interest from the image background required the best characterization of the unit of processing as the region of interest is defined by the uniqueness or rarity of the pixels, superpixels, or patches. Attracted by the computational efficiency and the ability to present the structure essential for the image segmentation, many studies have relied on regional or superpixel-based segmentation than pixel-level segmentation as reported in Table 5-1. Since the application of image segmentation is widespread and the diverse class of images, the determination of an optimal cluster count is challenging for superpixel-based methods. Singh, Kumar and Singh (2020) recommended multi-level abstraction of the input image by repetitively applying the superpixel technique to acquire the finest and coarsest abstraction of regions to overcome the issue of superpixel granularity. However, the iteration process increases computing complexity, which hurts the performance in real-time applications. Conversely, the proposed algorithm can select an optimum number of cluster counts based on the color distribution of the input image.

The findings of this study also showed that, when compared to the patch and pixel-wise methods, all region-based methods had demonstrated good performances. However, the effectiveness of these methods is significantly influenced by the selection of region granularity. Due to the heterogeneous properties of the input image determining a superpixel count that works ideally on a variety of images is a difficult task as illustrated in Figure 5-21. This supports the findings by Nikbakhsh, Baleghi and Agahi (2021) that a method with fixed parameter settings may provide undesired segmentation results. The performance of these superpixel-based methods is extremely hooked on the selection of the number of superpixel counts. In contrast, the proposed algorithm produced the optimum cluster count based on the image characteristics.

The summary of cluster count reported in Table 5-17 showed that the optimum cluster count is always hooked on to the image properties and is specific to the image dataset. According to Equation 4.1, the expected number of clusters is between 8 and 512, and the minimum cluster count of eight is reported in natural image datasets such as ECSSD, HKU-IS, and SOC also for the image category of the center. The maximum cluster counts of 400, 402, 403, and 415 were generated for the natural and real-scene image datasets and this showed the complexity of these datasets. As opposed to natural

images, the maximum cluster count generated for the medical image is comparatively lower and the maximum reported for medical images is 184 clusters for the Raabin-WBC dataset. It is worth observing that the range of cluster count for the PH2 dataset is 37-100 and it indicates that the images from this dataset are not heterogeneous as images of ISIC2018 and HAM10000. Generally, the most frequently used optimum cluster counts generated for the datasets used in this study are staying between 33 and 139. The identification of the optimum cluster count is the major problem suffered by clustering-based image segmentation, but the results demonstrated that the color histogram clustering algorithm developed in this study is an ideal solution to this problem.

6.6 Chapter summary

This chapter discussed the results obtained for this study based on the study objectives. This study discovered that automatic detection of cluster count using color histograms based on quantized RGB images is a viable solution for determining the optimum cluster count. The four features of color contrast, contrast ratio, center prior, and spatial features are highly suitable to detect salient objects from a diverse class of images. Another prominent achievement was the ability of the CHC algorithm to achieve quality segmentation results without the demand for preprocessing stage. The reduction of computation complexity by the proposed algorithm is an added advantage. The identification of the optimum cluster count and the preprocessing stage free segmentation approach strengthen the generalization ability of the proposed algorithm. The experimental comparison of the proposed algorithm against the state-of-the-art methods on seven image datasets and six categories of images selected from five image datasets showed that the proposed algorithm is an ideal solution for effective and efficient image segmentation on diverse classes of images. The final chapter will summarize this study with concluding remarks and recommendations for future work.

CHAPTER SEVEN: SUMMARY, CONCLUSION AND FUTURE WORK

This chapter reflects upon the complete study by summarizing the study findings and their contributions. This chapter also indicates the limitation of this study and recommends avenues for future work.

7.1 Thesis summary

Image segmentation is a core technique for visual information analysis and is widely applied in the field of computer vision. The delineation of the region of interest is an important prerequisite for the visual information analysis process. A single method that can be used for a variety of images is necessary to improve the generalizability of the segmentation method. Many factors such as the determination of optimum homogenous regions, feature selection, and image preprocessing stage can affect the generalization ability of the segmentation methods. Hence, the main aim of this study was to develop an image segmentation method based on clustering that automatically determines the best cluster count to represent homogenous regions and makes use of a set of salient features that would be most efficient on a broad range of images.

The Color Histogram Clustering (CHC) algorithm developed in this study, automatically detects the optimum number of homogeneous regions for image abstraction and extracts four features that successfully define the salient objects from the identified homogenous regions. These features of color contrast, contrast ratio, center prior, and spatial features are well agglutinated to compute a saliency map to cluster the input color image into salient and background regions. For the final segmentation of the silhouette salient objects, a two-level clustering based on Otsu thresholding and morphological post-processing is used. Investigating the impact of the preprocessing stage revealed that CHC can successfully handle the complexity of the input images without the additional need for image preprocessing.

The meta-analysis of related studies, the CHC algorithm introduced in this study, and the extensive experiments performed for the validation of the effectiveness and efficiency of the proposed image segmentation algorithm play a decisive role in accomplishing the study objectives, which are:

i. To conduct a meta-analysis of existing studies on image segmentation methods.

ii. To develop an effective and efficient clustering-based image segmentation algorithm that automatically identifies an optimum number of clusters and integrates a set of salient features to increase the generalizability of the segmentation method.
iii. To investigate the effect of image preprocessing on the performance of the newly developed image segmentation algorithm.

A meta-analysis to understand the existing trends in the image segmentation methods was conducted to accomplish the first study objective. The meta-analysis was focused on the general characteristics of image segmentation based on clustering and saliency. The main segmentation approaches, methods, preprocessing status, unit of processing and image data sources were presented to understand the recent trends and advances in image segmentation. The meta-results demonstrated the widespread use of unsupervised segmentation techniques based on saliency and clustering because of their ability to replicate visual attention mechanisms. In addition, the results showed that more studies did not include the image preprocessing step in the image segmentation process because of the computational complexity of image preprocessing. The results further revealed that many studies heavily rely on the concept of a region of pixels or superpixels for image abstraction to reduce computational complexity. This has demonstrated the need of developing a suitable technique to automatically identify the homogenous regions as the segmentation outcomes are largely dependent on the regional granularity of the homogenous regions. In addition, the meta-analysis findings indicated that 56.99 % between study variance is explained by the number of images used for segmentation evaluation.

The second study objective was accomplished by the development of color histogram clustering (CHC) algorithm. The newly developed color image segmentation algorithm can determine the appropriate number of homogenous clusters from the input image for the image segmentation. Unlike the existing image segmentation methods, the optimum cluster count is determined automatically by histogram clustering instead of a manual setting. The properties of the color histogram computed from the quantized input RGB image are used to generate the non-overlapped image regions. The four features of color contrast, contrast ratio, center prior, and the spatial features used in the color histogram clustering algorithm are successfully generating the saliency map to separate the foreground and background regions. Various levels of experimental validation employed on a wide range of images against state-of-the-art methods highlighted the superiority of the color histogram clustering algorithm. The qualitative and quantitative results demonstrated the ability of the proposed method to segment the

region of interest accurately and robustly from a wide range of challenging image categories by uniformly highlighting the salient objects regardless of their location, count, size, complex scene and low contrast to background regions. The extended evaluation of the proposed algorithm on the ECSSD, HKU-IS, SOC, PH2, ISIC2018, HAM10000 and Raabin-WBC datasets has further proved the efficacy of the algorithm in processing images from various datasets compared to the state-of-the-art image segmentation methods. The newly developed color histogram clustering algorithm proved its computational efficiency at a subsequently smaller running time compared with the rest of the state-of-the-art methods. The automatic finding of the homogenous regions, the specialized integration of the four identified features for the silhouette segmentation and morphological post-processing operations were all included in the development of color histogram clustering algorithm to achieve the second study objective.

Finally, the last study objective was accomplished by proving the ability of the proposed algorithm to perform an effective segmentation without the inclusion of any preprocessing stages. In contrast to existing image segmentation methods, CHC provides a region of interest segmentation solution that is robust, effective, and independent of preprocessing processes. The experimental findings are encouraging and demonstrate that CHC outperforms modern methods in handling the various types of artifacts without the need for any preprocessing steps. This significantly opens its application to a wide range of images.

In summary, the proposed CHC image segmentation algorithm showed good performance in terms of finding homogenous regions, and well-defined foreground and background separation for effective segmentation of silhouette objects. The introduction of the optimum cluster count generation, specialized integration of color contrast, contrast ratio, center prior and the spatial features, computational efficiency, and the preprocessing free nature contribute toward the universal application of the proposed algorithm.

7.2 Conclusion

Color image segmentation is one of the integral research areas in the field of image processing and computer vision. Due to the heterogeneous image properties and unpredictable complexity, the performance of the segmentation algorithm is subpar, time-consuming, imprecise, and unfeasible when applied to a gamut of image categories. A simple and robust image segmentation algorithm was developed in this study to address this problem. An automatic image segmentation algorithm, targeted

to deal with various types of image categories, has been presented in this study. The newly developed algorithm effectively and efficiently segments the region of interest by making use of histogram clustering for optimum cluster generation and integration of multiple features. The generalization ability is dependent on many factors such as the heterogeneous nature of the image including the presence of noise, various artifacts, and illumination variation. Identification of optimum cluster count, proper integration of color contrast, contrast ratio, center prior and spatial features, and preprocessing independent segmentation method were the major contribution toward the universal color image segmentation algorithm. The results from the extended experimental analysis have demonstrated the capability of the proposed algorithm to accurately segment the region of interest from images of varying undesirable properties. The results are robust because the proposed algorithm in a novel way incorporates the features of color contrast, contrast ratio, spatial feature, and center prior. It is pertinent to note that the proposed algorithm fruitfully addresses the intrinsic convolutions of images without the presence of preprocessing and contributes to a universal method for image segmentation.

7.3 Future work

Although the proposed algorithm showed remarkable results on a variety of image categories and datasets, the performance of the proposed algorithm on images with cluttered and occluded background still need to be improved. However, the CHC algorithm has a few flaws and shortcomings. Images with salient objects surrounded by pseudo salient objects with the same characteristics (Figure 7-1(1 and 2)), the presence of an extremely small salient object (Figure 7-1 (3)), ambiguous salient objects (Figure 7-1 (4 and 5)), and salient object share same color feature with the background region (Figure 7-1(6)) were produced inaccurate segmentation results as illustrated in Figure 7-1.

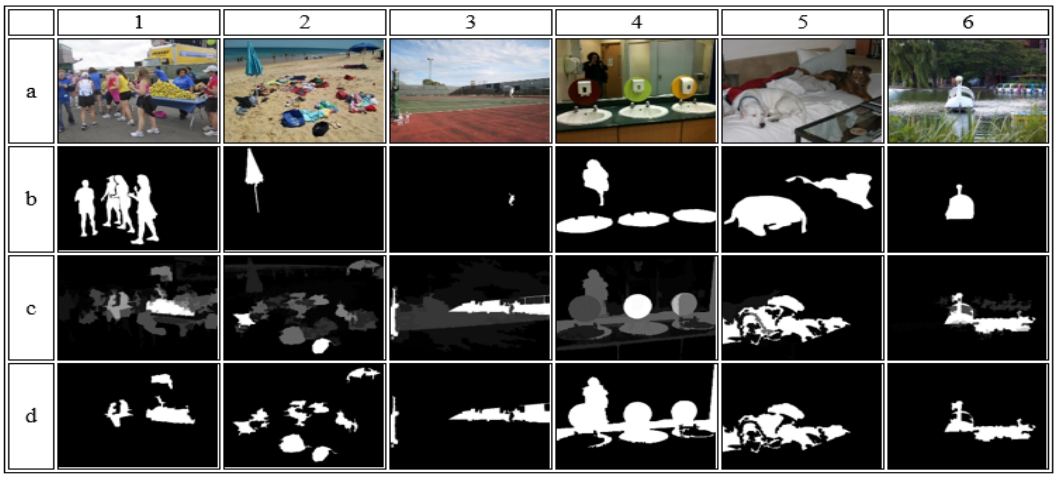

Figure 7-1 Some examples of failure cases with CHC algorithm: (a) original image; (b) Ground truth; (c) Saliency map generated by CHC; (d) Silhouette object segmented by CHC algorithm

The proposed algorithm failed to successfully segment salient objects that share the same color properties with the background region as in Figure 7-1(6). The addition of texture features can overcome this shortcoming of color-based segmentation models as the texture is the basic repeated pattern that distinguishes the surface of real-world objects. In the future, this study anticipates that adding other features, including texture, may help to increase segmentation accuracy. One of the failed cases of CHC involves images with an extremely small salient object surrounded by several enormous visually distinctive objects. These images are also problems for modern segmentation methods. Future work will look into how the aggregation of high-level features may be used to address this open problem. Further, the proposed algorithm failed on images with uncertainty in salient regions. For instance, in Figure 7-1(2) where the ground truth has only a single salient object as other foreground objects on this image are not reported as salient. There is wide disagreement on what makes an object salient, and few works take into account the possibility that individual perceptions of what makes an image stand out may differ.

There is room for the CHC algorithm to ameliorate the performance of these categories of images by integrating texture and high-level features while maintaining computational efficiency. With further improvement to the proposed algorithm, CHC can better handle convoluted images and can further enrich its performance. It would be also valuable to consider the proposed algorithm for more practical applications, hence in the future, the research will be intensely carried out on images from various datasets of video surveillance, content-based image retrieval, and remote sensing.

REFERENCES

Abd Elaziz, M., Abo Zaid, E. O., Al-qaness, M. A. and Ibrahim, R. A. 2021. Automatic superpixel-based clustering for color image segmentation using q-generalized pareto distribution under linear normalization and hunger games search. *Mathematics*, 9 (19): 1-18.

Abdalla, A., Cen, H. Y., El-manawy, A. and He, Y. 2019. Infield oilseed rape images segmentation via improved unsupervised learning models combined with supreme color features. *Computers and Electronics in Agriculture*, 162: 1057-1068.

Abdel-Maksoud, E., Elmogy, M. and Al-Awadi, R. 2015. Brain tumor segmentation based on a hybrid clustering technique. *Egyptian Informatics Journal*, 16 (1): 71-81.

Abdul-Nasir, A. S., Mashor, M. Y. and Mohamed, Z. 2013. Colour image segmentation approach for detection of malaria parasites using various colour models and K-means clustering. *WSEAS Transactions on Biology and Biomedicine*, 10 (1): 41-55.

Abkenar, M. R., Sadreazami, H. and Ahmad, M. O. 2018. Salient region detection using feature extraction in the non-subsampled contourlet domain. *IET Image Processing*, 12 (12): 2275-2282.

Achanta, R., Estrada, F., Wils, P. and Süsstrunk, S. 2008. Salient region detection and segmentation. In: Proceedings of *International Conference on Computer Vision Systems*. Santorini, Greece, 12-15 May 2008. Springer, 66-75.

Achanta, R., Hemami, S., Estrada, F. and Susstrunk, S. 2009. Frequency-tuned salient region detection. In: Proceedings of *2009 IEEE Conference on Computer Vision and Pattern Recognition (CVPR)* Miami, Florida, USA, 20 - 21 June 2009. IEEE, 1597-1604.

Achanta, R., Shaji, A., Smith, K., Lucchi, A., Fua, P. and Süsstrunk, S. 2010. *Slic Superpixels*. EPFL Technical Report 149300.

Adeel, A., Khan, M. A., Sharif, M., Azam, F., Shah, J. H., Umer, T. and Wan, S. 2019. Diagnosis and recognition of grape leaf diseases: An automated system based on a novel saliency approach and

canonical correlation analysis based multiple features fusion. *Sustainable Computing-Informatics & Systems*, 24: 1-11.

Afza, F., Sharif, M., Mittal, M., Khan, M. A. and Hemanth, D. J. 2021. A hierarchical three-step superpixels and deep learning framework for skin lesion classification. *Methods*, 202: 1-15.

Afzali, S., Al-Sahaf, H., Xue, B., Hollitt, C. and Zhang, M. 2018. Foreground and background feature fusion using a convex hull based center prior for salient object detection. In: Proceedings of *2018 International Conference on Image and Vision Computing New Zealand (IVCNZ)*. Auckland, New Zealand, 19-21 November 2018. IEEE, 1-9.

Aganj, I., Harisinghani, M. G., Weissleder, R. and Fischl, B. 2018. Unsupervised medical image segmentation based on the local center of mass. *Scientific Reports*, 8 (1): 1-8.

Agarwal, A., Issac, A., Dutta, M. K., Riha, K. and Uher, V. 2017. Automated skin lesion segmentation using K-means clustering from digital dermoscopic images. In: Proceedings of *40th International Conference on Telecommunications and Signal Processing (TSP)*. Barcelona, Spain, 5-7 July 2017. IEEE, 743-748.

Ahn, E., Bi, L., Jung, Y. H., Kim, J., Li, C., Fulham, M. and Feng, D. D. 2015. Automated saliency-based lesion segmentation in dermoscopic images. In: Proceedings of *37th Annual International Conference of the IEEE Engineering in Medicine and Biology Society (EMBC)*. Milano, Italy, 25 - 29 August 2015. IEEE, 3009-3012.

Ahn, E., Kim, J., Bi, L., Kumar, A., Li, C., Fulham, M. and Feng, D. D. 2017. Saliency-based lesion segmentation via background detection in dermoscopic images. *IEEE Journal of Biomedical and Health Informatics*, 21 (6): 1685-1693.

Al-Dulaimi, K., Tomeo-Reyes, I., Banks, J. and Chandran, V. 2020. Evaluation and benchmarking of level set-based three forces via geometric active contours for segmentation of white blood cell nuclei shape. *Computers in Biology and Medicine*, 116: 103568.

Al-jaboriy, S. S., Sjarif, N. N. A., Chuprat, S. and Abduallah, W. M. 2019. Acute lymphoblastic leukemia segmentation using local pixel information. *Pattern Recognition Letters*, 125: 85-90.

Ali, R., Hardie, R. C., Narayanan, B. N. and De Silva, S. 2019. Deep learning ensemble methods for skin lesion analysis towards melanoma detection. In: Proceedings of *2019 IEEE National Aerospace and Electronics Conference (NAECON)*. Dayton, Ohio, USA, 15-21 July 2019. IEEE, 311-316.

Alihodzic, A. and Tuba, M. 2014. Improved bat algorithm applied to multilevel image thresholding. *The Scientific World Journal*, 2014: 1-16.

Aljebory, K. M. and Mohammed, T. S. 2018. Modified fuzzy C-means clustering algorithm application in medical image segmentation. *JEA Journal of Electrical Engineering*, 2 (1): 1-9.

Alom, M. Z., Hasan, M., Yakopcic, C., Taha, T. M. and Asari, V. K. 2018. Recurrent residual convolutional neural network based on U-Net (R2U-Net) for medical image segmentation. *arXiv preprint arXiv:1802.06955*. Available: https://arxiv.org/abs/1802.06955 (Accessed 20 December 2020).

Alpert, S., Galun, M., Brandt, A. and Basri, R. 2011. Image segmentation by probabilistic bottom-up aggregation and cue integration. *IEEE transactions on Pattern Analysis and Machine Intelligence*, 34 (2): 315-327.

Ananthi, V. P. and Balasubramaniam, P. 2016. A new thresholding technique based on fuzzy set as an application to leukocyte nucleus segmentation. *Computer Methods and Programs in Biomedicine*, 134: 165-177.

Andrade, A. R., Vogado, L. H., de MS Veras, R., Silva, R. R., Araujo, F. H. and Medeiros, F. N. 2019. Recent computational methods for white blood cell nuclei segmentation: A comparative study. *Computer Methods and Programs in Biomedicine*, 173: 1-14.

Annum, R., Riaz, M. M. and Ghafoor, A. 2018. Saliency detection using contrast enhancement and texture smoothing operations. *Signal, Image and Video Processing*, 12 (3): 505-511.

Arbelaez, P., Maire, M., Fowlkes, C. and Malik, J. 2011. Contour detection and hierarchical image segmentation. *IEEE Transactions on Pattern Analysis and Machine Intelligence*, 33 (5): 898-916.

Arora, P. and Varshney, S. 2016. Analysis of K-means and K-medoids algorithm for big data. *Procedia Computer Science*, 78: 507-512.

Arya, R., Singh, N. and Agrawal, R. 2016. A novel hybrid approach for salient object detection using local and global saliency in frequency domain. *Multimedia Tools and Applications*, 75 (14): 8267-8287.

Ashour, A. S., Guo, Y., Kucukkulahli, E., Erdogmus, P. and Polat, K. 2018. A hybrid dermoscopy images segmentation approach based on neutrosophic clustering and histogram estimation. *Applied Soft Computing*, 69: 426-434.

Ayoub, N., Gao, Z., Chen, D., Tobji, R. and Yao, N. 2018. Visual saliency detection based on color frequency features under Bayesian framework. *KSII Transactions on Internet and Information Systems (TIIS)*, 12 (2): 676-692.

Aytekin, Ç., Kiranyaz, S. and Gabbouj, M. 2016. Learning to rank salient segments extracted by multispectral Quantum Cuts. *Pattern Recognition Letters*, 72: 91-99.

Babu, K., Subudhi, A. and Sabut, S. 2018. Segmentation of diabetic wound by multidimensional clustering for quantitative assessment of healing process. *Current Medical Imaging Reviews*, 14 (1): 71-76.

Bai, X. D., Cao, Z. G., Wang, Y., Yu, Z. H., Hu, Z., Zhang, X. F. and Li, C. N. 2014. Vegetation segmentation robust to illumination variations based on clustering and morphology modelling. *Biosystems Engineering*, 125: 80-97.

Banerjee, S., Mitra, S. and Shankar, B. U. 2018. Automated 3D segmentation of brain tumor using visual saliency. *Information Sciences*, 424: 337-353.

Bangare, S. L., Dubal, A., Bangare, P. S. and Patil, S. 2015. Reviewing Otsu's method for image thresholding. *International Journal of Applied Engineering Research*, 10 (9): 21777-21783.

Bao, L., Lu, J., Li, Y. and Shi, Y. 2015. A saliency detection model using shearlet transform. *Multimedia Tools and Applications*, 74 (11): 4045-4058.

Bargoti, S. and Underwood, J. P. 2017. Image segmentation for fruit detection and yield estimation in apple orchards. *Journal of Field Robotics*, 34 (6): 1039-1060.

Basar, S., Ali, M., Ochoa-Ruiz, G., Zareei, M., Waheed, A. and Adnan, A. 2020. Unsupervised color image segmentation: A case of RGB histogram based K-means clustering initialization. *PloS one*, 15 (10): e0240015.

Batra, D., Kowdle, A., Parikh, D., Luo, J. and Chen, T. 2010. iCoseg: Interactive co-segmentation with intelligent scribble guidance. In: Proceedings of *2010 IEEE Computer Society Conference on Computer Vision and Pattern Recognition*. San Francisco, CA, USA, 13-18 June 2010. IEEE, 3169-3176.

Benabdellah, A. C., Benghabrit, A. and Bouhaddou, I. 2019. A survey of clustering algorithms for an industrial context. *Procedia Computer Science*, 148: 291-302.

Benini, S., Khan, K., Leonardi, R., Mauro, M. and Migliorati, P. 2019. Face analysis through semantic face segmentation. *Signal Processing: Image Communication*, 74: 21-31.

Bi, L., Kim, J., Ahn, E., Feng, D. and Fulham, M. 2016. Automated skin lesion segmentation via image-wise supervised learning and multi-scale superpixel based cellular automata. In: Proceedings of *2016 IEEE 13th International Symposium on Biomedical Imaging (ISBI)*. Prague, Czech Republic, 13-16 April 2016. IEEE, 1059-1062.

Bi, L., Kim, J., Ahn, E., Kumar, A., Fulham, M. and Feng, D. 2017. Dermoscopic image segmentation via multistage fully convolutional networks. *IEEE Transactions on Biomedical Engineering*, 64 (9): 2065-2074.

Bodhe, T. S. and Mukherji, P. 2013. Selection of color space for image segmentation in pest detection. In: Proceedings of *2013 International Conference on Advances in Technology and Engineering (ICATE)*. Mumbai, India, 23-25 January 2013. IEEE, 1-7.

Bong, C.-W. and Rajeswari, M. 2011. Multi-objective nature-inspired clustering and classification techniques for image segmentation. *Applied soft computing*, 11 (4): 3271-3282.

Bora, D. J. and Gupta, A. K. 2014. Clustering approach towards image segmentation: an analytical study. *arXiv preprint arXiv:1407.8121*. Available: https://arxiv.org/abs/1407.8121 (Accessed 15 November 2020).

Bora, D. J. and Gupta, A. K. 2015. A novel approach towards clustering based image segmentation. *arXiv preprint arXiv:1506.01710*. Available: https://arxiv.org/abs/1506.01710 (Accessed 10 November 2020).

Bora, D. J., Gupta, A. K. and Khan, F. A. 2015. Comparing the performance of L* a* b* and HSV color spaces with respect to color image segmentation. *arXiv preprint arXiv:1506.01472*. Available: https://arxiv.org/abs/1506.01472 (Accessed 20 November 2020).

Borenstein, E. and Ullman, S. 2002. Class-specific, top-down segmentation. In: Proceedings of *European Conference on Computer Vision*. Copenhagen, Denmark, 28-31 May 2002. Springer, 109-122.

Borenstein, M., Hedges, L. V., Higgins, J. P. and Rothstein, H. R. 2009. *Introduction to meta-analysis*. Chichester, West Sussex: John Wiley & Sons.

Borji, A. 2014. What is a salient object? A dataset and a baseline model for salient object detection. *IEEE Transactions on Image Processing*, 24 (2): 742-756.

Borji, A., Cheng, M.-M., Jiang, H. and Li, J. 2015. Salient object detection: A benchmark. *IEEE Transactions on Image Processing*, 24 (12): 5706-5722.

Bozorgtabar, B., Abedini, M. and Garnavi, R. 2016. Sparse coding based skin lesion segmentation using dynamic rule-based refinement. In: Proceedings of *International Workshop on Machine Learning in Medical Imaging*. Athens, Greece, 17 October 2016. Springer, 254-261.

Bravo, M. J. and Farid, H. 2004. Recognizing and segmenting objects in clutter. *Vision Research*, 44 (4): 385-396.

Brunda, R., Divyashree, B. and Rani, N. S. 2018. Image segmentation technique- A comparative study. *International Journal of Engineering and Technology(UAE)*, 7 (4): 3131-3134.

Cai, Y., Dai, L., Wang, H., Chen, L. and Li, Y. 2020. A novel saliency detection algorithm based on adversarial learning model. *IEEE Transactions on Image Processing*, 29: 4489-4504.

Chebbout, S. and Merouani, H. F. 2012. Comparative study of clustering based colour image segmentation techniques. In: Proceedings of *Eighth International Conference on Signal Image Technology and Internet Based Systems (SITIS)*. Naples, Italy, 22 - 25 November 2012. IEEE, 839-844.

Chehreghani, M. H. 2020. Hierarchical correlation clustering and tree preserving embedding. *arXiv preprint arXiv:2002.07756*. Available: https://arxiv.org/abs/2002.07756 (Accessed 10 November 2020).

Chen, J., Cao, Y., Gao, J. and An, H. 2021. A polylobar nucleus identifying and extracting method for leukocyte counting. *Computational and Mathematical Methods in Medicine*, 2021: 1-12.

Chen, J., Li, Z. and Huang, B. 2017. Linear spectral clustering superpixel. *IEEE Transactions on Image Processing*, 26 (7): 3317-3330.

Chen, Z., Qi, Z., Meng, F., Cui, L. and Shi, Y. 2015. Image segmentation via improving clustering algorithms with density and distance. *Procedia Computer Science*, 55: 1015-1022.

Cheng, G. and Wei, J. 2019. Color quantization application based on K-means in remote sensing image processing. *Journal of Physics: Conference Series*, 1213 (4): 042012.

Cheng, M.-M., Mitra, N. J., Huang, X., Torr, P. H. and Hu, S.-M. 2015. Global contrast based salient region detection. *IEEE Transactions on Pattern Analysis and Machine Intelligence*, 37 (3): 569-582.

Chirici, G., Mura, M., McInerney, D., Py, N., Tomppo, E. O., Waser, L. T., Travaglini, D. and McRoberts, R. E. 2016. A meta-analysis and review of the literature on the k-Nearest Neighbors technique for forestry applications that use remotely sensed data. *Remote Sensing of Environment*, 176: 282-294.

Chuang, Y., Chen, L. and Chen, G. 2014. Saliency-guided improvement for hand posture detection and recognition. *Neurocomputing*, 133: 404-415.

Chuang, Y., Chen, L., Chen, G. and Woodward, J. 2014. Isophote based center-surround contrast computation for image saliency detection. *IEICE Transactions on Information and Systems*, 97 (1): 160-163.

Codella, N., Rotemberg, V., Tschandl, P., Celebi, M. E., Dusza, S., Gutman, D., Helba, B., Kalloo, A., Liopyris, K. and Marchetti, M. 2019. Skin lesion analysis toward melanoma detection 2018: A challenge hosted by the International Skin Imaging Collaboration (ISIC). *arXiv preprint arXiv:1902.03368*. Available: https://arxiv.org/abs/1902.03368 (Accessed 20 March 2021).

Cohen-Addad, V., Kanade, V., Mallmann-Trenn, F. and Mathieu, C. 2018. Hierarchical clustering: Objective functions and algorithms. In: Proceedings of *Twenty-Ninth Annual ACM-SIAM Symposium on Discrete Algorithms*. New Orleans, Louisiana, 7 - 10 January 2018. SIAM, 378-397.

Coleman, G. B. and Andrews, H. C. 1979. Image segmentation by clustering. *Proceedings of the IEEE*, 67 (5): 773-785.

Comaniciu, D. and Meer, P. 2002. Mean shift: A robust approach toward feature space analysis. *IEEE Transactions on Pattern Analysis and Machine Intelligence*, 24 (5): 603-619.

Cornuejols, A., Wemmert, C., Gançarski, P. and Bennani, Y. 2018. Collaborative clustering: Why, when, what and how. *Information Fusion*, 39: 81-95.

Crocetti, E. 2016. Systematic reviews with meta-analysis: Why, when, and how? *Emerging Adulthood*, 4 (1): 3-18.

Cuevas, E., Becerra, H., Luque, A. and Elaziz, M. A. 2021. Fast multi-feature image segmentation. *Applied Mathematical Modelling*, 90: 742-757.

Dai, Y., Deng, Y., Lin, Y., Ouyang, R. and Li, L. 2020. Long-term outcomes and quality of life of patients with Hirschsprung disease: a systematic review and meta-analysis. *BMC Gastroenterology*, 20 (1): 1-13.

Deeba, F., Bui, F. M. and Wahid, K. A. 2020. Computer-aided polyp detection based on image enhancement and saliency-based selection. *Biomedical Signal Processing and Control*, 55: 101530.

Dempster, A. P., Laird, N. M. and Rubin, D. B. 1977. Maximum likelihood from incomplete data via the EM algorithm. *Journal of the Royal Statistical Society. Series B (Methodological)*, 39 (1): 1-38.

Deng, L. L., Wang, Z. H., Wang, C., He, Y. F., Huang, T., Dong, Y. and Zhang, X. 2020. Application of agricultural insect pest detection and control map based on image processing analysis. *Journal of Intelligent & Fuzzy Systems*, 38 (1): 379-389.

Devi, S. S., Singh, N. H. and Laskar, R. H. 2020. Fuzzy C-Means clustering with histogram based cluster selection for skin lesion segmentation using non-dermoscopic images. *International Journal of Interactive Multimedia & Artificial Intelligence*, 6 (1): 1-6.

Dhanachandra, N. and Chanu, Y. J. 2017. A survey on image segmentation methods using clustering techniques. *European Journal of Engineering Research and Science*, 2 (1): 15-20.

Dhanachandra, N., Manglem, K. and Chanu, Y. J. 2015. Image segmentation using K-means clustering algorithm and subtractive clustering algorithm. *Procedia Computer Science*, 54: 764-771.

Dhua, A., Sarma, D. N., Singh, S. and Roy, B. 2015. Segmentation of images using density-based algorithms. *International Journal of Advanced Research in Computer and Communication Engineering*, 4 (5): 273-277.

Dice, L. R. 1945. Measures of the amount of ecologic association between species. *Ecology*, 26 (3): 297-302.

Ding, M., Xu, X., Zhang, F., Xiao, Z., Liu, Y., Geng, L., Wu, J., Wen, J. and Wang, M. 2020. Saliency detection via background prior and foreground seeds. *Multimedia Tools and Applications*, 79 (21): 14849-14870.

Du, L., Li, L., Wei, D. and Mao, J. 2020. Saliency-guided single shot multibox detector for target detection in SAR images. *IEEE Transactions on Geoscience and Remote Sensing*, 58 (5): 3366-3376.

Duan, L., Wu, C., Miao, J., Qing, L. and Fu, Y. 2011. Visual saliency detection by spatially weighted dissimilarity. In: Proceedings of *2011 IEEE Conference on Computer Vision and Pattern Recognition (CVPR)*. Washington DC, United States, 20 - 25 June 2011. IEEE, 473-480.

Dubey, S. R., Dixit, P., Singh, N. and Gupta, J. P. 2013. Infected fruit part detection using K-means clustering segmentation technique. *International Journal of Artificial Intelligence and Interactive Multimedia*, 2 (2): 65-72.

Dunn, J. C. 1973. A fuzzy relative of the ISODATA process and its use in detecting compact well-separated clusters. *Journal of Cybernetics*, 3 (3): 32-57.

El Sayed, A. R., El Chakik, A., Alabboud, H. and Yassine, A. 2017. 3D face detection based on salient features extraction and skin colour detection using data mining. *Imaging Science Journal*, 65 (7): 393-408.

Emre Celebi, M., Kingravi, H. A., Iyatomi, H., Alp Aslandogan, Y., Stoecker, W. V., Moss, R. H., Malters, J. M., Grichnik, J. M., Marghoob, A. A. and Rabinovitz, H. S. 2008. Border detection in dermoscopy images using statistical region merging. *Skin Research and Technology*, 14 (3): 347-353.

Erdem, E. and Erdem, A. 2013. Visual saliency estimation by nonlinearly integrating features using region covariances. *Journal of Vision*, 13 (4): 11-11.

Ester, M., Kriegel, H.-P., Sander, J. and Xu, X. 1996. A density-based algorithm for discovering clusters in large spatial databases with noise. In: Proceedings of *Knowledge Discovery and Data mining*. Portland, Oregon, 2 - 4 August 1996. AAAI, 226-231.

Fahad, A., Alshatri, N., Tari, Z., Alamri, A., Khalil, I., Zomaya, A. Y., Foufou, S. and Bouras, A. 2014. A survey of clustering algorithms for big data: Taxonomy and empirical analysis. *IEEE Transactions on Emerging Topics in Computing*, 2 (3): 267-279.

Fan, D.-P., Cheng, M.-M., Liu, J.-J., Gao, S.-H., Hou, Q. and Borji, A. 2018. Salient objects in clutter: Bringing salient object detection to the foreground. In: Proceedings of *The European Conference on Computer Vision (ECCV)*. Munich, Germany, 8-14 September 2018. Springer, 186-202.

Fan, H., Xie, F., Li, Y., Jiang, Z. and Liu, J. 2017. Automatic segmentation of dermoscopy images using saliency combined with Otsu threshold. *Computers in Biology and Medicine*, 85 (2017): 75-85.

Fan, P., Lang, G. D., Yan, B., Lei, X. Y., Guo, P. J., Liu, Z. J. and Yang, F. Z. 2021. A method of segmenting apples based on gray-centered RGB color space. *Remote Sensing*, 13 (6): 1-17.

Fareed, M. M. S., Chun, Q., Ahmed, G., Asif, M. R. and Fareed, M. Z. 2018. Saliency detection by exploiting multi-features of color contrast and color distribution. *Computers & Electrical Engineering*, 70: 551-566.

Farhang, Y. 2017. Face extraction from image based on K-Means clustering algorithms. *International Journal of Advanced Computer Science and Applications*, 8 (9): 96-107.

Feng, L., Li, H. B., Gao, Y. K. and Zhang, Y. K. 2020. A color image segmentation method based on region salient color and fuzzy C-means algorithm. *Circuits Systems and Signal Processing*, 39 (2): 586-610.

Feng, W., Zhang, J., Hu, C., Wang, Y., Xiang, Q. and Yan, H. 2018. A novel saliency detection method for wild animal monitoring images with WMSN. *Journal of Sensors*, 2018: 1-17.

Feng, X., Guoying, C., Richang, H. and Jing, G. 2015. Camouflage texture evaluation using a saliency map. *Multimedia Systems*, 21 (2): 169-175.

Filali, I., Allili, M. S. and Benblidia, N. 2016. Multi-scale salient object detection using graph ranking and global–local saliency refinement. *Signal Processing: Image Communication*, 47: 380-401.

Filali, Y., Abdelouahed, S. and Aarab, A. 2019. An improved segmentation approach for skin lesion classification. *Statistics, Optimization & Information Computing*, 7 (2): 456-467.

Fisher, D. J., Zwahlen, M., Egger, M. and Higgins, J. P. T. 2022. Meta-Analysis in Stata. In: *Systematic Reviews in Health Research*. Wiley Blackwell, 481-509.

Fukunaga, K. and Hostetler, L. 1975. The estimation of the gradient of a density function, with applications in pattern recognition. *IEEE Transactions on Information Theory*, 21 (1): 32-40.

Furtado, P. 2021. Loss, post-processing and standard architecture improvements of liver deep learning segmentation from Computed Tomography and magnetic resonance. *Informatics in Medicine Unlocked*, 24: 100585.

Galbraith, R. F. 1990. The radial plot: graphical assessment of spread in ages. *International Journal of Radiation Applications and Instrumentation. Part D. Nuclear Tracks and Radiation Measurements*, 17 (3): 207-214.

Galiano, G., Ramírez, I. and Schiavi, E. 2020. Non-convex non-local reactive flows for saliency detection and segmentation. *Journal of Computational and Applied Mathematics*, 377: 112873.

Ganesh, M., Naresh, M. and Arvind, C. 2017. MRI brain image segmentation using enhanced adaptive fuzzy K-Means algorithm. *Intelligent Automation & Soft Computing*, 23 (2): 325-330.

García-Lamont, F., Cervantes, J. and López-Chau, A. 2018. Human mimic color perception for segmentation of color images using a three-layered self-organizing map previously trained to classify color chromaticity. *Neural Computing and Applications*, 30 (3): 871-889.

Garcia-Lamont, F., Cervantes, J., López, A. and Rodriguez, L. 2018. Segmentation of images by color features: A survey. *Neurocomputing*, 292: 1-27.

Garnavi, R., Aldeen, M., Celebi, M. E., Varigos, G. and Finch, S. 2011. Border detection in dermoscopy images using hybrid thresholding on optimized color channels. *Computerized Medical Imaging and Graphics*, 35 (2): 105-115.

Ghosal, A., Nandy, A., Das, A. K., Goswami, S. and Panday, M. 2020. A short review on different clustering techniques and their applications. In: *Emerging Technology in Modelling and Graphics*. Springer, 69-83.

Gion, D., Takimoto, H., Kishihara, M. and Okubo, K. 2015. Interactive segmentation of color images based on color saliency. *Electronics and Communications in Japan*, 98 (3): 24-32.

Goferman, S., Zelnik-Manor, L. and Tal, A. 2012. Context-aware saliency detection. *IEEE Transactions on Pattern Analysis and Machine Intelligence*, 34 (10): 1915-1926.

Goh, T. Y., Basah, S. N., Yazid, H., Safar, M. J. A. and Saad, F. S. A. 2018. Performance analysis of image thresholding: Otsu technique. *Measurement*, 114: 298-307.

Gonzalez, R. C. and Woods, R. E. 2008. *Digital image processing Third Edition*. 3rd ed. Pearson-Prentice-Hall Upper Saddle River, New Jersey.

Gonzalez, R. C. and Woods, R. E. 2018. *Digital Image Processing*. 4th ed. Pearson Education, England.

Gonzalez, R. C., Woods, R. E. and Eddins, S. L. 2004. *Digital image processing using MATLAB*. Pearson-Prentice-Hall Upper Saddle River, New Jersey.

Gopi Krishna, T., Mishra, S., Satapathy, S. and Sunitha, K. V. N. 2020. Segmentation and classification of brain tumor from magnetic resonance images using K-Means algorithm and hybrid pso-wca based radial basis function neural network. *International Journal of Advanced Trends in Computer Science and Engineering*, 9 (5): 7800-7807.

Guan, J. Y., Li, S., He, X. X. and Chen, J. J. 2021. Peak-graph-based fast density peak clustering for image segmentation. *IEEE Signal Processing Letters*, 28: 897-901.

Guarracino, M. R. and Maddalena, L. 2019. SDI+: A novel algorithm for segmenting dermoscopic images. *IEEE Journal of Biomedical and Health Informatics*, 23 (2): 481-488.

Guo, Y., Şengür, A., Akbulut, Y. and Shipley, A. 2018. An effective color image segmentation approach using neutrosophic adaptive mean shift clustering. *Measurement*, 119: 28-40.

Gupta, A. K., Seal, A., Prasad, M. and Khanna, P. 2020. Salient object detection techniques in computer vision—A survey. *Entropy*, 22 (10): 1-49.

Gupta, T. and Panda, S. P. 2018. A comparison of K-Means clustering algorithm and CLARA clustering algorithm on Iris dataset. *International Journal of Engineering & Technology*, 7 (4): 4766-4768.

Hafeez, H., Yan, P. and Guoliang, L. 2021. Image processing approach for segmentation of WBC nuclei based on K-Means clustering. In: Proceedings of *The 4th International Conference on Image and Graphics Processing*. Sanya, China, 1-3 January 2021. Association for Computing Machinery, 175-181.

Han, A., Han, F., Hao, J. and Yuan, Y. 2017. An improved saliency detection method based on non-uniform quantification and channel-weighted color distance. *Multimedia Tools and Applications*, 76 (8): 11037-11050.

Han, J., Zhang, D., Wen, S., Guo, L., Liu, T. and Li, X. 2015. Two-stage learning to predict human eye fixations via SDAEs. *IEEE Transactions on Cybernetics*, 46 (2): 487-498.

Harel, J., Koch, C. and Perona, P. 2007. Graph-based visual saliency. In: Proceedings of *Advances in Neural Information Processing Systems*. British Columbia, Canada, 4-7 December 2006. NeurIPS, 545-552.

He, B. J., Hu, W. B., Zhang, K., Yuan, S. D., Han, X. L., Su, C., Zhao, J. M., Wang, G. Z., Wang, G. X. and Zhang, L. Y. 2021a. Image segmentation algorithm of lung cancer based on neural network model. *Expert Systems*, 2021 (e12822): 1-9.

He, F. L., Fu, C. Y., Shao, H. Z. and Teng, J. Q. 2019. An image segmentation algorithm based on double-layer pulse-coupled neural network model for kiwifruit detection. *Computers & Electrical Engineering*, 79: 106466.

He, J., Guo, Y. and Yuan, H. 2020. Ship target automatic detection based on hypercomplex flourier transform saliency model in high spatial resolution remote-sensing images. *Sensors*, 20 (9): 2536.

He, P., Zhao, X., Shi, Y. and Cai, L. 2021b. Unsupervised change detection from remotely sensed images based on multi-scale visual saliency coarse-to-fine fusion. *Remote Sensing*, 13 (4): 630.

He, S., Lau, R. W. and Yang, Q. 2016. Exemplar-driven top-down saliency detection via deep association. In: Proceedings of *IEEE Conference on Computer Vision and Pattern Recognition*. Las Vegas, NV, USA, 27-30 June 2016. IEEE, 5723-5732.

Hedges, L. V. and Vevea, J. L. 1998. Fixed-and random-effects models in meta-analysis. *Psychological Methods*, 3 (4): 486-504.

Henke, M., Neumann, K., Altmann, T. and Gladilin, E. 2021. Semi-automated ground truth segmentation and phenotyping of plant structures using K-Means clustering of eigen-colors (kmSeg). *Agriculture*, 11 (11): 1098.

Higgins, J. P., Thompson, S. G., Deeks, J. J. and Altman, D. G. 2003. Measuring inconsistency in meta-analyses. *BMJ*, 327 (7414): 557-560.

Hoshyar, A. N., Jumaily, A. A. and Hoshyar, A. N. 2014. Pre-processing of automatic skin cancer detection system: comparative study. *International Journal on Smart Sensing and Intelligent Systems*, 7 (3): 1364-1377.

Hou, X. and Zhang, L. 2007. Saliency detection: A spectral residual approach. In: Proceedings of *2007 IEEE Conference on Computer Vision and Pattern Recognition (CVPR)*. Minneapolis, MN, 17-22 June 2007. IEEE, 1-8.

Hu, K., Liu, S., Zhang, Y., Cao, C., Xiao, F., Huang, W. and Gao, X. 2020. Automatic segmentation of dermoscopy images using saliency combined with adaptive thresholding based on wavelet transform. *Multimedia Tools and Applications*, 79 (21): 14625-14642.

Hu, X., Yang, W., Wang, X. and Liao, Q. 2016. Salient object detection via spectral clustering. In: Proceedings of *2016 IEEE Information Technology, Networking, Electronic and Automation Control Conference*. Chongqing, China, 20-22 May 2016. IEEE, 165-169.

Hu, Z., Zhang, Z., Sun, Z. and Zhao, S. 2018. Saliency detection based on salient edges and remarkable discriminating for superpixel pairs. *Multimedia Tools and Applications*, 77 (5): 5949-5968.

Huang, D.-C., Hung, K.-D. and Chan, Y.-K. 2012. A computer assisted method for leukocyte nucleus segmentation and recognition in blood smear images. *Journal of Systems and Software*, 85 (9): 2104-2118.

Huang, H., Meng, F., Zhou, S., Jiang, F. and Manogaran, G. 2019. Brain image segmentation based on FCM clustering algorithm and rough set. *IEEE Access*, 7: 12386-12396.

Huang, L., Song, K., Gong, A., Liu, C. and Yan, Y. 2020. RGB-T saliency detection via low-rank tensor learning and unified collaborative ranking. *IEEE Signal Processing Letters*, 27: 1585-1589.

Huang, R., Feng, W. and Sun, J. 2017. Color feature reinforcement for cosaliency detection without single saliency residuals. *IEEE Signal Processing Letters*, 24 (5): 569-573.

Huang, R., Xing, Y. and Wang, Z. 2019. RGB-D salient object detection by a CNN with multiple layers fusion. *IEEE Signal Processing Letters*, 26 (4): 552-556.

Hui, H., Zhang, X., Wu, Z. and Li, F. 2021. Dual-path attention compensation U-Net for stroke lesion segmentation. *Computational Intelligence and Neuroscience*, 2021: 1-16.

Huo, G., Wu, Z., Li, J. and Li, S. 2018. Underwater target detection and 3D reconstruction system based on binocular vision. *Sensors*, 18 (10): 3570.

Hwang, I., Lee, S. H., Park, J. S. and Cho, N. I. 2017. Saliency detection based on seed propagation in a multilayer graph. *Multimedia Tools and Applications*, 76 (2): 2111-2129.

Ibraheem, M. R. and Elmogy, M. 2020. A non-invasive automatic skin cancer detection system for characterizing malignant melanoma from seborrheic keratosis. In: Proceedings of *2nd International Conference on Computer and Information Sciences (ICCIS)*. Manta, Ecuador, 27-29 July 2020. IEEE, 1-5.

Imamoglu, N., Gomez-Tames, J., Gonzalez, J., Gu, D. and Yu, W. 2014. Pulse-coupled neural network segmentation and bottom-up saliency-on feature extraction for thigh magnetic resonance imaging based 3D model construction. *Journal of Medical Imaging and Health Informatics*, 4 (2): 220-229.

Inbarani, H. and Azar, A. T. 2020. Leukemia image segmentation using a hybrid histogram-based soft covering rough k-means clustering algorithm. *Electronics*, 9 (1): 188.

Ishikura, K., Kurita, N., Chandler, D. M. and Ohashi, G. 2018. Saliency detection based on multiscale extrema of local perceptual color differences. *IEEE Transactions on Image Processing*, 27 (2): 703-717.

Islam, S. and Ahmed, M. 2013. Implementation of image segmentation for natural images using clustering methods. *International Journal of Emerging Technology and Advanced Engineering* 3(3): 175-180.

Itti, L., Koch, C. and Niebur, E. 1998. A model of saliency-based visual attention for rapid scene analysis. *IEEE Transactions on Pattern Analysis and Machine Intelligence*, 20 (11): 1254-1259.

Jaccard, P. 1912. The distribution of the flora in the alpine zone. 1. *New phytologist*, 11 (2): 37-50.

Jaglan, P., Dass, R. and Duhan, M. 2019. A comparative analysis of various image segmentation techniques. In: Proceedings of *2nd International Conference on Communication, Computing and Networking*. Chandigarh, India, 29-30 March 2018. Springer, 359-374.

Jahanifar, M., Tajeddin, N. Z., Asl, B. M. and Gooya, A. 2019. Supervised saliency map driven segmentation of lesions in dermoscopic images. *IEEE Journal of Biomedical and Health Informatics*, 23 (2): 509-518.

Jahanifar, M., Tajeddin, N. Z., Gooya, A. and Asl, B. M. 2017. Segmentation of lesions in dermoscopy images using saliency map and contour propagation. 15 March 2021. Available: https://arxiv.org/abs/1703.00087v2 (Accessed 15 March 2021).

Jaimes, B. R. A., Ferreira, J. P. K. and Castro, C. L. 2022. Unsupervised semantic segmentation of aerial images with application to UAV localization. *IEEE Geoscience and Remote Sensing Letters*, 19: 1-5.

Jain, A. K., Murty, M. N. and Flynn, P. J. 1999. Data clustering: a review. *ACM Computing Surveys (CSUR)*, 31 (3): 264-323.

Jain, S. and Pise, N. 2015. Computer aided melanoma skin cancer detection using image processing. *Procedia Computer Science*, 48 (2015): 735-740.

Jaisakthi, S., Chandrabose, A. and Mirunalini, P. 2017. Automatic skin lesion segmentation using semi-supervised learning technique. Available: https://arxiv.org/abs/1703.00087v2 (Accessed 26 March 2021).

Jamil, U., Akram, M. U., Khalid, S., Abbas, S. and Saleem, K. 2016. Computer based melanocytic and nevus image enhancement and segmentation. *BioMed Research International*, 2016: 1-13.

Javed, R., Rahim, M. S. M., Saba, T. and Rashid, M. 2019. Region-based active contour JSEG fusion technique for skin lesion segmentation from dermoscopic images. *Biomedical Research*, 30 (6): 1-10.

Ji, Y., Zhang, H., Tseng, K.-K., Chow, T. W. and Wu, Q. J. 2019. Graph model-based salient object detection using objectness and multiple saliency cues. *Neurocomputing*, 323: 188-202.

Jia, C., Li, S., Chen, W. and Kong, F. 2019a. Image salient object detection based on perceptually homogeneous patch. In: Proceedings of *IEEE 19th International Conference on Communication Technology (ICCT)*. Xi\'an , China, 16 - 19 October 2019. IEEE, 1644-1647.

Jia, N., Liu, X., Zhao, W., Zhang, H. and Zhuo, K. 2019b. An adaptive framework for saliency detection. *International Journal of Imaging Systems and Technology*, 29 (3): 382-393.

Jian, M., Qi, Q., Dong, J., Yin, Y. and Lam, K.-M. 2018. Integrating QDWD with pattern distinctness and local contrast for underwater saliency detection. *Journal of Visual Communication and Image Representation*, 53: 31-41.

Jian, M., Wang, J., Yu, H., Wang, G., Meng, X., Yang, L., Dong, J. and Yin, Y. 2021. Visual saliency detection by integrating spatial position prior of object with background cues. *Expert Systems with Applications*, 168: 114219.

Jiang, B., He, Z., Ding, C. and Luo, B. 2018. Saliency detection via a multi-layer graph based diffusion model. *Neurocomputing*, 314: 215-223.

Jiang, B., Zhang, L., Lu, H., Yang, C. and Yang, M.-H. 2013a. Saliency detection via absorbing markov chain. In: Proceedings of *IEEE International Conference on Computer Vision*. Sydney, Australia, 1-8 December 2013. IEEE, 1665-1672.

Jiang, F., Kong, B., Li, J., Dashtipour, K. and Gogate, M. 2021. Robust visual saliency optimization based on bidirectional Markov chains. *Cognitive Computation*, 13: 69-80.

Jiang, H., Wang, J., Yuan, Z., Liu, T., Zheng, N. and Li, S. 2011. Automatic salient object segmentation based on context and shape prior. In: Proceedings of *British Machine Vision Conference*. Dundee, Scotland, 29 August - 2 September, 2011. BMVA Press, 1-12.

Jiang, H., Wang, J., Yuan, Z., Wu, Y., Zheng, N. and Li, S. 2013b. Salient object detection: A discriminative regional feature integration approach. In: Proceedings of *IEEE Conference on Computer Vision and Pattern Recognition*. Washington, DC, United States, 23 - 28 June 2013. IEEE, 2083-2090.

Jiang, L., Zhong, H. and Lin*, X. 2017. Saliency detection via boundary prior and center prior *International Robotics & Automation Journal* 2(4): 134-139.

Jiang, P., Pan, Z., Tu, C., Vasconcelos, N., Chen, B. and Peng, J. 2020. Super diffusion for salient object detection. *IEEE Transactions on Image Processing*, 29: 2903-2917.

Jiao, X., Chen, Y. and Dong, R. 2020. An unsupervised image segmentation method combining graph clustering and high-level feature representation. *Neurocomputing*, 409: 83-92.

Jin, D. and Bai, X. 2020. Distribution information based intuitionistic fuzzy clustering for infrared ship segmentation. *IEEE Transactions on Fuzzy Systems*, 28 (8): 1557-1571.

Jin, F., Zhan, K., Chen, S. J., Huang, S. W. and Zhang, Y. S. 2021. Image segmentation method of mine pass soil and ore based on the fusion of the confidence edge detection algorithm and mean shift algorithm. *Gospodarka Surowcami Mineralnymi-Mineral Resources Management*, 37 (4): 133-152.

Jing, J., Li, H., Zhang, H., Su, Z. and Zhang, K. 2020. Detection of bobbin yarn surface defects by visual saliency analysis. *Fibers and Polymers*, 21 (11): 2685-2694.

Jing, M., Zhao, D., Zhou, M., Gao, Y., Jiang, Z. and Shi, Z. 2018. Unsupervised oil tank detection by shape-guide saliency model. *IEEE Geoscience and Remote Sensing Letters*, 16 (3): 477-481.

Jing, W. B., Jin, T. and Xiang, D. L. 2022. Fast superpixel-based clustering algorithm for SAR image segmentation. *IEEE Geoscience and Remote Sensing Letters*, 19: 1-5.

Johnson, S. C. 1967. Hierarchical clustering schemes. *Psychometrika*, 32 (3): 241-254.

Joseph, S. and Olugbara, O. O. 2021. Detecting salient image objects using color histogram clustering for region granularity. *J. Imaging*, 7 (9): 187.

Joseph, S. and Olugbara, O. O. 2022a. Experimental comparison of ten state-of-the-art saliency detection algorithms for segmenting leukocyte nucleus. In: Proceedings of *2022 Conference on Information Communications Technology and Society (ICTAS)*. Durban, South Africa, 9-10 March 2022. IEEE, 1-7.

Joseph, S. and Olugbara, O. O. 2022b. Preprocessing effects on performance of skin lesion saliency segmentation. *Diagnostics*, 12 (2): 344.

Joshi, A., Khan, M. S., Soomro, S., Niaz, A., Han, B. S. and Choi, K. N. 2020. SRIS: Saliency-based region detection and image segmentation of COVID-19 infected cases. *IEEE Access*, 8: 190487-190503.

Jung, C. and Kim, C. 2012. A unified spectral-domain approach for saliency detection and its application to automatic object segmentation. *IEEE Transactions on Image Processing*, 21 (3): 1272-1283.

Kaiyan, L., Junhui, W., Jie, C. and Huiping, S. 2013. A real time image segmentation approach for crop leaf. In: Proceedings of *Fifth International Conference on Measuring Technology and Mechatronics Automation (ICMTMA)*. Hong Kong, China, 16-17 January 2013. IEEE, 74-77.

Kamencay, P., Zachariasova, M., Hudec, R., Jarina, R., Benco, M. and Hlubik, J. 2013. A novel approach to face recognition using image segmentation based on SPCA-KNN method. *Radioengineering*, 22 (1): 92-99.

Kannan, S. 2020. Intelligent object recognition in underwater images using evolutionary-based Gaussian mixture model and shape matching. *Signal, Image and Video Processing*, 2020 (14): 877-885.

Karthik, M. D. N., Kathirvelan, I. and Srilatha, K. 2017. An effective image segmentation approach using DSETS and DBSCAN Algorithm. *Research Journal of Pharmaceutical Biological and Chemical Sciences*, 8 (3): 1116-1122.

Karthik, R., Menaka, R. and Hariharan, M. 2021. Learning distinctive filters for COVID-19 detection from chest X-ray using shuffled residual CNN. *Applied Soft Computing*, 99: 106744.

Kaur, A. and Kaur, I. 2018. An empirical evaluation of classification algorithms for fault prediction in open source projects. *Journal of King Saud University-Computer and Information Sciences*, 30 (1): 2-17.

Kaur, R. and Singh, E. N. 2014. Image restoration-A survey. *IOSR Journal of Computer Engineering (IOSR-JCE)*, 16 (4): 107-111.

Khan, M. A., Akram, T., Sharif, M., Javed, K., Raza, M. and Saba, T. 2020. An automated system for cucumber leaf diseased spot detection and classification using improved saliency method and deep features selection. *Multimedia Tools and Applications*, 79: 18627–18656.

Khan, M. A., Akram, T., Sharif, M., Saba, T., Javed, K., Lali, I. U., Tanik, U. J. and Rehman, A. 2019. Construction of saliency map and hybrid set of features for efficient segmentation and classification of skin lesion. *Microscopy Research and Technique*, 82 (6): 741-763.

Khan, M. A., Sharif, M., Akram, T., Damaševičius, R. and Maskeliūnas, R. 2021. Skin lesion segmentation and multiclass classification using deep learning features and improved moth flame optimization. *Diagnostics*, 11 (5): 811.

Khan, Z., Ni, J., Fan, X. and Shi, P. 2017. An improved k-means clustering algorithm based on an adaptive initial parameter estimation procedure for image segmentation. *International Journal Of Innovative Computing Information And Control*, 13 (5): 1509-1525.

Khan, Z., Yang, J. and Zheng, Y. J. 2019. Efficient clustering approach for adaptive unsupervised colour image segmentation. *IET Image Processing*, 13 (10): 1763-1772.

Kim, J.-S., Sim, J.-Y. and Kim, C.-S. 2014. Multiscale saliency detection using random walk with restart. *IEEE Transactions on Circuits and Systems for Video Technology*, 24 (2): 198-210.

Kim, J. 2019. Efficient vanishing point detection for driving assistance based on visual saliency map and image segmentation from a vehicle black-box camera. *Symmetry*, 11 (12): 1492.

Kim, J., Han, D., Tai, Y.-W. and Kim, J. 2016. Salient region detection via high-dimensional color transform and local spatial support. *IEEE Transactions on Image Processing*, 25 (1): 9-23.

Kim, W., Kanezaki, A. and Tanaka, M. 2020. Unsupervised learning of image segmentation based on differentiable feature clustering. *IEEE Transactions on Image Processing*, 29: 8055-8068.

Kim, W. and Kim, C. 2014. Spatiotemporal saliency detection using textural contrast and its applications. *IEEE Transactions on Circuits and Systems for Video Technology*, 24 (4): 646-659.

Kirati, I. and Tlili, Y. 2014. Unsupervised color image segmentation based on non parametric clustering. *CIT. Journal of Computing and Information Technology*, 21 (4): 247-254.

Kohonen, T. 1990. The self-organizing map. *Proceedings of the IEEE*, 78 (9): 1464-1480.

Kompella, A. and Kulkarni, R. V. 2020. Weakly supervised multi-scale recurrent convolutional neural network for co-saliency detection and co-segmentation. *Neural Computing and Applications*, 32 (21): 16571-16588.

Kothari, C. R. 2004. *Research methodology: Methods and techniques*. 2nd ed. New Delhi: New Age International.

Kouzehkanan, Z. M., Saghari, S., Tavakoli, E., Rostami, P., Abaszadeh, M., Mirzadeh, F., Satlsar, E. S., Gheidishahran, M., Gorgi, F., Mohammadi, S. and Hosseini, R. 2021. Raabin-WBC: a large free access dataset of white blood cells from normal peripheral blood. bioRxiv. 2021. Available: https://doi.org/10.1101/2021.05.02.442287 (Accessed 17 August 2021).

Krestanova, A., Kubíček, J., Skandera, J., Vilimek, D., Oczka, D., Penhaker, M., Augustynek, M. and Cerny, M. 2020. Quantitative analysis and objective comparison of clustering algorithms for medical image segmentation. In: Proceedings of *Asian Conference on Intelligent Information and Database Systems*. Phuket, Thailand, 23-26 March 2020. Springer, 114-125.

Kumar, N. and Meenpal, T. 2022. Salient keypoint-based copy–move image forgery detection. *Australian Journal of Forensic Sciences*: 1-24.

Lamine, B. and Nadia, B. 2016. Image segmentation using clustering methods. In: Proceedings of *SAI Intelligent Systems Conference*. London, UK, 21-22 September 2016. Springer, 129-141.

Leckie, G. and Charlton, C. 2013. Runmlwin: a program to run the MLwiN multilevel modeling software from within Stata. *Journal of Statistical Software*, 52 (11): 1-40.

Lee, K., Wee, S. and Jeong, J. 2021. Pre-processing filter reflecting human visual perception to improve saliency detection performance. *Electronics*, 10 (23): 2892.

Lee, S., Xin, J. H. and Westland, S. 2005. Evaluation of image similarity by histogram intersection. *Color Research & Application*, 30 (4): 265-274.

Lei, J., Jiang, T., Wu, K., Du, H., Zhu, G. and Wang, Z. 2016. Robust K-Means algorithm with automatically splitting and merging clusters and its applications for surveillance data. *Multimedia Tools and Applications*, 75 (19): 1-17.

Lei, T., Liu, P., Jia, X. H., Zhang, X. D., Meng, H. Y. and Nandi, A. K. 2020. Automatic fuzzy clustering framework for image segmentation. *IEEE Transactions on Fuzzy Systems*, 28 (9): 2078-2092.

Li, C., Cong, R., Guo, C., Li, H., Zhang, C., Zheng, F. and Zhao, Y. 2020a. A parallel down-up fusion network for salient object detection in optical remote sensing images. *Neurocomputing*, 415: 411-420.

Li, C., Cong, R., Hou, J., Zhang, S., Qian, Y. and Kwong, S. 2019a. Nested network with two-stream pyramid for salient object detection in optical remote sensing images. *IEEE Transactions on Geoscience and Remote Sensing*, 57 (11): 9156-9166.

Li, E., Xu, S., Meng, W. and Zhang, X. 2017a. Building extraction from remotely sensed images by integrating saliency cue. *IEEE Journal of Selected Topics in Applied Earth Observations and Remote Sensing*, 10 (3): 906-919.

Li, G., Lan, D., Zheng, X., Li, X. and Zhou, J. 2021a. Automatic pavement crack detection based on single stage salient-instance segmentation and concatenated feature pyramid network. *International Journal of Pavement Engineering*: 1-17

Li, G. and Yu, Y. 2015. Visual saliency based on multiscale deep features. In: Proceedings of *IEEE Conference on Computer Vision and Pattern Recognition*. Boston, MA, USA, 7-12 June 2016. IEEE, 5455-5463.

Li, H., Chen, J., Lu, H. and Chi, Z. 2017b. CNN for saliency detection with low-level feature integration. *Neurocomputing*, 226: 212-220.

Li, H., Meng, F. and Ngan, K. N. 2013. Co-salient object detection from multiple images. *IEEE Transactions on Multimedia*, 15 (8): 1896-1909.

Li, H., Yu, X., Tang, Y. and Wang, X. 2020b. Shadow detection in SAR images based on greyscale distribution, a saliency model, and geometrical matching. *International Journal of Remote Sensing*, 41 (19): 7446-7471.

Li, H., Yu, X., Zou, L., Zhou, Y. and Wang, X. 2022. A feed-forward framework integrating saliency and geometry discrimination for shadow detection in SAR images. *IET Radar, Sonar & Navigation*, 16 (2): 249-266.

Li, J., Levine, M. D., An, X., Xu, X. and He, H. 2012. Visual saliency based on scale-space analysis in the frequency domain. *IEEE Transactions on Pattern Analysis and Machine Intelligence*, 35 (4): 996-1010.

Li, L., Du, L. and Wang, Z. 2018. Target detection based on dual-domain sparse reconstruction saliency in SAR images. *IEEE Journal of Selected Topics in Applied Earth Observations and Remote Sensing*, 11 (11): 4230-4243.

Li, L., Zhou, F. and Bai, X. 2018. Infrared pedestrian segmentation through background likelihood and object-biased saliency. *IEEE Transactions on Intelligent Transportation Systems*, 19 (9): 2826-2844.

Li, N., Bi, H., Zhang, Z., Kong, X. and Lu, D. 2018a. Performance comparison of saliency detection. *Advances in Multimedia*, 2018: 1-13.

Li, R., Cai, J., Zhang, H. and Wang, T. 2017c. Aggregating complementary boundary contrast with smoothing for salient region detection. *The Visual Computer*, 33 (9): 1155-1167.

Li, T., Zhang, J., Lu, X. and Zhang, Y. 2017d. SDBD: A hierarchical region-of-interest detection approach in large-scale remote sensing image. *IEEE Geoscience and Remote Sensing Letters*, 14 (5): 699-703.

Li, W., Raj, A. N. J., Tjahjadi, T. and Zhuang, Z. 2021b. Digital hair removal by deep learning for skin lesion segmentation. *Pattern Recognition*, 117: 107994.

Li, X., Li, Y., Shen, C., Dick, A. and Hengel, A. V. D. 2013a. Contextual hypergraph modeling for salient object detection. In: Proceedings of *2013 IEEE International Conference on Computer Vision*. Sydney, Australia, 1-8 December 2013. IEEE, 3328-3335.

Li, X., Lu, H., Zhang, L., Ruan, X. and Yang, M.-H. 2013b. Saliency detection via dense and sparse reconstruction. In: Proceedings of *IEEE International Conference on Computer Vision*. Sydney, Australia, 1-8 December 2013. IEEE, 2976-2983.

Li, X., Zhao, L., Wei, L., Yang, M.-H., Wu, F., Zhuang, Y., Ling, H. and Wang, J. 2016. Deepsaliency: Multi-task deep neural network model for salient object detection. *IEEE Transactions on Image Processing*, 25 (8): 3919-3930.

Li, Y., Cui, F., Xue, X. and Chan, J. C.-W. 2018b. Coarse-to-fine salient object detection based on deep convolutional neural networks. *Signal Processing: Image Communication*, 64: 21-32.

Li, Y., Hou, X., Koch, C., Rehg, J. M. and Yuille, A. L. 2014. The secrets of salient object segmentation. In: Proceedings of *IEEE Conference on Computer Vision and Pattern Recognition*. Columbus, OH, USA, 23-28 June 2014. IEEE, 280-287.

Li, Y., Li, Z., Zhu, Y., Li, B., Xiong, W. and Huang, Y. 2019b. Thermal infrared small ship detection in sea clutter based on morphological reconstruction and multi-feature analysis. *Applied Sciences*, 9 (18): 3786.

Liang, F., Duan, L., Ma, W., Qiao, Y., Cai, Z., Miao, J. and Ye, Q. 2020. CoCNN: RGB-D deep fusion for stereoscopic salient object detection. *Pattern Recognition*, 104: 107329.

Liang, Y., Liu, H. and Ma, N. 2019. A novel deep network and aggregation model for saliency detection. *The Visual Computer*, 2020 (36): 1883–1895.

Liang, Z. J., Wang, M. J., Zhou, X. C., Lin, L. and Li, W. J. 2014. Salient object detection based on regions. *Multimedia Tools and Applications*, 68 (3): 517-544.

Light, R. J., Richard, J., Light, R. and Pillemer, D. B. 1984. *Summing up: The science of reviewing research*. Cambridge, MA: Harvard University Press.

Lin, G. and Fan, W. 2020. Unsupervised video object segmentation based on mixture models and saliency detection. *Neural Processing Letters*, 51 (1): 657-674.

Lin, T.-Y., Maire, M., Belongie, S., Hays, J., Perona, P., Ramanan, D., Dollár, P. and Zitnick, C. L. 2014. Microsoft coco: Common objects in context. In: Proceedings of *European conference on computer vision*. Zurich, Switzerland, 6-12 September 2014. Springer, 740-755.

Liu, G.-H. and Yang, J.-Y. 2019. Exploiting color volume and color difference for salient region detection. *IEEE Transactions on Image Processing*, 28 (1): 6-16.

Liu, H. and Zhao, F. 2021. Multiobjective fuzzy clustering with multiple spatial information for Noisy color image segmentation. *Applied Intelligence*, 51: 5280–5298.

Liu, J. and Wang, S. 2015. Salient region detection via simple local and global contrast representation. *Neurocomputing*, 147: 435-443.

Liu, L., Kuang, L. and Ji, Y. 2020. Multimodal MRI brain tumor image segmentation using sparse subspace clustering algorithm. *Computational and Mathematical Methods in Medicine*, 2020: 1-13.

Liu, T., Yuan, Z., Sun, J., Wang, J., Zheng, N., Tang, X. and Shum, H.-Y. 2011. Learning to detect a salient object. *IEEE Transactions on Pattern Analysis and Machine Intelligence*, 33 (2): 353-367.

Liu, X., Song, L., Liu, S. and Zhang, Y. 2021. A review of deep-learning-based medical image segmentation methods. *Sustainability*, 13 (3): 1224.

Liu, Y., Liu, G., Liu, C. and Sun, C. 2019. A novel color-texture descriptor based on local histograms for image segmentation. *IEEE Access*, 7: 160683-160695.

Liu, Y. and Yuan, P. 2019. Saliency detection using global and local information under multilayer cellular automata. *IEEE Access*, 7: 72736-72748.

Liu, Y., Zhang, Y., Liu, S., Coleman, S., Wang, Z. and Qiu, F. 2022. Salient object detection by aggregating contextual information. *Pattern Recognition Letters*, 153: 190-199.

Liu, Z., Shi, R., Shen, L. Q., Xue, Y. Z., Ngan, K. N. and Zhang, Z. Y. 2012. Unsupervised salient object segmentation based on kernel density estimation and two-phase Graph Cut. *IEEE Transactions on Multimedia*, 14 (4): 1275-1289.

Lopez-Alanis, A., Lizarraga-Morales, R. A., Contreras-Cruz, M. A., Ayala-Ramirez, V., Sanchez-Yanez, R. E. and Trujillo-Romero, F. 2020. Rule-based aggregation driven by similar images for visual saliency detection. *Applied Intelligence*, 50 (6): 1745-1762.

Lopez-Alanis, A., Lizarraga-Morales, R. A., Sanchez-Yanez, R. E., Martinez-Rodriguez, D. E. and Contreras-Cruz, M. A. 2019. Visual saliency detection using a rule-based aggregation approach. *Applied Sciences*, 9 (10): 2015.

Lou, J., Ren, M. and Wang, H. 2014. Regional principal color based saliency detection. *PloS one*, 9 (11): e112475.

Lou, J., Wang, H., Chen, L., Xu, F., Xia, Q., Zhu, W. and Ren, M. 2020. Exploiting color name space for salient object detection. *Multimedia Tools and Applications*, 79 (15): 10873-10897.

Lou, J., Zhu, W., Wang, H. and Ren, M. 2017. Small target detection combining regional stability and saliency in a color image. *Multimedia Tools and Applications*, 76 (13): 14781-14798.

Luo, H., Han, G., Liu, P. and Wu, Y. 2018. Salient region detection using diffusion process with nonlocal connections. *Applied Sciences*, 8 (12): 2526.

Lyu, X., Zhang, L., Zhu, W. and Zhang, L. 2021. Common regions of interest extraction based on saliency statistic analysis for multiple remote sensing images. In: Proceedings of *2021 IEEE International Geoscience and Remote Sensing Symposium IGARSS*. Brussels, Belgium, 11-16 July 2021. IEEE, 4779-4782.

Ma, F., Gao, F., Wang, J., Hussain, A. and Zhou, H. 2020. A novel biologically-inspired target detection method based on saliency analysis for synthetic aperture radar (SAR) imagery. *Neurocomputing*, 402: 66-79.

Ma, G., Li, S., Chen, C., Hao, A. and Qin, H. 2021a. Rethinking image salient object detection: Object-level semantic saliency reranking first, pixelwise saliency refinement later. *IEEE Transactions on Image Processing*, 30: 4238-4252.

Ma, L., Li, M., Ma, X., Cheng, L., Du, P. and Liu, Y. 2017. A review of supervised object-based land-cover image classification. *ISPRS Journal of Photogrammetry and Remote Sensing*, 130: 277-293.

Ma, W.-P., Li, W.-X., Sun, J.-C. and Cao, P.-X. 2021b. Saliency detection via manifold ranking based on robust foreground. *International Journal of Automation and Computing*, 18 (1): 1-12.

Ma, X., Xie, X., Lam, K.-M., Hu, J. and Zhong, Y. 2015. Saliency detection based on singular value decomposition. *Journal of Visual Communication and Image Representation*, 32: 95-106.

MacQueen, J. 1967. Some methods for classification and analysis of multivariate observations. In: Proceedings of *Fifth Berkeley Symposium on Mathematical Statistics and Probability*. Oakland, CA, USA, 27 December - 7 January. University of California Press, 281-297.

Majumder, S. and Ullah, M. A. 2019. Feature extraction from dermoscopy images for melanoma diagnosis. *SN Applied Sciences*, 1 (7): 1-11.

Makem, M. and Tiedeu, A. 2020. An efficient algorithm for detection of white blood cell nuclei using adaptive three stage PCA-based fusion. *Informatics in Medicine Unlocked*, 20: 100416.

Manke, R. and Jalal, A. 2015. Poisson-distribution-based approach for salient region detection. *Electronics Letters*, 51 (1): 37-38.

Manno-Kovacs, A. 2018. Direction selective contour detection for salient objects. *IEEE Transactions on Circuits and Systems for Video Technology*, 29 (2): 375-389.

Márquez-de-Silva, S., Felipe-Riverón, E. and Fernández, L. P. S. 2008. A simple and effective method of color image quantization. In: Proceedings of *Iberoamerican Congress on Pattern Recognition*. Havana, Cuba, 9-12 September 2008. Springer, 749-757.

Maru, M. and Parikh, M. 2017. Image Restoration Techniques: A Survey. *International Journal of Computer Applications*, 160 (6): 15 - 19.

Masood, S., Sharif, M., Masood, A., Yasmin, M. and Raza, M. 2015. A Survey on Medical Image Segmentation. *Current Medical Imaging Reviews*, 11 (1): 3-14.

Matheron, G. and Serra, J. 2002. The birth of mathematical morphology. In: Proceedings of *6th International Symposium on Mathematical Morphology*. Sydney, Australia, 3-5 April 2002. CSIRO, 1-16.

Matta, S. 2014. Review: Various image segmentation techniques. *Internation Journal of Computer Science and Information Technologies*, 5 (6): 7536-7539.

Mendonça, T., Ferreira, P. M., Marques, J. S., Marcal, A. R. and Rozeira, J. 2013. PH 2-A dermoscopic image database for research and benchmarking. In: Proceedings of *35th Annual International Conference of the IEEE Engineering in Medicine and Biology Society (EMBC)*. Osaka, Japan, 3-7 July 2013. IEEE, 5437-5440.

Michel, J., Youssefi, D. and Grizonnet, M. 2015. Stable mean-shift algorithm and its application to the segmentation of arbitrarily large remote sensing images. *IEEE Transactions on Geoscience and Remote Sensing*, 53 (2): 952-964.

Ming, L. 2010. Image segmentation algorithm research and improvement. In: Proceedings of *3rd international conference on advanced Computer theory and Engineering (ICACTE)*. Chengdu, China, 20-22 August 2010. IEEE, V5-211-V215-214.

Mittal, H., Pandey, A. C., Saraswat, M., Kumar, S., Pal, R. and Modwel, G. 2021. A comprehensive survey of image segmentation: clustering methods, performance parameters, and benchmark datasets. *Multimedia Tools and Applications*: 1-26.

Moghaddam, S. A. V., Al-Sahaf, H., Xue, B., Hollitt, C. and Zhang, M. 2021. An automatic feature construction method for salient object detection: A genetic programming approach. *Expert Systems with Applications*, 186: 115726.

Mohammadpour, M. and Mozaffari, S. 2015. A new method for saliency detection using top-down approach. In: Proceedings of *7th Conference on Information and Knowledge Technology (IKT)*. Urmia, Iran., 26 - 28 May 2015. IEEE, 1-5.

Mohammdian-Khoshnoud, M., Soltanian, A. R., Dehghan, A. and Farhadian, M. 2022. Optimization of Fuzzy C-Means (FCM) clustering in cytology image segmentation using the gray wolf algorithm. *BMC Molecular and Cell Biology*, 23 (1): 1-9.

Moher, D., Liberati, A., Tetzlaff, J., Altman, D. G. and Group*, P. 2009. Preferred reporting items for systematic reviews and meta-analyses: the PRISMA statement. *Annals of Internal Medicine*, 151 (4): 264-269.

Mokayed, H., Shivakumara, P., Saini, R., Liwicki, M., Hin, L. C. and Pal, U. 2021. Anomaly detection in natural scene images based on enhanced fine-grained saliency and fuzzy logic. *IEEE Access*, 9: 129102-129109.

Monteiro, F. C. and Campilho, A. C. 2006. Performance evaluation of image segmentation. In: Proceedings of *International Conference on Image Analysis and Recognition*. Póvoa de Varzim, Portugal, 18-20 September 2006. Springer, 248-259.

Monteiro, R. J., Dhanush, J. K. and Nausheeda, B. S. 2016. Comparison of various segmentation algorithms in image procesing. *International Journal of Latest Trends In Engineering And Technology*, Special Issue 241-247.

Moradi, M. and Bayat, F. 2021. A salient object segmentation framework using diffusion-based affinity learning. *Expert Systems with Applications*, 168: 114428.

Moradi, M., Bayat, F. and Charmi, M. 2021. A salient object detection framework using linear quadratic regulator controller. *Journal of Visual Communication and Image Representation*, 79: 103259.

Movahedi, V. and Elder, J. H. 2010. Design and perceptual validation of performance measures for salient object segmentation. In: Proceedings of *IEEE Computer Society Conference on Computer Vision and Pattern Recognition-Workshops*. San Francisco, CA, 13-18 June 2010. IEEE, 49-56.

Mujica-Vargas, D., Kinani, J. M. V. and Rubio, J. d. J. 2020. Color-based image segmentation by means of a robust intuitionistic Fuzzy C-Means algorithm. *International Journal of Fuzzy Systems*, 22 (3): 901-916.

Mukherjee, P. and Lall, B. 2017. Saliency and KAZE features assisted object segmentation. *Image and Vision Computing*, 61: 82-97.

Murray, N., Vanrell, M., Otazu, X. and Parraga, C. A. 2011. Saliency estimation using a non-parametric low-level vision model. In: Proceedings of *2011 IEEE conference on Computer Vision and Pattern Recognition (CVPR)*. Washington, DC, United States, 20 - 25 June 2011. IEEE, 433-440.

Nagaraju, M., Babu, B. S., Sai Somayajulu, M. V. N. S. S. R. K., Sarma, K. S. K. and Vetagiri, A. 2021. An accurate foreground moving object detection based on segmentation techniques and optimal classifier. *Concurrency and Computation: Practice and Experience*: 1-12.

Naik, D. and Shah, P. 2014. A review on image segmentation clustering algorithms. *International Journal of Computer Science and Information Technologies*, 5 (3): 3289-3293.

Nailussa'ada, Harsono, T. and Basuki, A. 2019. Improvement of segmentation performance for feature extraction on whirlwind cloud-based satellite image using DBSCAN clustering algorithm. *Emitter-International Journal of Engineering Technology*, 7 (1): 301-325.

Namburu, A., Samayamantula, S. K. and Edara, S. R. 2017. Generalised rough intuitionistic Fuzzy C-Means for magnetic resonance brain image segmentation. *IET Image Processing*, 11 (9): 777-785.

Nan, B. F., Mu, Z. C., Chen, L. and Cheng, J. 2015. A local texture-based superpixel feature coding for saliency detection combined with global saliency. *Applied Sciences*, 5 (4): 1528-1546.

Nasiripour, R., Farsi, H. and Mohamadzadeh, S. 2019. Visual saliency object detection using sparse learning. *IET Image Processing*, 13 (13): 2436-2447.

Nawaz, M. and Yan, H. 2020. Saliency detection via multiple-morphological and superpixel based fast fuzzy C-mean clustering network. *Expert Systems with Applications*, 161: 113654.

Nawaz, M. and Yan, H. 2021. Saliency detection using deep features and affinity-based robust background subtraction. *IEEE Transactions on Multimedia*, 23: 2902-2916.

Nazeer, K. A. and Sebastian, M. 2009. Improving the accuracy and efficiency of the K-Means clustering algorithm. In: Proceedings of *The World Congress on Engineering*. London, U.K, 1 - 3 July 2009. WCE, 1 - 5.

Ndayikengurukiye, D. and Mignotte, M. 2022. Salient object detection by LTP texture characterization on opposing color pairs under SLICO superpixel constraint. *Journal of Imaging*, 8 (4): 110.

Nida, N., Irtaza, A., Javed, A., Yousaf, M. H. and Mahmood, M. T. 2019. Melanoma lesion detection and segmentation using deep region based convolutional neural network and fuzzy C-means clustering. *International Journal of Medical Informatics*, 124 (2019): 37-48.

Nikbakhsh, N., Baleghi, Y. and Agahi, H. 2021. A novel approach for unsupervised image segmentation fusion of plant leaves based on G-mutual information. *Machine Vision and Applications*, 32 (1): 1-12.

Ning, Z., Zhong, S., Feng, Q., Chen, W. and Zhang, Y. 2022. SMU-Net: Saliency-guided morphology-aware U-Net for breast lesion segmentation in ultrasound image. *IEEE Transactions on Medical Imaging*, 41 (2): 476-490.

Niu, M., Song, K., Huang, L., Wang, Q., Yan, Y. and Meng, Q. 2021. Unsupervised saliency detection of rail surface defects using stereoscopic images. *IEEE Transactions on Industrial Informatics*, 17 (3): 2271-2281.

Niu, X., Guo, S., Wang, M., Zhang, H., Chen, X. and He, D. 2014. Image segmentation algorithm for disease detection of wheat leaves. In: Proceedings of *International Conference on Advanced Mechatronic Systems (ICAMechS)*. Kumamoto, Japan, 10-12 August 2014. IEEE, 270-273.

Niu, Y., Chen, J. and Guo, W. 2018. Meta-metric for saliency detection evaluation metrics based on application preference. *Multimedia Tools and Applications*, 77 (20): 26351-26369.

Niu, Y., Su, C. and Guo, W. 2018. Salient object segmentation based on superpixel and background connectivity prior. *IEEE Access*, 6: 56170-56183.

Nouri, F., Kazemi, K. and Danyali, H. 2018. Salient object detection using local, global and high contrast graphs. *Signal, Image and Video Processing*, 12 (4): 659-667.

Ogunsakin, R. E., Olugbara, O. O., Moyo, S. and Israel, C. 2021. Meta-analysis of studies on depression prevalence among diabetes mellitus patients in Africa. *Heliyon*, 7 (5): e07085.

Oh, K., Lee, M., Lee, Y. and Kim, S. 2017a. Salient object detection using recursive regional feature clustering. *Information Sciences*, 387: 1-18.

Oh, S. J., Benenson, R., Khoreva, A., Akata, Z., Fritz, M. and Schiele, B. 2017b. Exploiting saliency for object segmentation from image level labels. In: Proceedings of *IEEE Conference on Computer Vision and Pattern Recognition*. Honolulu, HI, USA, 21-26 July 2017. IEEE, 5038-5047.

Okuboyejo, D. and Olugbara, O. O. 2021. Segmentation of melanocytic lesion images using gamma correction with clustering of keypoint descriptors. *Diagnostics*, 11 (8): 1366.

Okuboyejo, D. A., Olugbara, O. O. and Odunaike, S. A. 2014. CLAHE inspired segmentation of dermoscopic images using mixture of methods. In: Kim, H. K., Ao, S.-I. and Amouzegar, M. A. eds. *Transactions on Engineering Technologies*. Springer, 355-365.

Olugbara, C. T., Letseka, M., Ogunsakin, R. E. and Olugbara, O. O. 2021. Meta-analysis of factors influencing student acceptance of massive open online courses for open distance learning. *The African Journal of Information Systems*, 13 (3): 370-400.

Olugbara, O. O., Adetiba, E. and Oyewole, S. A. 2015. Pixel intensity clustering algorithm for multilevel image segmentation. *Mathematical Problems in Engineering*, 2015: 1 - 19.

Olugbara, O. O., Taiwo, T. B. and Heukelman, D. 2018. Segmentation of melanoma skin lesion using perceptual color difference saliency with morphological analysis. *Mathematical Problems in Engineering*, 2018: 1 - 19.

Oskouei, A. G., Hashemzadeh, M., Asheghi, B. and Balafar, M. A. 2021. CGFFCM: CLuster-weight and group-local feature-weight learning in fuzzy C-means clustering algorithm for color image segmentation. *Applied Soft Computing*, 113: 108005.

Otsu, N. 1979. A threshold selection method from gray-level histograms. *IEEE Transactions on Systems, Man, and Cybernetics*, 9 (1): 62-66.

Ouyang, W. B., Xu, B. G. and Yuan, X. H. 2019. Color segmentation in multicolor images using node-growing self-organizing map. *Color Research and Application*, 44 (2): 184-193.

Pahuja, A., Majumder, A., Chakraborty, A. and Venkatesh Babu, R. 2019. Enhancing salient object segmentation through attention. In: Proceedings of *2019 IEEE/CVF Conference on Computer Vision and Pattern Recognition (CVPR)*. Long Beach, California, 15-20 June 2019. 27-36.

Palus, H. 2005. Performance evaluation of preprocessing in color image segmentation. *Journal of Imaging Science and Technology*, 49 (6): 583-587.

Pang, Y., Wu, Y., Wu, C. and Zhang, M. 2020a. Salient object detection via effective background prior and novel graph. *Multimedia Tools and Applications*, 79 (35): 25679-25695.

Pang, Y., Yu, X., Wu, Y., Wu, C. and Jiang, Y. 2020b. Bagging-based saliency distribution learning for visual saliency detection. *Signal Processing: Image Communication*, 87: 115928.

Paramanandam, M., O'Byrne, M., Ghosh, B., Mammen, J. J., Manipadam, M. T., Thamburaj, R. and Pakrashi, V. 2016. Automated segmentation of nuclei in breast cancer histopathology images. *PloS one*, 11 (9): e0162053.

Pathan, S., Prabhu, K. G. and Siddalingaswamy, P. 2018. Hair detection and lesion segmentation in dermoscopic images using domain knowledge. *Medical & Biological Engineering & Computing*, 56 (11): 2051-2065.

Patiño, D., Avendaño, J. and Branch, J. W. 2018. Automatic skin lesion segmentation on dermoscopic images by the means of superpixel merging. In: Proceedings of *International Conference on Medical Image Computing and Computer-Assisted Intervention*. Granada, Spain, 16-20 September 2018. Springer, 728-736.

Peizhuang, W. 1983. *Pattern recognition with fuzzy objective function algorithms (James C. Bezdek)*. SIAM.

Pennisi, A., Bloisi, D. D., Nardi, D., Giampetruzzi, A. R., Mondino, C. and Facchiano, A. 2016. Skin lesion image segmentation using Delaunay Triangulation for melanoma detection. *Computerized Medical Imaging and Graphics*, 52: 89-103.

Perazzi, F., Krähenbühl, P., Pritch, Y. and Hornung, A. 2012. Saliency filters: Contrast based filtering for salient region detection. In: Proceedings of *IEEE Conference on Computer Vision and Pattern Recognition*. Providence, RI, USA, 16-21 June 2012. IEEE, 733-740.

Pereira, P. M. M., Fonseca-Pinto, R., Paiva, R. P., Assuncao, P. A. A., Tavora, L. M. N., Thomaz, L. A. and Faria, S. M. M. 2020. Dermoscopic skin lesion image segmentation based on Local Binary Pattern Clustering: Comparative study. *Biomedical Signal Processing and Control*, 59: 101924.

Petrus, J. 2019. Soft and hard clustering for abstract scientific paper in Indonesian. In: Proceedings of *2019 International Conference on Informatics, Multimedia, Cyber and Information System (ICIMCIS)*. Jakarta, Indonesia, 24-25 October 2019. IEEE, 131-136.

Piao, Y., Li, X., Zhang, M., Yu, J. and Lu, H. 2020. Saliency detection via depth-induced cellular automata on light field. *IEEE Transactions on Image Processing*, 29: 1879-1889.

Pizer, S. M., Amburn, E. P., Austin, J. D., Cromartie, R., Geselowitz, A., Greer, T., ter Haar Romeny, B., Zimmerman, J. B. and Zuiderveld, K. 1987. Adaptive histogram equalization and its variations. *Computer Vision, Graphics, and Image processing*, 39 (3): 355-368.

Pizer, S. M., Johnston, E. R., Ericksen, J. P., Yankaskas, B. C. and Muller, K. E. 1990. Contrast-limited adaptive histogram equalization: Speed and effectiveness. In: Proceedings of *First Conference on Visualization in Biomedical Computing*. Atlanta, Georgia, 22-25 May 1990. IEEE, 337-345.

Plataniotis, K. N. and Venetsanopoulos, A. N. 2013. *Color image processing and applications*. 1st ed. Springer Science & Business Media.

Pont-Tuset, J. and Marques, F. 2013. Measures and meta-measures for the supervised evaluation of image segmentation. In: Proceedings of *IEEE Conference on Computer Vision and Pattern Recognition*. Portland, OR, USA, 23-28 June 2013. IEEE, 2131-2138.

Poorolajal, J. and Noornejad, S. 2021. Metaplot: A new Stata module for assessing heterogeneity in a meta-analysis. *PloS one*, 16 (6): e0253341.

Prabhu, V., Kuppusamy, P. G., Karthikeyan, A. and Varatharajan, R. 2018. Evaluation and analysis of data driven in expectation maximization segmentation through various initialization techniques in medical images. *Multimedia Tools and Applications*, 77 (8): 10375-10390.

Pravitasari, A. A., Qonita, S. F., Iriawan, N., Irhamah, Fithriasari, K., Purnami, S. W. and Ferriastuti, W. 2020. MRI-based brain tumor segmentation using Gaussian and hybrid Gaussian mixture model-spatially variant finite mixture model with expectation-maximization algorithm. *Malaysian Journal of Mathematical Sciences*, 14 (1): 77-93.

Premaladha, J. and Ravichandran, K. 2016. Novel approaches for diagnosing melanoma skin lesions through supervised and deep learning algorithms. *Journal of Medical Systems*, 40 (4): 1-12.

Qaddoura, R., Manaseer, W. A., Abushariah, M. A. M. and Alshraideh, M. A. 2020. Dental radiography segmentation using expectation-maximization clustering and grasshopper optimizer. *Multimedia Tools and Applications*, 79: 22027-22045.

Qi, H. 2021. Research on a segmentation algorithm for the Tujia Brocade images based on unsupervised Gaussian mixture clustering. *Frontiers in Neurorobotics*, 15: 1-15.

Qi, N. X., Yang, X. G., Li, C. X., Lu, R. T., He, C. and Cao, L. J. 2019. Unstructured road detection via combining the model-based and feature-based methods. *IET Intelligent Transport Systems*, 13 (10): 1533-1544.

Qi, S., Ma, J., Lin, J., Li, Y. and Tian, J. 2015. Unsupervised ship detection based on saliency and S-HOG descriptor from optical satellite images. *IEEE Geoscience and Remote Sensing Letters*, 12 (7): 1451-1455.

Qian, M., Qi, J., Zhang, L., Feng, M. and Lu, H. 2019. Language-aware weak supervision for salient object detection. *Pattern Recognition*, 96: 106955.

Qin, W., Wu, J., Han, F., Yuan, Y., Zhao, W., Ibragimov, B., Gu, J. and Xing, L. 2018. Superpixel-based and boundary-sensitive convolutional neural network for automated liver segmentation. *Physics in Medicine & Biology*, 63 (9): 095017.

Qiu, Y., Tang, L., Li, B., Niu, S. and Niu, T. 2020. Uneven illumination surface defects inspection based on saliency detection and intrinsic image decomposition. *IEEE Access*, 8: 190663-190676.

Rahtu, E., Kannala, J., Salo, M. and Heikkilä, J. 2010. Segmenting salient objects from images and videos. In: Proceedings of *European Conference on Computer Vision*. Heraklion, Crete, Greece, 5-11 September 2010. Springer, 366-379.

Rajput, A. S., Tanwar, V. K. and Raman, B. 2021. Score-based secure biomedical model for effective skin lesion segmentation over eHealth cloud. *ACM Transactions on Multimedia Computing, Communications, and Applications*, 17 (2s): 1-19.

Ramadan, H., Lachqar, C. and Tairi, H. 2020. Saliency-guided automatic detection and segmentation of tumor in breast ultrasound images. *Biomedical Signal Processing and Control*, 60: 101945.

Ramella, G. 2021. Saliency-based segmentation of dermoscopic images using colour information. *Computer Methods in Biomechanics and Biomedical Engineering-Imaging and Visualization*, 10 (2): 1-15.

Ramella, G. and Di Baja, G. S. 2016. From color quantization to image segmentation. In: Proceedings of *12th International Conference on Signal-Image Technology & Internet-Based Systems (SITIS)*. Naples, Italy, 28 November - 1 December 2016. IEEE, 798-804.

Ramesh, B. and Nandhini, K. 2017. Clustering algorithms–A literature review. *International Journal of Computer Sciences and Engineering*, 5 (10): 302 - 306.

Ramesh, K., Kumar, G. K., Swapna, K., Datta, D. and Rajest, S. S. 2021. A review of medical image segmentation algorithms. *EAI Endorsed Transactions on Pervasive Health and Technology*, 7 (27): 1-9.

Ren, D., Jia, Z., Yang, J. and Kasabov, N. K. 2017. A practical grabcut color image segmentation based on bayes classification and simple linear iterative clustering. *IEEE Access*, 5: 18480-18487.

Ren, L., Liu, Y., Tong, Y., Cao, X. and Wu, Y. 2020. Calcification segmentation based on a different scales superpixels saliency detection algorithm. *Ultrasound in Medicine & Biology*, 46 (12): 3404-3412.

Ren, X. and Malik, J. 2003. Learning a classification model for segmentation. In: Proceedings of *Ninth IEEE International Conference on Computer Vision*. Nice, France, 13-16 October 2003. IEEE, 10.

Renjith, S., Sreekumar, A. and Jathavedan, M. 2020. Performance evaluation of clustering algorithms for varying cardinality and dimensionality of data sets. *Materials Today: Proceedings*, 27: 627-633.

Rocha, A., Hauagge, D. C., Wainer, J. and Goldenstein, S. 2010. Automatic fruit and vegetable classification from images. *Computers and Electronics in Agriculture*, 70 (1): 96-104.

Ross-Howe, S. and Tizhoosh, H. R. 2018. The effects of image pre-and post-processing, wavelet decomposition, and local binary patterns on U-nets for skin lesion segmentation. In: Proceedings of *2018 International Joint Conference on Neural Networks (IJCNN)*. Rio de Janeiro, Brazil, 8-13 July 2018. IEEE, 1-8.

Rosyadi, A. W. and Suciati, N. 2020. Image segmentation using transition region and K-means clustering. *IAENG International Journal of Computer Science*, 47 (1): 47-55.

Rothstein, H. R., Sutton, A. J. and Borenstein, M. 2006. *Publication bias in meta-analysis: Prevention, assessment and adjustments*. West Sussex, England: John Wiley & Sons.

Rousseeuw, P. J. and Kaufman, L. 1990. *Finding Groups in Data-An Introduction to Cluster Analysis*. New York: John Wiley & Sons Inc.

Sae-Lim, W., Wettayaprasit, W. and Aiyarak, P. 2019. Convolutional neural networks using mobilenet for skin lesion classification. In: Proceedings of *16th International Joint Conference on Computer Science and Software Engineering (JCSSE)*. Chonburi, Thailand, 10-12 July 2019. IEEE, 242-247.

Saini, S. and Arora, K. 2014. A study analysis on the different image segmentation techniques. *International Journal of Information & Computation Technology*, 4 (14): 1445-1452.

Saleem, A., Bhatti, M. N. A., Ashraf, M. A., Zia, M. and Mahmood, H. 2019. Segmentation and classification of consumer-grade and dermoscopic skin cancer images using hybrid textural analysis. *Journal of Medical Imaging*, 6 (3): 034501.

Salih, O. and Viriri, S. 2020. Skin lesion segmentation using stochastic region-merging and pixel-based Markov random field. *Symmetry*, 12 (8): 1224.

Salve, M. V. P., Salve, M. A. K. and Jondhale, M. K. 2017. Brain tumor segmentation using MS algorithm. *International Journal of Engineering Technology Science and Research (IJETSR)*, 4 (4): 118 - 123.

Sammouda, R., Adgaba, N., Touir, A. and Al-Ghamdi, A. 2014. Agriculture satellite image segmentation using a modified artificial Hopfield neural network. *Computers in Human Behavior*, 30: 436-441.

Sarmah, S. and Bhattacharyya, D. K. 2012. A grid-density based technique for finding clusters in satellite image. *Pattern Recognition Letters*, 33 (5): 589-604.

Saxena, A., Prasad, M., Gupta, A., Bharill, N., Patel, O. P., Tiwari, A., Er, M. J., Ding, W. and Lin, C.-T. 2017. A review of clustering techniques and developments. *Neurocomputing*, 267: 664-681.

Scharr, H., Minervini, M., Fischbach, A. and Tsaftaris, S. A. 2014. Annotated image datasets of rosette plants. In: Proceedings of *13th European Conference on Computer Vision*. Zurich, Switzerland, 6-12 September 2014. Springer, 6-12.

Seo, H. J. and Milanfar, P. 2009. Static and space-time visual saliency detection by self-resemblance. *Journal of Vision*, 9 (12): 1-27.

Serra, J. 1986. Introduction to mathematical morphology. *Computer Vision, Graphics, and Image Processing*, 35 (3): 283-305.

Sethy, P., Negi, B. and Bhoi, N. 2017. Detection of healthy & defected diseased leaf of rice crop using K-Means clustering technique. *International Journal of Computer Applications*, 157 (1): 0975-8887.

Setitra, I. and Larabi, S. 2014. Background subtraction algorithms with post-processing: a review. In: Proceedings of *22nd International Conference on Pattern Recognition*. Washington, DC, USA, 24 - 28 August 2014. IEEE, 2436-2441.

Shafii, M. S. 2018. Reviewing the techniques of data clustering. *International Journal on Contemporary Computer Research (IJCCR)*, 2 (1): 11-16.

Shahin, A. I. and Almotairi, S. 2021. SVA-SSD: saliency visual attention single shot detector for building detection in low contrast high-resolution satellite images. *PeerJ Computer Science*, 7: e772.

Shan, P. F. 2018. Image segmentation method based on K-mean algorithm. *Eurasip Journal on Image and Video Processing*, 2018 (81): 1-9.

Shan, X., Zhao, D., Pan, M., Wang, D. and Zhao, L. 2019. Sea–Sky line and its nearby ships detection based on the motion attitude of visible light sensors. *Sensors*, 19 (18): 4004.

ShanmugaPriya, S. and Valarmathi, A. 2018. Efficient fuzzy c-means based multilevel image segmentation for brain tumor detection in MR images. *Design Automation for Embedded Systems*, 22: 81 - 93.

Sharma, A., López, Y. and Tsunoda, T. 2017. Divisive hierarchical maximum likelihood clustering. *BMC Bioinformatics*, 18 (16): 139-147.

Sharma, D. and Singhai, J. 2020. Fuzzy clustering algorithm with histogram based initialization for remotely sensed imagery. *Advances in Electrical and Electronic Engineering*, 18 (1): 41-49.

Sharma, N., Mishra, M. and Shrivastava, M. 2012. Colour image segmentation techniques and issues: an approach. *International Journal of Scientific & Technology Research*, 1 (4): 9-12.

Sheikholeslami, G., Chatterjee, S. and Zhang, A. 2000. WaveCluster: a wavelet-based clustering approach for spatial data in very large databases. *The VLDB Journal—The International Journal on Very Large Data Bases*, 8 (3-4): 289-304.

Sheng, D.-B., Kim, S.-B., Nguyen, T.-H., Kim, D.-H., Gao, T.-S. and Kim, H.-K. 2016. Fish injured rate measurement using color image segmentation method based on K-means clustering algorithm and Otsu's threshold algorithm. *Journal of the Korean Society for Power System Engineering*, 20 (4): 32 - 37.

Shi, J., Yan, Q., Xu, L. and Jia, J. 2015. Hierarchical image saliency detection on extended CSSD. *IEEE Transactions on Pattern Analysis and Machine Intelligence*, 38 (4): 717-729.

Shin, H.-C., Orton, M. R., Collins, D. J., Doran, S. J. and Leach, M. O. 2012. Stacked autoencoders for unsupervised feature learning and multiple organ detection in a pilot study using 4D patient data. *IEEE Transactions on Pattern Analysis and Machine Intelligence*, 35 (8): 1930-1943.

Shivhare, P. and Gupta, V. 2015. Review of image segmentation techniques including pre & post processing operations. *International Journal of Engineering and Advanced Technology*, 4 (3): 153-157.

Siddique, M., Bakr, A., Arif, R. B., Khan, M. M. R. and Ashrafi, Z. 2018. Implementation of Fuzzy C-Means and possibilistic C-Means clustering algorithms, cluster tendency analysis and cluster validation. *arXiv preprint arXiv:1809.08417*. Available: https://arxiv.org/abs/1809.08417 (Accessed 10 June 2021).

Sikha, O., Kumar, S. S. and Soman, K. 2018. Salient region detection and object segmentation in color images using dynamic mode decomposition. *Journal of Computational Science*, 25: 351-366.

Singh, M., Govil, M. C., Pilli, E. S. and Vipparthi, S. K. 2019. SOD-CED: salient object detection for noisy images using convolution encoder–decoder. *IET Computer Vision*, 13 (6): 578-587.

Singh, N. and Agrawal, R. 2015. Combination of Kullback–Leibler divergence and Manhattan distance measures to detect salient objects. *Signal, Image and Video Processing*, 9 (2): 427-435.

Singh, N., Arya, R. and Agrawal, R. 2014. A novel approach to combine features for salient object detection using constrained particle swarm optimization. *Pattern Recognition*, 47 (4): 1731-1739.

Singh, N., Arya, R. and Agrawal, R. 2016. A convex hull approach in conjunction with Gaussian mixture model for salient object detection. *Digital Signal Processing*, 55: 22-31.

Singh, N., Arya, R. and Agrawal, R. 2017. A novel position prior using fusion of rule of thirds and image center for salient object detection. *Multimedia Tools and Applications*, 76 (8): 10521-10538.

Singh, N., Arya, R. and Agrawal, R. 2018. Performance enhancement of salient object detection using superpixel based Gaussian mixture model. *Multimedia Tools and Applications*, 77 (7): 8511-8529.

Singh, N., Mishra, K. and Bhatia, S. 2020. SEAM-an improved environmental adaptation method with real parameter coding for salient object detection. *Multimedia Tools and Applications*, 79 (19): 12995-13010.

Singh, P. S. and Karthikeyan, S. 2022. Salient object detection in hyperspectral images using deep background reconstruction based anomaly detection. *Remote Sensing Letters*, 13 (2): 184-195.

Singh, R. P. and Dixit, M. 2015. Histogram equalization: a strong technique for image enhancement. *International Journal of Signal Processing, Image Processing and Pattern Recognition*, 8 (8): 345-352.

Singh, S. and Patnaik, T. 2015. An efficient shadow removal method using HSV color space for video surveillance. In: Proceedings of *Advances in Computing, Communications and Informatics (ICACCI), 2015 International Conference on*. IEEE, 1454-1460.

Singh, V. and Misra, A. K. 2017. Detection of plant leaf diseases using image segmentation and soft computing techniques. *Information Processing in Agriculture*, 4 (1): 41-49.

Singh, V. K. and Kumar, N. 2020. Saliency bagging: a novel framework for robust salient object detection. *The Visual Computer*, 36 (7): 1423-1441.

Singh, V. K., Kumar, N. and Singh, N. 2020. A hybrid approach using color spatial variance and novel object position prior for salient object detection. *Multimedia Tools and Applications*, 79 (39): 30045-30067.

Sisodia, D., Singh, L., Sisodia, S. and Saxena, K. 2012. Clustering techniques: a brief survey of different clustering algorithms. *International Journal of Latest Trends in Engineering and Technology (IJLTET)*, 1 (3): 82-87.

Sonawane, M. S. and Dhawale, C. A. 2015. A Brief survey on image segmentation methods. *IJCA Proceedings on National conference on Digital Image and Signal Processing*, 1 (DISP 2015): 1-5.

Song, H., Liu, Z., Du, H., Sun, G., Le Meur, O. and Ren, T. 2017. Depth-aware salient object detection and segmentation via multiscale discriminative saliency fusion and bootstrap learning. *IEEE Transactions on Image Processing*, 26 (9): 4204-4216.

Song, S., Jia, Z., Yang, J. and Kasabov, N. K. 2020a. A fast image segmentation algorithm based on saliency map and neutrosophic set theory. *IEEE Photonics Journal*, 12 (5): 1-16.

Song, S., Miao, Z., Yu, H., Fang, J., Zheng, K., Ma, C. and Wang, S. 2022. Deep domain adaptation based multi-spectral salient object detection. *IEEE Transactions on Multimedia*, 24: 128-140.

Song, S., Yu, H., Miao, Z., Guo, D., Ke, W., Ma, C. and Wang, S. 2019. An easy-to-hard learning strategy for within-image co-saliency detection. *Neurocomputing*, 358: 166-176.

Song, Y., Peng, G., Sun, D. and Xie, X. 2020b. Active contours driven by Gaussian function and adaptive-scale local correntropy-based K-means clustering for fast image segmentation. *Signal Processing*, 174: 107625.

Song, Z., Sui, H. and Hua, L. 2021. A hierarchical object detection method in large-scale optical remote sensing satellite imagery using saliency detection and CNN. *International Journal of Remote Sensing*, 42 (8): 2827-2847.

Soni, A. K., Lobiyal, D. K., Shaik, K. B., Ganesan, P., Kalist, V., Sathish, B. S. and Jenitha, J. M. M. 2015. Comparative study of skin color detection and segmentation in HSV and YCbCr color space. *Procedia Computer Science*, 57: 41-48.

Sreelatha, T., Subramanyam, M. and Prasad, M. G. 2019. Early detection of skin cancer using melanoma segmentation technique. *Journal of Medical Systems*, 43 (7): 1-7.

Sridevi, S. and Sundaresan, M. 2013. Survey of image segmentation algorithms on ultrasound medical images. In: Proceedings of *2013 International Conference on Pattern Recognition, Informatics and Mobile Engineering (PRIME)*. Tamilnadu, India, 21-22 February 2013. IEEE, 215-220.

Srivastava, G. and Srivastava, R. 2020. User-interactive salient object detection using YOLOv2, lazy snapping, and gabor filters. *Machine Vision and Applications*, 31 (3): 1-7.

Steen, K. A., Therkildsen, O. R., Green, O. and Karstoft, H. 2015. Detection of bird nests during mechanical weeding by incremental background modeling and visual saliency. *Sensors*, 15 (3): 5096-5111.

Su, T., Li, H., Zhang, S. and Li, Y. 2015. Image segmentation using mean shift for extracting croplands from high-resolution remote sensing imagery. *Remote Sensing Letters*, 6 (12): 952-961.

Sulakshana A. Gaikwad, Kalyani S.Deore, Monali K. Waykar, and Priyanka R.Dudhane, P. G. S. 2017. Fruit disease detection and classification. *International Research Journal of Engineering and Technology (IRJET)*, 4 (12): 1151 - 1154.

Sun, J., Lu, H. and Liu, X. 2015. Saliency region detection based on markov absorption probabilities. *IEEE Transactions on Image Processing*, 24 (5): 1639-1649.

Sun, L., Tang, Y. and Zhang, H. 2016. Visual saliency detection based on multi-scale and multi-channel mean. *Multimedia Tools and Applications*, 75 (1): 667-684.

Sun, S., Yan, S., Wang, Y. and Li, Y. 2016. Brain MRI image segmentation based on improved Fuzzy C-means algorithm. In: Proceedings of *International Conference on Smart City and Systems Engineering (ICSCSE)*. Hunan, China, 25-26 November 2016. IEEE, 503-505.

Sun, S. H., Jiang, M., He, D. J., Long, Y. and Song, H. B. 2019. Recognition of green apples in an orchard environment by combining the GrabCut model and Ncut algorithm. *Biosystems Engineering*, 187: 201-213.

Sutton, A. J., Song, F., Gilbody, S. M. and Abrams, K. R. 2000. Modelling publication bias in meta-analysis: a review. *Statistical Methods in Medical Research*, 9 (5): 421-445.

Taha, A. A. and Hanbury, A. 2015. Metrics for evaluating 3D medical image segmentation: analysis, selection, and tool. *BMC Medical Imaging*, 15 (1): 1-28.

Takács, P., Kovács, L. and Manno-Kovacs, A. 2021. A fusion of salient and convolutional features applying healthy templates for MRI brain tumor segmentation. *Multimedia Tools and Applications*, 80 (15): 22533-22550.

Tan, T. Y., Zhang, L. and Lim, C. P. 2020. Adaptive melanoma diagnosis using evolving clustering, ensemble and deep neural networks. *Knowledge-Based Systems*, 187: 104807.

Tang, J., Fan, D., Wang, X., Tu, Z. and Li, C. 2020. RGBT salient object detection: Benchmark and a novel cooperative ranking approach. *IEEE Transactions on Circuits and Systems for Video Technology*, 30 (12): 4421-4433.

Tang, J., Yang, G., Sun, Y., Xin, J. and He, D. 2019. Salient object detection of dairy goats in farm image based on background and foreground priors. *Neurocomputing*, 332: 270-282.

Tang, Y. and Wu, X. 2016. Saliency detection via combining region-level and pixel-level predictions with CNNs. In: Proceedings of *European Conference on Computer Vision*. Amsterdam, Netherlands, 11 - 14 October 2016. Springer, 809-825.

Tao, Z., Liu, H., Fu, H. and Fu, Y. 2019. Multi-view saliency-guided clustering for image cosegmentation. *IEEE Transactions on Image Processing*, 28 (9): 4634-4645.

Tavakoli, H. R., Rahtu, E. and Heikkilä, J. 2011. Fast and efficient saliency detection using sparse sampling and kernel density estimation. In: Proceedings of *Scandinavian Conference on Image Analysis*. Ystad, Sweden, 23 - 25 May 2011. Springer, 666-675.

Thi Le, P., Pham, T., Hsu, Y.-C. and Wang, J.-C. 2022. Convolutional blur attention network for cell nuclei segmentation. *Sensors*, 22 (4): 1586.

Tian, Y., Li, J., Yu, S. and Huang, T. 2015. Learning complementary saliency priors for foreground object segmentation in complex scenes. *International Journal of Computer Vision*, 111 (2): 153-170.

Tschandl, P., Rosendahl, C. and Kittler, H. 2018. The HAM10000 dataset, a large collection of multi-source dermatoscopic images of common pigmented skin lesions. *Scientific Data*, 5 (1): 1-9.

Tu, J., Gao, F., Sun, J., Hussain, A. and Zhou, H. 2021. Airport detection in SAR images via salient line segment detector and edge-oriented region growing. *IEEE Journal of Selected Topics in Applied Earth Observations and Remote Sensing*, 14: 314-326.

Tu, Z., Xia, T., Li, C., Wang, X., Ma, Y. and Tang, J. 2020. RGB-T image saliency detection via collaborative graph learning. *IEEE Transactions on Multimedia*, 22 (1): 160-173.

Ullah, I., Jian, M., Hussain, S., Guo, J., Yu, H., Wang, X. and Yin, Y. 2020. A brief survey of visual saliency detection. *Multimedia Tools and Applications*, 79: 34605–34645.

Umeki, Y., Funahashi, I., Yoshida, T. and Iwahashi, M. 2020. Salient object detection with importance degree. *IEEE Access*, 8: 147059-147069.

Ünver, H. M. and Ayan, E. 2019. Skin lesion segmentation in dermoscopic images with combination of YOLO and grabcut algorithm. *Diagnostics*, 9 (3): 72.

Varalakshmi, P., Devi, V. A., Ezhilarasi, M. and Sandhiya, N. 2021. Enhanced dermatoscopic skin lesion classification using machine learning techniques. In: Proceedings of *Sixth International Conference on Wireless Communications, Signal Processing and Networking (WiSPNET)*. Chennai, India, 25-27 March 2021. IEEE, 68-71.

Vincent, L. 1993. Morphological grayscale reconstruction in image analysis: applications and efficient algorithms. *IEEE Transactions on Image Processing*, 2 (2): 176-201.

Vocaturo, E., Zumpano, E. and Veltri, P. 2018. Image pre-processing in computer vision systems for melanoma detection. In: Proceedings of *2018 IEEE International Conference on Bioinformatics and Biomedicine (BIBM)*. Madrid, Spain, 3-6 December 2018. IEEE, 2117-2124.

Wang, A. and Wang, M. 2017. RGB-D salient object detection via minimum barrier distance transform and saliency fusion. *IEEE Signal Processing Letters*, 24 (5): 663-667.

Wang, H.-l., Zhu, M., Lin, C.-b. and Chen, D.-b. 2017a. Ship detection in optical remote sensing image based on visual saliency and AdaBoost classifier. *Optoelectronics Letters*, 13 (2): 151-155.

Wang, H., Zhu, C., Shen, J., Zhang, Z. and Shi, X. 2021a. Salient object detection by robust foreground and background seed selection. *Computers & Electrical Engineering*, 90: 106993.

Wang, J., Jiang, H., Yuan, Z., Cheng, M.-m., Hu, X. and Zheng, N. 2017b. Salient object detection: A discriminative regional feature integration approach. *International Journal of Computer Vision*, 123 (2): 251-268.

Wang, J., Lu, H., Li, X., Tong, N. and Liu, W. 2015. Saliency detection via background and foreground seed selection. *Neurocomputing*, 152: 359-368.

Wang, J., Wang, L. Q., Han, Y. L., Zhang, Y. and Zhou, R. Y. 2021b. On combining DeepSnake and global saliency for detection of orchard apples. *Applied Sciences*, 11 (14): 1-15.

Wang, M., Liu, X., Gao, Y., Ma, X. and Soomro, N. Q. 2017c. Superpixel segmentation: A benchmark. *Signal Processing: Image Communication*, 56: 28-39.

Wang, N. and Zhang, Y. 2021. Adaptive and fast image superpixel segmentation approach. *Image and Vision Computing*, 116: 104315.

Wang, W., Lai, Q., Fu, H., Shen, J., Ling, H. and Yang, R. 2022a. Salient object detection in the deep learning era: An in-depth survey. *IEEE Transactions on Pattern Analysis and Machine Intelligence*, 44 (6): 3239-3259.

Wang, X., Ning, C. and Xu, L. 2015. Saliency detection using mutual consistency-guided spatial cues combination. *Infrared Physics & Technology*, 72: 106-116.

Wang, X., Sun, T., Yang, R., Li, C., Luo, B. and Tang, J. 2019. Quality-aware dual-modal saliency detection via deep reinforcement learning. *Signal Processing: Image Communication*, 75: 158-167.

Wang, X. Q., Wang, S., Guo, Y. C., Hu, K. and Wang, W. S. 2022b. Coal gangue image segmentation method based on edge detection theory of star algorithm. *International Journal of Coal Preparation and Utilization*, (2022): 1-16.

Wang, Y. and Cao, Y. 2019a. Leukocyte nucleus segmentation method based on enhancing the saliency of saturation component. *Journal of Algorithms & Computational Technology*, 13: 1-10.

Wang, Y. and Cao, Y. 2019b. Quick leukocyte nucleus segmentation in leukocyte counting. *Computational and Mathematical Methods in Medicine*, 2019: 1-10.

Wang, Y., Qi, Q. and Shen, X. 2020. Image segmentation of brain MRI based on LTriDP and superpixels of improved SLIC. *Brain Sciences*, 10 (2): 116.

Wang, Z. and Tian, G. 2020. Integrating manifold ranking with boundary expansion and corners clustering for saliency detection of home scene. *Neurocomputing*, 379: 182-196.

Wang, Z. and Wu, X. 2016. Salient object detection using biogeography-based optimization to combine features. *Applied Intelligence*, 45 (1): 1-17.

Wang, Z., Xu, G., Wang, Z. and Zhu, C. 2016. Saliency detection integrating both background and foreground information. *Neurocomputing*, 216: 468-477.

Wazarkar, S. and Keshavamurthy, B. N. 2018. A survey on image data analysis through clustering techniques for real world applications. *Journal of Visual Communication and Image Representation*, 55: 596-626.

Wehrens, R., Buydens, L. M., Fraley, C. and Raftery, A. E. 2004. Model-based clustering for image segmentation and large datasets via sampling. *Journal of Classification*, 21 (2): 231-253.

Wu, C. and Yang, X. 2020. Robust credibilistic intuitionistic fuzzy clustering for image segmentation. *Soft Computing*, 24 (14): 10903-10932.

Wu, C. and Zhang, X. 2020. Total Bregman divergence-based fuzzy local information C-means clustering for robust image segmentation. *Applied Soft Computing*, 94: 106468.

Wu, C., Zheng, J., Feng, Z., Zhang, H., Zhang, L., Cao, J. and Yan, H. 2020. Fuzzy SLIC: Fuzzy simple linear iterative clustering. *IEEE Transactions on Circuits and Systems for Video Technology*, 31 (6): 2114-2124.

Wu, X., Ma, X., Zhang, J., Wang, A. and Jin, Z. 2018. Salient object detection via deformed smoothness constraint. In: Proceedings of *25th IEEE International Conference on Image Processing (ICIP)*. Athens, Greece, 7-10 October 2018. IEEE, 2815-2819.

Wu, Y., Jia, T., Pang, Y., Sun, J. and Xue, D. 2021. Salient object detection via a boundary-guided graph structure. *Journal of Visual Communication and Image Representation*, 75: 103048.

Xia, C. and Zhang, H. 2018. Unsupervised Salient object detection by aggregating multi-level cues. *IEEE Photonics Journal*, 10 (6): 1-11.

Xia, C., Zhang, H., Gao, X. and Li, K. 2020. Exploiting background divergence and foreground compactness for salient object detection. *Neurocomputing*, 383: 194-211.

Xiang, R., Jiang, H. Y. and Ying, Y. B. 2014. Recognition of clustered tomatoes based on binocular stereo vision. *Computers and Electronics in Agriculture*, 106: 75-90.

Xiong, L., Tang, G., Chen, Y. C., Hu, Y. X. and Chen, R. S. 2020. Color disease spot image segmentation algorithm based on chaotic particle swarm optimization and FCM. *Journal of Supercomputing*, 76 (11): 8756-8770.

Xu, D. and Tian, Y. 2015. A comprehensive survey of clustering algorithms. *Annals of Data Science*, 2 (2): 165-193.

Xu, L., Li, H., Zeng, L. and Ngan, K. N. 2013. Saliency detection using joint spatial-color constraint and multi-scale segmentation. *Journal of Visual Communication and Image Representation*, 24 (4): 465-476.

Xu, L. M., He, K. R. and Lv, J. D. 2019. Bayberry image segmentation based on manifold ranking salient object detection method. *Biosystems Engineering*, 178: 264-274.

Xu, M., Fralick, D., Zheng, J. Z., Wang, B., Tu, X. M. and Feng, C. 2017. The differences and similarities between two-sample t-test and paired t-test. *Shanghai Archives of Psychiatry*, 29 (3): 184-188.

Xu, R. and Wunsch, D. 2005. Survey of clustering algorithms. *IEEE Transactions on neural networks*, 16 (3): 645-678.

Yadav, H., Bansal, P. and Sunkaria, R. K. 2015. Color dependent K-means clustering for color image segmentation of colored medical images. In: Proceedings of *1st International Conference on Next Generation Computing Technologies (NGCT)* Dehradun, India, 4-5 September 2015. IEEE, 858-862.

Yan, K., Wang, X., Kim, J. and Feng, D. 2020. A new aggregation of DNN sparse and dense labeling for saliency detection. *IEEE Transactions on Cybernetics* 51(12): 5907 - 5920

Yang, C., Pu, J., Xie, G.-S., Dong, Y. and Liu, Z. 2017. Extended locality-constrained linear self-coding for saliency detection. *IEEE Signal Processing Letters*, 24 (10): 1458-1462.

Yang, C., Wang, X., Pu, J., Xie, G.-S., Liu, Z., Dong, Y. and Liang, L. 2018. Hybrid of extended locality-constrained linear coding and manifold ranking for salient object detection. *Journal of Visual Communication and Image Representation*, 56: 27-37.

Yang, C., Zhang, L. and Lu, H. 2013. Graph-regularized saliency detection with convex-hull-based center prior. *IEEE Signal Processing Letters*, 20 (7): 637-640.

Yang, C., Zhang, L., Lu, H., Ruan, X. and Yang, M.-H. 2013. Saliency detection via graph-based manifold ranking. In: Proceedings of *IEEE Conference on Computer Vision and Pattern recognition*. Washington, DC, United States, 23 - 28 June 2013. IEEE, 3166-3173.

Yang, J. and Yang, M.-H. 2017. Top-down visual saliency via joint CRF and dictionary learning. *IEEE Transactions on Pattern Analysis and Machine Intelligence*, 39 (3): 576-588.

Yang, Y. Y., Wang, R. F. and Feng, C. 2020. Level set formulation for automatic medical image segmentation based on fuzzy clustering. *Signal Processing-Image Communication*, 87: 115907.

Yanulevskaya, V., Uijlings, J. and Geusebroek, J.-M. 2013. Salient object detection: From pixels to segments. *Image and Vision Computing*, 31 (1): 31-42.

Yao, Q. and Gong, X. 2020. Saliency guided self-attention network for weakly and semi-supervised semantic segmentation. *IEEE Access*, 8: 14413-14423.

Ye, L., Liu, Z., Li, L., Shen, L., Bai, C. and Wang, Y. 2017. Salient object segmentation via effective integration of saliency and objectness. *IEEE Transactions on Multimedia*, 19 (8): 1742-1756.

Yeh, H.-H., Liu, K.-H. and Chen, C.-S. 2014. Salient object detection via local saliency estimation and global homogeneity refinement. *Pattern Recognition*, 47 (4): 1740-1750.

Yerpude, A. and Dubey, S. 2012. Colour image segmentation using K-medoids clustering. *International Journal of Computer Technology and Applications*, 3 (1): 152-154.

Youssef, A., Bloisi, D. D., Muscio, M., Pennisi, A., Nardi, D. and Facchiano, A. 2018. Deep convolutional pixel-wise labeling for skin lesion image segmentation. In: Proceedings of *2018 IEEE International Symposium on Medical Measurements and Applications (MeMeA)*. Rome, 11 - 13 June 2018. IEEE, 1-6.

Yu, B., Lu, J., Li, X. and Zhou, J. 2021a. Salience-aware face presentation attack detection via deep reinforcement learning. *IEEE Transactions on Information Forensics and Security*, 17: 413-427.

Yu, C.-y., Zhang, W.-s. and Wang, C.-l. 2015. A saliency detection method based on global contrast. *International Journal of Signal Processing, Image Processing and Pattern Recognition*, 8 (7): 111-122.

Yu, X., Wang, Y., Wang, S. and Hu, N. 2021b. Fully convolutional network and visual saliency-based automatic optic disc detection in retinal fundus images. *Journal of Healthcare Engineering*, 2021: 1-11.

Yu, Y., Ren, J., Zhang, Q., Yang, W. and Jiao, Z. 2020. Research on tire marking point completeness evaluation based on k-means clustering image segmentation. *Sensors*, 20 (17): 1-16.

Yuan, B., Han, L. and Yan, H. 2021. Explore double-opponency and skin color for saliency detection. *Neurocomputing*, 425: 219-230.

Yuan, J., Wang, D. and Li, R. 2014. Remote sensing image segmentation by combining spectral and texture features. *IEEE Transactions on Geoscience and Remote Sensing*, 52 (1): 16-24.

Yuan, X., Yu, H., Liang, J. and Xu, B. 2021. A novel density peaks clustering algorithm based on K nearest neighbors with adaptive merging strategy. *International Journal of Machine Learning and Cybernetics*, 12 (10): 2825-2841.

Yuheng, S. and Hao, Y. 2017. Image segmentation algorithms overview. *arXiv preprint arXiv:1707.02051*. Available: https://arxiv.org/abs/1707.02051 (Accessed 10 January 2021).

Yurtsever, U., Evirgen, H. and Avunduk, M. C. 2018. A new augmented K-Means algorithm for seed segmentation in microscopic images of the colon cancer. *Technical Gazette* 25 (2): 382-389.

Zafar, K., Gilani, S. O., Waris, A., Ahmed, A., Jamil, M., Khan, M. N. and Sohail Kashif, A. 2020. Skin lesion segmentation from dermoscopic images using convolutional neural network. *Sensors*, 20 (6): 1601.

Zanaty, E. 2018. An improved Fuzzy C-Means algorithm for MR brain image segmentation. *International Journal of Computer Science and Network Security*, 18 (4): 54 - 57.

Zhang, C. and He, D. 2020. A deep multiscale fusion method via low-rank sparse decomposition for object saliency detection based on urban data in optical remote sensing images. *Wireless Communications and Mobile Computing*, 2020: 1-14.

Zhang, C., Xiao, X., Li, X., Chen, Y.-J., Zhen, W., Chang, J., Zheng, C. and Liu, Z. 2014. White blood cell segmentation by color-space-based K-Means clustering. *Sensors*, 14 (9): 16128-16147.

Zhang, D. Y., Wang, Z. C., Jin, N., Gu, C. Y., Chen, Y. and Huang, Y. B. 2020a. Evaluation of efficacy of fungicides for control of wheat fusarium head blight based on digital imaging. *IEEE Access*, 8: 109876-109890.

Zhang, H., Xia, C. and Gao, X. 2017. Robust saliency detection via corner information and an energy function. *IET Computer Vision*, 11 (6): 379-388.

Zhang, J., Guo, Z., Jiao, T. and Wang, M. 2018a. Defect detection of aluminum alloy wheels in radiography images using adaptive threshold and morphological reconstruction. *Applied Sciences*, 8 (12): 2365.

Zhang, J., Wang, M., Lin, L., Yang, X., Gao, J. and Rui, Y. 2017a. Saliency detection on light field: A multi-cue approach. *ACM Transactions on Multimedia Computing, Communications, and Applications (TOMM)*, 13 (3): 1-22.

Zhang, L. 2020. A medical image segmentation methods based on SOM and wavelet transforms. In: Proceedings of *Eleventh International Symposium on Multispectral Image Processing and Pattern Recognition*. Wuhan, China, 14 February 2020. SPIE, 1142905.

Zhang, L., Li, C. and Sun, H. 2022. Object detection/tracking toward underwater photographs by remotely operated vehicles (ROVs). *Future Generation Computer Systems*, 126: 163-168.

Zhang, L., Li, Y., Wu, W., Chen, H. and Peng, Y. 2021a. Salient detection network for lung nodule detection in 3D Thoracic MRI Images. *Biomedical Signal Processing and Control*, 66: 102404.

Zhang, L. and Ma, J. 2021. Salient object detection based on progressively supervised learning for remote sensing images. *IEEE Transactions on Geoscience and Remote Sensing*, 59 (11): 9682-9696.

Zhang, L., Sun, Y., Luo, T. and Rahman, M. M. 2016. Note: A manifold ranking based saliency detection method for camera. *Review of Scientific Instruments*, 87 (9): 096103.

Zhang, L., Tong, M. H., Marks, T. K., Shan, H. and Cottrell, G. W. 2008. SUN: A Bayesian framework for saliency using natural statistics. *Journal of Vision*, 8 (7): 1-27.

Zhang, L., Wang, S., Liu, C. and Wang, Y. 2018b. Saliency-driven oil tank detection based on multidimensional feature vector clustering for SAR images. *IEEE Geoscience and Remote Sensing Letters*, 16 (4): 653-657.

Zhang, L. B., Ma, J., Lv, X. R. and Chen, D. H. 2020b. Hierarchical weakly supervised learning for residential area semantic segmentation in remote sensing images. *IEEE Geoscience and Remote Sensing Letters*, 17 (1): 117-121.

Zhang, L. B. and Yang, K. N. 2014. Region-of-Interest extraction based on frequency domain analysis and salient region detection for remote sensing image. *IEEE Geoscience and Remote Sensing Letters*, 11 (5): 916-920.

Zhang, L. B., Zhang, J., Wang, S. and Chen, J. 2015. Residential area extraction based on saliency analysis for high spatial resolution remote sensing images. *Journal of Visual Communication and Image Representation*, 33: 273-285.

Zhang, Q., Lin, J., Tao, Y., Li, W. and Shi, Y. 2017b. Salient object detection via color and texture cues. *Neurocomputing*, 243: 35-48.

Zhang, Q. R. and Wang, Y. F. 2021. A multi-cues based approach for visual saliency detection. *International Journal of Innovative Computing Information and Control*, 17 (4): 1435-1446.

Zhang, S., You, Z. and Wu, X. 2019. Plant disease leaf image segmentation based on superpixel clustering and EM algorithm. *Neural Computing and Applications*, 31 (2): 1225-1232.

Zhang, X., Jian, M., Sun, Y., Wang, H. and Zhang, C. 2020c. Improving image segmentation based on patch-weighted distance and fuzzy clustering. *Multimedia Tools and Applications*, 79 (1): 633-657.

Zhang, X., Wang, Y., Chen, Z., Yan, J. and Wang, D. 2020d. Saliency detection via image sparse representation and color features combination. *Multimedia Tools and Applications*, 79: 23147-23159.

Zhang, X., Wang, Y., Yan, J., Chen, Z. and Wang, D. 2020e. A unified saliency detection framework for visible and infrared images. *Multimedia Tools and Applications*, 79: 17331–17348.

Zhang, X. F., Sun, Y. J., Liu, H., Hou, Z. J., Zhao, F. and Zhang, C. M. 2021b. Improved clustering algorithms for image segmentation based on non-local information and back projection. *Information Sciences*, 550: 129-144.

Zhang, Y.-Y., Zhang, S., Zhang, P., Song, H.-Z. and Zhang, X.-G. 2020f. Local regression ranking for saliency detection. *IEEE Transactions on Image Processing*, 29: 1536-1547.

Zhang, Y., Zhang, F. and Guo, L. 2016. Saliency detection by selective color features. *Neurocomputing*, 203: 34-40.

Zhang, Y. Y., Wang, H., Lv, X. and Zhang, P. 2021c. Capturing the grouping and compactness of high-level semantic feature for saliency detection. *Neural Networks*, 142: 351-362.

Zhang, Y. Y., Zhang, S., Zhang, P. and Zhang, X. 2019. Saliency detection via background and foreground null space learning. *Signal Processing: Image Communication*, 70: 271-281.

Zhao, D., Li, J., Shi, Z., Jiang, Z. and Meng, C. 2019. Subjective saliency model driven by multi-cues stimulus for airport detection. *IEEE Access*, 7: 32118-32127.

Zhao, D., Ma, Y., Jiang, Z. and Shi, Z. 2017. Multiresolution airport detection via hierarchical reinforcement learning saliency model. *IEEE Journal of Selected Topics in Applied Earth Observations and Remote Sensing*, 10 (6): 2855-2866.

Zhao, M., Yue, L., Hu, J., Du, S., Li, P. and Wang, L. 2021a. Salient target detection in hyperspectral image based on visual attention. *IET Image Processing*, 15 (10): 2301-2308.

Zhao, M. Y., Jha, A., Liu, Q., Millis, B. A., Mahadevan-Jansen, A., Lu, L., Landman, B. A., Tyska, M. J. and Huo, Y. K. 2021b. Faster Mean-shift: GPU-accelerated clustering for cosine emb e dding-base d cell segmentation and tracking. *Medical Image Analysis*, 71: 102048.

Zhao, R., Ouyang, W., Li, H. and Wang, X. 2015a. Saliency detection by multi-context deep learning. In: Proceedings of *IEEE Conference on Computer Vision and Pattern Recognition*. Boston, MA, USA, 7-12 June 2015. IEEE, 1265-1274.

Zhao, R., Ouyang, W., Li, H. and Wang, X. 2015b. Saliency detection by multi-context deep learning. In: Proceedings of *Proceedings of the IEEE Conference on Computer Vision and Pattern Recognition*. Boston, MA, USA, June 7 - 12,. 1265-1274.

Zhao, T., Li, L., Ding, X., Huang, Y. and Zeng, D. 2016. Saliency detection with spaces of background-based distribution. *IEEE Signal Processing Letters*, 23 (5): 683-687.

Zhao, X., Qu, Y. and Zhang, H. 2014. Sports video segmentation using spectral clustering. *Journal of Multimedia*, 9 (7): 873-878.

Zhao, Y., Ma, J. L., Li, X. H. and Zhang, J. 2018. Saliency detection and deep learning-based wildfire identification in UAV imagery. *Sensors*, 18 (3): 712.

Zheng, J., Zhang, D., Huang, K. and Sun, Y. 2017. Adaptive image segmentation method based on the fuzzy c-means with spatial information. *IET Image Processing*, 12 (5): 785-792.

Zheng, X., Wang, Y., Wang, G. and Liu, J. 2018. Fast and robust segmentation of white blood cell images by self-supervised learning. *Micron*, 107: 55-71.

Zheng, X., Wang, Y., Wang, G. Y. and Chen, Z. 2014. A novel algorithm based on visual saliency attention for localization and segmentation in rapidly-stained leukocyte images. *Micron*, 56: 17-28.

Zhong, X. and Shih, F. Y. 2021. Automatic image pixel clustering based on mussels wandering optimization. *International Journal of Pattern Recognition and Artificial Intelligence*, 35 (02): 2154005.

Zhou, C. and Liu, C. 2015. An efficient segmentation method using saliency object detection. *Multimedia Tools and Applications*, 74 (15): 5623-5634.

Zhou, D., Tian, Y., Chen, W.-G. and Huang, G. 2021. Self-supervised saliency estimation for pixel embedding in road detection. *IEEE Signal Processing Letters*, 28: 1325-1329.

Zhou, J.-X., Liu, X.-d., Xu, T.-w., Gan, J.-h. and Liu, W.-q. 2018a. A new fusion approach for content based image retrieval with color histogram and local directional pattern. *International Journal of Machine Learning and Cybernetics*, 9 (4): 677-689.

Zhou, J., Zhai, J., Ren, Y. and Lu, A. 2018b. Background prior-based salient object detection via adaptive figure-ground classification. *KSII Transactions on Internet & Information Systems*, 12 (3): 1264-1286.

Zhou, J. B. and Jin, Z. 2013. A new framework for multiscale saliency detection based on image patches. *Neural Processing Letters*, 38 (3): 361-374.

Zhou, L. and Yang, Z. 2014. Salient region detection based on spatial and background priors. In: Proceedings of *IEEE International Conference on Information and Automation (ICIA)*. Hailar, china, 28-30 July 2014. IEEE, 262-266.

Zhou, L., Yang, Z., Yuan, Q., Zhou, Z. and Hu, D. 2015. Salient region detection via integrating diffusion-based compactness and local contrast. *IEEE Transactions on Image Processing*, 24 (11): 3308-3320.

Zhou, L., Yang, Z., Zhou, Z. and Hu, D. 2017. Salient region detection using diffusion process on a two-layer sparse graph. *IEEE Transactions on Image Processing*, 26 (12): 5882-5894.

Zhou, S. and Xu, Z. 2020. Automatic grayscale image segmentation based on affinity propagation clustering. *Pattern Analysis and Applications*, 23 (1): 331-348.

Zhou, X., Wang, Y., Zhu, Q., Xiao, C. and Lu, X. 2019. Ssg: superpixel segmentation and grabcut-based salient object segmentation. *The Visual Computer*, 35 (3): 385-398.

Zhu, W., Liang, S., Wei, Y. and Sun, J. 2014. Saliency optimization from robust background detection. In: Proceedings of *IEEE Conference on Computer Vision and Pattern Recognition*. Washington, DC, USA, 23-28 June 2014. IEEE, 2814-2821.

Zhu, W., Lou, J., Chen, L., Xia, Q. and Ren, M. 2017. Scene text detection via extremal region based double threshold convolutional network classification. *PloS one*, 12 (8): e0182227.

Zhu, X., Tang, C., Wang, P., Xu, H., Wang, M., Chen, J. and Tian, J. 2018. Saliency detection via affinity graph learning and weighted manifold ranking. *Neurocomputing*, 312: 239-250.

Zhuang, Y., Qi, B., Chen, H., Bi, F., Li, L. and Xie, Y. 2018. Locally oriented scene complexity analysis real-time ocean ship detection from optical remote sensing images. *Sensors*, 18 (11): 3799.

Zou, W., Liu, Z., Kpalma, K., Ronsin, J., Zhao, Y. and Komodakis, N. 2015. Unsupervised joint salient region detection and object segmentation. *IEEE Transactions on Image Processing*, 24 (11): 3858-3873.

Zuo, Q., Chen, S. and Wang, Z. 2021. R2AU-Net: Attention recurrent residual Convolutional Neural Network for multimodal medical image segmentation. *Security and Communication Networks*, 2021: 1-10.

APPENDIX A: Characteristics of included studies in the meta-analysis

Author	Country	Year	Approach	Method	Technique	Preprocessing	Unit of Processing	Dataset	No of Dataset	No of Images	Pre	Rec	F-Score
(Gion et al. 2015)	Japan	2015	Unsupervised	Saliency	Bottom-up, graph cut	No	Patch	Caltech; Grabcut	2	10	0.942	0.718	0.815
(Ramella 2021)	Italy	2021	Unsupervised	Saliency	Bottom-up	Yes	Pixel	PH2; ISBI2016 TRAIN; ISIC 2016 TEST	3	1507	0.934	0.894	0.880
(Ren et al. 2017)	China	2017	Unsupervised	Clustering	SLIC, grabcut	No	Region	ECSSD	1	17	0.929	0.943	0.936
(Li et al. 2021)	China	2021	Supervised	Saliency	Top-down, deep learning	Yes	Patch	Private	1	1200	0.879	0.900	0.889
(Tu et al. 2020)	China	2021	Unsupervised	Saliency	Bottom-up, region growing	No	Region	Private SARS Image dataset	1	8	0.811	0.877	0.816
(Ren et al. 2020)	China	2020	Unsupervised	Saliency and clustering	Bottom-up, SLIC	No	Region	Private Medical data	1	191	0.849	0.625	0.720
(Kompella and Kulkarni 2020)	India	2020	Supervised	Saliency and clustering	SLIC, Deep learning	No	Region	Imagepair, iCoseg	2	853	0.852	0.818	0.8345
(Galiano, Ramírez and Schiavi 2020)	Spain	2020	Supervised	Saliency	CNN	No	Patch	BRATS	1	220	0.766	0.732	0.728
(Joshi et al. 2020)	South Korea	2020	Unsupervised	Saliency	level set energy	No	Region	COVID-CT	1	216	0.985	0.970	0.977
(Kim 2019)	Korea	2019	Unsupervised	Saliency	Bottom-up, watershed	Yes	Patch	Private	1	70	0.930	0.917	0.923
(Xu, He and Lv 2019)	China	2019	Unsupervised	Saliency and clustering	Bottom-up, SLIC	Yes	Region	Private	1	120	0.930	0.830	0.900
(Song et al. 2017)	China	2017	Supervised	Saliency and clustering	Bootstrap learning, spectral clustering-based region	Yes	Region	NJUDS-2000	2	3000	0.772	0.840	0.757
(Zou et al. 2015)	China	2015	Unsupervised	Saliency	Bottom-up, mean shift-based regions	No	Region	MSRA-B, PASCAL	2	6500	0.725	0.760	0.741
(Zhou and Liu 2015)	China	2015	Unsupervised	Saliency and clustering	Mean Shift partitioning for superpixel	No	Region	MSRC-v2	1	1000	0.940	0.720	0.815
(Xu et al. 2013)	China	2013	Unsupervised	Saliency	Bottom-up	No	Pixel	MSRA-B	1	5000	0.860	0.630	0.727
(Yanulevskaya, Uijlings and Geusebroek 2013)	Italy	2013	Unsupervised	Saliency	Object based attention theory	No	Patch	Stereopair image dataset	1	5000	0.876	0.830	0.834
(Jung and Kim 2012)	Korea	2012	Unsupervised	Saliency	Visual attention model	No	Patch	MSRA; PASCAL	2	2352	0.890	0.920	0.904
(Ning et al. 2022)	China	2022	Supervised	Saliency and clustering	Deep learning, linear spectral clustering superpixel	No	Region	Private (Dataset 1-5)	5	3034	0.847	0.907	0.850
(Singh and Karthikeyan 2022)	India	2022	Supervised	Saliency	Deep learning	No	Pixel	HIS-SOD	1	60	0.840	0.760	0.798
(Kumar and Meenpal 2022)	India	2022	Unsupervised	Saliency	SIFT feature	Yes	Patch	CoMoFoD; MICC-F220	2	420	0.971	0.937	0.953
(Liu et al. 2022)	China	2022	Supervised	Saliency	CNN	No	Pixel	ECSSD; DUTs; PASCAL-S; HKU-IS; DUT-OMRON, SOD	6	22318	0.854	0.847	0.852
(Song et al. 2020)	China	2022	Supervised	Saliency	Deep learning	No	Pixel	RGBN-SOD; RGBN-3000	2	5000	0.872	0.885	0.847
(Moghaddam et al. 2021)	New Zealand	2021	Supervised	Saliency	Genetic programming, region	No	Region	ECSSD; PASCAL; HKU-IS; DUT-OMRON; SED1; ASD	6	2684	0.782	0.709	0.766

(Li et al. 2022)	China	2021	Unsupervised	Saliency and clustering	Bottom-up, SLIC	Yes	Region	MSTAR	1	195	0.941	0.880	0.910
(Shahin and Almotairi 2021)	Saudi Arabia	2021	Supervised	Saliency	Deep learning	Yes	Pixel	Inria; Massachusetts datasets	2	100	0.600	0.840	0.808
(Zhang and Ma 2021)	China	2021	Supervised	Saliency	CNN	No	Pixel	GeoEye-1; SPOT5	2	20	0.899	0.801	0.870
(Zhang et al. 2021)	China	2021	Unsupervised	Saliency and clustering	High level semantic features and k-Means, entropy based superpixel	No	Region	ECSSD; DUTOMRON; PASAL-S; HKU-IS	4	11465	0.770	0.705	0.752
(Joseph and Olugbara 2021)	South Africa	2021	Unsupervised	Saliency and clustering	Bottom-up and histogram clustering	No	Region	ECSSD; HKUIS; SOC; Boundary dataset; Center dataset; Complex background dataset; Low contrast dataset; Multiple objects dataset; Overlap dataset	9	8452	0.879	0.738	0.841
(Yu et al. 2021)	China	2021	Unsupervised	Saliency and clustering	SLIC, CNN	No	Region	DRISHTI-GS; RIM-ONE	1	270	0.932	0.905	0.918
(Moradi, Bayat and Charmi 2021)	Iran	2021	Unsupervised	Saliency and clustering	SLIC and linear quadratic regulator	No	Region	ECSSD; PASCAL; SED2	3	1950	0.757	0.677	0.709
(Zhang and Wang 2021)	China	2021	Unsupervised	Saliency and clustering	Bottom-up, SLIC	No	Region	ECSSD; PASCAL-S; DUTOMRON; SOD	4	2318	0.713	0.545	0.678
(Wang et al. 2021)	China	2021	Supervised	Saliency	Deep learning	No	Pixel	Private (apple images)	1	1036	0.957	0.882	0.919
(Song, Sui and Hua 2021)	China	2021	Supervised	Saliency	CNN	No	Pixel	GE	1	10000	0.932	0.950	0.933
(Jian et al. 2021)	China	2021	Unsupervised	Saliency and clustering	Bottom-up, SLIC	No	Region	ECSSD; MSRA; SOD	3	11300	0.803	0.510	0.769
(Moradi and Bayat 2021)	Iran	2021	Supervised	Saliency and clustering	Bottom-up, SLIC	Yes	Region	ECSSD; PASCAL; SED1	3	1950	0.801	0.535	0.651
(Zhao et al. 2021)	China	2021	Unsupervised	Saliency	Frequency tuned	No	Pixel	HS-SOD	1	60	0.900	0.880	0.898
(Zhang et al. 2021a)	China	2021	Supervised	Saliency	CNN	No	Pixel	Private MRI dataset	1	142	0.115	0.911	0.124
(Niu et al. 2020)	China	2021	Unsupervised	Saliency and clustering	SLIC, binocular line scanning	No	Region	RSDD	1	113	0.839	0.783	0.810
(Yuan, Han and Yan 2021)	China	2021	Unsupervised	Saliency and clustering	skin saliency, superpixel	No	Region	ECSSD	1	1000	0.726	0.578	0.639
(He et al. 2021)	China	2021	Unsupervised	Saliency and clustering	SLIC, Multi scale visual saliency	No	Region	Sardinia; Ottawa; Mexico	3	6	0.934	0.751	0.828
(Ma et al. 2021)	China	2021	Supervised	Saliency	Siamese network	No	Pixel	DUTOMRON; ECSSD; HKU-IS; PASCAL; SOD	5	11765	0.917	0.891	0.908
(Nawaz and Yan 2021)	Hong Kong	2021	Supervised	Saliency and clustering	SLIC, CNN	No	Region	MSRA-10K; SED1; SED2; ECSSD; DUT-OMRON; HKU-IS	6	20815	0.824	0.749	0.794
(Zhou et al. 2021)	China	2021	Supervised	Saliency and clustering	FCN (full convolutional network), k-means clustering	No	Region	KITTI road dataset; Tian traffic dataset	2	3289	0.860	0.861	0.873
(Tang et al. 2020)	China	2020	Unsupervised	Saliency and clustering	SLIC and graph based	No	Region	VT1000	1	1000	0.819	0.661	0.739
(Li et al. 2020a)	China	2020	Supervised	Saliency	CNN	No	Pixel	ORSSD	1	200	0.914	0.803	0.886

(Jing et al. 2020)	China	2020	Unsupervised	Saliency	Wavelet thresholding	Yes	Pixel	Private- Bobbin yarn images	1	600	0.952	0.980	0.967
(Takács, Kovács and Manno-Kovacs 2021)	Hungary	2021	Supervised	Saliency	Deep learning	No	Pixel	BRATS2015; BRATS2018	2	57	0.890	0.825	0.880
(Li et al. 2020b)	China	2020	Unsupervised	Saliency and clustering	SLIC, Thresholding	Yes	Region	MSTAR; MiniSAR	2	198	0.967	0.803	0.928
(Song et al. 2020a)	China	2020	Unsupervised	Saliency	Saliency and thresholding	Yes	Pixel	MSRA10K	1	10000	0.679	0.680	0.680
(Pang et al. 2020)	China	2020	Supervised	Saliency and clustering	SLIC, Bagging based learning	No	Region	ECSSD; PASCAL-S; DUT-OMRON; SOD	4	7322	0.768	0.665	0.744
(Ma et al. 2020)	China	2020	Unsupervised	Saliency and clustering	SLIC, Hierarchical self-diffusion	Yes	Region	MSTAR	1	20	0.769	1.000	0.813
(Liang et al. 2020)	China	2020	Supervised	Saliency	CNN based learning	No	Pixel	SSB; NJUDS	2	3000	0.801	0.869	0.798
(Singh and Kumar 2020)	India	2020	Unsupervised	Saliency	Saliency bagging, superpixel	No	Region	MSRA10K; DUT-OMRON; ECSSD; PASCAL-S; SED2; THUR15K	6	23118	0.759	0.687	0.735
(Hu et al. 2020)	China	2020	Unsupervised	Saliency and clustering	Bottom-up, K-Means, Adaptive thresholding, SLIC	Yes	Region	PH2; ISBI2016	2	1100	0.939	0.854	0.891
(Zhang and He 2020)	China	2020	Supervised	Saliency and clustering	SLIC and deep learning	No	Region	Google Earth	1	6	0.967	0.666	0.864
(Du et al. 2020)	China	2020	Unsupervised	Saliency	CNN	No	Pixel	MiniSAR	1	2	0.919	0.966	0.942
(He, Guo and Yuan 2020)	China	2020	Supervised	Saliency	Flourier Transform	No	Pixel	Google Earth	1	1210	0.925	0.985	0.954
(Srivastava and Srivastava 2020)	India	2020	Supervised	Saliency and clustering	Saliency, K-Means and deep learning, Texture segmentation	Yes	Region	ASD; ECSSD; PASCAL-S	3	2850	0.809	0.746	0.799
(Lopez-Alanis et al. 2020)	Mexico	2020	Supervised	Saliency	Conditional Random rule-based aggregation	No	Pixel	MSRA1000; ECSSD; iCoseg	3	2643	0.826	0.734	0.805
(Singh, Mishra and Bhatia 2020)	India	2020	Unsupervised	Saliency	Environment adaptation	No	Pixel	MSRA-B; ASD; SAA_GT; SOD; SED1; SED2	6	11500	0.889	0.918	0.904
(Deeba, Bui and Wahid 2020)	Canada	2020	Unsupervised	Saliency	Bottom-up	Yes	Patch	CVC-ColonDB; ETIS-Larib	2	1120	0.442	0.670	0.530
(Huang et al. 2020)	China	2020	Unsupervised	Saliency and clustering	Graph based, SLIC	No	Region	VT1000; VT821	2	1821	0.847	0.675	0.748
(Jiang et al. 2019)	USA	2020	Unsupervised	Saliency and clustering	Bottom-up, SLIC	No	Region	MSRA10K; ECSSD; DUT-OMRON	3	16168	0.749	0.787	0.754
(Piao et al. 2019)	China	2020	Unsupervised	Saliency and clustering	Optimization model, SLIC	No	Region	LFSD	1	100	0.894	0.750	0.831
(Qiu et al. 2020)	China	2020	Unsupervised	Saliency	Bottom-up	Yes	Pixel	NEU; MT; RSDD; MCSD	4	572	0.845	0.891	0.845
(Tu et al. 2019)	China	2020	Unsupervised	Saliency and clustering	Bottom-up, SLIC	No	Region	VT1000; VT821	2	1821	0.824	0.687	0.736
(Yao and Gong 2020)	China	2020	Supervised	Saliency	Self-attention model and Classification network	No	Pixel	PASCAL VOC	1	1449	0.764	0.574	0.730
(Zhang et al. 2019)	China	2020	Unsupervised	Saliency and clustering	Pretrianed network for Saliency and Entropy based superpixel	No	Region	ECSSD; DUT-OMRON; PASCAL-S; HKU-IS	4	11465	0.791	0.624	0.742

(Qian et al. 2019)	China	2019	Supervised	Saliency and clustering	Recurrent fine-tune network, geodesic k-means algorithm for superpixel	No	Region	DUTS: HKU-IS; DUT-OMRON; ECSSD	4	21168	0.782	0.731	0.742
(Li et al. 2019)	Hong Kong	2019	Supervised	Saliency	Deep learning	No	Pixel	optical RSI	1	800	0.867	0.765	0.841
(Song et al. 2019)	USA	2019	Supervised	Saliency and clustering	SLIC, multiple instance learning	No	Region	WICOS; SYN-Normal; SYN-Noisy	3	536	0.863	0.789	0.834
(Jia et al. 2019)	China	2019	Unsupervised	Saliency	Bottom-up, superpixel graph cut	No	Region	ECSSD	1	1000	0.755	0.620	0.681
(Singh et al. 2019)	India	2019	Supervised	Saliency and clustering	K-Means, CNN, superpixel using K-Means	No	Region	MSRA-B; ASD; BSDS500; SOD; SED1; SED2	6	7000	0.858	0.898	0.867
(Wang et al. 2019)	China	2019	Supervised	Saliency	Deep learning	Yes	Pixel	RGBT- images	1	821	0.855	0.863	0.844
(Lopez-Alanis et al. 2019)	Mexico	2019	Unsupervised	Saliency	Rule based learning	No	Pixel	MSRA10K; ECSSD; iCoseg	3	11643	0.847	0.513	0.770
(Huang, Xing and Wang 2019)	China	2019	Unsupervised	Saliency	Deep learning	No	Pixel	NJU2000; NJU400	2	797	0.880	0.899	0.885
(Jahanifar et al. 2019)	Iran	2019	Supervised	Saliency	Regional feature integration, superpixel by graph-based segmentation	Yes	Region	PH2. ISIC2016; ISIC2017	3	4097	0.905	0.894	0.899
(Jing et al. 2018)	China	2018	Unsupervised	Saliency and clustering	SLIC, top-down	No	Region	private	1	200	0.964	0.923	0.932
(Zhou et al. 2019)	China	2019	Unsupervised	Saliency and clustering	SLIC, DBSCAN and bottom-up	No	Region	MSRA-K; ECSSD; SED1	3	2100	0.883	0.800	0.861
(Manno-Kovacs 2018)	Hungary	2018	Unsupervised	Saliency	Bottom-up	No	Pixel	SED	1	100	0.883	0.783	0.830
(Zhang et al. 2019b)	China	2019	Unsupervised	Saliency and clustering	Bottom-up, SLIC	No	Region	MSRA-10K; ECSSD; DUT-OMRON; JuddDB	4	17068	0.675	0.591	0.651
(Liu and Yang 2019)	China	2019	Unsupervised	Saliency and clustering	Bottom-up, SLIC	No	Region	ECCSD; DUT-OMRON; MSRA-10K	3	16168	0.706	0.546	0.611
(Liu and Yuan 2019)	China	2019	Supervised	Saliency and clustering	SLIC, CNN	No	Region	MSRA-10K; ECSSD; DUT-OMRON; HKU-IS; THUR-15K; XPIE	6	25399	0.840	0.893	0.850
(Zhao et al. 2019)	China	2019	Unsupervised	Saliency and clustering	Bottom-up, SLIC	No	Region	Airport dataset	1	360	0.884	0.891	0.887
(Abkenar, Sadreazami and Ahmad 2018)	Canada	2018	Unsupervised	Saliency and clustering	Bottom-up, SLIC	No	Region	MSRA; MSRA10K; HKU-IS; PASCAL-S; DUT-OMRON	5	21465	0.784	0.732	0.766
(Li, Du and Wang 2018)	China	2018	Unsupervised	Saliency and clustering	Bottom-up, SLIC	No	Region	miniSAR	1	2	0.656	0.906	0.761
(Yang et al. 2018)	China	2018	Supervised	Saliency and clustering	SLIC, K-Means, linear coding	Yes	Region	DUT-OMRON; SED2; ECSSD	3	6268	0.756	0.602	0.670
(Li, Zhou and Bai 2017)	China	2018	Unsupervised	Saliency	Bottom-up	Yes	Patch	Private	1	200	0.871	0.787	0.825
(Jian et al. 2018)	China	2018	Unsupervised	Saliency and clustering	Bottom-up, SLIC	No	Region	OUC-VISION	1	4400	0.641	0.652	0.644
(Li et al. 2018)	China	2018	Unsupervised	Saliency and clustering	SLIC, CNN	No	Region	ECSSD; Pascal-s; SOD; DUT-OMRON	4	7318	0.771	0.749	0.764

(Singh, Arya and Agrawal 2018)	India	2018	Unsupervised	Saliency and clustering	SLIC, K-Means, bottom-up	No	Region	MSRA-B; ASD; SAA_GT; SOD; SED1; SED1; SED1	7	12500	0.795	0.842	0.817
(Annum, Riaz and Ghafoor 2018)	P-akistan	2018	Unsupervised	Saliency and clustering	Bottom-up, SLIC	Yes	Region	ASD; MSRA-B; THUS-10000; ECSSD; DUT-OMRON	5	22168	0.799	0.746	0.759
(Zhao et al. 2018)	China	2018	Supervised	Saliency	Deep learning	Yes	Pixel	Private Dataset1 and 2	2	450	0.981	0.937	0.958
(Ayoub et al. 2018)	China	2018	Unsupervised	Saliency	Bottom-up	No	Pixel	MSRA; SED2	2	5100	0.781	0.644	0.714
(Feng et al. 2018)	China	2018	Unsupervised	Saliency	Bottom-up	No	Pixel	Wild animal dataset	1	1000	0.490	0.732	0.530
(Olugbara, Taiwo and Heukelman 2018)	South Africa	2018	Unsupervised	Saliency	Bottom-up	No	Patch	PH2; ISBI2016	2	120	0.921	0.976	0.947
(Zhou et al. 2017)	China	2017	Unsupervised	Saliency and clustering	Bottom-up, K-Means, SLIC	No	Region	ASD; DUR-OMRON; ECSSD; MSRA5K; MSRA10K	5	22168	0.809	0.740	0.764
(Yang et al. 2017)	China	2017	Unsupervised	Saliency and clustering	Bottom-up, SLIC	No	Region	DUT; ECSSD; SED2	3	6268	0.759	0.581	0.661
(Zhang, Xia and Gao 2017)	China	2017	Unsupervised	Saliency and clustering	Bottom-up, SLIC	Yes	Region	ASD; ECSSD; SED1	3	2100	0.886	0.738	0.847
(Ye et al. 2017)	China	2017	Unsupervised	Saliency and clustering	SLIC	No	Region	MSRA-B; MSRA-10K; PASCAL1500	3	16500	0.845	0.778	0.800
(Zhang et al. 2017)	China	2017	Unsupervised	Saliency and clustering	Bottom-up, SLIC	No	Region	HFUT_Lytro; LFSD	2	355	0.724	0.707	0.718
(Lou et al. 2017)	China	2017	Unsupervised	Saliency and clustering	Spatial clustering, Bottom-up	No	Pixel	Sky; Sea-sky; Ground	3	1093	0.772	0.998	0.835
(Fan et al. 2017)	China	2017	Unsupervised	Saliency	Bottom-up	No	Patch	EDRA; PH2; ISBI 2016	3	1666	0.973	0.852	0.906
(Zhao et al. 2017)	China	2017	Supervised	Saliency and clustering	Bottom-up, top-down, SLIC	No	Region	RSI	1	730	0.677	0.774	0.711
(Huang, Feng and Sun 2017)	China	2017	Unsupervised	Saliency and clustering	Bottom-up, SLIC	No	Region	iCoseg; image Pair	2	853	0.937	0.635	0.863
(Wang and Wang 2017)	China	2017	Unsupervised	Saliency	Bottom-up	Yes	Pixel	RGBD1000	1	1000	0.651	0.717	0.635
(Singh, Arya and Agrawal 2017)	India	2017	Unsupervised	Saliency and clustering	Bottom-up, K-Means based superpixel	No	Region	MSRAB; ASD; SAA_GT; SOD; SED1; SED2	6	11500	0.852	0.879	0.865
(Wang et al. 2017)	China	2017	Unsupervised	Saliency and clustering	Bottom-up, SLIC	No	Region	Remote sensing data	1	261	0.966	0.966	0.966
(Hwang et al. 2017)	Korea	2017	Supervised	Saliency and clustering	SLIC, seed propagation	No	Region	ASD	1	1000	0.937	0.866	0.920
(Zhang et al. 2016)	China	2016	Unsupervised	Saliency and clustering	Bottom-up, SLIC	No	Region	ASD; ECSSD; THUS10000	3	12000	0.903	0.840	0.890
(Singh, Arya and Agrawal 2016)	India	2016	Unsupervised	Saliency and clustering	Bottom-up, EM, SLIC	No	Region	MSRAB; ASD; SED1; SOD; SED2; SAA_GT	6	11500	0.848	0.905	0.875
(Arya, Singh and Agrawal 2016)	India	2016	Unsupervised	Saliency	Bottom-up	No	Patch	MSRA; SOD	2	5000	0.686	0.877	0.770
(Wang and Wu 2016)	China	2016	Unsupervised	Saliency	Bottom-up and top-down	Yes	Pixel	MSRA; SED and iCoseg	3	300	0.879	0.844	0.851
(Zhao et al. 2016)	China	2016	Unsupervised	Saliency and clustering	Bottom-up, SLIC	No	Region	MSRA; PASCAL	2	6500	0.740	0.688	0.697
(Shi et al. 2015)	Hong Kong	2016	Unsupervised	Saliency	Bottom-up	No	Patch	ECSSD	1	1000	0.764	0.656	0.678

(Aytekin, Kiranyaz and Gabbouj 2016)	Finland	2016	Unsupervised	Saliency and clustering	SLIC, learn to rank	No	Region	MSRA10K; DUT-OMRON; MSRA; PASCAL; ECSSD; BSD	6	18968	0.838	0.793	0.814
(Kim et al. 2016)	Korea	2016	Supervised	Saliency and clustering	SLIC	No	Region	MSRA-B; PASCAL; ECSSD	3	4350	0.797	0.613	0.707
(Sun, Tang and Zhang 2016)	China	2016	Unsupervised	Saliency	Bottom-up	No	Pixel	MSRA	1	1000	0.803	0.715	0.781
(Nan et al. 2015)	China	2015	Unsupervised	Saliency and clustering	Mean shift	No	Region	MSRA-1000	1	1000	0.891	0.727	0.832
(Ma et al. 2015)	Hong Kong	2015	Supervised	Saliency	Machine learning	No	Pixel	MSRA	1	500	0.929	0.731	0.804
(Wang, Ning and Xu 2015)	China	2015	Unsupervised	Saliency	Bottom-up	No	Patch	Private	1	400	0.665	0.768	0.704
(Qi et al. 2015)	China	2015	Unsupervised	Saliency	Bottom-up	No	Pixel	Private	1	337	0.881	0.863	0.872
(Bao et al. 2015)	China	2015	Unsupervised	Saliency	Bottom-up	No	Pixel	ASD; MSRA-B	2	6000	0.613	0.652	0.610
(Steen et al. 2015)	Denmark	2015	Unsupervised	Saliency	Bottom-up	Yes	Pixel	Private	1	30	0.537	0.460	0.496
(Singh and Agrawal 2015)	India	2015	Unsupervised	Saliency and clustering	Bottom-up and K-Means	No	Patch	MSRA-B	1	5000	0.806	0.874	0.817
(Manke and Jalal 2015)	India	2015	Unsupervised	Saliency	Bottom-up	No	Pixel	MSRA	1	1000	0.700	0.530	0.603
(Tian et al. 2015)	China	2015	Supervised	Saliency	Saliency and Maximum likelihood learning	No	Pixel	MOCB; SOCB	2	2474	0.850	0.865	0.860
(Lou, Ren and Wang 2014)	China	2014	Unsupervised	Saliency and clustering	SLIC, graph based	No	Region	MSRA-1000	1	1000	0.824	0.719	0.797
(Chuang, Chen and Chen 2014)	China	2014	Unsupervised	Saliency	Bottom-up	No	Pixel	ASD	1	1000	0.665	0.857	0.697
(Imamoglu et al. 2014)	Japan	2014	Unsupervised	Saliency	PDF, PCNN	No	Pixel	Private Dataset1 and 2	2	130	0.956	0.960	0.957
(Kim and Kim 2014)	Korea	2014	Unsupervised	Saliency	Bottom-up	No	Patch	MSRA and PASCAL	2	800	0.738	0.882	0.803
(Singh, Arya and Agrawal 2014)	India	2014	Unsupervised	Saliency	Bottom-up	No	Pixel	MSRA-B	1	5000	0.811	0.957	0.878
(Yeh, Liu and Chen 2014)	Taiwan	2014	Unsupervised	Saliency	Bottom-up, Region growing	Yes	Patch	MSRA-B	1	5000	0.878	0.878	0.878
(Kim, Sim and Kim 2013)	Korea	2014	Unsupervised	Saliency and clustering	Random Walk, K-Means superpixel grouping	No	Region	MSRA; TORONTO; FIFA; MIT	4	2355	0.387	0.597	0.411
(Liang *et al.* 2014)	China	2014	Unsupervised	Saliency and clustering	Region clustering pixel grouping	No	Region	MSRA-B	1	5000	0.847	0.404	0.617
(Chuang et al. 2014)	China	2014	Unsupervised	Saliency	Isophate	No	Pixel	ASD	1	1000	0.665	0.857	0.697
(Zheng et al. 2014)	China	2014	Unsupervised	Saliency and clustering	Average absolute difference, MS clustering	Yes	Region	Private-Leukocyte dataset	1	157	0.919	0.994	0.955
(Li, Meng and Ngan 2013)	China	2013	Unsupervised	Saliency and clustering	Minimum spanning tree, K-Means	No	Region	iCoseg; MSRC	2	1234	0.542	0.726	0.644
(Zhou and Jin 2013)	China	2013	Unsupervised	Saliency	Bottom-up	No	Patch	ASD	1	1000	0.900	0.880	0.900
(Liu et al. 2012)	China	2012	Unsupervised	Saliency and clustering	Mean Shift partitioning for superpixel	No	Region	MSRA-B	1	1000	0.909	0.823	0.879
(Thi Le et al. 2022)	Taiwan	2022	Supervised	Saliency	Convolution blur attention network	Yes	Pixel	MonuSeg; DSB	2	358	0.901	0.856	0.876
(Joseph and Olugbara 2022)	South Africa	2022	Unsupervised	Saliency and clustering	Bottom-up, Histogram clustering	No	Region	PH2; ISIC2018; HAM10000	3	12809	0.843	0.800	0.833
(Hui et al. 2021)	China	2021	Supervised	Saliency	DPAC-Unet	No	Pixel	ATLAS	1	239	0.656	0.599	0.598

(Karthik, Menaka and Hariharan 2021)	India	2021	Supervised	Saliency	CNN	No	Region	Covid-19 Chess X-ray images	1	512	0.984	0.961	0.972
(Liu, Kuang and Ji 2020)	China	2020	Unsupervised	Clustering	SLIC and sparse subspace clustering	Yes	Region	BRATS 2015	1	25	0.961	0.774	0.858
(Shan et al. 2019)	China	2019	Unsupervised	Saliency	Bottom-up	Yes	Pixel	Private	1	450	0.685	0.883	0.772
(Saleem et al. 2019)	Pakistan	2019	Unsupervised	Saliency	Bottom-up, texture segment for superpixel generation	Yes	Region	ISIC 2017	1	2000	0.921	0.795	0.909
(Zhuang et al. 2018)	China	2018	Unsupervised	Saliency and clustering	Bottom-up, Feature clustering	No	Pixel	SPOT-5; GF-1	1	3215	0.799	0.732	0.793
(Qin et al. 2018)	China	2018	Supervised	Saliency and clustering	SLIC, CNN	Yes	Region	LiTS-Liver Tumour dataset	1	100	0.920	0.840	0.913
(Zhu et al. 2017)	China	2017	Supervised	Saliency and clustering	K-Means, CNN, region generation using k-means	No	Region	ICDAR 2011; ICDAR 2013	2	255	0.880	0.797	0.835
(Paramanandam et al. 2016)	India	2016	Unsupervised	Saliency	Bottom-up	Yes	Patch	Clinical dataset	1	8	0.928	0.767	0.853